Computational study of internal and external condensing flows and experimental synthesis to investigate their attainability and stability in ground-based and space-based environments

Shantanu Kulkarni
Michigan Technological University

Computational Study of Internal and External Condensing Flows and

Experimental Synthesis to Investigate their Attainability and Stability in

Ground-Based and Space-Based Environments

By

Shantanu Kulkarni

A DISSERTATION

In partial fulfillment of the requirements for the degree of

DOCTOR OF PHILOSOPHY

(Mechanical Engineering-Engineering Mechanics)

MICHIGAN TECHNOLOGICAL UNIVERSITY

2010

This dissertation, "Computational Study of Internal and External Condensing Flows and Experimental Synthesis to Investigate their Attainability and Stability in Ground-Based and Space-Based Environments," is hereby approved in partial fulfillment of the requirements for the degree of DOCTOR OF PHILOSOPHY in the field of Mechanical Engineering-Engineering Mechanics.

DEPARTMENT:
Mechanical Engineering-Engineering Mechanics

Signatures:

Dissertation Advisor   _____

Dr.Amitabh Narain, Professor
Mechanical Engineering-Engineering Mechanics

Department Chair   _____

William W. Predebon, Professor
Mechanical Engineering-Engineering Mechanics

Date Approved   _____

ABSTRACT

Shantanu Kulkarni

Michigan Technological University, August 2010

Advisor: Professor Amitabh Narain, MEEM, Michigan Tech University

This doctoral thesis presents the computational work and synthesis with experiments for internal (tube and channel geometries) as well as external (flow of a pure vapor over a horizontal plate) condensing flows. The computational work obtains accurate numerical simulations of the full two dimensional governing equations for steady and unsteady condensing flows in gravity/0g environments.

This doctoral work investigates flow features, flow regimes, attainability issues, stability issues, and responses to boundary fluctuations for condensing flows in different flow situations. This research finds new features of unsteady solutions of condensing flows; reveals interesting differences in gravity and shear driven situations; and discovers novel boundary condition sensitivities of shear driven internal condensing flows. Synthesis of computational and experimental results presented here for gravity driven in-tube flows lays framework for the future two-phase component analysis in any thermal system.

It is shown for both gravity and shear driven internal condensing flows that steady governing equations have *unique* solutions for given inlet pressure, given inlet vapor mass flow rate, and fixed cooling method for condensing surface. But unsteady equations of shear driven internal condensing flows can yield different "quasi-steady" solutions

based on different specifications of exit pressure (equivalently exit mass flow rate) concurrent to the inlet pressure specification. This thesis presents a novel categorization of internal condensing flows based on their sensitivity to concurrently applied boundary (inlet and exit) conditions.

The computational investigations of an external shear driven flow of vapor condensing over a horizontal plate show limits of applicability of the analytical solution. Simulations for this external condensing flow discuss its stability issues and throw light on flow regime transitions because of ever-present bottom wall vibrations. It is identified that laminar to turbulent transition for these flows can get affected by ever present bottom wall vibrations. Detailed investigations of dynamic stability analysis of this shear driven external condensing flow result in the introduction of a new variable, which characterizes the ratio of strength of the underlying stabilizing attractor to that of destabilizing vibrations.

Besides development of CFD tools and computational algorithms, direct application of research done for this thesis is in effective prediction and design of two-phase components in thermal systems used in different applications. Some of the important internal condensing flow results about sensitivities to boundary fluctuations are also expected to be applicable to flow boiling phenomenon. Novel flow sensitivities discovered through this research, if employed effectively after system level analysis, will result in the development of better control strategies in ground and space based two-phase thermal systems.

ACKNOWLEDGEMENTS

TABLE OF CONTENTS

NOMENCLATURE

Variable Symbols

C_{p1} Specific heat of the liquid condensate, J/(kg-K).

D Inner diameter of tubular test-section for gravity driven in-tube experiments, m.

$\mathcal{D}_{max}$ Physical value of amplitude of displacement waves of bottom wall noise, m.

$\mathcal{D}^*_{max}$ Non-diemsional value of $\mathcal{D}_{max}$ ($\equiv \mathcal{D}_{max}/L_{Char}$).

f Non-dimensional frequency f_p of bottom wall vibraions given by $1/T_b$ $\equiv f_p \cdot Y_e/U_\infty$.

f_p Physical value of frequency of bottom wall vibraions, Hz.

g Gravitational acceleration, m/s^2.

G Non-dimensional parameter given by $(Ja /Pr_1) \cdot (\rho_1\mu_1/ \rho_2\mu_2)^{1/2}$. This parameter is used to obtain the correlation for steady values of film thickness for external condensing flow of vapor over a horizontal plate.

h Channel gap for internal condensing flows, m.

Ja Condensate liquid Jakob number, $(C_{p1} \cdot \Delta T)/ h_{fg}(p_{in})$.

k_1 Conductivity of condensate liquid, W/(m-K).

L Length of the test-section in experiments or domain in computations, m.

L_C Characteristic length, $L_C = D$ (diameter) for tubes and $L_C = h$ (gap height) for channels, $L_c = Y_e$ for external condensing flow problem, m.

L_{Char} Intrinsic characteristic length given by $\mu_1/(\rho_1 \cdot h_{fg}^{1/2})$, m. This characteristic length is occassionally used to non-dimensionalize important flow parameters for exterenal condensing flow over a flat plate outside the computational and problem formulation context.

$\dot{m}$ Non-dimensional value of interfacial mass flux, $\dot{m} \equiv \dot{m}/(\rho_1 \cdot U_\infty)$ for external condensation and $\dot{m} \equiv \dot{m}/(\rho_1 \cdot U)$ for internal condensation.

$\dot{m}$ Physical value of interfacial mass flux, kg/(m^2·s).

ni   Representative number of grid points in x direction for simulations.

nj   Representative number of grid points in y direction for simulations.

P   A non-dimensional measure of the ratio of noise-sensitivity to strength of stability.

p_{in} Pressure at the test-section inlet, kPa.

p_{exit} Pressure at the test-section exit, kPa.

Pr_1 Condensate liquid Prandtl number, $\mu_1 . C_{p1} / k_1$.

p_{xP-i} Test-section pressures at locations $x_P = x_{P-i}$ (i = 1, 2, …), kPa.

$\dot{Q}_{total}$ Net heat rate out of the test-section, W.

Re_{in} Inlet vapor Reynolds number, $\rho_2 U L_c / \mu_2$.

Re_x Reynolds number, $Re_x = \rho_1 U x / \mu_1$ for internal condensation and

$Re_x = \rho_1 U_\infty \chi/\mu_1$ for external condensation.

$Re_{x|Trans-cr}$ Critical Reynolds number that marks the transition to turbulence or to a qualitatvely different type of flow for external condensing flow problem.

$Re_{x|wavy-cr}$ Critical Reynolds number at which the amplitude of waves on the interface due to persistent condensing-surface noise grows up to 15% of the mean film thickness for external condensing flow problem.

T_b Non-dimnesional time period of bottom wall vibraions.

θ Non-dimensional temperature.

$T_{sat}(p)$ Saturation temperature at pressure p, ^oC.

$\overline{T}_w$ Mean condensing surface temperature, ^oC.

$T_w(x_P)$ Non-uniform steady condensing surface temperature at x_P, ^oC.

U   Average inlet vapor velocity for channel or tube in the direction of test section length, m/s. This peed U for internal condensing flow can be interchangeably used with vapor speed U_∞ for external condensing flow of vapor over a horizontal plate for non-dimnesionalization of different flow vaiables.

U_{Char} Intrinsic characteristic speed ($\equiv h_{fg}^{1/2}$), m/s. This speed is occassionally used to non-dimensionalize important flow parameters outside the computational and problem formulation context for external flow of vapor condesning over a flat plate.

u*   Non-dimensional far upstream vapor speed given by $U_\infty / U_{Char.}$

u^*_{cr} Non-dimensional value of U_∞^* ($\equiv U_\infty^*/U_{Char}$).

U_∞ Far upstream vapor speed for external condensation of vapor over a horizontal plate, m/s. This speed is used to non-dimensionalize regular flow field variables like liquid and vapor velocities, interfacial mass flow rate, time, pressure, etc. in the computational and problem formulation context.

U_∞^* Lower threshold of vapor speed U_∞ given by simulations for film wise condensation of external condensing flow problem, m/s.

(u,v) Values of x and y components of velocity, m/s.

(u,v)   Non-dimensional values of u and v, $(u,v) \equiv (u/U, v/U)$ for internal condensation and $(u,v) \equiv (u/U_\infty, v/U_\infty)$ for external condensation.

v_{max} Physical value of the amplitude of a standing velocity wave associated with condensing surface noise, m/s.

x, y Physical distances along and perpendicular to the condensing surface, m.

x, y   Non-dimensional distances along and perpendicular to the condensing surface.

x_{fc} Approximate length needed for full condensation (estimted by computations), m.

x_{fc} Non-dimensional x_{fc}.

x_e	Non-dimensional value of domain length for external condensing flow of vapor over a flat plate, X_e/Y_e.
x^*	Distance from the leading edge beyond which pressure gradient in liquid or vapor domain is nearly equal to zero for external condensing flow of vapor over a flat , m.
x^*	Non-dimensional value of x^*, $x^* = x^*/Y_e$.
X_e	Physical value of domain length for external condensing flow of vapor over a horizontal plate , m.
$Z(x)$	Ratio of vapor mass to the total inlet mass at any x for internal condensing flows.
δ	Non-dimensional value of condensate thickness.
Δ	Physical value of film thickness, m.
P	Density, kg/m^3.
μ	Viscosity, kg/(m-s).
π	Non-dimensional pressure.
ν	Kinematic viscosity μ/ρ, m^2/s
σ	Surface tension, N/m.
λ	Non-dimensional wave-length for the bottom wall vibrations ($\lambda = \lambda_p/Y_e$).
λ_p	Physical/dimensional value of wavelength for the bottom wall

vibraions, m.

λ_o Non-dimensional wave-length for the initial disturbance $\delta'(x, 0)$ on the

interface.

δ' Non-dimensional value of disturbance on the interface

Subscripts

comp   Obtained from computations.

exit   Test-section exit.

expt   Obtained from experiments.

I $I = 1$ for liquid and $I = 2$ for vapor.

in   Test-section inlet.

Na   Natural exit condition.

sat   Saturation condition.

w   Condensing surface.

Superscripts

i   Value of a variable at an interface location

LIST OF FIGURES

LIST OF TABLES

Chapter 1 CONDENSING FLOW RESEARCH ISSUES AND FUNDAMENTALS

1.1 Introduction

Recent technological advancements in cooling/heating applications require use of state-of-the-art thermal systems that employ actively pumped two-phase flows for dissipating large heat fluxes (often > 1kW/cm^2). Use of two-phase components (flow condenser, flow boilers, etc.) in any thermal system demands good flow attainability as well as reliable flow prediction capabilities for the multiphase flows occurring in these two-phase components. This, in turn, requires development of physics-based software programs that can accurately predict two-phase component behavior under different operating conditions. Computational results obtained from such programs can be synthesized with laboratory-based experimental results to develop better understanding of two-phase systems and, can, ultimately lead to sophisticated designs of thermal systems employing them. The research presented in this dissertation focuses on computational study of flow condensation and its synthesis with available experiments and analytical solutions. The computational study presented here mainly involves continued development of 2-D CFD codes on FORTRAN platform and comparisons of the results from these codes with 1-D simulation tools [1], analytical solutions, and wherever applicable, with the experimental results. Some of the key results obtained in this research are expected to qualitatively applicable to flow boiling as well.

To better understand flow condensation, both the external and internal condensing flows were studied computationally. Some of the errors in previous understanding [2]-[6] for internal condensing flows has been corrected and novel results [7]-[8] regarding boundary condition sensitivities of these flows have been developed which is critical for the development of ground based as well space based thermal systems. The computational study for internal condensing flows was carried out for two geometries: tube and channel. Simulations for both gravity driven as well as shear driven internal condensing flows were developed and computational results were successfully compared with the experimental results. These investigations of *internal condensing flows* are of significant practical importance and constitute *half* of this thesis with computational results and comparisons with experiments as discussed in chapter 4.

During investigations of internal condensing flows, it was found that shear driven internal condensing flows differ a lot from gravity driven internal condensing flows as far as nature steady solutions, different unsteady flow features, sensitivities to boundary condition, and flow regimes are concerned. As compared to gravity driven flows, steady shear driven internal condensing flows were found to be more sensitive to boundary condition fluctuations as well as prone to instability arising from initial disturbances. To gain hitherto unavailable understanding of exact nature of steady and unsteady features of external condensing shear driven flows, a classical academic problem of flow condensation over a flat plate (problem of Cess [9] and Koh [10]) has been thoroughly studied ([8]) - using a newly developed code that is based on an earlier computational methodology ([2]). This study is not only helpful in validating the computational

methodology implemented here (as an analytical solution for the steady problem based on similarity solution is already available) but it also discovers some new flow physics regarding a certain limiting criteria when steady solution – as reported by analytical solutions - may not exist. This external condensation flow study also provides valuable unsteady response of the flow - which the analytical solution could not predict. Thus study of unsteady solutions of this external flow problem complements the internal flow condensation study in the first half of this thesis and throws light on different interesting features inherent to the shear driven condensing flows and their full non-linear stability analyses. Detailed investigations of this *external condensing flow* problem of pure vapor condensing over a horizontal plate make the *other half* of this thesis report.

In summary, this research has investigated the effects of following different parameters on condensing flow: (i) gravity, (ii) shear, (iii) condensing flow geometry, (iv) cooling method (thermal boundary condition at condensing surface), (v) inlet conditions, (vii) exit condition fluctuations, (viii) initial disturbances, and (ix) micro-meter scale effects such as disjoining pressures at interface and non-equilibrium thermodynamics. The very fundamental and novel result regarding existence of a unique steady flow (termed "natural") for internal condensing flows (for both gravity driven and shear driven flows) has been established along with the *novel* response of shear driven internal condensing flows exhibiting multiple quasi-steady solutions in presence of the time-periodic fluctuating boundary conditions (inlet, exit, or concurrent). These new and hitherto unknown flow sensitivities (named "quasi-steady parabolicity" and "ellipticity") were computationally shown ([7]) to exist for shear driven internal condensing flows and

3

have been experimentally established ([7]). Relying on the reported synthesis of theoretical ([1]-[8]) and experimental results ([7], [11]) novel categorization of internal condensing flows is presented regarding their sensitivity to simultaneously prescribed boundary conditions at the inlet and the exit. In addition, impact of these results on condensing flow morphologies (annular/stratified, plug/slug, etc.), condensing flow sensitivities, condensing flow instabilities (structural instability, dynamic instability, etc.), condensing flow attainability, and predictability are given as part of major investigations that were carried out during this doctoral research.

The simulation results presented here and their synthesis with experiments are believed to be of great value not only to the condensing flow problems but also to other two-phase flow problems (flow boiling, etc.). The reported study of external condensing flow problem is of significant academic importance while the reported investigation of internal condensing flow problem is of great practical importance. Also the *tool development* done here will provide definite guidance for the ongoing development of enhanced computational capabilities in the area of two-phase flows and associated computational physics. Furthermore, the *research results* presented here can significantly assist in the design and development of much needed modern two-phase thermal systems.

1.2 Development of Computational Tools

To investigate condensing flows in various geometries (tubes or channels), different configurations (external or internal) and different environments (gravity or

shear) - the existing in-house codes were modified and new 2-D CFD programs were developed on FORTRAN 77. The code development work consisted of the following:

- Modifications of unsteady codes for "in-tube" geometries for gravity driven situations for unspecified exit conditions: Comparisons for gravity driven in-tube condensing flow simulation results with experimental results and generation of comparison matrices for partial and fully condensing flows as reported in section 4. This work has been published in [5].

- Debugging and modifications of steady and unsteady codes (discussed in section 4) for gravity driven and shear driven flows inside a channel for unspecified exit conditions: This work has been submitted for publication in [7].

- Development of new codes to solve internal shear driven/0g condensing flows in channel geometry to understand flow sensitivities (specified exit conditions, fluctuating inlet conditions, etc.): This work has been submitted for publication in [7].

- Development of new 2-D codes to solve external flow problem (steady and unsteady versions) of vapor condensing over a flat plate (problem of Cess and Koh [9]-[10]): This work has been published in [8].

A detailed description of the 2-D steady/unsteady computational approach utilized to obtain results in this thesis is given in section 3 of Narain et al. [2]. The boundary conditions, formulations of computational problems, and numerical algorithms to solve external and internal condensing flows are given in detail in [8] and [7] respectively. The *interface tracking equation* used here and in [2]-[6] is the same one that is used for locating the interface in the *interface capturing approaches* for flow with phase change

5

(level-set method of Son and Dhir [12], etc.) or without phase-change (level-set method of Sussman et al. [13], VOF method of Hirt and Nichols [14], etc.). The *interface tracking approaches* of Esmaeeli and Tryggvason [15], Juric and Tryggvason [16], Tezduyar [17], M. A. Cruchaga et al. [18], etc. also use the same interfacial mass-flux and energy conditions but in somewhat different order and combination. The numerical scheme used here exploits the rigorous analytical and numerical knowledge that exists (see Abbott and Basco [19]) for solving the first order hyperbolic form of the *interface tracking partial differential equation* – this ensures convergence and accuracy of both the amplitude and the phase of the predicted interfacial waves. The above code development work was accompanied by data analysis, synthesis with the experimental works of [5], [11], and collaborative assistance in development of the MTU's experimental systems.

1.3 Internal Condensing Flow Problems Investigated

1.3.1 Terminology

The liquid and vapor phases in the flow (see Figure 1) are denoted by $\mathcal{L}$ (subscript I: I = 1) for liquid and $\mathcal{V}$ (I = 2) for vapor. The fluid properties (density ρ, viscosity μ, specific heat C_p, and thermal conductivity k) with subscript I are assumed to take their representative constant values for each phase (I = 1 or 2). Let T_I be the temperature fields, p_I be the pressure fields, T_s (p) be the saturation temperature of the vapor as a function of local pressure at the interface p, Δ be the film thickness, be the local interfacial mass flux (kg/s/m^2), T_w (x) (< T_s (p)) be a known temperature variation of the condensing

surface (with its length average mean value being $\overline{T}_w$), and $\mathbf{V_I} = u_I \hat{i} + v_I \hat{j}$ be the velocity

fields. The flow fields are defined at every point **x** (a 3-D Euclidean position vector) and

time t. Furthermore, the characteristic length L_c for the channel geometry is its channel

gap 'h' shown in Figure 1 and, for the tube geometry (see Figure 2), L_c is the diameter D.

Let g_x and g_y be the components of gravity along x and y axes, p_0 be the inlet pressure, ΔT

$\equiv T_s (p_0)$ - $\overline{T}_w$ be a representative controlling temperature difference between the vapor

and the bottom plate, h_{fg} be the heat of vaporization at temperature T_s (p), and U be the

average inlet vapor speed determined by the inlet mass flow rate $\dot{M}_{in}$ ($\equiv \rho_2 \bullet U \bullet h$ for the

channel flow). Let t represent the actual time and (x, y) represent the physical distances

of a point with respect to the axes shown in Figure 1 for the channel flow (for tube flows

in Figure 2, $x = 0$ is at the inlet, $y = 0$ is at the condensing surface). For the channel of

height 'h,' $y = h$ is an isothermal plate and is a slightly superheated non-condensing

surface. For the tube, $y = D/2$ (i.e. r = 0) is the center-line where symmetry condition

holds for all flow variables of interest. Note that, $y \equiv L_c.y$ represents the distance from the

condenser surface, for both channel (Figure 1) and in-tube (Figure 2) flows. A new list of

fundamental non-dimensional variables – viz. (x, y, t, δ, u_I, v_I, π_I, θ_I, m) is introduced

through the following definitions:

$$\{x, y, \Delta, u_I, \dot{m}\} \equiv \{L_c \cdot x, L_c \cdot y, L_c \cdot \delta, U \cdot u_I, \rho_1 \cdot U \cdot \dot{m}\}$$
$$\{v_I, T_I, p_I, t\} \equiv \{U \cdot v_I, (\Delta T) \cdot \theta_I, p_0 + \rho_I U^2 \cdot \pi_I, (L_c / U) \cdot t\} \tag{1}$$

1.3.2 Steady and unsteady Flow Behavior of Internal Condensing Flows

For the convenience of communication, a distinction has been proposed among: (i) parabolic/elliptic boundary conditions, (ii) parabolic/elliptic governing equations, and (iii) parabolic/elliptic flow behavior. These terms are defined as:

<u>Parabolic Boundary Conditions</u>

In one computational approach, parabolic boundary conditions for the two dimensional flow in Figure 1 requires prescription of the values of inlet mass flow rate $\dot{M}_{in}$ (more precisely, for 2-D computations, x-velocity profile $u_2(0, y, t)$ and a suitable $v_2(0, y, t)$), inlet temperature $T_2(0, y, t)$, the thermal and hydrodynamic wall conditions on the channel walls (at $y = 0$ and $y = h$), and either the inlet pressure p_{in} ($= p_2(0, y, t)$) or the exit pressure p_{exit} ($= p_2(x_e, y, t)$) at any "one point" on the inlet or the outlet cross-section. The procedure for specifying pressure at a point is quite similar to specifying reference pressure at one point in an incompressible single-phase flow. In a second computational approach, parabolic boundary conditions for a two dimensional problem consists of: prescription of the inlet pressure p_{in} ($= p_2(0, y, t)$) and the exit pressure p_{exit} ($= p_2(x_e, y, t)$ that are concurrently specified across an arbitrary line $y = y^*$ and $0 \le x \le x_e$ (i.e. the pressure-difference $\Delta p \equiv p_{in} - p_{exit}$ is specified), inlet temperature $T_2(0, y, t)$, the thermal and hydrodynamic wall conditions on the channel walls (at $y = 0$ and $y = h$), and, in addition, the specification of the complete pressure variation across either the inlet *or* the exit cross-section as the normal stress for the stress boundary condition (which requires normal and tangential stresses) on that boundary.

Elliptic Boundary Conditions

In addition to the parabolic boundary conditions in the first computational approach described above, if one can specify the pressure variation across the boundary (say the inlet or the outlet) where the "pressure at a point" was *not* specified as part of the parabolic boundary condition, then such a specification is called an elliptic boundary condition. In the second computational approach for the parabolic boundary conditions, if besides the point pressure p_{in}, point pressure p_{exit}, and a cross-sectional pressure variation (over an inlet or outlet boundary); one specifies the inlet mass flow rate then this specification will be called an elliptic boundary condition.

Parabolic Governing Equations

If the duct flow governing equations (steady or unsteady) are such that the parabolic boundary conditions in the first approach are sufficient to fully determine the pressure, velocity, and temperature fields elsewhere, then the governing equations are said to be parabolic. The parabolic governing equations discretization and solution technique in this computational approach (for which the "pressure at a point" at the inlet is prescribed) are such that to determine the value of a flow variable at a point one does not need information from any downstream location. If the governing equations (steady or unsteady) are such that the parabolic boundary conditions for the second computational approach are sufficient to fully determine the mass flow rate $\dot{M}_{in}$ (more precisely, the x-velocity profile $u_2(0, y, t)$ and a suitable y-velocity profile $v_2(0, y, t)$), then again the governing equations are said to be parabolic. Different approaches (e.g. the

9

second approach discussed above) to specify parabolic boundary conditions are all equivalent to the first approach (for which the "pressure at a point" on the inlet was specified) because they all indirectly exploit the parabolic governing equations' feature that the flow at a point is only affected by the upstream conditions.

Elliptic Governing Equations

If the duct flow governing equations (steady or unsteady) are such that the elliptic boundary conditions need to be added to parabolic boundary conditions for either the first or the second approach to fully determine (within the domain and relevant parts of its boundary) the pressure, velocity, and temperature fields, then the governing equations are said to be elliptic.

Strictly Parabolic Flow Behavior

Steady or unsteady incompressible single phase flows (and some immiscible two-fluid flows) are examples of strictly parabolic flows. A strict parabolic problem has the following two features: (i) for repeatable realization of the flow, the available knowledge of the parabolic boundary conditions is sufficient without any knowledge or specification of the remaining "elliptic" boundary condition, and (ii) any impositions (with or without fluctuations) of the remaining "elliptic" boundary condition is impossible as it can only affect the flow outside the flow domain of interest.

Strictly Elliptic Flow Behavior

A *strictly* "elliptic" flow (steady or unsteady) will have the following feature: for repeatable realization of the flow, one needs specifications or knowledge of all the boundary conditions – the parabolic *and* elliptic boundary conditions defined above.

Incompressible single-phase flows of common experience are always parabolic in behavior and never elliptic. This is because information to an interior point does not travel from both upstream and downstream locations. Some compressible duct flows are, however, elliptic in the above sense.

Unique and Mixed (Parabolic and Elliptic) Nature of Internal Condensing Flow Behavior

These flows' behavior are characterized by the fact that: (i) steady condensing flow governing equations are parabolic, (ii) unsteady condensing flow governing equations can be parabolic for unspecified exit conditions (i. e. parabolic boundary conditions), and (iii) unsteady condensing flow governing equations can also be typically (i.e. for most thermal boundary conditions for the condensing surface) elliptic for elliptic boundary condition specification. The ability to impose unsteady elliptic boundary condition for shear driven internal condensing flows was found to become gradually impossible as gravity component in the direction of the flow becomes large enough to make the flow gravity dominant. The unique feature of "elliptic" nature of unsteady shear driven internal condensing flows is discussed in detail in section 4.

1.3.3 Existence of "Unique" Steady Solutions (Termed as "Natural" Solutions)

Attainability and controllability of annular/stratified internal condensing flows under gravity or shear driven conditions are of prime importance in different practical applications. The interest in annular/stratified flow regime is because of their high thermal efficiencies for a given length of the condenser – i.e. higher heat exchange rates and lower pumping powers. The computational results in this dissertation corrects some of our earlier results ([2]-[6]) and supports some of our recent results ([1], [7]–[8], [11]). It is computationally found for the internal condensing flows that (in a channel of Figure 1 or tube of Figure 2) under "parabolic" boundary condition – e.g. a given steady inlet vapor mass flow rate, steady inlet pressure, and a known steady *thermal* (temperature or heat-flux) boundary condition for the condensing surface – there exists a *unique* "natural" steady solution of the strictly steady governing equations. This result is found to be hold for both for shear driven and gravity driven cases. The uniqueness of the steady solution also means there are no multiple *steady* annular/stratified solutions of the strictly steady equations for different *steady* exit condition specifications (as was erroneously concluded in [2]-[6]). The experiments ([7] and [11]) and independent 1-D simulation results [1] also confirm repeated realization of the above stated "natural" steady solutions. This unique annular/stratified solution and its quasi-steady neighbors (arising from minuscule or large periodic fluctuations in the parabolic boundary conditions) - called "natural" steady or quasi-steady solutions - always exist for strictly steady or quasi-steady "parabolic" boundary conditions.
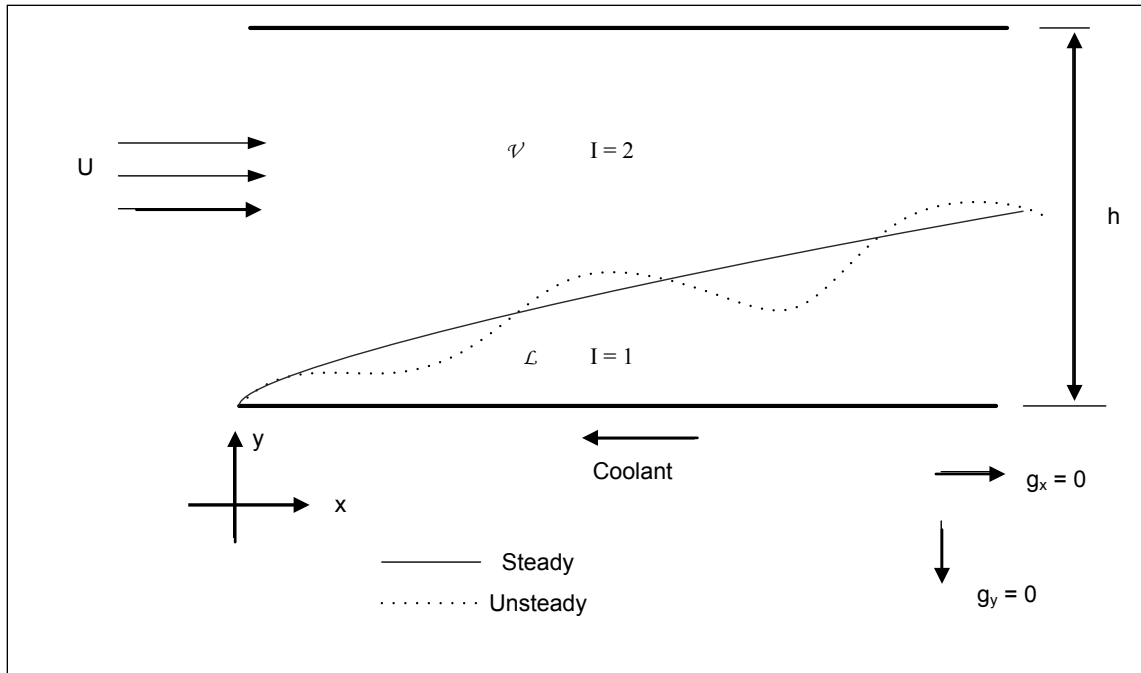
Figure 1: A schematic describing a representative condensing

flow problem in a horizontal channel.

Here "parabolic" boundary conditions mean specification of either the inlet or the exit pressure- but not both, inlet mass flow rate, and a known steady *thermal* (temperature or heat-flux) boundary condition for the condensing surface associated with a certain well defined cooling approach.

Experimental results reported in ([7] and [11]) confirm that under quasi-steady "parabolic" boundary conditions, the remaining pressure boundary condition (exit pressure if inlet pressure was part of the "parabolic" boundary condition and vice versa) was steady or quasi-steady and was self sought - and this value has been termed a "natural" pressure condition. The unique steady pressure-difference Δp between the inlet

and the exit is termed a "natural" pressure difference and is denoted as $\Delta p|_{Na}$. Experiments ([7] and [11]) also confirm the computational result that, for steady *partially condensing flows*, the "natural" remaining exit pressure value is equivalent to the specification of the "natural" exit liquid or vapor mass flow rate.
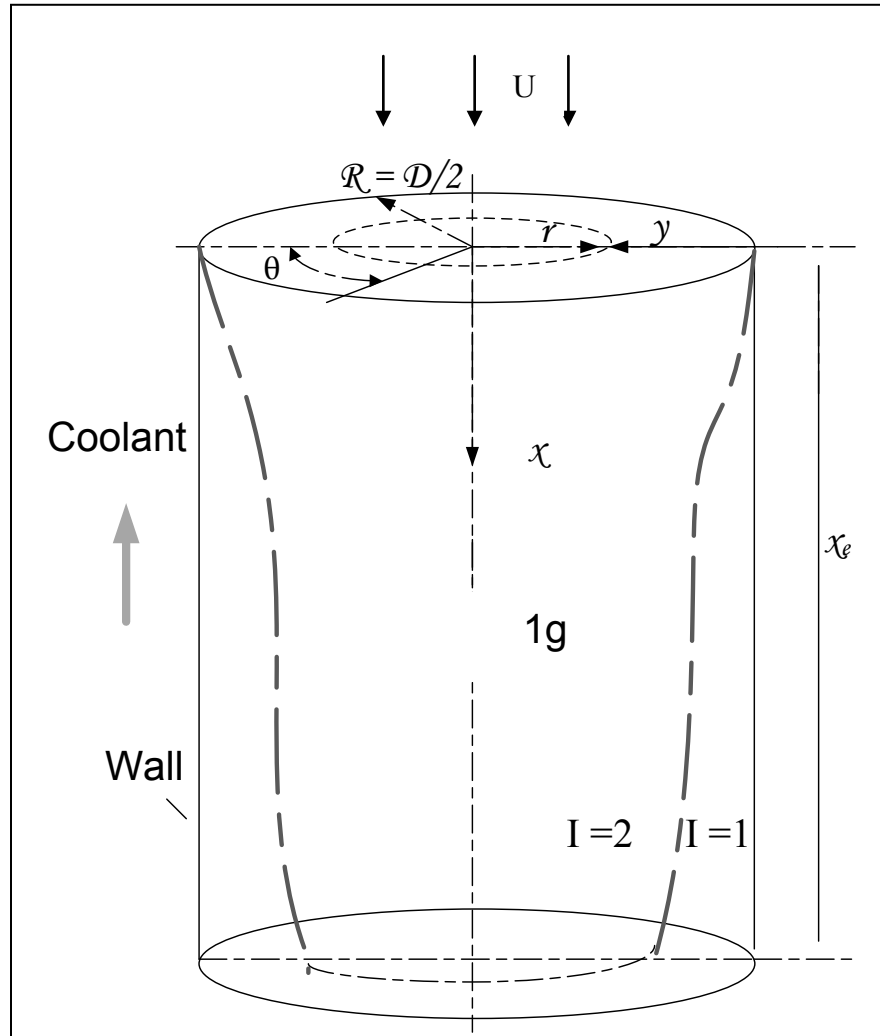
Figure 2: A schematic describing a representative condensing

flow problem inside a tube

1.3.4 Flow Sensitivities of Shear Driven Internal Condensing Flows

The computations find that the "strength" of the "natural" steady solutions for shear driven internal condensing flows is very weak as compared to the gravity driven internal condensing flows. By "strength," it is meant that for shear driven condensing flows, it takes longer time as compared to gravity driven condensing flows (i.e. $g_x \neq 0$ as opposed to $g_x = 0$ in Figure 1) for an arbitrary initial guess (say interfacial location at time t = 0) to converge (as t $\rightarrow$ ∞) to steady solution in a 2D unsteady solver under parabolic boundary conditions. In addition to this, computations also find that *steady* governing equations for *annular/stratified* shear driven flows are not strictly "parabolic," because the *unsteady* equations exhibit "elliptic-sensitivity" in the sense that the self-sought "natural" pressure value at the inlet or outlet boundary associated with the parabolic problem can be "actively" changed in the mean to a different quasi-steady (with superposed periodic fluctuations) pressure value. The "elliptic-sensitivity" of a shear driven annular/stratified portion of a partially condensing flow is computationally found to mean that though there exists a unique "natural" steady solution associated with the strictly steady equations under steady "parabolic" boundary conditions (i.e. either the inlet or the exit pressure is unspecified for a given inlet mass flow rate and thermal/hydraulic call conditions), the unsteady version of this problem exhibits limited "ellipticity" or "elliptic sensitivity" in the sense that concurrent steady-in-the-mean time-periodic inlet *and* exit pressures can be specified. This means that shear driven flows allow a certain class of different "non-natural" time-periodic impositions on the remaining boundary (which was not specified for the underlying parabolic problem)

which allows different quasi-steady annular/stratified flows with mean features of the flow variables different than those obtained from the "natural" solution. For the computational results reported here, the different "non-natural" time-periodic impositions for the exit pressure are replaced by different mean "non-natural" exit liquid mass flow rates superposed with certain classes of time-periodic fluctuations. The experiments ([7] and [11]) also show that the superposed time-periodic fluctuations on the mean pressure condition on the remaining boundary (which is the inlet for experiments in [7] and [11]) – for partially or fully condensing flows – can be externally prescribed by an active energy source (compressor or pump) that facilitates presence of time-periodic fluctuations on the mean pressure. In the experiments, under constrained imposition of active "non-natural" pressure, the flow self-selects the needed time periodic fluctuations associated with the new mean pressure imposition at the remaining boundary and achieves a new quasi-steady solution different than the "natural" solution. It has been experimentally found that, for fully condensing flows (and expected to be shown for certain partially condensing situations), "elliptic" Δp impositions also lead to some shifts in the flow regime transition boundary between the "annular/stratified" regime and the nearby "plug/slug" flow regimes and a larger shift in the transition boundary between the "plug/slug" regime and the nearby "bubbly" flow regime.

The computations find, with the help of the reported study of quasi-steady partially condensing shear driven flows, that the above described "elliptic sensitivity" is possible because of the flows' inherent bi-directional coupling of liquid and vapor motions which allows these flows to redistribute the changed mechanical power

16

consumed by the condenser under impositions of certain "non-natural" steady-in-the-mean exit conditions. The flows accommodate this "elliptic" imposition by exploiting the limited freedom they have to change the steady-in-the-mean values for the interfacial location, interfacial mass-flux, and how the net mechanical power consumption in the condenser is distributed between bulk consumption and interfacial consumption (such as interfacial pressure working, interfacial kinetic energy exchanges, etc.). This kind of "elliptic sensitivity" is not present for gravity dominated Nusselt flows (see [20]) as, in that case, there is only a uni-directional connectivity between the motions of the two phases. This is because the liquid motion and the interface location is completely determined by gravity (see [20]) and the vapor motion must adapt itself in a way that it does not affect the predeterminations done by the dominant gravity.

For the computational problem studied for this dissertation, the purely shear driven flows respond unsteadily to imposition of time-periodic (but steady-in-the-mean) "non-natural" exit liquid flow rate condition and this leads to a quasi-steady flow with a mean $\Delta p \neq \Delta p|_{Na}$ and enhanced heat transfer rates. But, for "fixed" condensing-surface temperature – the assumed cooling approach (or thermal boundary condition) - these flows continue to have a tendency to return to the "natural" flow and associated natural value $\Delta p|_{Na}$ whenever the constraining non-natural "elliptic" boundary condition is removed or no longer "actively" imposed. We term this behavior elastic or "spring" like. It should be noted that if the *steady thermal* boundary condition for the condensing-surface is changed from a given *temperature* condition to the less common situation of a given and "actively" fixed *heat-flux* condition, the above reported "elliptic sensitivity" of

17

the shear driven flows will no longer exist. From here and henceforth, unless otherwise stated, *temperature* boundary condition for the condensing surface will be assumed when "elliptic sensitivity" of these flows is discussed. Because of the fact that the unsteady simulation tool employed for this research is limited to the annular/stratified morphology, investigation of the response of the shear driven flow is limited to investigation of only those exit condition imposition for which the time evolution of the flow remains within the category of annular/stratified morphology. This limitation is restrictive when one wants to study fully condensing shear driven flows for which there is an abundant experimental data ([21]-[23] etc.) – including that from our own research group that is reported in this thesis and in ([7], [11]) – which indicates downstream presence of non-annular liquid-vapor morphology (plug/slug, bubbly, etc.).

Besides the "elliptic-sensitivity," computations/experiments have found a different sensitivity for shear driven flows called "quasi-steady parabolicity." This means that for shear driven flows, different "non-natural" time-periodic impositions on the parabolic boundary also leads to somewhat different quasi-steady annular/stratified flows with mean features of the flow variables different than those obtained from the "natural" solution in absence of these fluctuations. These differences, however, are not found to be significant as are the differences in quasi-steady solutions due to "elliptic" constraining. This sensitivity is also found to cause changes (relatively of smaller magnitudes as compared to "elliptic" constraining) in the heat transfer rates inside the condenser and induce thermal transients in the condensing surface for the thermal condition in which temperature of condensing surface is allowed to change. This thesis presents only

preliminary results on the "quasi-steady parabolic" sensitivity and detailed investigations of this sensitivity are part of a future thesis work of another doctoral student.

The results of this thesis and future research can make it possible, to design pumped two-phase systems that can either suppress/eliminate the impact of "elliptic sensitivity" and "quasi-steady parabolicity" or exploit this sensitivity to enhance heat transfer rates (up to > 30%) and improve the efficiency of the condenser and the system.

With the above background information, computational investigations and experimental syntheses of internal condensing flows done for this dissertation can be classified in the following three groups:

Gravity Driven Internal Condensing Flows inside a Tube

This work involved:

- Obtaining steady and unsteady solutions for "natural" partially and fully condensing flows and basic comparisons with experimental results obtained in [5].

- Obtaining a preliminary surface that represents "natural" solutions in a 3-D space defined by inlet mass flow rate, vapor-to-wall temperature difference, and pressure drop across the test section.

- Unsteady solutions for "natural" parabolic boundary conditions to investigate flow regime transitions from smooth-laminar to wavy-laminar regime.

Shear Driven/0g Internal Condensing Flows inside a Channel

This work involved:

- Obtaining "natural" steady solutions of partially condensing flows and comparing their unsteady responses (attraction rates etc.) with gravity driven flows.

- Investigations for the newly discovered phenomenon of "elliptic sensitivity:" This involved obtaining unsteady solutions and associated flow results for "non-natural" exit conditions achieved for different exit liquid mass flow rate controls.

- Dynamic (stability) analysis in the presence of different exit condition impositions/ controls.

- Effects of different parameters like wall temperature variations, inlet fluctuations, etc on steady and unsteady "natural" solutions.

Preliminary Investigation of Micro-scale Effects for Internal Condensing Flows inside a Channel

This work involved:

- Assessing effects of disjoining pressures across the interface for "natural" steady solutions.

- Assessing effects of non-equilibrium thermodynamic across the interface for "natural" steady solutions.

All the computational results/comparisons with experiments for internal condensing flows are discussed in chapter 4.

1.4 External Condensing Flow Problem of Vapor Condensing Over a Flat Plate

The problem studied by Cess [9] and Koh [10] deals with forced flow of saturated vapor (with a uniform upstream speed U_∞) that approaches a semi-infinite

horizontal plate and starts experiencing film-wise condensation over the plate (see Figure 3). This classical problem being external, may or may not relate to the internal condensing flow problem and the interest here is to understand its similarities and differences to the internal condensing flow problem discussed above.

The central interest of this research was to solve the steady and unsteady governing equations for the full two dimensional version of this problem.
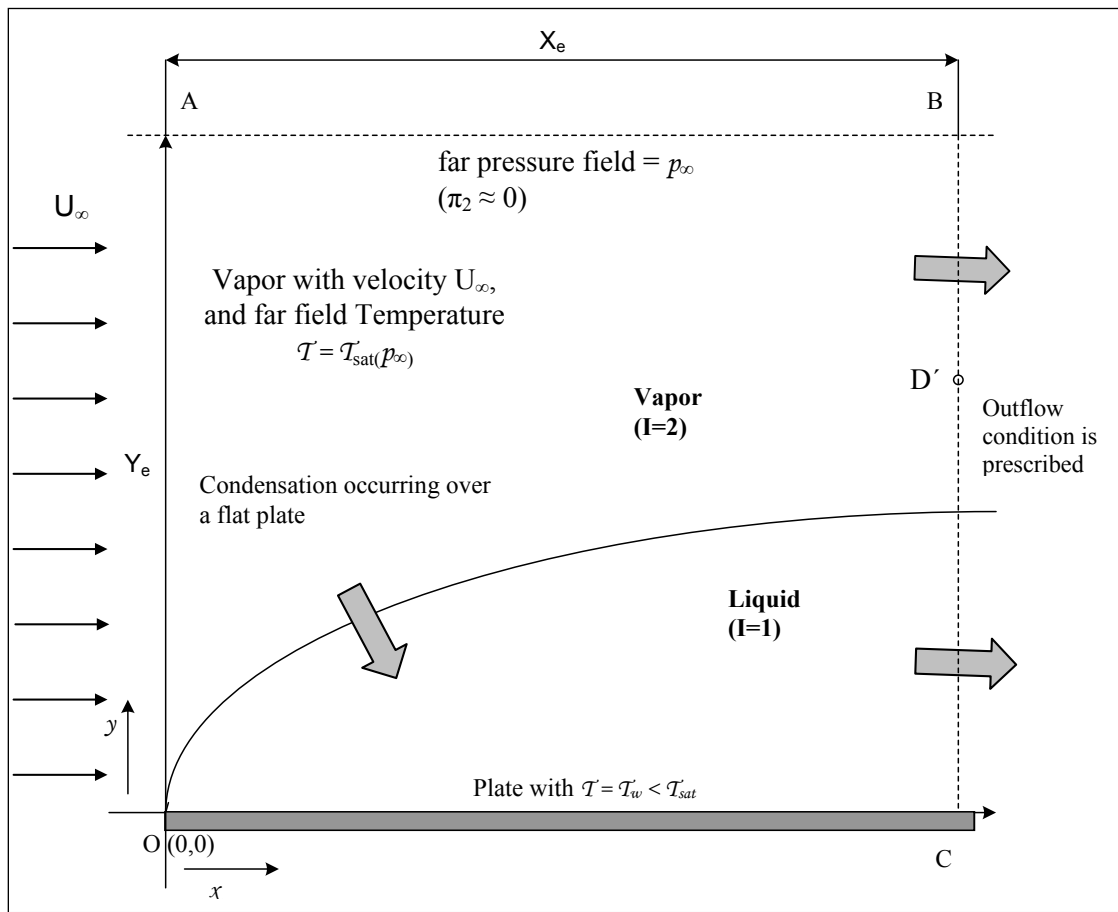
Figure 3: A schematic for a typical finite computational domain for a film condensation flow over a horizontal plate due to a forced uniform vapor flow

This research focused on investigatation of features associated with unsteady solutions (attraction rates, etc.), comparisons of steady solutions with the relevant classical similarity solutions offered by Cess [9] and Koh [10], and improvements in the existing understanding of the feasibility of the film wise condensation assumption underlying the Cess [9] and Koh [10] solutions.

The results of Koh [10] have been pivotal to the studies that rely on (e.g. Rose [24]) or use (e.g. Balasubramaniam et. al [25]) this solution to predict or estimate the features of shear driven external condensing flows.

The ordinary differential equations associated with the solution of Koh [10], which are numerically solved, result from a boundary layer and constant pressure approximation of an assumed film-wise condensation behavior and a "similarity" solution formulation of the resulting model equations. This solution's approach is very similar to other similarity solutions (Sparrow and Gregg [26], Koh et. al [27]) for gravity-driven condensing flows that are well-cited in the literature.

One reason why this similarity solution for the shear driven condensate case ([10]) has not been experimentally verified is, perhaps, significant differences exist between shear driven and gravity driven flows with regard to ease of attainment of film wise or annular condensation and another reason is the difficulty in implementing a suitable experiment that meets the requirements of the theory ([9], [10]). This is in contrast with the similarity solutions (e.g. Sparrow and Gregg [26] and Koh et al. [27]) for film wise condensation over a plate under conditions of gravity-driven condensate motion. The gravity driven cases' similarity solutions are in good agreement with the

Nusselt solution [28] and, also, known to be experimentally feasible and in reasonable agreement with related experiments [29]. With regard to ease of achieving film wise or annular condensation, similar differences are known to exist between gravity driven and shear driven internal condensing flows. The experiments involving gravity driven internal condensing flows inside a vertical tube (see [30], [31], etc.) or large hydraulic diameter slightly inclined (downward) channels demonstrate easy attainment of a rather robust quasi-steady wavy annular (or film condensation) flows but annular or film wise shear driven internal condensing flows in mm to µm-scale horizontal tubes and channels are more difficult to achieve and show ([21], [23], [32]-[33]) the possibility of more complex vapor-liquid morphologies (such as steady or intermittent injection annular, mist, slug/plug, bubbly, etc.).

It is shown in [8] and reported here that for a certain range of vapor speeds and vapor-to-wall temperature differences, Koh's analytical solution [10] of this external condensing flow problem agrees well with the reported computational solution's steady film thickness predictions. However the reported simulations in ([8]) differ from the Koh solution [10] in pressure and associated variables' variation near the leading edge of the plate. While the analytical solution of Koh [10] assumes that the pressure stays constant even in the interior of the flow, computationally obtained steady solutions show that there are pressure variations near the leading edge part of the plate and though the resulting pressure differences are miniscule in value relative to the far field pressure p_∞, they are important for determining the dynamics of the flow and in determining the feasibility of maintaining film wise condensation at low vapor speeds. It is found that the leading edge

23

pressure gradients become large as the vapor speed U_∞ becomes sufficiently small. The unsteady solutions of this problem help assess attainability of the steady solutions. This is done by looking at limiting solutions (as t $\rightarrow \infty$) of the unsteady problem obtained for different initial guesses. Additionally, in this study, important assessment/new methods of stability through unsteady response of these flows are obtained and proposed. The effort to obtain and analyze unsteady solutions results in introduction and quantification of the following features of the steady solutions: (i) "attraction rate" values that measure the attainability of the steady solutions from different initial guesses, (ii) response of the steady solutions to initial disturbances, and (iii) noise-sensitivity of the steady solutions to ever-present minuscule noise and, as a result, expected waviness levels on the steady solutions. The above approach is expected to work even when linearized stability analysis and associated assumptions of exponential growth/decay may be of limited value.

For the range of vapor speeds (0.2 m/s -20 m/s) considered for investigation of film wise condensation of typical non-metallic vapors (R113, FC-72, etc.), when an arbitrary initial guess (at t = 0) is used to obtain an unsteady solution in the idealized case of no condensing surface vibrations (no matter how minuscule), the unsteady solutions tend to a smooth wave free long term steady solution. The limiting steady solution, when obtained this way as opposed to obtaining it as a steady solution of the steady governing equations, has been termed a steady "attractor." This unsteady attraction process has been studied and "attraction rates" to the limiting steady solution are defined. Though these "attraction rates" associated with attainability of a steady solution may appear to be a new idea, it is related to the well known idea of "decay rates" in linearized stability analyses

24

that assume exponential time evolution of initial disturbances. Thus increased monotonic (i.e. non-oscillatory) "attraction rates" that are reported here and in [8] correlate with the idea of stronger "decay rates" (i.e. larger, real, and negative coefficients multiplying time in the exponential decay assumption in linear stability analyses). That is large "attraction rates" mean both attainability and stronger stability of the steady solution. The "attraction rates" are used because in the present non-linear context, they were both more general and computationally easier to obtain than "decay rates" in the linear context. It has been found that this "attraction rate" when plotted as a function of time for any given point on the steady solution (which is close to Koh solution [10] – at least as far as steady film thickness values are concerned) may, in general, depend on the steady solution of the system (that is the underlying partial differential equations under no-noise conditions) as well as the starting initial conditions. However it is shown that a proper segment of the time-history associated with the rate of change of film thickness yields a definition of "attraction rate" which is more or less independent of the choice of initial guess. This properly chosen measure of "attraction rate" is shown to diminish with increasing distance from the leading edge and also with decreasing speed U_∞. As a result, it has been found that the assumed film wise steady condensation is difficult to achieve at very low free stream speeds and, for free stream speeds that are sufficiently large, attainment difficulty is predicted for large downstream distances.

For example, unsteady results find that at low vapor speeds ($U_\infty < U_\infty^* \approx 0.2$ m/s for the case discussed here), a long term steady limit is not reached and hence a film wise steady solution or a steady "attractor" does not exist. This result is further supported by

25

the fact that the steady "attractor" (for $U_\infty > 0.2$ m/s in the example considered here) exhibits an approach to near zero mechanical energy availability for viscous dissipation in the interior of any chosen control volume.

For sufficiently fast vapor speeds, since the "attraction rate" diminishes with downstream distance, one expects sensitivity to the effects of: transverse gravity (see [30] for similar effects for condensation inside a horizontal channel), to unintended variations in the far field uniform pressure p_∞, and to ever present minuscule noise on the condensing surface. It is found that when an arbitrary initial guess (at $t = 0$) is used to obtain an unsteady solution (for $t > 0$) in the presence of minuscule noise on the condensing surface, the underlying long term solution's diminishing attraction rates with distance cause the noise induced interfacial waves to grow with the distance from the leading edge. This thesis reports a measure of spatial growth as well as its growth rate with distance. A new parameter is introduced here which can characterize effects of attraction rates versus effects of forces that distract the solution from the smooth attractor.

All the computational results/comparisons with analytical solution for this external condensing flow are discussed in chapter 5 of this thesis report.

Chapter 2 MATHEMATICAL MODELS FOR INTERNAL AND EXTERNAL CONDESING FLOWS

This research considers condensing flows with smooth and wavy interfaces in annular/stratified laminar flows in which incoming vapor is assumed to be at saturation temperature (as 5-10° superheat does not matter for the refrigerants considered). The computational domain is split in to two domains, vapor and liquid, which are assumed to be connected by a single continuous interface that can adequately model wavy/annular stratified flows. Both the liquid film and the vapor domains are modeled as incompressible Newtonian fluids. The full governing equations (Navier Stokes) are employed in each of the domain and all the essential interface conditions are employed and satisfied. Based on the problem under investigation, appropriate boundary conditions are applied at domain boundaries and the interface conditions are applied at the interface. Steady and unsteady interface configurations are respectively located for steady and unsteady flows. The interface is smooth for steady analysis but can be wavy for unsteady analysis.

2.1 Internal Condensing Flows in Channels/Tubes

The 2-D governing equations, interface conditions and boundary conditions for in-tube flows are similar to the ones for channel flows discussed below but are modified to take in to account curvature of the tube and axis symmetric nature of the flow (see [34]).

Interior Equations, Interface Conditions, Inlet Conditions, Wall Conditions, and Exit Conditions

Interior Equations

The non-dimensional differential forms of mass, momentum (x and y components), and energy equations for flow in the interior of either of the incompressible phases are the well-known equations:

$$\frac{\partial u_I}{\partial x} + \frac{\partial v_I}{\partial y} = 0$$

$$\frac{\partial u_I}{\partial t} + u_I \frac{\partial u_I}{\partial x} + v_I \frac{\partial u_I}{\partial y} = -\left(\frac{\partial \pi_I}{\partial x}\right) + Fr_x^{-1} + \frac{1}{Re_I}\left(\frac{\partial^2 u_I}{\partial x^2} + \frac{\partial^2 u_I}{\partial y^2}\right)$$

$$\frac{\partial v_I}{\partial t} + u_I \frac{\partial v_I}{\partial x} + v_I \frac{\partial v_I}{\partial y} = -\left(\frac{\partial \pi_I}{\partial y}\right) + Fr_y^{-1} + \frac{1}{Re_I}\left(\frac{\partial^2 v_I}{\partial x^2} + \frac{\partial^2 v_I}{\partial y^2}\right) \qquad (2)$$

$$\frac{\partial \theta_I}{\partial t} + u_I \frac{\partial \theta_I}{\partial x} + v_I \frac{\partial \theta_I}{\partial y} \approx \frac{1}{Re_I Pr_I}\left(\frac{\partial^2 \theta_I}{\partial x^2} + \frac{\partial^2 \theta_I}{\partial y^2}\right),$$

where $Re_I \equiv \rho_I U \hbar / \mu_I, Pr_I \equiv \mu_I C_{pI} / k_I, Fr_x^{-1} \equiv g_x \hbar / U^2$ and $Fr_y^{-1} \equiv g_y \hbar / U^2$.

Interface Conditions

The nearly exact interface conditions (see Delhaye [35], Narain et. al. [2] etc.) for condensing flows are given in the Appendix (see Eqs. (A.1) - (A.8)). Utilizing a superscript "i" for values of flow variables at the interface $\phi \equiv y - \Delta(x,t) = 0$, non-dimensional forms of the interface conditions are given below.

• The non-dimensional form of the requirement of continuity of tangential component of velocities (see Eq. (A. 2)) becomes:

$$u_2^i = u_1^i - \delta_x (v_2^i - v_1^i), \qquad (3)$$

28

where $\delta_x \equiv \partial\delta/\partial x$.

• The non-dimensional form of the normal component of momentum balance at the interface (see Eq. (A. 3)) becomes:

$$\pi_1^i = \frac{\rho_2}{\rho_1}\pi_2^i - \frac{1}{We}\left(\frac{\delta_{xx}}{[1+\delta_x^2]^{3/2}}\right) + \dot{m}^2\left(\frac{\rho_1}{\rho_2}-1\right),$$

(4)

where $We \equiv \rho_1 U^2 h/\sigma$, and surface tension $\sigma = \sigma(T)$ where T is the interfacial temperature.

• The tangential component of momentum balance at the interface (see Eq. (A. 4) in Narain et al. [2]) becomes:

$$\frac{\partial u_1}{\partial y}\Big|^i = \frac{\mu_2}{\mu_1}\frac{\partial u_2}{\partial y}\Big|^i + [t],$$

(5)

where the term [t] in Eq. (5) is defined in Eq. (A.9).

• The non-dimensional form of non-zero interfacial mass fluxes $\dot{m}_{LK}$ and $\dot{m}_{VK}$ (defined in Eq. (A.5)) impose kinematic constraints on the interfacial values of the liquid and vapor velocity fields and are given by:

$$\dot{m}_{LK} \equiv \left[u_1^i(\partial\delta/\partial x) - (v_1^i - \partial\delta/\partial t)\right]/\sqrt{1+(\partial\delta/\partial x)^2}, \text{ and}$$
$$\dot{m}_{VK} \equiv (\rho_2/\rho_1)\left[u_2^i(\partial\delta/\partial x) - (v_2^i - \partial\delta/\partial t)\right]/\sqrt{1+(\partial\delta/\partial x)^2}.$$

(6)

• The non-dimensional form of non-zero interfacial mass flux $\dot{m}_{Energy}$ (as given by Eq. (A.6)) represents the constraint imposed by net energy transfer across the interface and is given by:

$$\dot{m}_{Energy} \equiv Ja/(Re_1 Pr_1)\{\partial\theta_1/\partial n\big|^i - (k_2/k_1)\partial\theta_2/\partial n\big|^i\},$$

(7)

where $Ja \equiv C_{p1}\Delta T / \hbar^0{}_{fg}$, and $\hbar^0{}_{fg} \equiv \hbar_{fg}(T_s(p_o)) \cong \hbar_{fg}(T_s(p_2^i))$.

• The interfacial mass balance requires that the net mass flux (in kg/m²/s) at a point on the interface, as given by Eq. (A.7), be single-valued regardless of which physical process is used to obtain it. The non-dimensional form of this requirement becomes:

$$\dot{m}_{LK} = \dot{m}_{VK} = \dot{m}_{Energy} \equiv \dot{m}. \tag{8}$$

It should be noted that negligible interfacial thermal resistance and equilibrium thermodynamics on either side of the interface is assumed to hold for all x values slightly downstream of the origin (i. e., second or third computational cell onwards). And hence, as per discussions leading to Eq. (A.8) in the Appendix, no model for the interfacial mass-flux $\dot{m}$ is needed to obtain a solution.

• The non-dimensional thermodynamic restriction on interfacial temperatures (as given by Eq. (A.8)) becomes:

$$\theta_1^i \cong \theta_2^i = T_s(p_2^i)/\Delta T \equiv \theta_s(\pi_2^i). \tag{9}$$

Within the vapor phase, for the refrigerants considered here, changes in absolute pressure relative to the inlet pressure are big enough to affect vapor motion but, at the same time, they are usually very small (except in micro-scale ducts) to affect saturation temperatures. Therefore, we have $\theta_s(\pi_2^i) \cong \theta_s(0)$.

Boundary Conditions

The problem posed by Eqs. (2) − (9) are computationally solved subject to the well-known (see [2]) boundary conditions on the top and bottom walls.

Top wall: No slip condition (i.e. $u_2(x, 1, t) = 0$ and $v2(x, 1, t) = 0$) holds for the top wall. Furthermore, the top wall temperature $T_2(x, h, t) = T_{20} > T_{sat}(p_0)$ is at a superheated value

30

close to saturation temperature to allow the assumption of a nearly constant saturation temperature for the vapor at all location. This is reasonable because effects of superheat (in the typical $5 - 10^{\circ}$C range) are negligible.

Bottom wall: Besides the no-slip condition ($u_1(x, 0, t) = v_1(x, 0, t) = 0$) at the condensing surface, one could have one of *two* types of thermal boundary conditions. If the condensing-surface temperature ($T_1(x, 0, t) = T_w(x)$) is prescribed, its non-dimensional form is written as

$$\theta_1(x, 0, t) = \theta_W(x) \equiv T_W(x) / \Delta T \tag{10}$$

Here Eq. (10) is known as steady temperature boundary condition for a known condensing surface temperature distribution $T_W(x)$.

Alternatively, one could have the physical heat flux (i.e. $q''_w(x) = - k_1(\partial T_1/\partial y) = q''_{w0} * \tilde{q}''(x)$) specified where q'_{w0} is any known representative constant value of heat flux. Then the thermal boundary condition, instead of Eq. (10), becomes:

$$(\partial\theta_1/\partial y) \, (x, 0, t) = (q''_{w0} \cdot h \cdot \tilde{q}''(x)) / (k_1 \cdot \Delta T) \tag{11}$$

Equation (11) is known as steady heat flux boundary condition for a known heat-flux distribution $q''_w(x)$. This type of boundary condition does not allow flows to exhibit 'elliptical sensitivity' and is not considered here. Often the heat-flux $q'_w(x, t)$ is only implicitly known through the convection condition. In such case, Eq. (11) is replaced by

$$(\partial\theta_1/\partial y) \, (x, 0, t) = (h_{ext} h/k_1) \, \{\theta_1(x,0,t) - \theta_{res}\}$$

where, ($1/h_{ext}$) is known as external thermal resistance and $\theta_{res} = T_{res} / \Delta T$ is the non dimensional value of the reference temperature.

<u>Inlet Conditions:</u> At the inlet $x = 0$, $u_2 = U$ and hence:

$$u_2(0, y, t) = 1, \ \left.\partial v_2/\partial x\right|_{x=0} = 0 . \tag{12}$$

Pressure is not prescribed across the inlet boundary but its value p_0 appears indirectly through important thermodynamic properties such as $h_{fg}(p_2^i) \approx h_{fg}(p_0)$ and $T_{sat}(p_2^i) \approx T_{sat}(p_0)$. The interfacial pressure variations are obtained from the non-dimensional computed pressures $\pi_2^i(x, y, t)$ through the relation $p_2 = p_0 + \rho_2 . U^2 \pi_2 (x, \delta(x, t), t)$.

<u>Exit Conditions:</u>

In the computational study, "parabolic" boundary conditions include a prescribed inlet pressure p_0 along with inlet mass flow rate and wall condition. As far as exit conditions are concerned, it is assumed that none is needed for temperature. Whether response to exit condition impositions (pressure or equivalent) occur or not can only be investigated by attempting to solve condensing flow problem under such impositions. For this, we do not make any a priori assumption (based on single phase flows or air water flows) as to whether exit condition can or cannot be imposed. The approach here focuses on investigating partially condensing (film condensation) shear driven (annular/stratified) flows under two situations: one in which a steady-in-the-mean – but time periodic and unsteady - exit condition (exit pressure or exit liquid mass flow rate or exit vapor mass flow rate) is specified as if the unsteady problem has some "ellipticity" and the other in which exit condition is left unspecified and both the steady and unsteady problem is solved under steady "parabolic" boundary conditions.

Earlier results [2]-[6] in our research group correctly established that for steady inlet and wall conditions (i.e. "parabolic" boundary conditions), a long term t $\rightarrow \infty$ solution could be obtained from the unsteady equations (in absence of exit conditions) and that the resulting solution was the same as the steady solution obtained from the steady equations. Research work for this thesis shows that a steady and unique annular/stratified solution (also termed "natural" solution) can be obtained without specification of exit conditions – and, in fact, the solution predicts a unique steady exit condition (also termed "natural" exit condition) as a part of the solution.

After knowing the existence of unique steady "natural" solution for steady governing equations, the question regarding whether the unique steady annular/stratified solution for the self-sought exit condition is the only annular/stratified solution possible (as in "parabolic" single phase flows where exit pressure can not be independently specified) or other steady-in-the-mean exit conditions can be imposed such that the resulting condensing flows lead to different long term steady-in-the-mean (or quasi-steady) solutions with significantly changed interface location and/or liquid/vapor morphology. Note that the computational code used here is somewhat limited and, cannot find solutions unless the resulting morphology is also of the unsteady annular/stratified type. Despite the fact that these simulation results are limited to the annular/stratified morphology of Figure 1, response of the flow has been investigated – within the unsteady annular/stratified context – by imposing different steady and time-periodic unsteady exit conditions for the case in Figure 1. The reason for this investigation is an abundance of experimental data ([21]-[23]) for fully condensing shear driven flows that show the

presence of non-annular (plug/slug, bubbly, etc.) liquid vapor morphologies without well defined flow regime boundaries as well as experimental data (see Carey [36]) for heat transfer rates that are not useful because their scatter (see Figure 5.1 in [11]) results from sensitivity to specific experimental conditions and flow geometry.

For these reasons, one would like to experimentally and/or computationally investigate the impact of imposition of "off-natural" mean values of time-periodic exit conditions on the mean interface locations and flow regime transition locations for shear driven condensing flows. To better understand this issue, the full 2-D steady/unsteady approach of Narain et al. [2] needs to be re-examined. In this approach, at any instance of time t, the liquid domain and the vapor domain in Figures 4-5 are solved separately after a tentative guess of interfacial location δ.
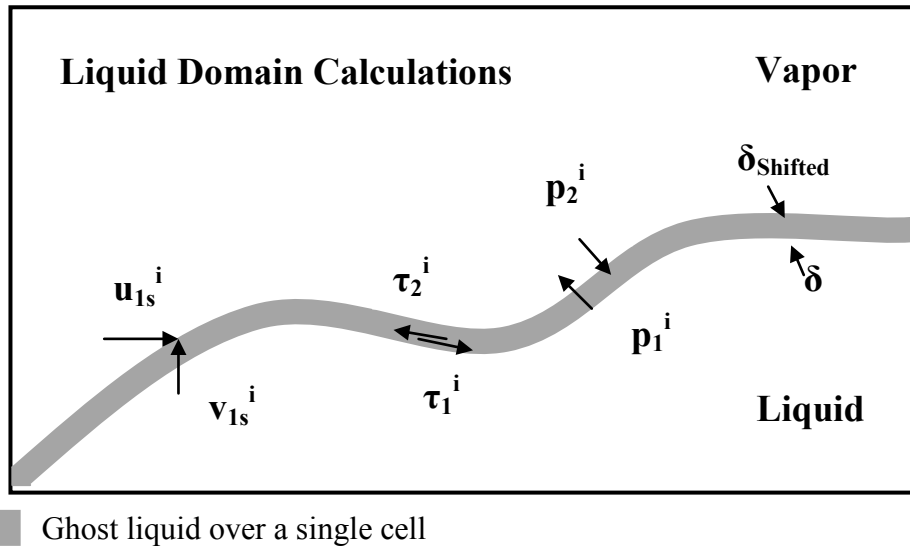
Figure 4: A schematic depicting computational procedure to solve liquid domain

The liquid domain calculations underneath $\delta_{shift}(x,t)$ with prescribed values of u_{1s}^i and v_{1s}^i on $\delta_{shift}(x,t)$ satisfy the correct shear and pressure condition on the actual liquid domain underneath $\delta(x,t)$.

34
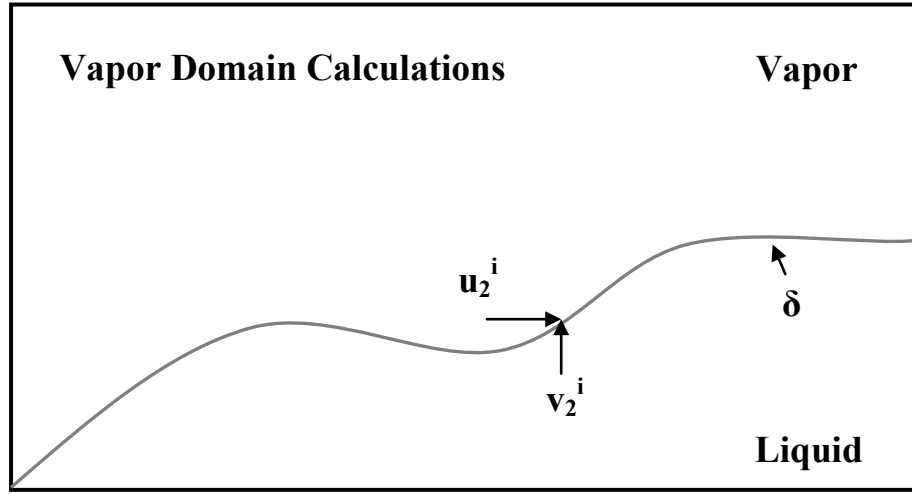
Figure 5: A schematic depicting computational procedure to solve vapor domain

The vapor domain calculations above $\delta(x,t)$ with prescribed values of u2i and v2i on $\delta(x,t)$ satisfy the requirement of continuity of tangential velocities and equality of interfacial mass balance.

The liquid domain is solved subject to stress boundary conditions (namely shear stress τ^i and pressure p^i in Figure 4) and the vapor domain is solved subject to the velocity boundary condition (u_2^i and v_2^i in Figure 5).

The temperature boundary condition at the interface - viz. values of θ_1^i and θ_2^i - are determined by the saturation condition in Eq. (9) – which, for all current purposes, equal known temperatures $\theta_s(0)$. In this approach, the five guesses of $\{u_2^i, v_2^i, \tau_1^i, p_1^i, \delta\}$ are equivalent to the five guesses of $\{u_2^i, v_2^i, u_{1s}^i, v_{1s}^i, \delta\}$ where, $\{\tau_1^i, p_1^i\}$ are replaced, in Figure 4, by $\{u_{1s}^i, v_{1s}^i\}$. The $\{u_{1s}^i, v_{1s}^i\}$ are liquid velocities imposed on the shifted interface that is approximately one cell above the actual interface and adjustment of their

values is used to satisfy stress condition at the actual interface locations. These five guesses are iteratively updated with the help of five interfacial conditions, viz. two from tangential and normal stress conditions (Eq. (4) and Eq. (5)), two from interface mass balance (Eq. 8), and one from continuity of tangential velocity (Eq. (3)).

Since the liquid flow in Figure 4 is solvable as a "parabolic" problem for a given $\{\delta, \tau_1^i, p_1^i\}$ and the vapor flow in Figure 5 is solvable as a "parabolic" problem for $\{\delta, u_2^i, v_2^i\}$, the question is what *overall* boundary conditions for the control volume are needed, or can be imposed, to deterministically predict these five key variables $\{\delta, \tau_1^i, p_1^i, u_2^i, v_2^i\}$ at all times t > 0 if the flow condition at some t = 0 were known. To begin with, the structure of the governing equations for these complex problems is not assumed as the physics of the flow suggests that at least, for shear driven flows, it is possible that some of the experimentally observed changes in the interface location within the annular/stratified flow regimes as well as uncertainty in locating flow regime transition boundaries may be a result of the fact that these flow are more susceptible to inadvertently imposed fluctuations at the inlet and the outlet boundaries. To investigate this issue, the unsteady annular/stratified problems (for gravity and shear driven flows) are to be solved, as per definitions to follow, under "unspecified" exit conditions in formulation [A] and under "specified" exit conditions in formulation [B].

Unspecified Exit Condition or "Parabolic" Formulation [A]: The "natural" specification of liquid or vapor exit flow rate is one that does not constrain the flow because it allows the flow to "self-seek" its exit condition. This is achieved by the imposition of the following "outflow" type condition at the exit:

$$\frac{\partial v_I}{\partial x}\bigg|_{x = x_e} \cong 0$$

(13)

for I = 1 and 2, while also ensuring that the x-component of the exit velocities $u_I|_{x=xe}$ are positive (for I = 1 and 2) and satisfy the overall mass balance for the entire partially condensing control volume in Figure 1.

It is shown here that in the absence of specification of exit condition (i.e. the above formulation [A]), there exists a unique annular steady solution of strictly steady equations for gravity driven as well as shear driven internal condensing flows. Furthermore, it is also found that the unsteady solutions for these flows under formulation [A] and assumed annular/stratified morphology also seek the same steady solution as t → ∞. In addition, as shown later, these steady solutions are found to be stable – at least for the partially condensing flow lengths investigated here. This "unique" solution of the parabolic problem is termed as "natural" solution and corresponding exit condition (exit pressure or exit liquid mass flow rate or exit vapor mass flow rate obtained as a part of the solution) and pressure difference are termed "natural" exit condition and "natural" pressure difference respectively. It is also found that, in the unsteady solution procedure, any reasonable initial guess of the interface location and other variables are attracted, in time, to the same unique "natural" solution.

The unique steady solutions for shear and gravity driven flows that have been obtained by the 2-D approach described above, were also obtained by a computationally more efficient and powerful (though more approximate) 1-D solution technique [1] that has been recently developed to support and reinforce the 2-D solution technique.

37

However, the fact that steady annular/stratified solutions are obtainable for internal condensing flows under unspecified exit condition (formulation [A]) does not preclude the possibility that the flow is only *partially* parabolic and it can respond differently (with different steady liquid-vapor morphology or different quasi-steady – both in waviness and mean values - annular/stratified morphology) to certain (steady or unsteady) exit condition specifications imposed through the formulation [B] given below.

In the present context of unsteady equations, formulation [B] below is used for "*elliptic/specified*" condition at the exit of unsteady shear driven flows. An imposition of exit condition through this same formulation [B] for gravity dominated flows proved unsuccessful. As discussed in [11], such impositions proved unsuccessful for gravity dominated experiments as well. The reason behind absence of this kind of suspected "elliptic sensitivity" for gravity *dominated* flows (see [9]) is now understood. For these conditions, there is uni-directional connectivity between liquid and vapor domain flows as liquid domain determines the vapor motion completely and the liquid motion as well as the interface location is determined only by an external agency, namely gravity. Thus, any imposition of "non-natural" exit condition cannot be accommodated by changes in liquid motion without altering the "parabolic" boundary conditions themselves. For a closed flow loop, it is experimentally found [11] that the changes in the "parabolic" boundary conditions under changes in the exit conditions only leads to a new "natural" solution consistent with the new "parabolic" boundary conditions.

Formulation [B]: For *unsteady* annular/stratified internal condensing flow problems (purely shear driven flows – 0g or horizontal channel in Figure 1), it is

tentatively assumed that exit condition can be specified in terms of exit flow rate (either non dimensional exit vapor flow rate $\dot{M}_{V-e}(t)$ at the exit or non dimensional liquid flow rate $\dot{M}_{L-e}(t)$ at the exit) or suitable exit pressure specifications (not implemented in this paper). Equation (14) below shows one of the ways in which exit condition can be specified in terms of non-dimensional liquid exit mass flow rate:

$$\hat{\dot{M}}_{L-e}(t) = \int_{y=0}^{\delta(x_e,t)} u_1(x_e,y,t) \cdot dy \equiv \frac{1}{\rho_1 U_0 h} \left[\int_{y=0}^{\varLambda(x_e,t)} \rho_1 u_1(x_e,y,t) \cdot dy \right]$$

$$\equiv \text{Known function of time t for each } t \geq 0 \qquad (14)$$

Even though one can test different constants or time varying values on the right hand side of Eq. (14), it is already known that there must exist only one unique time independent *constant* value for the right side of Eq. (14) for which a long term (t → ∞) steady solution can be obtained for the unsteady problem under exit condition imposition through Eq. (14). This unique constant must be the same as the one obtained from the solution of the steady equations under formulation [A]. Physically these solutions are realized when one does not constrain the flow from seeking its "natural" exit condition. A key question here is whether steady-in-the-mean time periodic specification in Eq. (14) – corresponding to a system imposed mean exit condition superposed with time-periodic fluctuations can or can not lead to a quasi-steady solutions that are different in the mean than the mean features associated with steady or quasi-steady "natural" solutions under formulation [A].

<u>Initial Conditions</u>

If t = 0 is chosen to be the time when saturated vapor first comes in contact and condenses on a dry sub-cooled (T_w (x) < T_s (p_0)) bottom plate, the above described *continuum* equations do not apply at very early times (t ~ 0). This is because these equations do not model and incorporate various inter-molecular forces that are important in determining the time evolution of very thin (10 - 100 nm) condensate film thickness δ (x, t). Because of the above modeling limitations, the strategy here is to start at a time (t = 0) for which one has a sufficiently thick arbitrary *guess* of the *steady* solution of the *continuum* equations (where all the governing equations clearly apply) and then, from there, one can obtain the natural large time (t → ∞) steady/quasi-steady solutions with the help of the unsteady equations. That is, if ϕ(x,y,t) is any variable (such as u_I, v_I, π_I, θ_I, etc.), the initial values of ϕ and film thickness δ(x,t) are such that:

$$\phi(x, y, 0) = \phi_{steady}(x, y) \text{ or } \phi_{guess}(x,y)$$

$$\text{and } \delta(x,0) = \delta_{steady}(x) \text{ or } \delta_{guess}(x) \tag{15}$$

where ϕ_{guess} and δ_{guess} are reasonable but arbitrary initial guesses and ϕ_{steady} and δ_{steady} are solutions of the governing equations obtained by dropping all time dependencies in equations (2) – (9) and solving the resulting steady equations.

2.2 External Condensing Flow of Vapor over a Horizontal Plate

2.2.1 Mathematical Model for Computational Problem

The governing equations in individual domains (Eq. (2)), interface conditions (Eqs. (3)-(9)), variables denotations, and initial conditions for this flow problem remain similar to that discussed for internal condensing flows discussed in section 2.1. The non-dimensional forms of all the variables are also the same except for the fact that the far upstream speed of forced vapor (used as characteristic speed) and height of flow domain (used as characteristic length) used in non-dimensionalization in Eq. (1) are denoted as U_∞ and Y_e respectively (see Figure 3). From mathematical modeling perspective, the difference lies in the applied boundary conditions and this is discussed in this section. As shown in Figure 3, instead of the original infinite domain ($x \geq 0$ and $y \geq 0$), considered for the Koh problem [10] computational solutions for this problem are to be computationally obtained over a finite domain ($0 \leq x \leq X_e$ and $0 \leq y \leq Y_e$).

For convenience, the characteristic length for this problem is chosen to be Y_e, where Y_e can be chosen to be a known numerical multiple of the well known physical value of steady film thickness for an altogether different problem – the one associated with a vertical inclination of the plate (gravity driven condensate) and for $U_\infty = 0$ - viz. the Nusselt problem (see [20], [28]). That is, $Y_e \equiv c_1 \cdot \Delta_N(X_e)$, where $c_1 = 47$ for most of the cases considered in this research and $\Delta_N(X_e)$ is the Nusselt film thickness at $x = X_e$. An equivalent alternative is $Y_e \equiv (c_2 \cdot \mu_1)/(\rho_1 \cdot h_{fg})^{0.5}$, where $c_2 = 1.133 \text{x} 10^5$ for most of the cases considered in this research. These choices make Y_e an *a priori* known number that is sufficiently large to capture all the relevant vapor flow domain of interest. Though

other choices of intrinsic characteristic length Y_e are also possible (e.g. $Y_e = \mu_1/(\rho_1.U_\infty)$

or $Y_e = \mu_1^{3/4} k_1^{1/4} \Delta T^{-1/2} C_{p1}^{-3/4} \rho_1^{-1}$), the earlier two choices suffice for this problem.

Furthermore, as discussed in the later section, either of the two choices of Y_e is *a posteriori* verified to be effective by showing that the numerically obtained values of the flows' physical variables are independent of different choices of the number for Y_e. The above choice of Y_e for characteristic length and U_∞ for characteristic speed are used for defining the non-dimensional variables in Eq. (1). As needed, these values can easily be related to the results obtained from other commonly used choices of characteristic length and speed. Let g_y be gravitational acceleration acting along y axis (gravity along x direction is zero for this horizontal flow), p_∞ be the pressure of the far field vapor at y $\geq$ Y_e, $\Delta T \equiv T_s(p_\infty) - T_w(0)$ be the representative controlling temperature difference between the vapor and the bottom plate, and h_{fg} be the heat of vaporization at saturation temperature $T_s(p)$.

With *t* representing the physical time, a new list of fundamental non-dimensional variables is introduced through the following definitions which is similar to what is given in Eq. (1):

$$\{x, y, \delta, u_I, \dot{m}\} \equiv \{\frac{x}{Y_e}, \frac{y}{Y_e}, \frac{\Delta}{Y_e}, \frac{u_I}{U_\infty}, \frac{\dot{m}}{\rho_1 U_\infty}\},$$

$$\{v_I, \theta_I, \pi_I, t\} \equiv \{\frac{v_I}{U_\infty}, \frac{T_I}{\Delta T}, \frac{p_I - p_\infty}{\rho_1 U_\infty^2}, \frac{t}{(Y_e/U_\infty)}\}$$

(16)

Boundary Conditions

Since the vapor flow is nearly uniform at locations at large y, appropriate boundary conditions are prescribed along lines OA ($x = 0$), AB ($y = Y_e$ or y = 1) and BC ($x = X_e$ or $x = x_e = X_e/Y_e$) in Figure 3. Assuming onset of condensation at x = 0(i.e. Δ (0, t) = 0), the boundary conditions are:

Inlet: At the inlet x = 0, we have:

$$u_2(0,\ y,\ t) = U_\infty,\ \left.\partial v_2 \middle/ \partial x\right|_{x=0} = 0 \text{ on OA in Figure 3} \tag{17}$$

Pressure is not prescribed across the inlet boundary but is prescribed to be the far field pressure p_∞ at the top corner reference location (point A with $x = 0$ and $y =$ OA in Figure 3) on the inlet boundary. Pressures within the entire domain, including the inlet values p_2 (0, y, t), are calculated as part of the solution of the problem being considered. However, outside and above the control volume, one expects the far field pressures to be:

p_2 - $p_\infty \equiv (\rho_2.U_\infty{}^2) \cdot \pi_2$ (0, y, t) = 0 for $y \geq$ OA (see Figure 3) or $y \geq 1$. For temperature, one also iteratively imposes the condition $T_2(0,$ y, t) = T_{sat} (p_2 (0, y, t)) - which is, in principle, a non-constant prescription of vapor temperature at the inlet.

It should be noted that prescription of pressure at reference location (point A in Figure 3) does not make inlet boundary condition one of pressure-inlet. It remains a boundary where x-component of vapor velocity u_2 is uniform but y-component of vapor velocity v_2 is given the requisite freedom through the condition $\left.\partial v_2 \middle/ \partial x\right|_{x=0} = 0$.

Top: On the top boundary, where $y =$ OA (see Figure 3) or y = 1, the pressure is p_∞ and shear stress is nearly zero. This leads to standard far field boundary modeling condition:

$$\pi_2(x,1,t) = 0 \text{ and } \partial u_2/\partial y|_{(x,1,t)} = 0 \text{ on AB in Figure 3} \tag{18}$$

The temperature at the top boundary is also considered to be one of saturated vapor, i. e. $T_2(x, Y_e, t) = T_{sat}(p_\infty)$. Therefore, according to Eq. (1), $\theta_2(x,1,t) = T_{sat}(p_\infty)/\Delta T$. If the temperature at the top boundary is allowed some superheat (5-10 ^{o}C), a non-zero thickness for temperature boundary layer develops near the interface. For *saturated* vapor flow conditions considered here, this thermal boundary layer thickness is not present. Even if the boundary layer has non-zero thickness because of presence of vapor superheat, a non-zero superheat has no impact on the reported results for most vapors (this well known fact has been computationally verified and the physical reasons are discussed later).

Exit:

As far as exit condition is concerned, none is needed for temperature. For the Koh problem [10], and the steady solution, the exit pressure remains externally unspecified and, as a result, it remains close to the far field pressure p_∞ if the exit is sufficiently far from the inlet. This is not only the original assumption of Koh formulation [10] but is also the assumption for most parabolic external flow problems (such as single phase flow over a flat plate, etc.). For this modeling, either of the two formulations [A] or [B] below is used.

[A] The pressure is prescribed to be the uniform steady pressure p_∞ (i.e. non dimensional pressure π_2 of zero) along some of the vapor phase at the exit section (along BD' in Figure 3) that is close to the top boundary. Thus the best way to faithfully reproduce the above assumption for pressure at the exit, is

$$\pi_2(x_{e,}, y, t) \approx 0 \text{ and } \frac{\partial v_2}{\partial x}\Big|_{(x_e,y,t)} \cong 0 \qquad (19)$$

whenever x_e and y are sufficiently large (i.e., y is on D´B in Figure 3) . For smaller y

values (i.e., y on CD´ in Figure 3 where the point D´ at $x = X_e$ can be taken to be any

point that is sufficiently close to the interface), no boundary condition is prescribed

except for the "outflow" boundary condition. The "outflow" condition is simply that the

mass flow across CD´ – which specifically includes the liquid portion $0 \leq y \leq \Delta(X_e, t)$ – is

such that it satisfies the overall mass balance for a control volume formed by the

bounding surfaces $x = 0$, $x = X_e$, $y = 0$, and $y = Y_e$.

[B] The pressure is left unspecified along the entire (or most) vapor phase at the

exit section (along BC in Figure 3). Because uniform pressure p_∞ is already prescribed

along the top (AB in Figure 3), only an "outflow" condition at the exit section is enforced

to preserve an overall mass balance for the entire control volume (see OABC in Figure

3). This formulation is adequate as the resulting computational solution obtained under

this formulation also satisfies the requisite $\pi_2(x_e, y, t) \approx 0$ condition. The steady or

unsteady solution obtained under [B] is found to be nearly identical (within

computational convergence bounds) to the solution under [A] above. So, from here and

henceforth, unless otherwise stated, this exit formulation [B] is used to closely follow the

original intent of the Koh formulation [10] – that is to assume that the uniform far field

pressure (= p_∞) condition holds for the exit section if it is sufficiently far from the inlet

and, as a result, at these locations no significant adjustments in cross-sectional kinetic

energy takes place.

The exit condition related "elliptic sensitivity" discussed for internal condensing

flows is not investigated here as meaningful physical ways to impose steady-in-the-mean

but periodic exit pressure or exit liquid flow rate are possible but make problem significantly different than the one of Cess [9] and Koh [10].

Condensing Surface:

At the condensing surface (y = 0), we have:

$$u_1(x,0,t) = v_1(x,0,t) = 0 \text{ and } \theta_1(x,0,t) = \theta_w \equiv T_w/\Delta T. \tag{20}$$

An inspection of all the non-dimensional governing equations, interface conditions, and boundary conditions reveals the fact that the computational solutions are affected by the following set of seven independent non-dimensional parameters:

$$\left\{ Re_1, Ja, Fr_y^{-1}, \frac{\rho_2}{\rho_1}, \frac{\mu_2}{\mu_1}, Pr_1, We \right\}, \tag{21}$$

where $Fr^{-1}_y = U_\infty^2/g_y Y_e$ and $Re_1 \equiv \rho_1 U_\infty Y_e/\mu_1$. For the downstream distances considered in this research, the role of Fr^{-1}_y is insignificant. The role of surface tension, through We, is also found to be insignificant for cases considered here.

2.2.2 Koh's Formulation for a Similarity Solution of the Steady Problem

The formulation for this problem (see Cess [9] or Koh [10]) is posed by governing equations (A.16) – (A. 19) in the Appendix A.4 being replaced by Eq. (A.20) of the Appendix A.4 along with the interface and boundary conditions given earlier being replaced by (A.21)-(A.25) of the Appendix A.4. The "similarity" formulation is sought after rewriting (A.20)-(A.25) following an introduction of certain assumed forms of velocity and temperature functions in terms of two new similarity variables (η for the liquid phase and ξ for the vapor phase) that replace x and y. These "new" similarity variables are defined as

46

$$\eta(x,y) \equiv y\sqrt{\frac{U_\infty}{\nu_1 x}} \quad , \quad \xi(x,y) \equiv (y - \Delta(x))\sqrt{\frac{U_\infty}{\nu_2 x}} . \qquad (22)$$

The physical variables of velocity and temperature are sought as functions (viz. f_1, f_2, g_1, and g_2) of the variables introduced above. The defining relations for these physical variables (see Koh [10]) are:

$$p_I(x,y) = p_\infty = \text{constant} \quad (I = 1 \text{ or } 2), \quad \Delta(x) \equiv \Delta_{Koh}(x) \equiv \eta_\delta \sqrt{\frac{\nu_1 x}{U_\infty}}$$

$$u_1(x,y) \equiv U_\infty f_1'(\eta) \qquad (23)$$

$$u_2(x,y) \equiv U_\infty f_2'(\xi) , \; T_1(x,y) - T_w \equiv \Delta T \cdot g_1(\eta), \; T_2(x,y) - T_w \equiv \Delta T \cdot g_2(\xi) \qquad (24)$$

Eqs. (22) - (24) transform the governing equations (A.20) and interface/boundary conditions (A.21)-(A.25) given in the Appendix A.4 for the Koh formulation [10], to a set of ordinary differential equations (ODE) over the liquid ($0 \leq \eta \leq \eta_\delta$) and vapor ($0 \leq \xi < \infty$) domains with proper boundary conditions at $\eta = 0$, $\eta = \eta_\delta$, $\xi = 0$, and $\xi \to \infty$. This ODE formulation – unlike the formulation in section 2.2.1 – is *always* such that a unique steady solution exists and can be numerically obtained by a suitable method (e.g. fourth order Runge-Kutta method combined with a shooting technique that can satisfy all the boundary conditions). Thus, the steady Koh formulation (which is *always* well-posed and solvable for plates of large finite length) cannot, by itself, assess attainability issues for these solutions. The solution obtained by Koh's method, based on the results presented here, are found to represent a meaningful approximate solution, when a solution exists, either as a *steady* solution of the steady version of the formulation in section 2.2.1 or as the long term steady limit of the *unsteady* formulation.

47

Chapter 3 COMPUTATIONAL METHODOLOGY

3.1 Internal Condensing Flows in Channels and Tubes

In its broad outline, the computational methodology for the channel and in-tube cases is similar to the methodology described in Narain et al. [2], Liang et al. [3] and Phan et al. [4] for the channel case. But there have been significant changes/improvements in the flow algorithms and codes for channel cases to establish: (i) unique "steady" solutions of steady governing equations for internal condensing flows in gravity and shear driven environments for unspecified exit cases (formulation [A] in section 2.1), (ii) existence of multiple "quasi-steady" solutions for unsteady governing equations under elliptically specified quasi-steady exit conditions for shear driven internal condensing flows (formulation [B] in section 2.1), (iii) "quasi-steady" solutions pertaining to "quasi-steady parabolic" boundary conditions for shear and gravity driven situations, and (iv)modifications to steady solutions under modeling changes that account for some micro-scale effects (see later section).

In addition, for in-tube cases, this research work includes modifying/running the codes developed in [34] to obtain steady/unsteady solutions for unspecified exit conditions (formulation [A]) for fully condensing flows and partially condensing flows to compare with the experiments. Whether it is an unspecified or a specified exit condition case, the computational algorithm broadly consists of the steps described in the Appendix A.2.

48

3.2 External Condensing Flow of Vapor Condensing over a Flat Plate

Even though the computational approach and methodology adopted here remains the same as for internal condensing flows, unlike the internal flows discussed in [2] and [7], the imposition of the top and exit boundaries for this external flow is different from the internal flow situations but is the same as the one given by us in Phan and Narain [20] for the external flow Nusselt problem [28]. The difference is primarily another use of the earlier established ([2]) τ-p method towards prescribing stress boundary-conditions – i.e., pressure (with τ = normal derivative of the tangential velocity component = 0) on the top (AB in Figure 3) and side (BD' in Figure 3) boundaries. The τ-p method was originally developed (see [2]) for prescribing τ (tangential velocity gradient in the normal direction) and p (pressure) at the interface.

In general for any computational problem (internal or external condensation), the solution must show convergence in the interior of each phase, grid independence, and satisfaction of interface and boundary conditions. The converged solutions reported here exhibited all these features and are good (i.e. they are within 5% of each other). On any interface with propagating waves, the critical and difficult to satisfy requirement is Eq. (7) – the requirement of the equality of three differently computed/obtained values of interfacial mass flux (this is known to be difficult for the more general interface capturing techniques such as level-set [13] or VOF [14]). However, this requirement is met by the interface tracking approach employed in this research. The spatial and temporal grid spacings and total lengths impose a restriction on wavelength λ and frequency f that can be adequately resolved. If the maximum spacing of the grid in x direction is Δx_m and its

49

total length is x_e while the total time duration is t_e and is divided in equal intervals of duration Δt; the restrictions imposed by Nyquist criteria [19] are well satisfied for $\lambda \geq 4 \cdot \Delta x_m$ and $f \leq (4 \cdot \Delta t)^{-1}$ and the restrictions imposed by the domain lengths are well satisfied for $\lambda \leq x_e/2$ and $f \geq 2/t_e$. The initial ($t = 0$) spatial and temporal grids are defined by (ni × nj × nt), where "ni" is the total number of initial grid points along x, "nj" is the total number of initial grid points along y (0 to 1), and nt is number of time steps with equal intervals (Δt). Typical values of ni were 30-40, nj were within 50-70, x values were within 0-50 and y values were within 0-1. Attainable values of nt depend on ni, nj, Δt, interfacial variables, numerical methodology, and the available computer memory for the storage of flow variables. A new way to march for any number of time steps nt (as long as the solution was obtainable) was formulated by periodically deleting and replacing the values stored in the storage variable arrays of size nt.

Chapter 4 COMPUTATIONAL RESULTS AND COMPARISONS WITH EXPERIMENTS FOR INTERNAL CONDENSING FLOWS[1]

4.1. Existence of "Natural" Steady Solutions for Gravity and Shear Driven Flows

2-D computational results correct the previous results [2]-[6] and establish that, for a parabolic problem (given values of vapor inlet mass flow rate, inlet pressure, vapor-to-wall temperature difference), steady equations of internal condensing flows have a unique annular steady solution and the solution does not need exit-condition prescription. Because of the nature of the equations there are other "almost" steady solutions which, because of the inaccuracies in the previously reported solutions ([2]-[6]), led us to believe

---

[1] Some of the results described in this section have been published in

(A) Narain, A., S. Kulkarni, S. Mitra, J. H. Kurita, M. Kivisalu, 2009, "Computational and Ground Based Experimental Investigations of the Effects of Specified and Unspecified (Free) Pressure Conditions at Condenser Exit for Condensing Flows in Terrestrial and Micro-Gravity Environments," *Annals of New York Academy of Sciences , Interdisciplinary Transport Phenomena in Space Sciences*, Vol. 1161, pp. 321-360. **Please see Appendix A.5 for the copyright permission to reproduce these results in this thesis.**

(B) Narain, A., J. H. Kurita, M. Kivisalu, S. D. Kulkarni, A. Siemionko, T. W. Ng, N. Kim, and L. Phan, 2007, "Internal Condensing Flows Inside a Vertical Pipe – Experimental/Computational Investigations of the Effects of Specified and Unspecified (Free) Conditions at Exit," ASME *Journal of Heat Transfer*, pp. 1352-1372. **Please see Appendix A.6 for the copyright permission to reproduce these results in this thesis.**

that these were multiple steady solutions for multiple exit conditions (as if the problem were fully "elliptic").

This solution is termed "natural" solution and can be obtained as steady solution of the steady governing equations or a *long-term* steady solution of the unsteady governing equations under formulation [A] discussed in section 2.1. The exit pressure (equivalently exit vapor quality for partially condensing flows and length of full condensation for fully condensation) found as part of the solution is termed "natural" exit condition.
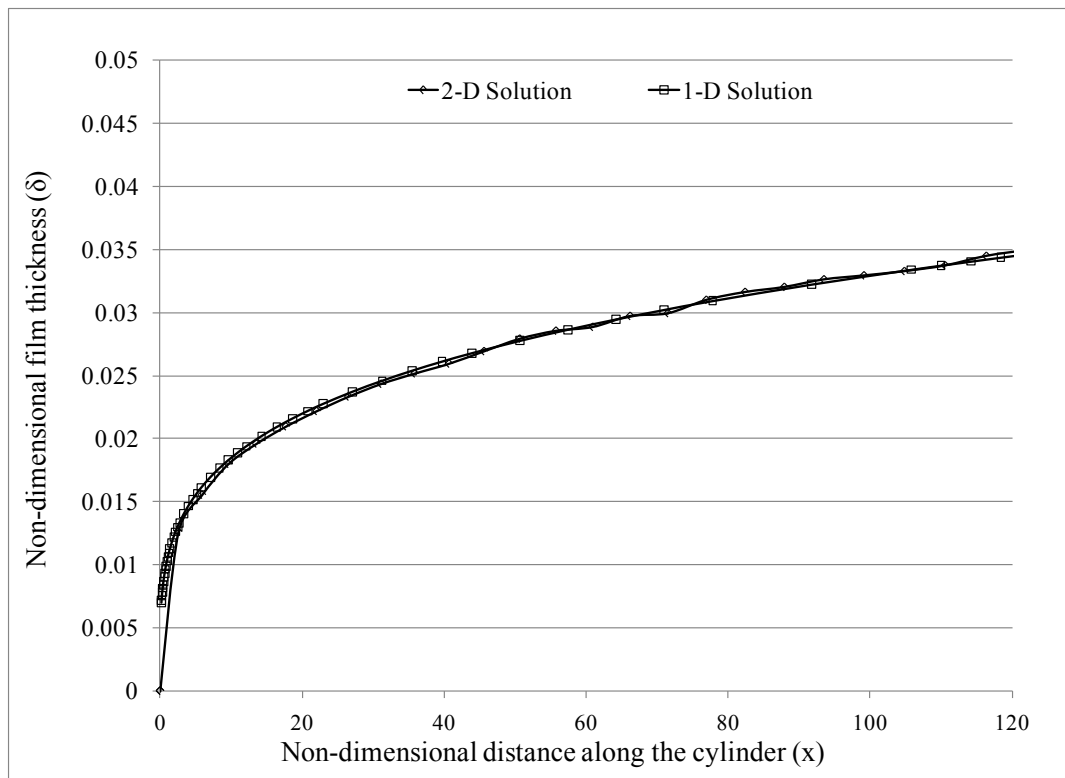
Figure 6: Existence of "natural" steady solution for gravity driven condensing flows

The figure compares steady/quasi-steady solutions for a vertical channel obtained by 2-D and 1-D techniques. The solutions are obtained for R-113 vapor with inlet speed of U = 0.41 m/s, $\Delta T = 5$ °C, h = 0.004 m, and $g_x = 9.8$ m/s^2.
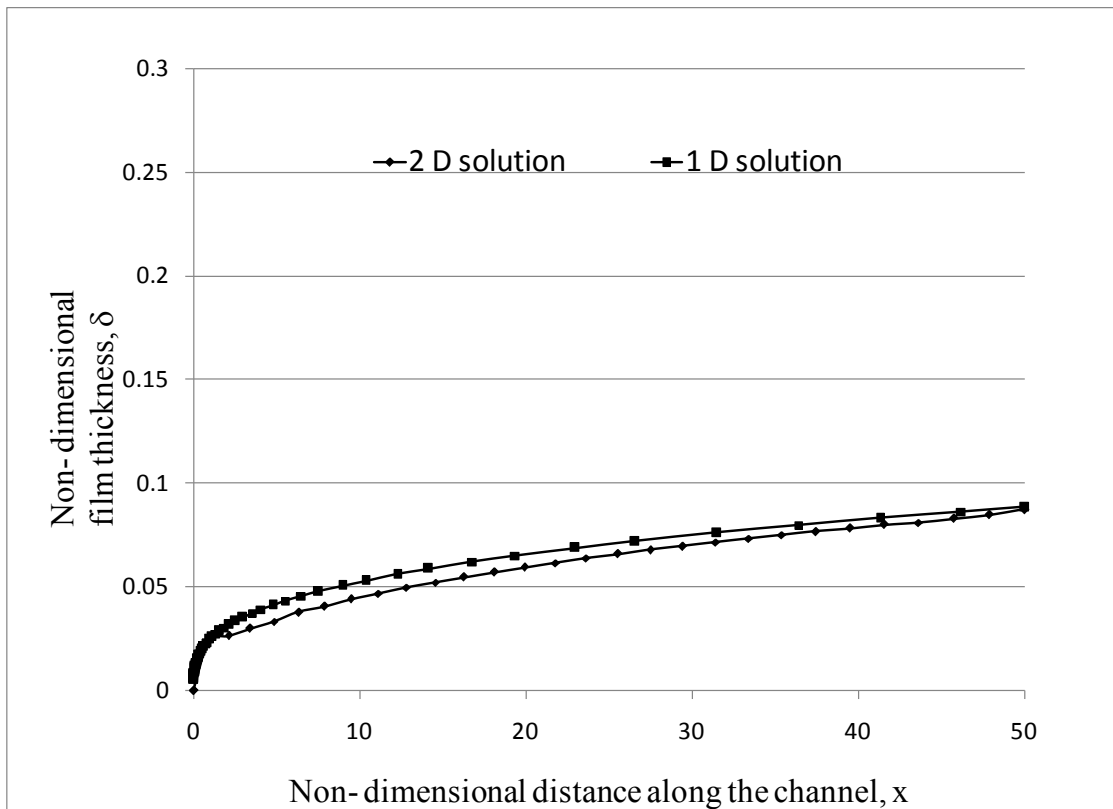
Figure 7: Existence of "natural" steady solution for shear driven condensing flows

The figure compares steady/quasi-steady solutions for a channel under 0g conditions. The results are obtained by 2-D and 1-D techniques. The solutions are obtained for R-113 vapor with inlet speed of U = 0.6 m/s, ΔT = 5 °C, and h = 0.004 m.

This result has been independently obtained by a newly developed 1-D technique [1]. Figure 6 (for gravity driven flows) and Figure 7 (for shear driven flows) compare unique steady solutions of the strictly steady governing equations obtained by 1-D and 2-D techniques for a partially condensing flow inside a channel. It is found that both results are in very good agreement with each other.
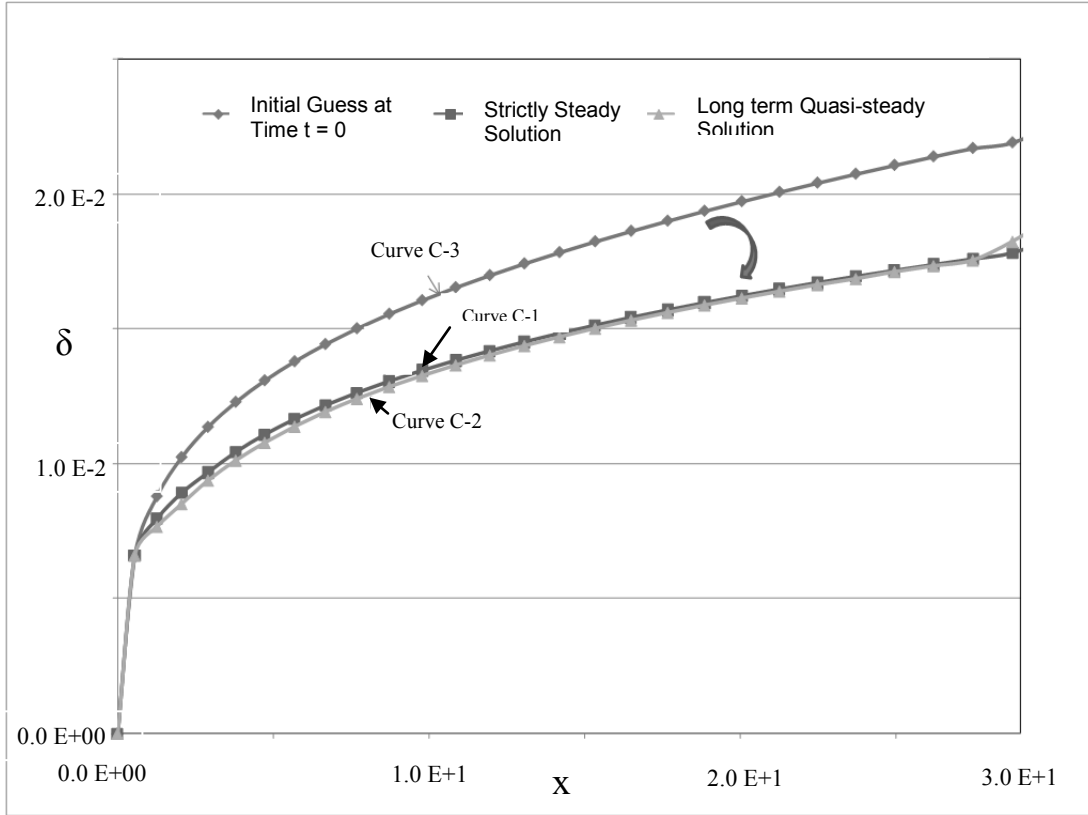
Figure 8: Existence of an "attractor" for gravity driven condensing flows

This figure for a condensing flow in vertical channel shows that any initial guess (Curve C-3) at time t = 0, gets attracted towards long-term "natural" quasi-steady solution (Curve C-2) in time which is same as the solution (Curve C-1) obtained by solving steady governing equations. These solutions are obtained for R-113 vapor with inlet speed of U = 0.41 m/s, $\Delta T = 5$ °C, h = 0.004 m, and $g_x = 9.8$ m/s^2.

Figures 8-9 show that this "natural" steady solution can also be obtained as *long-term* steady solution of unsteady equation under formulation [A] of section 2.1. This solution is also called an "attractor" as any initial guess, as shown in Figures 8-9 for gravity and shear driven cases respectively, gets attracted towards this "attracting" steady solution as time t → ∞.
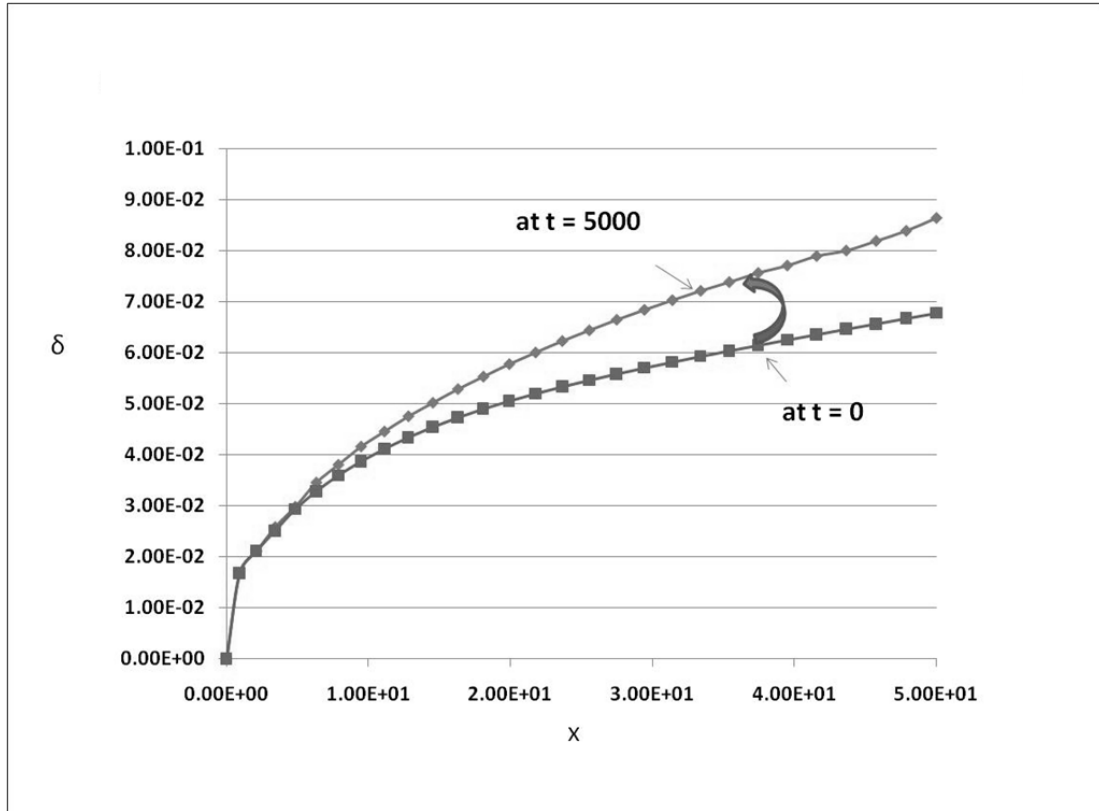
Figure 9: Existence of an "attractor" for shear driven condensing flows

This figure for a condensing flow in a horizontal channel shows that any initial guess (red curve) at time t = 0, gets attracted towards long-term "natural" quasi-steady solution (blue curve) in time. These solutions are obtained for R-113 vapor with inlet speed of U = 0.41 m/s, ΔT = 5 °C, h = 0.004 m, and $g_x = g_y = 0$ m/s2.

4.2 Synthesis of Simulations and Experiments for Gravity Driven In-tube Condensing Flows.

4.2.1 Partially Condensing Flows in a Vertical Tube

Gravity driven internal condensing flows were thoroughly studied by synthesizing computational results of this thesis work with the experimental work of Jorge Kurita (see

55

[11]). Experiments were carried by employing 0.8 m long, vertical, stainless steel (316 SS) tube with 6.6 mm inner diameter, D, and 12.7 mm outer diameter. The experiments involved a single pure working fluid (viz. FC-72 by 3M Corp.) and focused on inlet mass flow rates that correspond to inlet vapor Reynolds numbers in the range of 10,000 - 40,000 and vapor to wall temperature differences of 3 - 60$^{\mathrm{o}}$C (i.e. $0 \leq$ Ja ≤ 0.4). The experimental procedures to obtain "natural" (unspecified exit condition) cases for partial and full condensation have been discussed in detail in [5] and [11].

The experimentally obtained partial condensation cases in unspecified exit ("natural" solutions) are listed in Table 1 with all the essential details including exit vapor quality Z_e (fourth column) and its value obtained from simulations (fifth column). It can be seen that there is very good agreement between exit vapor quality (thus film thickness and average heat transfer coefficient values) predicted by simulations and experiments.

The test matrix for all partial condensation cases is limited by the system limits and flow regime boundaries indicated on the plane marked by inlet mass flow rate $\dot{M}_{in}$ and temperature difference $\overline{\Delta T}$ values.

Figure 10 shows all the partial condensation cases plotted on the two dimensional plane formed by $\dot{M}_{in}$ and $\overline{\Delta T}$. These parameters were found to be the key variables controlling the dynamics of the condensing flows in the test section. The typical values for lower and upper limits for inlet mass flow rate were found to be 1 g/s and 2 g/s respectively and that for the $\overline{\Delta T}$ were recorded to be 2° C and 12 ° C respectively. The interior shaded zone in Figure 10 represents $\dot{M}_{in}$ and $\overline{\Delta T}$ values for which "natural" quasi-steady partially condensing annular flows were attained. For most of the cases (except for

56

non-annular flows) in this shaded zone, simulations were run to obtain local variation of film thickness, velocities, heat transfer, pressure values, etc. The bounding curves B and C are experimental in nature and represent flow boundaries for the test-section. They are discussed in [5]. The dotted curve-A on the left bottom has been experimentally noticed. It does not represent a flow regime boundary for the test-section, as it is a result of the exit pressure oscillations or unsteadiness in test section imposed by oscillatory or other plug/slug instabilities occurring elsewhere in the system (in this case, in the auxiliary condenser downstream of the test section).
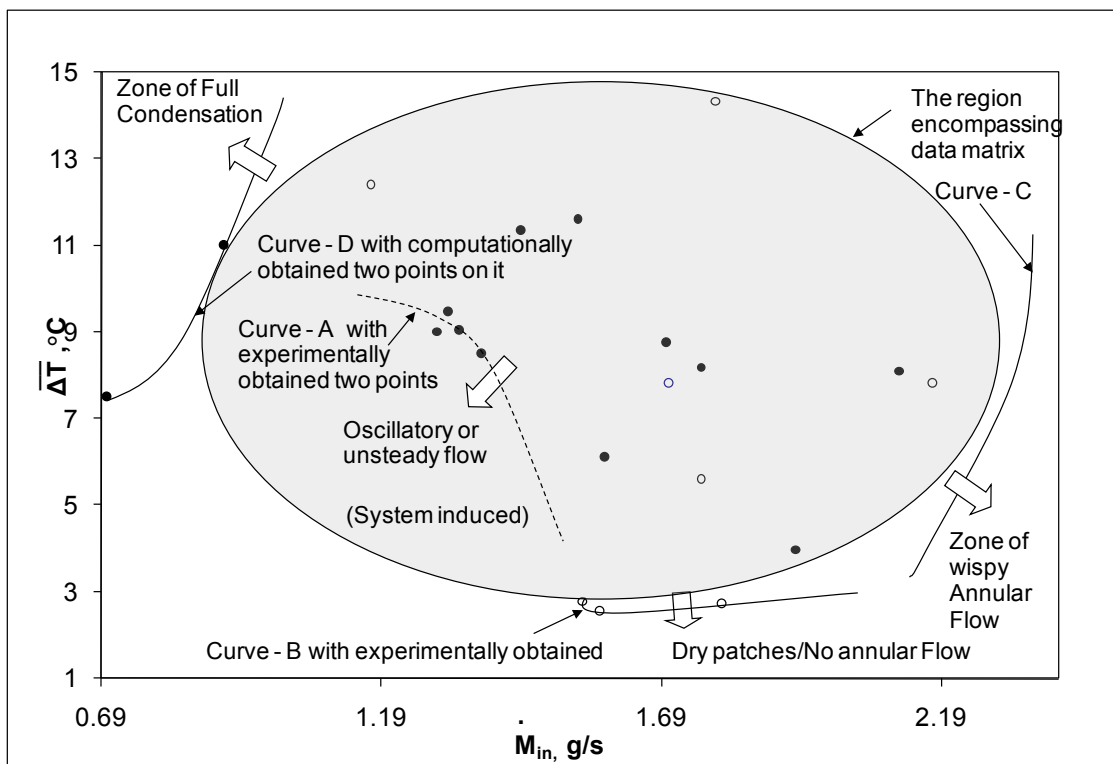
Figure 10: Two-dimensional test data matrix for "natural" partial condensation

cases' points and different bounding curves represented on $\dot{M}_{in}$ - $\overline{\Delta T}$ - plane

Its possible cause can be explained by "ellipticity" sensitivity results (that may apply to auxiliary condenser) discussed in the next section for shear driven condensing flows. The bounding curve in the upper left corner of Figure 10 is marked as curve-D. This curve represents transition from partial condensation to full condensation. If $\dot{M}_{in}$ is reduced and $\overline{\Delta T}$ is increased further, computations show that the left side of curve-D represent the zone for which the entire vapor coming in condenses inside the test section

The values of pressure drop Δp (p_{in}-p_{exit}) obtained from simulations for all the "natural" partial cases were negative and below 50 Pa indicating p_{exit} was greater than p_{in} for all the condensation cases in given $\dot{M}_{in}$ range. This is confirmed by the experimental values of Δp (see Table 1) which are also all negative (except a very few cases). However, as expected, the magnitudes for experimental values of Δp were found to be greater than those from simulations. The reason behind this is that the simulations assume laminar vapor/laminar liquid flows with smooth interface while, in reality, the interface is wavy and vapor Reynolds numbers are in the higher range (20000-30000) and this makes vapor flows significantly turbulent in the core. The turbulence in vapor core does not affect the mass transfer across the interface by much because condensate motion is laminar and gravity dominated. However, turbulent vapor core significantly increases Δp values in the vapor domain. Because of this, the values of vapor quality obtained from the simulation are in good agreement with the experiments but the values of pressure drop Δp obtained from experiments are higher in magnitudes. The predicted pressure drop Δp values can be made comparable to experimental values if suitable corrections for vapor turbulence are made.

4.2.2 Complete or Full Condensation Flows in a Vertical Tube

The test matrix for the "natural" steady/quasi-steady full condensation cases accommodates a range of vapor mass flow rates and temperature difference $\overline{\Delta T}$ values that are shown in Figure 11. The shaded region in Figure 11 contains most of the experimentally (as well as computationally) obtained data points for steady full condensation cases. These full condensation cases lie in a zone bounded by semi-schematic curves X, and Y as shown in Figure 11.

Table 1: Experimentally measured data and some key calculated and computed variables for steady states achieved for unspecified exit condition partial condensation flows

- *The error values for this case were greater than the representative error values shown in the column headers due to small $\overline{\Delta T}$ and high relative error associated with its measurement.
- NA: The data was not available due to some equipment problem

Run No.	$\dot{M}_{in}$	$\dot{M}_V$	Z_e exp	Z_e comp	$\overline{T}_W$	T_{sat}	$\overline{\Delta T}$	Δp	Re	Ja	Pr_l	$\dot{Q}_{out}$	$\overline{q''}$	$\overline{h}$
	(g/s)	(g/s)			(K)	(K)	(K)	(kPa)				(J/s)	(W/m²)	(W/m²K)
	±0.05	±0.04	±0.04		±1	±0.15	±1	±0.05	±900	±0.02	±0.02	±5	±800	±80
1	1.44	0.48	0.33	0.33	320	331.49	11	-0.82	23900	0.14	9.61	81	5200	453
2	1.76	1.08	0.62	0.57	317	325.23	8	-0.36	29700	0.10	10.11	58	3700	450
3	1.54	0.69	0.44	0.36	323	335.55	12	-0.19	25300	0.15	9.21	71	4500	387
4	1.29	0.49	0.38	0.38	320	329.64	10	-2.09	21500	0.11	9.69	68	4300	476
5	1.70	0.83	0.51	0.52	324	332.55	9	-0.93	28100	0.11	9.37	70	4400	508
6	1.17	0.47	0.40	0.39	320	332.64	13	-0.12	19325	0.16	9.55	59	3700	298
7	1.31	0.49	0.37	0.37	321	330.85	10	-2.06	21700	0.12	9.58	69	4400	462
8*	1.93	1.39	0.72	0.72	322	325.55	4	0.01	32500	0.05	9.85	47	3000	742
9	1.59	1.11	0.69	0.63	328	334.25	6	NA	26200	0.08	9.07	40	2500	418
10	2.12	1.37	0.64	0.64	320	327.85	8	-0.10	35500	0.10	9.83	64	4100	503
11	1.30	0.45	0.35	0.38	321	329.29	8	-1.62	21700	0.10	9.70	72	4600	537
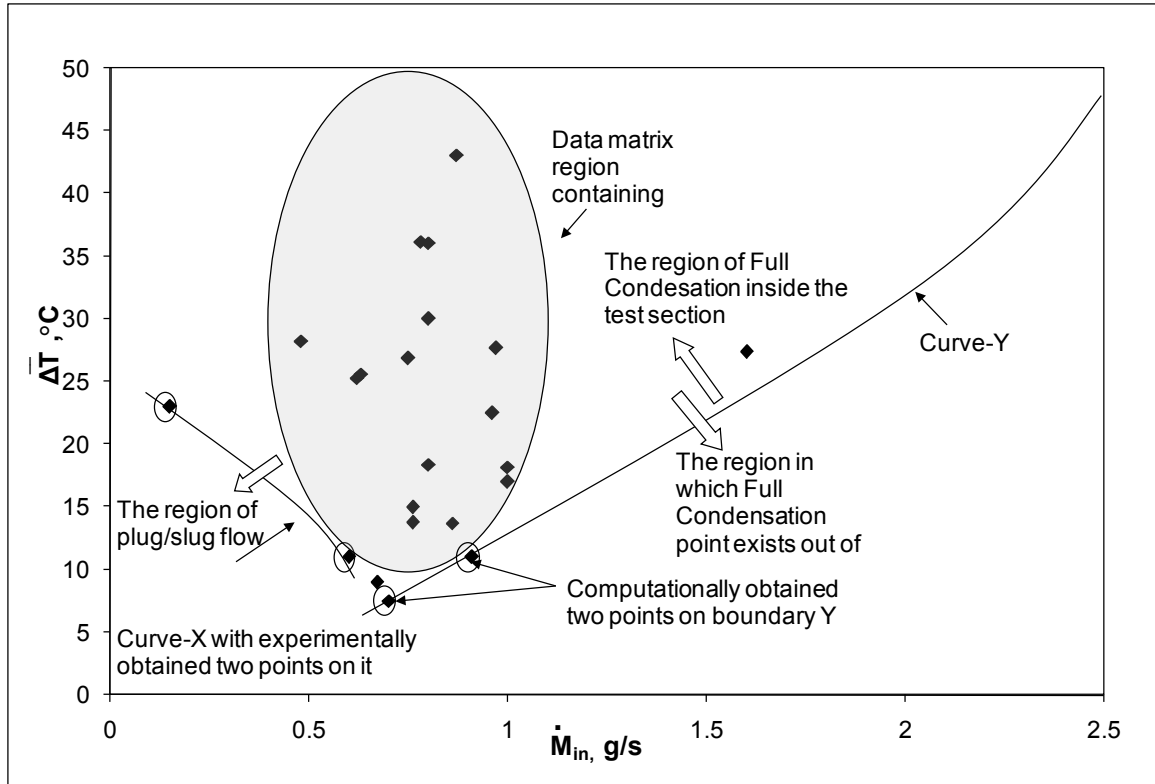
Figure 11: Two-dimensional test data matrix for full condensation cases' points with unspecified exit condition ("natural" flows) represented on $\dot{M}_{in}$ - $\overline{\Delta T}$ - plane

The curve Y (with two computationally obtained points) in Figure 11 schematically depicts the right upper bound on the test matrix. For cases to the right hand side of this curve, the "natural" point of full condensation is outside the test-section (in other words, flow is expected to become partially condensing). Curve X (with two experimentally obtained points), on the left hand side in Figure 11, represents the lower left bound on the test matrix. As mass flow rate decreases below the value given by this curve, there is an experimentally observed instability in the flow, which, in all likelihood (flow visualization pictures are difficult to produce), marks the transition from quasi-steady annular to a plug/slug (see Carey [36]) regime.

The simulations for most of the "natural" (unspecified exit condition) full condensation cases confirm the fact that the point of full condensation lies within the test section and almost all the cases lie in the region bounded by the curves X and Y shown in Figure 11. The simulations were performed only approximately up to x_{fc} (distance to the point of full condensation) and they predict that the length x_{fc} for full condensation decreases as the mass flow decreases or value of $\overline{\Delta T}$ increases.
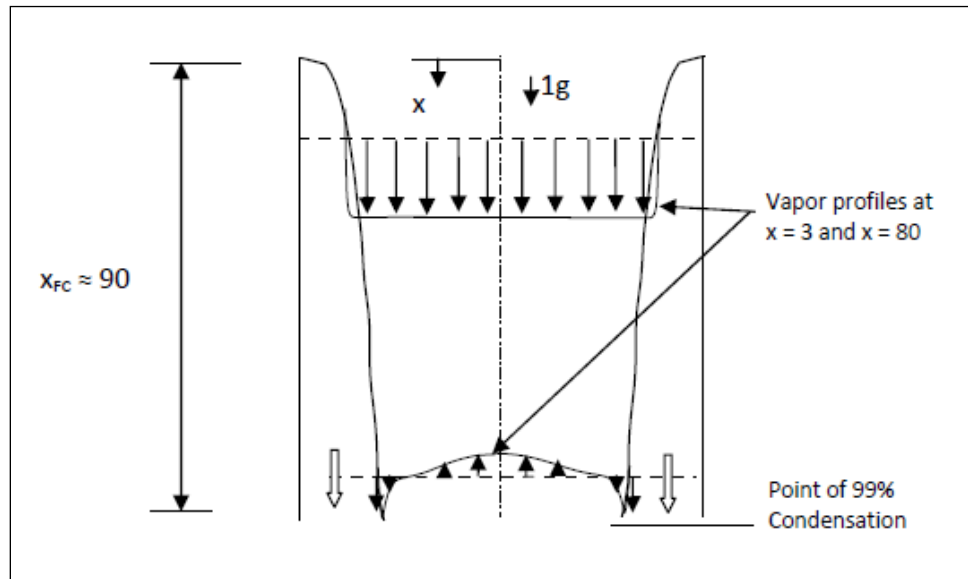
Figure 12: Film thickness and vapor velocity profiles for a representative fully condensing flow in a tube

This figure shows computational results for steady/quasi-steady "natural" fully condensing 1g flow in a cylinder for FC-72 with inlet vapor speed 1 m/s, and $\overline{\Delta T}$ (difference between the vapor saturation temperature at the inlet and average wall temperature) of 26 ℃. It shows the quasi-steady film thickness profile and steady vapor velocity profiles at two different cross sections.
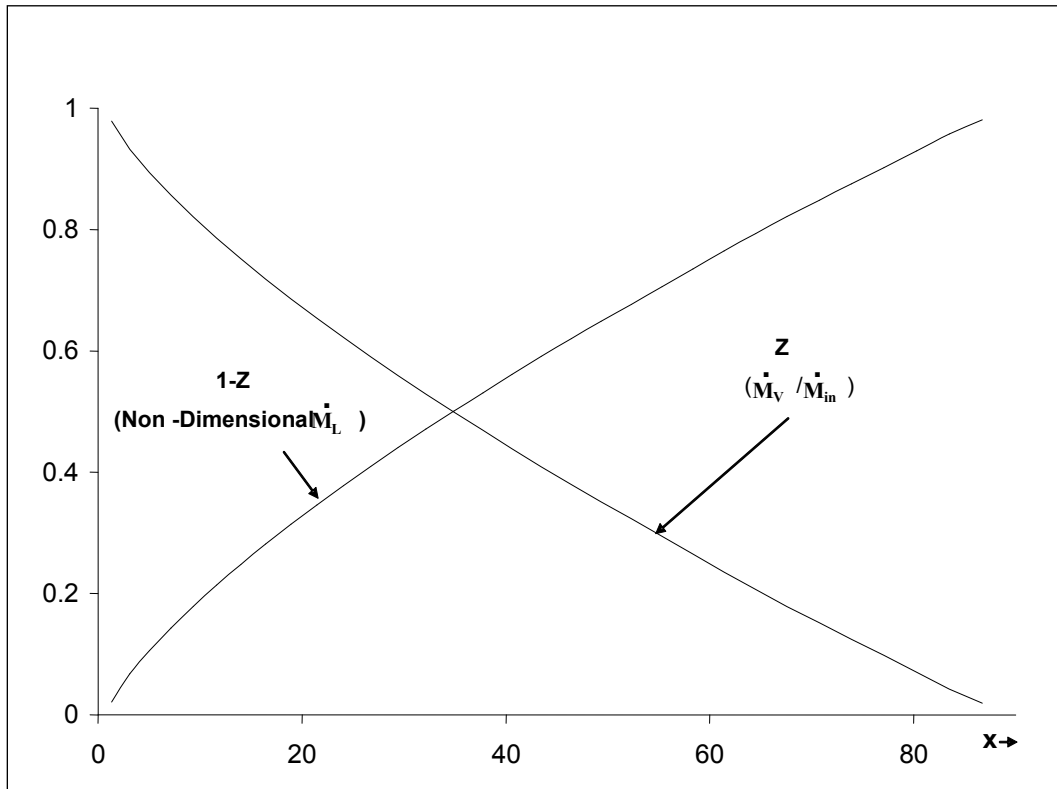
Figure 13: Vapor mass fraction profile for a representative fully condensing flow

inside a tube

For the same case as in Figure 12, this figure shows the vapor mass fraction Z (x) versus x values.

As an example, Figures 12-14 show computational results for a "natural" full condensation in-tube case for which $x_{fc} \approx 90$. These results are obtained as *long term* (t $\rightarrow$ ∞) solutions of unsteady problem with exit condition formulation [A] in section 2.1. The steady/quasi-steady vapor velocity at the centerline becomes negative near the point of full condensation for steady solution, indicating the intrinsic possibility (i.e. if the

interfacial configuration was stable) of the presence of re-circulating vortices responsible for the flow reversal. The interface shown in Figures 12-14 is quasi-steady in nature i.e. as t → ∞, it remains steady-in-the-mean but exhibits waves around the mean value. The flow typically does this after certain x location up to which it is in the *smooth annular* regime and after this location it shifts in to the *wavy annular* regime.
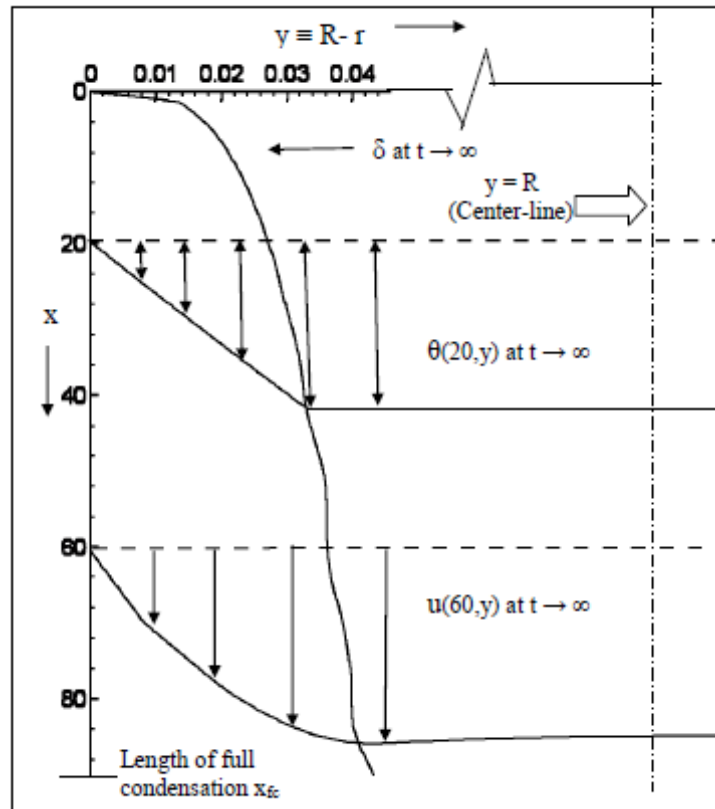
Figure 14: Temperature and liquid velocity profiles for a representative fully condensing flow inside a tube

For the same case as in Figure 12, Figure 14 shows the "quasi-steady" graphs of non-dimensional film thickness δ, non-dimensional temperature (θ) profile and non-dimensional u-velocity profile at certain x locations.

This waviness in the interface is due to the amplification of very small initial disturbances or small computational disturbances. These amplifications appear on the interface only after certain downstream distance x*. For example for the case in Figures 12-14, the intrinsic waviness and associated instability occur over $24 < x < 90$ ($Re_\delta > 100$). The quantitative study of flows' response to the superimposed initial disturbances in gravity driven situation has been done in detail for the external condensing flow (Nusselt case) in [20]. For the gravity driven in-tube flows being discussed here, this waviness associated instability was observed for all the simulations for the different flow cases marked in Figures 10-11. Figure 15 re-plots all the points of Figure 10-11 that include different partial condensation and full condensation "natural" (unspecified exit condition) cases. In Figure 15, for each computationally-run "natural" case, a number is marked followed by (in case of full condensation) the non-dimensional length of full condensation x_{fc}. This number indicates the ratio of downstream distance x* at which waviness starts appearing on the interface in *long term* unsteady solutions to the total length of the test-section used in experiments (0.7 m). It is conjectured that in experiments, a quasi-steady flow with approximately same x_{FC} will actually be realized for full condensation – however, the annular flow regime over part of $x^* < x < x_{FC}$ will most likely be more wavy (higher amplitude) liquid condensate flow. Since this work, an actual correlation for x_{FC} has been obtained and reported in [1].

The waviness inducing instability (growth of initial disturbance as opposed to response to ubiquitous noise) in these cases was primarily due to condensate speeding up in the presence of gravity and this kind of instability was not found to exist for shear

driven flows. The detailed analysis of stability of these gravity driven flows for classical problem of Nusselt [28] has been accomplished in [20] and was not considered during this research.

The above discussed synthesis (Figure 10-11) of "natural" gravity driven partially and fully condensing flow experiments with simulation was a preliminary work and more extensive synthesis of experimental and computations has since been developed in [11].
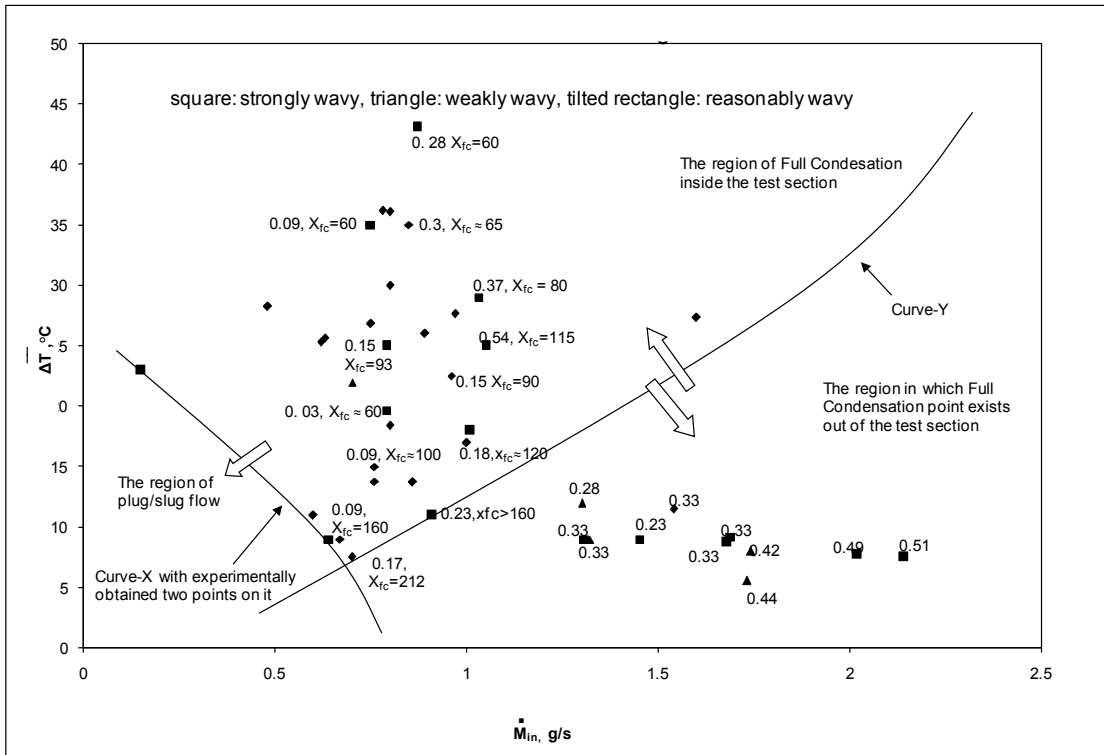
Figure 15: Test matrix plot showing quasi-steady features of fully condensing flows

inside a tube

This test matrix re-plots all the "natural" partial and full condensation cases of experiments marked in Figures 10-11 and marks, for computationally run cases, the ratio x^*/L followed by (for fully condensing flows)the non-dimensional length of full condensation. The non-dimensional length x^* denotes the downstream distance after which interface was computationally found to become wavy in presence of computationally generated disturbances.

65

4.3 Differences between Gravity Driven and Shear Driven Internal Condensing Flows

Even though "natural" attracting steady/quasi-steady solutions exist for unspecified exit condition (formulation [A] of 2.1) in both gravity driven and shear driven internal condensing flow cases, there are basic and important differences between these attractors. In general (see Figures 11a-11b of [7]), for all else remaining the same, shear driven flows have much thicker condensate and, hence, much lower heat transfer rates (which is typically inversely proportional to film thickness). The velocity profile for gravity driven flow is parabolic with nearly zero slope at the interface (the condensate does not need shear for its motion) while the one for the shear driven flow is linear (which provides adequate shear for condensate motion). For a method of cooling that results in only moderate imposition of wall heat-flux, the pressure variations for gravity driven flows often amount to a pressure rise (see Figure 11b of [7]) where as a small pressure drop is associated with shear driven 0g flows (also see Figure 11b of [7]).

Besides the "steady" features of the "steady" solutions, there are differences in unsteady characters of gravity and shear driven condensing flows.

Because of the logarithmic nature of the time scale, Figure 16 shows that steady solutions are much more quickly attained for gravity driven condensing flows as opposed to shear driven condensing flows - if the initial guess is away from the steady solution by the same margin. For example, to achieve steady/quasi-steady attracting solutions at a particular downstream location for the flow conditions in Figure 8 (gravity driven) -9 (shear driven) from initial guesses equally apart from the final attracting solution, Figure

16 shows the time required in both the cases. Figure 16 plots $\partial\Delta/\partial t$ (rate of change of film thickness) values on time log plot at non-dimensional x = 10. It can be seen that: (i) in gravity driven case solution is attained much quicker than the shear driven case ($t^*_{gravity} \ll t^*_{shear}$), (ii) initial values of rate of change of film thickness are much higher for gravity driven case, (iii) initially rate of change of film thickness increases for gravity driven case while it is somewhat constant for shear driven case, and (iv) values of final decelerations (slope of $\partial\Delta/\partial t$ versus t curves) to the steady solution are higher in case of gravity driven flows.

Additionally, the solution for gravity driven case can be seen to be wavy and quasi-steady (as $\partial\Delta/\partial t$ oscillates about mean zero value after reaching zero value) while for shear driven case, the final attracting solution is smooth and steady (as $\partial\Delta/\partial t$ goes smoothly to zero value). It was further noticed during the investigations of shear driven external condensing flows that these attractors have strengths which are functions of distance and vapor speed. The strengths of attractors have been defined ([8]) and quantified for this external condensing flow problem and these computational results are discussed in the next section. Even though detailed analysis of attraction rates and stability theory for internal condensing flows (as it is done for external condensing flows in the next section) is not part of this research thesis, the basic approach given in [8] and section 5 can be applied for detailed characterization of the internal flow behavior in Figure 16.
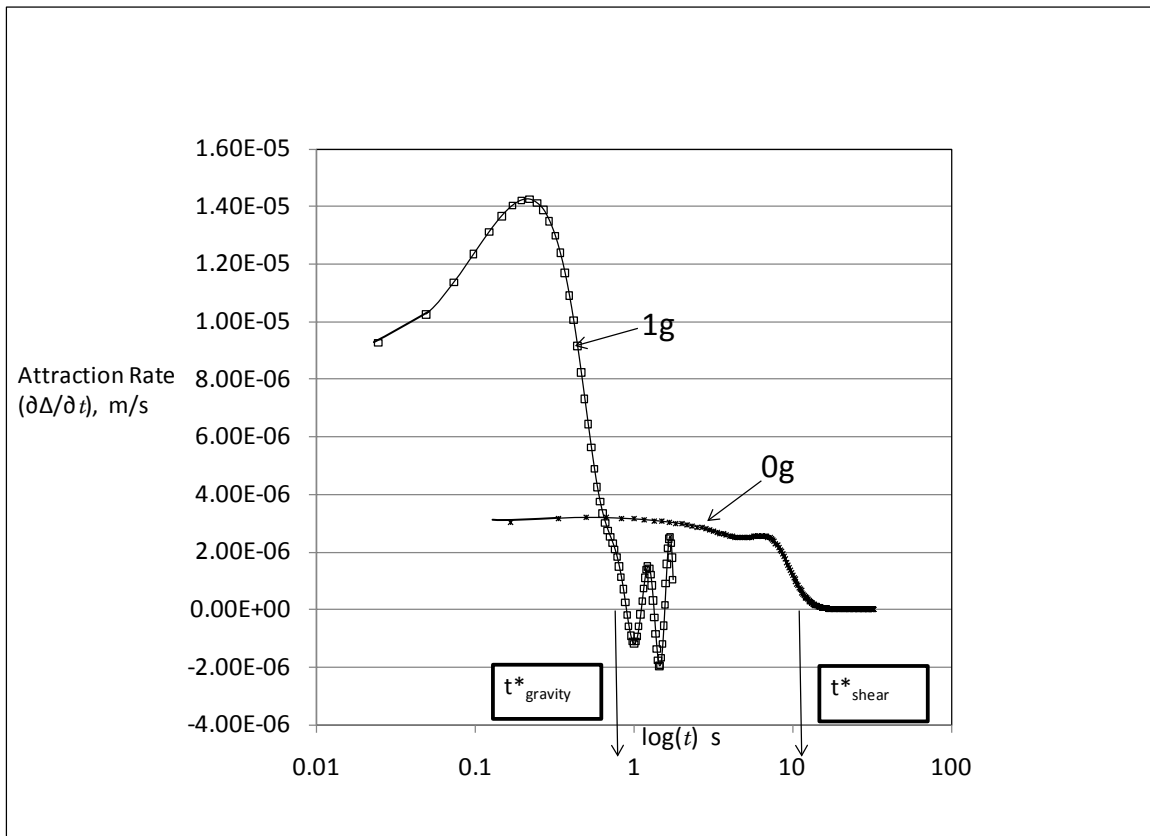
Figure 16: Comparison of attraction rates for gravity and shear driven internal

condensing flows

This figure plots and compares $\partial\Delta/\partial t$ values indicating "attraction rates" (see definition in [8]) versus times for shear and gravity internal condensing flows. The figure also compares the times (t*gravity and t*shear) required, at a particular downstream location (x = 10), for a typical gravity driven internal condensing flow and a typical shear driven (0g) internal condensing flow solution to reach the respective quasi-steady "natural" attractors from arbitrary initial guesses which are 10 % away from the respective attracting "natural" solutions. The propensity towards the oscillating wavy behavior associated with positive and negative values of $\partial\Delta/\partial t$ is clearly present for 1g flows at longer times. The flow is clearly monotonic for shear driven 0g flows.

4.4   Nature of Governing Equations for Internal Condensing Flows

Considering relatively much weaker attractions associated with steady shear driven internal condensing flows, one can conjecture the possibility of controlling and stabilizing internal shear driven condensing flow by controlling both its inlet and the exit pressures. In other words, one can ask what if, for given inlet mass flow rate $\dot{M}_{in}$, inlet pressure p_{in}, and a given cooling approach of known condensing surface temperatures; the exit liquid mass flow rate (and thus exit pressure) could be varied/controlled such that the mean splitting of the inlet mass flow rate $\dot{M}_{in}$ in to exit vapor mass flow rate and exit liquid mass flow rate is not "natural"? In the above question, "natural" splitting of inlet mass flow rate is defined by "natural" steady solution obtained for unspecified exit condition (formulation [A] given in section 2.1).

From the steady simulations for shear driven flows, it is clear that flow can not respond to any "non-natural" exit condition specification as there exists only one unique annular/stratified steady solution for the steady governing equations. This is only half of the requirement of parabolic behavior. The answer to the above question was then obtained by obtaining unsteady solutions for the shear driven internal condensing flow under a completely new algorithm (developed to implement exit condition formulation [B] given in section 2.1) under various unsteady impositions of "non-natural" exit conditions. This should normally be impossible for any "fully" parabolic problem but it is possible for elliptic unsteady equations. We term this mixed behavior parabolic (for steady equations) with elliptic sensitivity (arising from unsteady equations).

69
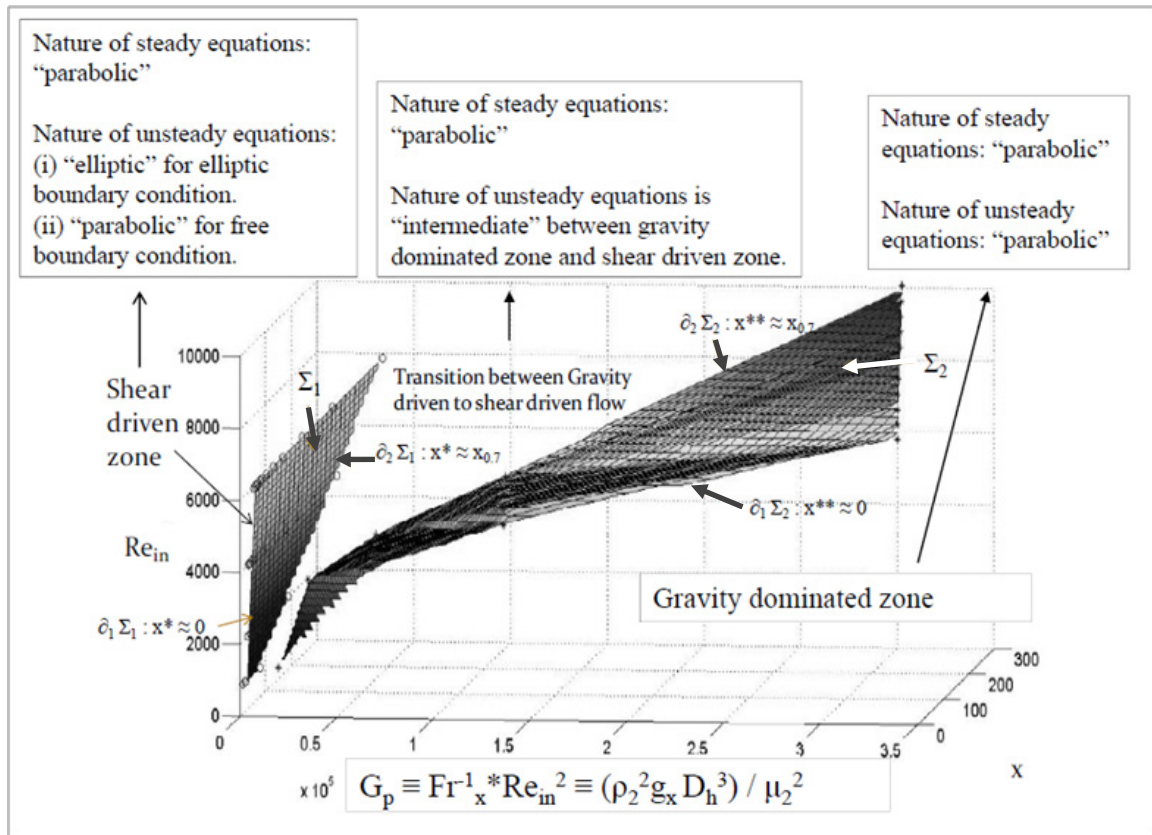
Figure 17: A representative 3D plot showing computationally obtained boundaries that mark transitions between gravity and shear dominated regimes for internal condensing flows

The figure shows the computationally obtained boundaries in $\{x, Re_{in}, G_p\}$ space that mark various transitions from gravity dominated regime to shear dominated regime for a flow of FC-72 vapor with $Ja_1/Pr_1 = 0.004$, $\rho_2/\rho_1 = 0.0148$ and $\mu_2/\mu_1 = 0.0241$. The nature of steady governing equations is parabolic over the entire parameter space while the nature of unsteady equations changes from "parabolic" to "elliptic" as one moves from gravity driven to shear driven flow regime.
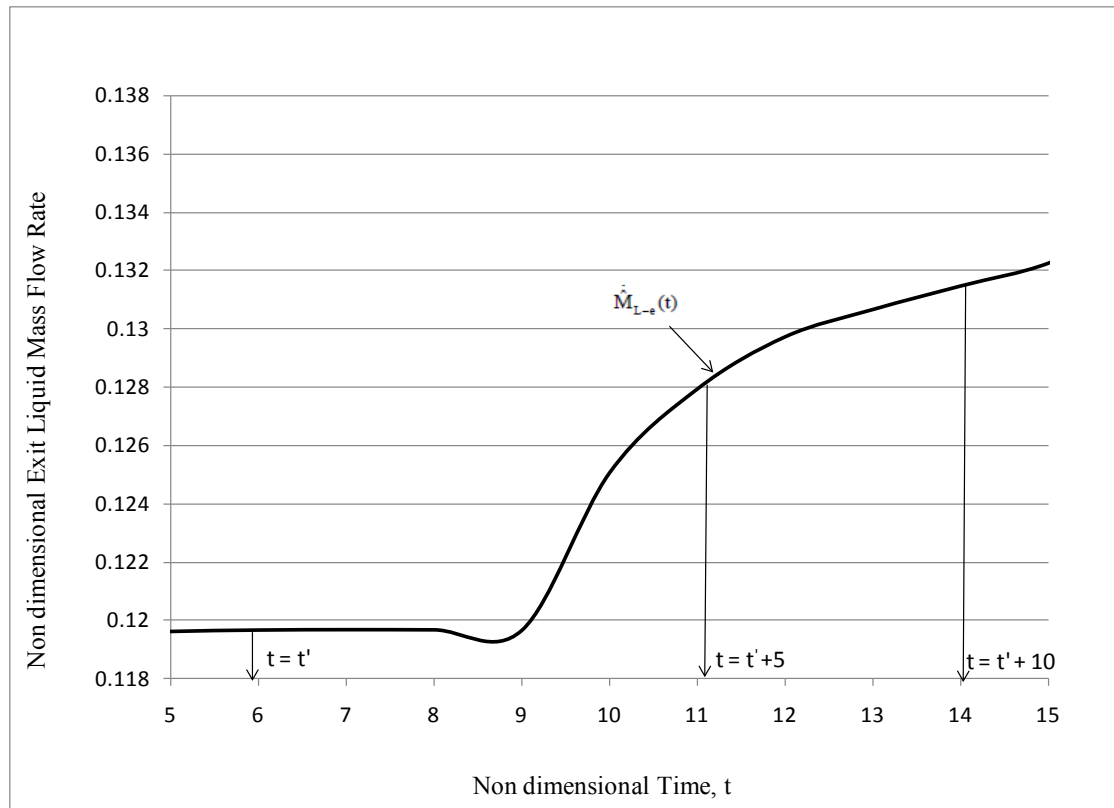
Figure 18: Computational example of exit condition control through unsteady control of exit liquid mass flow rate for a shear driven internal condensing flow.

It has been found during this research that the unsteady governing equations for annular/stratified flows allow "elliptic" impositions in the shear driven zone while they only allow "parabolic" boundary condition impositions for the gravity dominated zone. In a shear dominated zone, unsteady equations can be solved using parabolic boundary conditions and , also, they allow elliptic prescription of exit condition.The zones shown in Figure 17 have been identified using 1-D tool in the work of Mitra et al. [1] based on the differences between gravity and shear driven flows. The 1-D tool has yielded such zones (see Figure 17) which demarcate gravity driven, shear driven, and transitional

annular stratified flows in a 3-D parameter space defined by $\{x, Re_{in}, G_p\}$. Here $x \equiv \chi/L_c$, $Re_{in} \equiv \rho_2 U D_h/\mu_2$, and $G_p \equiv \rho_2^2 g_x D_h^3/\mu_2^2$.

The zones in Figure 17 have been discussed in detail in [1]. Figure 17 states that the nature of unsteady governing equation changes from being "elliptic" to purely "parabolic" as one moves in the parameter zone from a shear driven flow to a gravity dominated flow. This fact is established in this thesis. Figure 18 shows an example of ellipticity related to unsteady equations of shear driven condensing flows by showing an unsteady (time varying) exit condition prescription realized through controlling exit liquid mass flow rates.
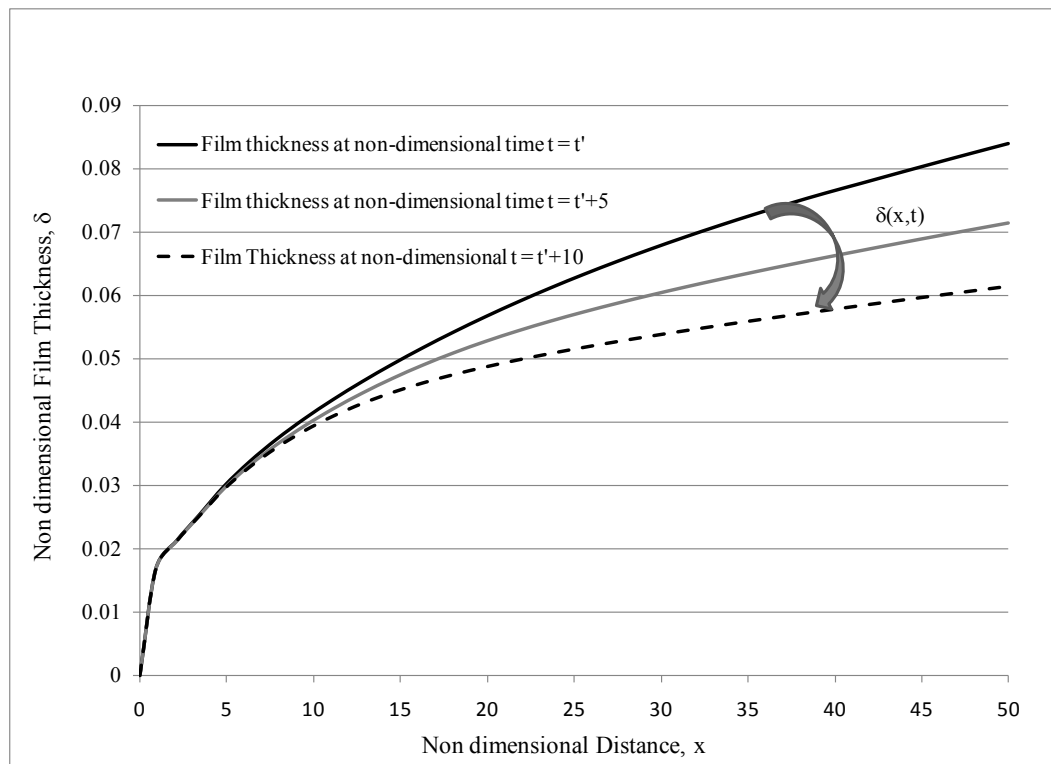
Figure 19: Film thickness response to the unsteady exit liquid mass flow rate prescription of Figure 18.

72

It can be seen from Figure 18 that exit condition (exit liquid mass flow rate) can be controlled in unsteady fashion by following one of the many possible different curves of exit liquid mass liquid mass flow rates with respect to time.

The multiplicity of such curves indicates "ellipticity" in unsteady equations of shear driven condensing flows. The response of the flow to the prescription in Figure 18 is shown in Figure 19. The question arises what happens if the control curve steadies up at a certain particular value at or way from the "natural" value of exit liquid mass flow rate? This answer to this question is discussed in detail in the next section. Here, Figures 18-19 are shown just to exemplify unsteady ellipticity of shear driven condensing flows. This nuance in understanding the character of the internal condensing flow equations is new for condensing flows but is not new in fluid dynamics. For example, the gas dynamics Tricomi equation (see chapter 26 of [37]) undergoes a change in character from "elliptic" to "hyperbolic" as one moves in the parameter space of Mach number (Ma) from the sub-sonic regime (Ma < 1) to the super-sonic regime (Ma > 1).

4.5   Parabolicity and Ellipticity Issues for Shear Driven Internal Condensing Flows

4.5.1 Definitions of Strict Parabolicity and Strict Ellipticity

Computational result discussed in Figures 6-7 shows that *steady* shear driven and gravity driven internal condensing flows exhibit the first of the two mentioned features of a *strictly* parabolic flow (i.e. parabolic boundary conditions suffice to determine the

73

steady solution) and computational results in the next section (or in [7]) show that *unsteady* shear driven internal condensing flows also exhibit the second of the two above mentioned features of the *strictly* elliptic flows (i.e. the solution in the interior changes when unsteady elliptic boundary conditions are imposed). This means that shear driven flows are neither *strictly* "parabolic" nor *strictly* "elliptic" but behave more like "parabolic" flows with "elliptic-sensitivity" to actively imposed quasi-steady pressures at the inlet and the outlet. While the computational results presented in this thesis so far are for fixed condensing-surface temperature condition, the nature of governing equations for shear driven internal condensing flows should be looked at from a generalized perspective in which wall's *thermal conditions* are determined by *any fixed cooling approach* (temperature, heat flux, or convection boundary condition for the condensing surface through a conjugate problem). Depending on the cooling approach, either the temperature of the condensing surface remains fixed between one steady state to another (as in the theory), or all or part of the temperatures of the condensing surface may vary between one steady state to another while a thermal boundary condition is being satisfied for a conjugate problem.

4.5.2 Parabolicity of Shear Driven Internal Condensing Flows

As discussed earlier, the strictly steady shear driven flows exhibit one of the features of a parabolic flow – e.g., if inlet (pressure and mass flow rate) and condensing-surface cooling conditions (known steady temperature of condensing surface) are prescribed in a steady fashion in a noise free environment, a unique (termed "natural") steady noise-free flow and unique steady noise-free exit pressure is achieved. This has

been experimentally and computationally established for shear driven internal condensing flows ([7], [11]).

4.5.3 Quasi-steady Parabolic Nature of Shear Driven Internal Condensing Flows

The "*quasi-steady* parabolicity" result (obtained from experiments/computations) says that when fluctuations are added on the prescribed conditions of the strictly steady parabolic problem, fluctuations appear within the flow as well as in the unspecified variables at the boundary (including thermal boundary). In presence of these fluctuations, the flow exhibits "quasi-steady parabolicity." The effects of fluctuations on "quasi-steady parabolic" flows are found to be unique in two ways: (i) they are important even for these laminar/laminar flows with wavy interface, and (ii) their effects depend on the cooling approach. For fixed condensing surface temperature cooling, the mean flow variables in the interior and the boundary are not significantly affected, as the increased interfacial waves are not able to significantly enhance heat transfer rates. For the cooling approach that allows variation in *most of* the local condensing surface temperatures, the mean flow variables in the interior and at the exit change to significantly enhance heat transfer rates. This 'quasi-steady parabolicity" result says that there are a continuum of quasi-steady pressures (inlet or outlet) and condensing surface temperatures that results from solutions for a "continuum" of fluctuation levels. The result of quasi-steady parabolicity has been experimentally found ([7], [11]) and some preliminary computational results about this quasi-steady parabolicity are given in this thesis. It has been experimentally found in [7] that the long term impact of this quasi-steady parabolic behavior under variable condensing-surface temperature cooling is quite significant for the condenser ($> 20 - 30$

% heat transfer enhancement). Detailed computational work on "quasi-steady parabolicity" is part of future work of this research.

4.5.4 Elliptic Sensitivity or Ellipticity of Unsteady Equations of Shear Driven Internal Condensing Flows

In addition to the above described *quasi-steady parabolic* feature, shear driven flows exhibit a *special* additional feature of "*elliptic-sensitivity*" that says that the unspecified pressure boundary condition for the parabolic problem can also be *additionally* specified or forced by an energy source in the presence of suitable time-periodic fluctuations. This is possible because the as mentioned in section 4.4, unsteady equations for shear driven flows allow "elliptic" boundary condition. This results in changes in heat transfer inside condenser, changes in flow regimes, and mean flow variables for shear driven internal condensing flows. This is different from *strict* "ellipticity" where no forcing (against an initially elastic response) would be necessary. This additional pressure boundary condition imposition can be at the exit or the inlet depending on what parabolic conditions are being specified. The result on "elliptic sensitivity" also depends on the method of cooling and computations in this research thesis show the "elliptic sensitivity" results when the thermal boundary at the condensing surface holds the temperature fixed. However, the experiments reported here show that this "elliptic sensitivity" can also manifest even if the temperature of the condensing surface is allowed to change through a conjugate problem. In such case, imposition of "elliptic" boundary brings in thermal transients in the condensing surface. This thesis work involves investigating elliptic sensitivity issues for shear driven internal condensing

flows by looking at the impacts of different exit condition controls and these results are discussed in the next section. These results are also reported in [7].

4.6   Computational Results for Internal Condensing Shear Driven Flows for Different Exit Condition Specifications ("Elliptic Sensitivity" Results)

4.6.1 Results on Flow Controllability through Exit Liquid Mass Flow Rate Control

As discussed in section 2.1, the solutions to the unsteady equations of internal condensing shear driven flows are sought to assess the physics of the problem. For the unsteady flow, under steady parabolic boundary conditions (of steady inlet mass flow rate, steady condensing surface temperature, and steady inlet pressure) and an unsteady exit condition specification of exit liquid mass flow rate in Eq. (14) shown in Figure 18, it is found that there is an unsteady solution whose unsteady film-thickness response is shown in Figure 19. This unsteady exit condition imposition was computationally found to be feasible for the shear driven case and not feasible for the gravity driven (and dominated) flow cases. For gravity dominated flow cases, the film thickness profile, for $T_w(x)$ = constant cases considered in this study, is found to be same as in the Nusselt solution [28] regardless of the inlet mass-flow rate. This means that the purely elliptic behavior of the unsteady annular/stratified flows as exhibited in Figures 18-19 is limited to the shear driven zone in the parameter space of Figure 17 and that the unsteady equations are strictly parabolic in the far right gravity dominated zone of Figure 17. The

steady and unsteady shear driven flows considered here are for 0g and horizontal channel flows.

It has been observed that, for the relatively small condenser length involving partially condensing flows investigated, the shear driven flows for 0g (i.e. $g_x = 0$ and $g_y = 0$ in Figure 1) are approximately the same as the shear driven horizontal channel flows with transverse gravity (i.e. $g_x = 0$ and $g_y \neq 0$ in Figure 1).
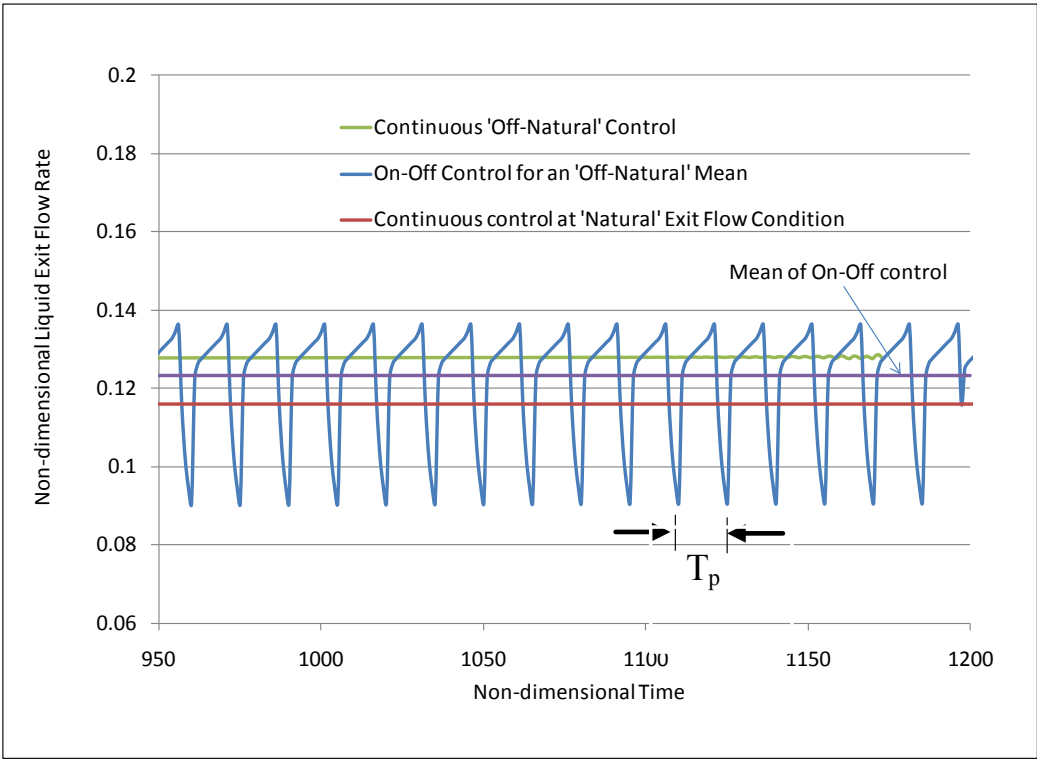
Figure 20: Time histories for different exit liquid mass flow rate controls with the mean higher than the "natural" value for a shear driven internal condensing flow

For condensing flow in Figure 1 in zero gravity with inlet vapor speed of 0.6 m/s and vapor-to-wall temperature difference of 5ºC, this figure shows three different time histories of "specified" exit liquid flow mass rates. The vapor is R113 and the channel gap height is 0.004 m.
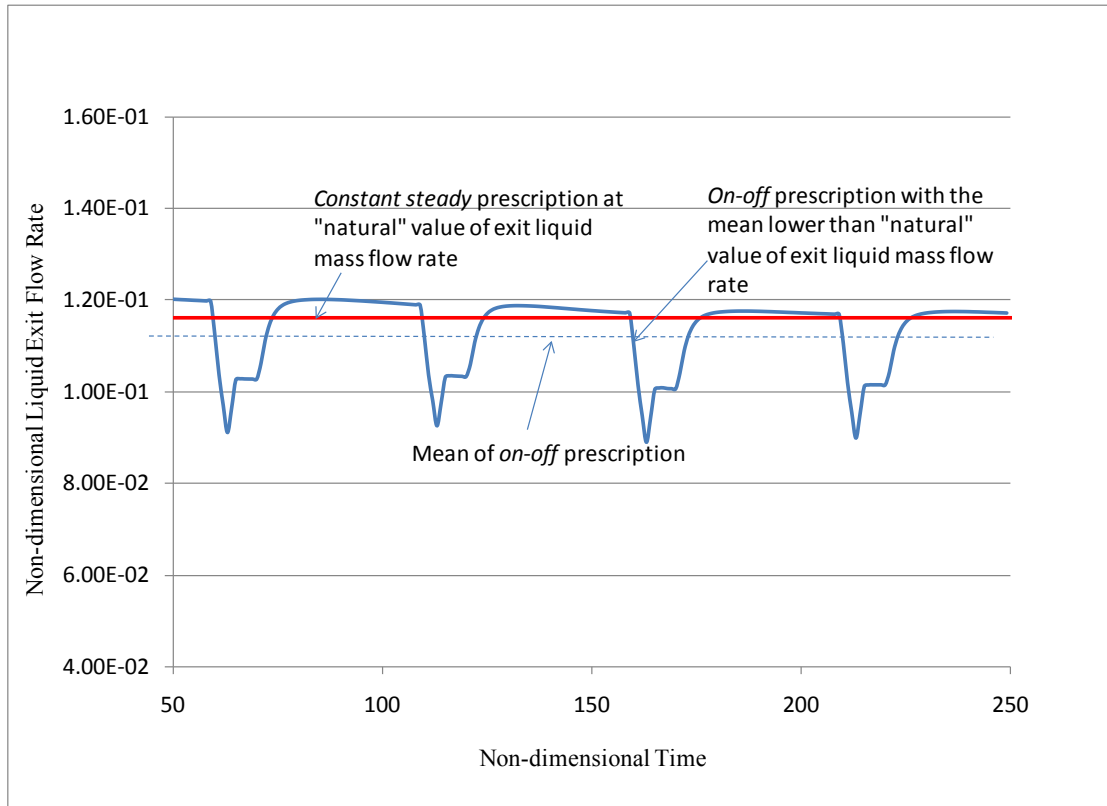
Figure 21: Time histories for different exit liquid mass flow rate controls with the

mean lower than the "natural" value for a shear driven internal condensing flow

For condensing flow in zero gravity with inlet vapor speed of 0.6 m/s and vapor-to-wall temperature difference of 5ºC, this figure shows a time history of "specified" exit liquid flow mass rate for an on-off type of fluctuations such that the mean liquid mass flow rate at the exit is slightly less than the "natural" one. This example shows that the exit liquid mass flow rate can, in principle, be controlled such that during the on portion of the control, liquid exit mass flow rate is on the lower side of the "natural" and during off portion of the control, flow bounces back to seek its "natural" exit condition while the mean of the prescription stays near the "natural" value.

Therefore the computational results shown in this paper for 0g are also applicable for partially condensing horizontal channel flows.

Although the unsteady imposition in Figures 20-21 alone is reported here, several non-periodic finite duration unsteady impositions (not shown) were implemented and they led to accurate unsteady solutions in the annular regime. It should be further noted that unsteady solutions for the unsteady governing equations are possible without specifying the exit conditions (for example, by using parabolic exit condition formulation [A]) provided there are sources of unsteadiness either in the parabolic boundary conditions or in the initial conditions.

Computational results in Figures 20-28 show that shear driven internal condensing channel flows operating under steady "parabolic" boundary conditions may additionally respond to certain "non-natural" time periodic exit condition impositions and thus, in this sense, these flows show "*elliptic-sensitivity.*"

Figure 20 shows three different time history prescriptions for non-dimensional exit liquid mass flow rate $\dot{M}_{L-e}(t)$ in Eq. (14). The red curve is associated with a *constant steady* control at "natural" steady exit condition i.e. $\dot{M}_{L-e}(t) = \dot{M}_{L-e}|_{Na} \approx 0.116$. The blue curve is associated with a time-periodic prescription ($\dot{M}_{L-e}(t) = \dot{M}_{L-e}|_{on-off}$) that has an "off-natural" mean ($\dot{M}_{L-e}|_{on-off-mean} \approx 0.123$) above the "natural" value and the green curve is an attempt to prescribe a *constant steady* control ($\dot{M}_{L-e}(t) = \dot{M}_{L-e}|_{constant}$) at an "off-natural" mean ($\dot{M}_{L-e}|_{constant} \approx 0.127$).

Figure 21 shows another time-periodic control with an "off-natural" mean very slightly below the "natural" value. Figures 22-23 show the response of the flow on film

thickness that results from the exit liquid mass flow rate control depicted in Figure 20 and 21. For the *constant steady* control with the mean at the "natural" value of exit liquid mass flow rate, film thickness attains a steady value in time, which is also the same as the film thickness obtained by solving the steady equations. For the *on-off* control of Figure 20, film thickness keeps on oscillating, for all times $t > 0$, in a band (as shown in Figure 22) which has a mean that is different than the one associated with "natural" curve given by the red curve. Similar but much smaller impact of the imposition in Figure 21 leads to a response in Figure 23, which has a slightly higher mean film thickness than the "natural" one. Also, for the kind of imposed exit condition (which has a "non-natural" mean and superposed periodic fluctuations in Figure 22), a new quasi-steady flow is achieved with different steady-in-the-mean values of the exit liquid mass flow rate, the exit vapor mass flow rate, and the rest of flow variables. Note, for the *constant steady* control at "natural" exit condition and for the *on-off* control at an "off-natural" mean, flow continues to remain in the annular/stratified flow regime for all times $t > 0$ (see Figures 22-23).

However, for the *constant steady* "off-natural" control case given by the green curve in Figure 22, the flow cannot remain steady despite its ability to handle this imposition of steady exit condition for a short while. This case represents impossibility of this imposition and a strong desire of the flow to seek a fluctuating energy source to accept this imposition in a quasi-steady fashion. In the absence of this energy source, the solution shows breakdown of the resulting monotonically unsteady response after a certain time $t = t^*$ (≈ 1170 in Figure 22).

Figure 22: Response of film thickness for exit condition controls shown in Figure 20

for a shear driven internal condensing flow

For the flow conditions and exit liquid mass flow-rate prescription of Figure 20, this figure shows response of film thickness values with distance x and non-dimensional time t (t is a parameter). For all times t > 0, annular/stratified solutions exist for the on-off prescriptions as well as for the constant steady prescription at the "natural" exit condition. For the constant steady prescription at an "off-natural" mean, film-thickness can be seen to have become wavy at time t ($\approx$ 1150) well before time t* after which no annular/stratified solutions exist for this type of constant "off-natural" steady prescription.

Note that in Figure 22, the waves start appearing on the interface before the annular/stratified solution becomes impossible for t≥ t*. As discussed later, the flow will simply disallow this imposition unless one of the boundary conditions (e.g. mass flow rate oscillations in Wedekind and Bhatt [38]-[41], fluctuations in pressure, etc.) is able to provide time-periodic fluctuations to realize an oscillatory or quasi-steady response.
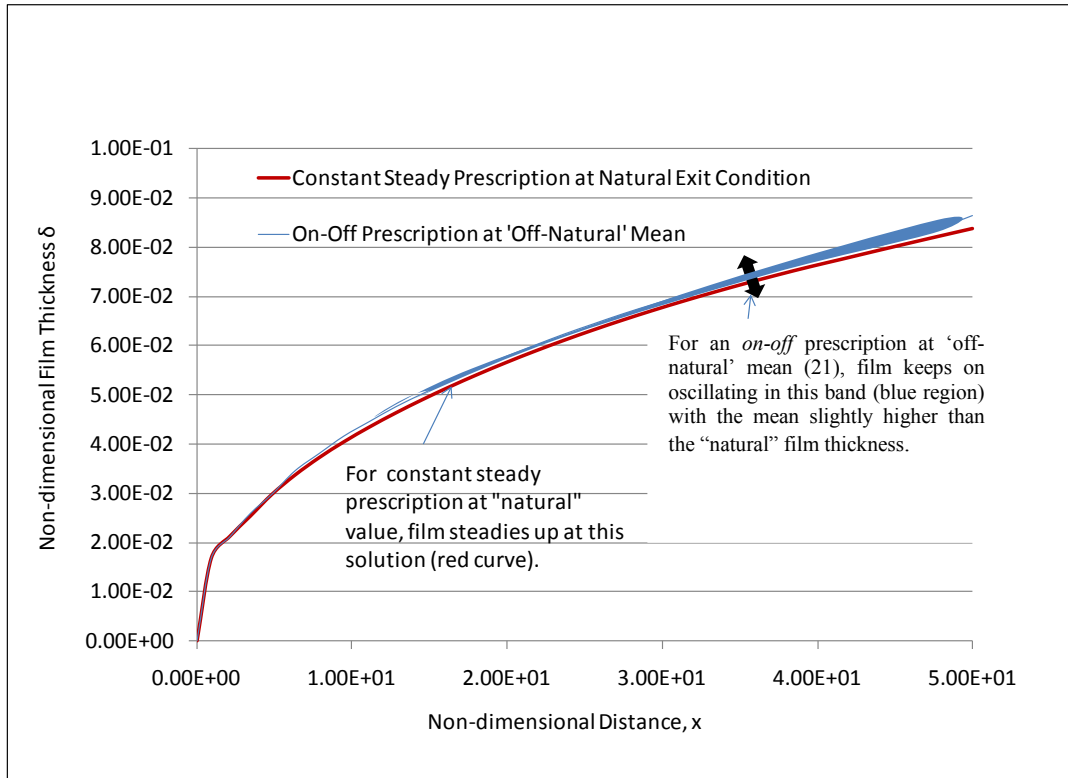
Figure 23: Response of film thickness for exit condition controls shown in Figure 21

for a shear driven internal condensing flow

For the flow conditions and exit liquid mass flow-rate control of Figure 21, this figure shows response of film thickness values with distance x and non-dimensional time t (t is a parameter). This figure shows that at all times t > 0, annular/stratified solutions exist for the *on-off* prescription as well as for the *constant steady* prescription at the "natural" exit condition. For *constant steady* prescription at the "natural" exit condition, film thickness steadies up at unique "natural" solution (red curve) while for the *on-off* prescription with a mean slightly lower than the "natural" liquid exit mass flow rate, the solution keeps on oscillating in a band near (on the higher side) the natural film thickness solution.
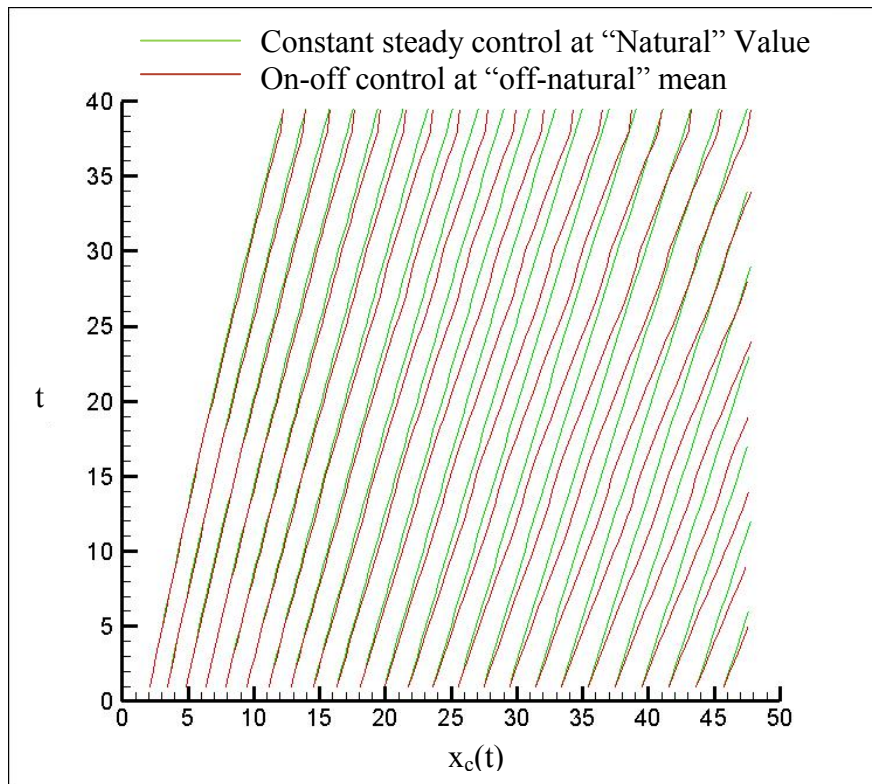
Figure 24: Computationally obtained characteristic curves for representative exit

condition control cases for a shear driven internal condensing flow

This figure shows the characteristic curves $x_c(t)$ originating at different x values along which film thickness δ evolves for two different exit liquid mass flow rate controls: (i) control at "natural" value (see the green curves) (ii) *on-off* control with the "off-natural" mean value.

Figure 24 show *characteristic curves* $x_c(t)$ (see [2] for definition of characteristic curves) for two exit liquid mass flow rate controls, namely constant steady control at "natural" value (green curves in Figure 24) and the other *on-off* control at "off-natural" mean shown in Figure 20 (red curves in Figure 24). These characteristics curves are obtained by integrating the following equation:

84

$$\frac{dx_c}{dt} = \bar{u}(x_c(t), t)$$
$$x_c(0) = x^*, \text{ or } x_c(x^*) = 0 \tag{25}$$

where x* is any given value of x between the inlet and the outlet in Figure 1. The evolution of film thickness δ(x, t) takes place along the *characteristic curves* and is governed by Eq. 26 of [2]. Here the Figure 24 is used to show that for exit condition control at "non-natural" value; characteristic curves originating from any x location are seen to bend away from those for exit condition control at the "natural" value. Also, this bending can be seen (see Figure 24) to increase with x at any particular time. In Figure 24 zigzag nature of characteristics given by the red curves indicate the "on-off" nature of the exit condition control. For the on-off exit liquid mass flow rate control, during the "on" portion of the control characteristics bend away from the "natural" curves while during "off" portion they bend towards the "natural" curves.

It should be further noted that even when the film thickness in Figure 22 significantly decreases (the blue curve), the mean pressure increase needed to decelerate the vapor (see Figures 25-26) is small. It is clear that imposition of the type in Figure 21 is difficult and very small film thickness increase in Figure 23 and pressure drop is possible. This fact is also verified by the experiments (see next section).

For certain other situations, this type of quasi-steady response for quasi-steady exit condition imposition may also involve flow morphology change because of a shift in flow regime boundary.
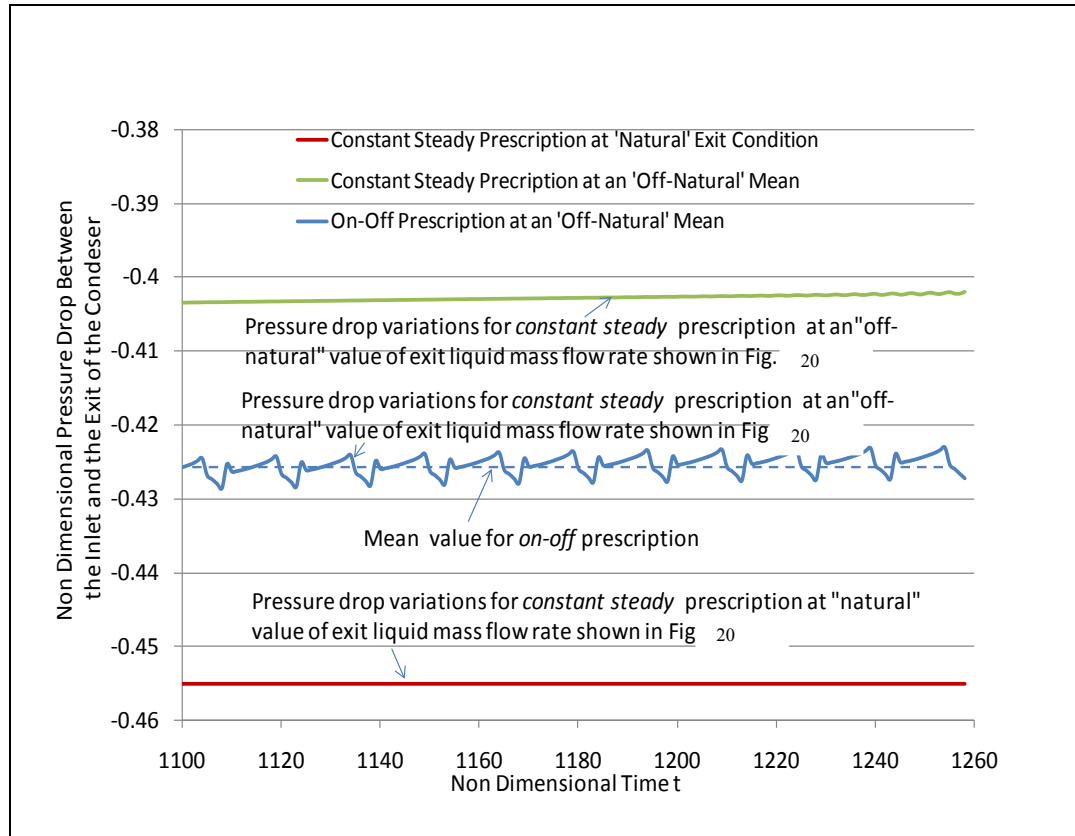
Figure 25: Pressure drop variations for different exit condition controls shown in

Figure 20 for a shear driven internal condensing flow

For the exit condition impositions shown in Figure 20, this figure shows response of the non-dimensional pressure drop values between the inlet and the outlet of the condenser.

This important physics cannot be captured by the current simulation tool that can only handle annular/stratified morphology. For the impositions in Figures 20 –21, Figures 27 – 28 respectively show the time histories of non-dimensional values of net mechanical energy input rate $\dot{W}_{\text{Mech-in}}$ (see definition in Eq. (A.11) in the Appendix) into the condenser control volume. Figure 27 shows that the mean value of the net

mechanical energy for the new quasi-steady solution (blue curve) is lower than the "natural" value whereas, in Figure 28, it is slightly higher than the natural value.

Figure 29 shows how the time averaged values of $\dot{W}_{Mech-in}$ get affected by the different mean quasi-steady exit-conditions imposition. The reduction and increase in these overall time averaged values are associated with changes in total interface energy transfer rate $\dot{D}_{\Sigma}$ shown in Figure 30.
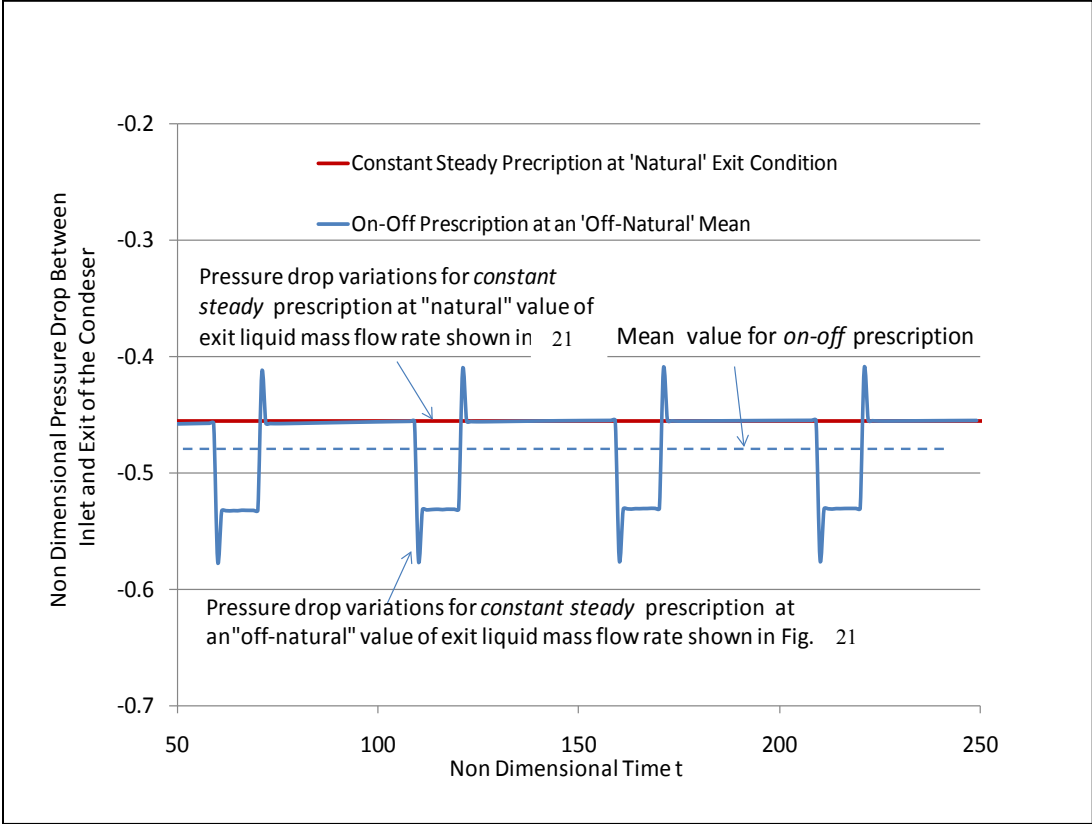
Figure 26: Pressure drop variations for different exit condition controls shown in

Figure 21 for a shear driven internal condensing flow

For the exit conditions impositions shown in Figure 21, this figure shows response of non-dimensional pressure drop values between the inlet and the outlet of the condenser.

87
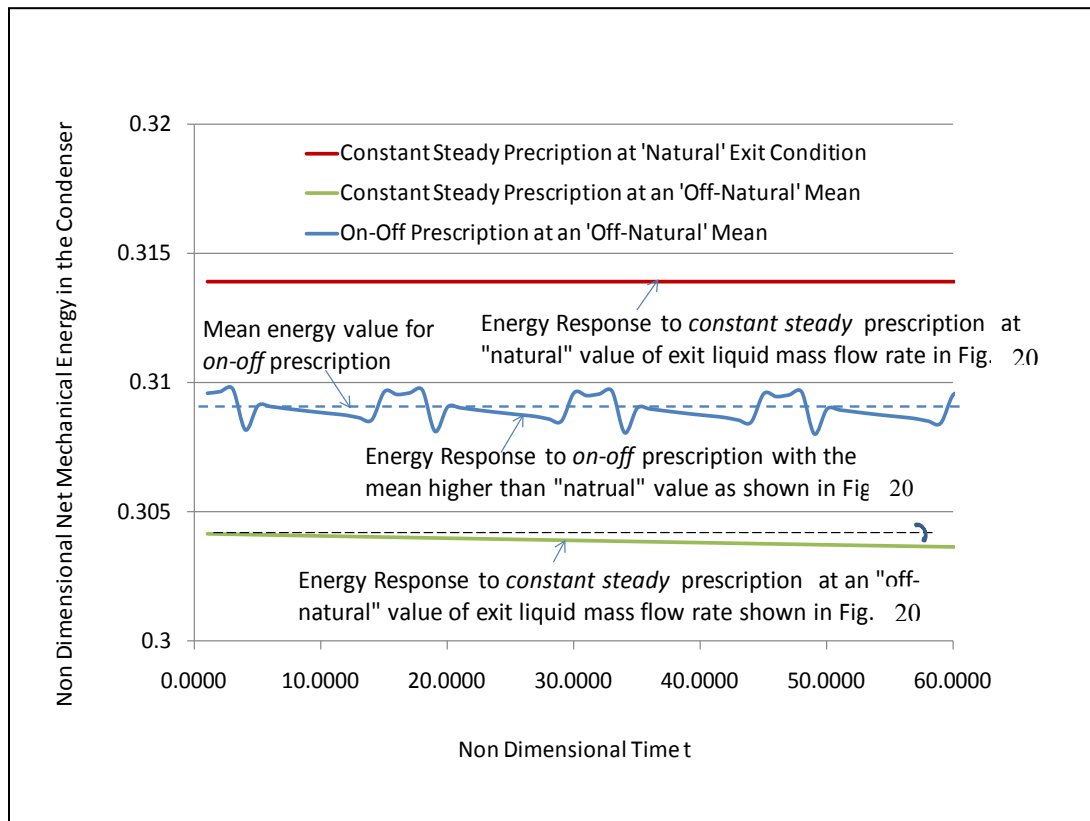
Figure 27: Control volume energy response for different exit condition controls

shown in Figure 20 for a shear driven internal condensing flow

For the flow conditions and exit liquid mass flow-rate control shown in Figure 20, this figure shows the response of non-dimensional values of net mechanical energy in to the condenser over non-dimensional time t. It is shown that typically negative slopes are associated with the constant steady "off-natural" prescription and this suggests no long-term quasi-steady solution exists. However, for the on-off prescriptions at "off-natural" means, net mechanical energy in to the condenser steadies up at a mean lower but near the "natural" value.
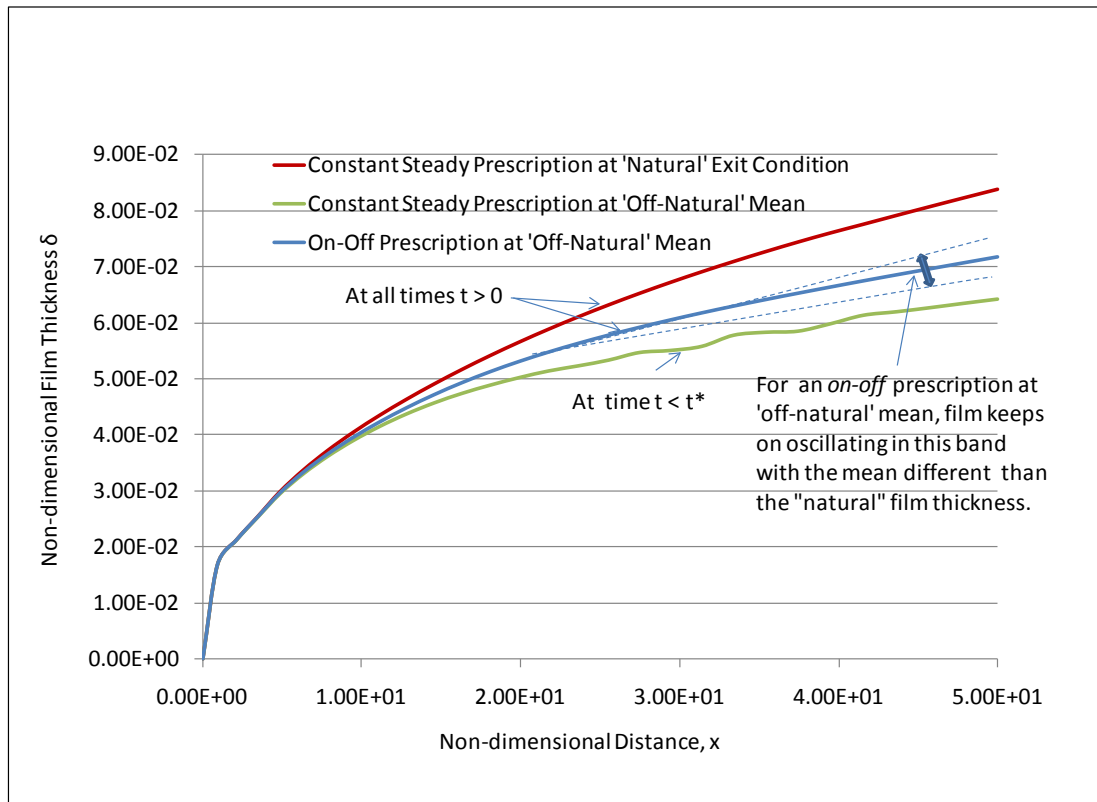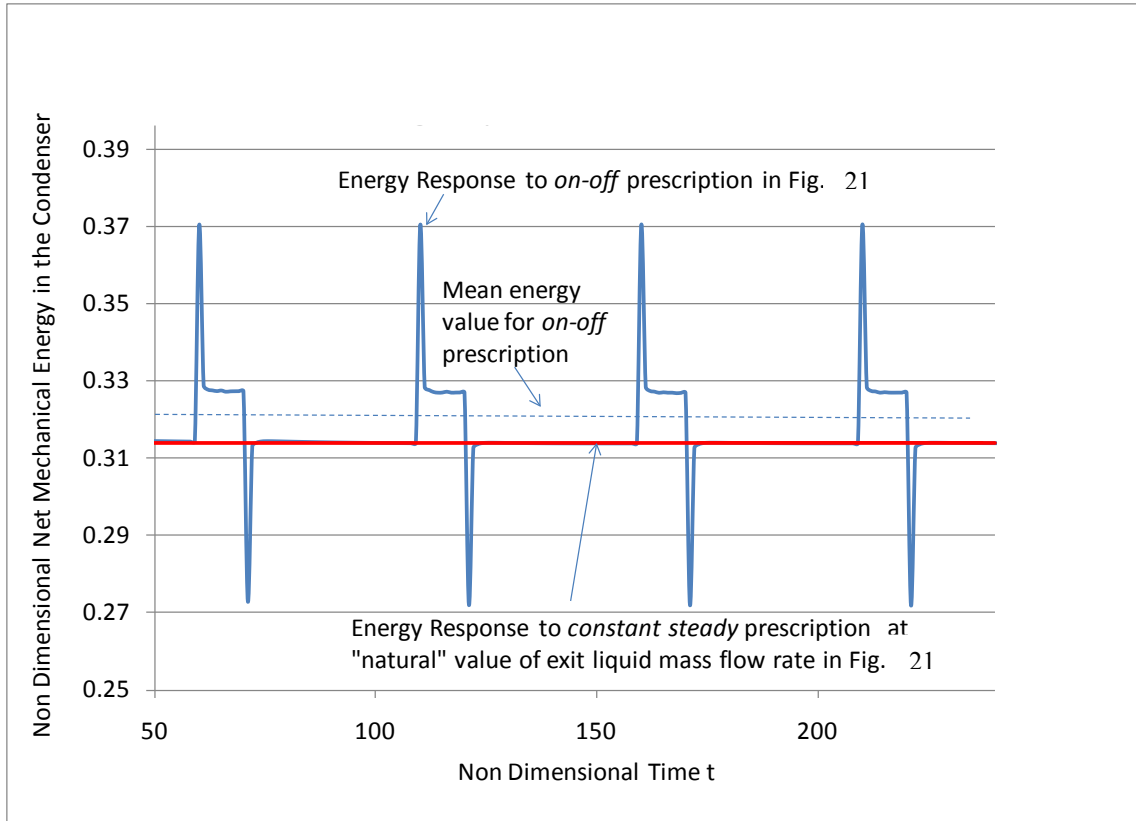
Figure 28: Control volume energy response for different exit condition controls

shown in Figure 21 for a shear driven internal condensing flow

For the flow conditions and exit liquid mass flow-rate control shown in Figure 21, this figure shows the response of non-dimensional values of net mechanical energy in to the condenser with non-dimensional time t. It is shown that for the on-off prescriptions at "off-natural" mean, net mechanical energy in to the condenser steadies up at a mean slightly higher but near the "natural" value.

The interface energy transfer rate $\dot{D}_\Sigma$ is defined in (A.13) of the Appendix A.2 and

is made up of pressure and kinetic energy transfer across the interface. The fact that

increases on either side of the "natural" exit condition is indicative of the energetic

resistance at the interface to consume energy at non-natural rates. Table 2 shows non-

dimensional values of various energies related to condenser control volume and

89

redistribution of these energies as quasi-steady exit liquid mass flow rate control changes. For the *constant steady* control of exit liquid mass flow rate at "off-natural" value, energy keeps decreasing with a non-zero negative slope (see Figure 27) inside the domain before the solution becomes impossible. This is another indicator of eventual impossibility of this imposition in the absence of suitable superposed time periodic fluctuations.
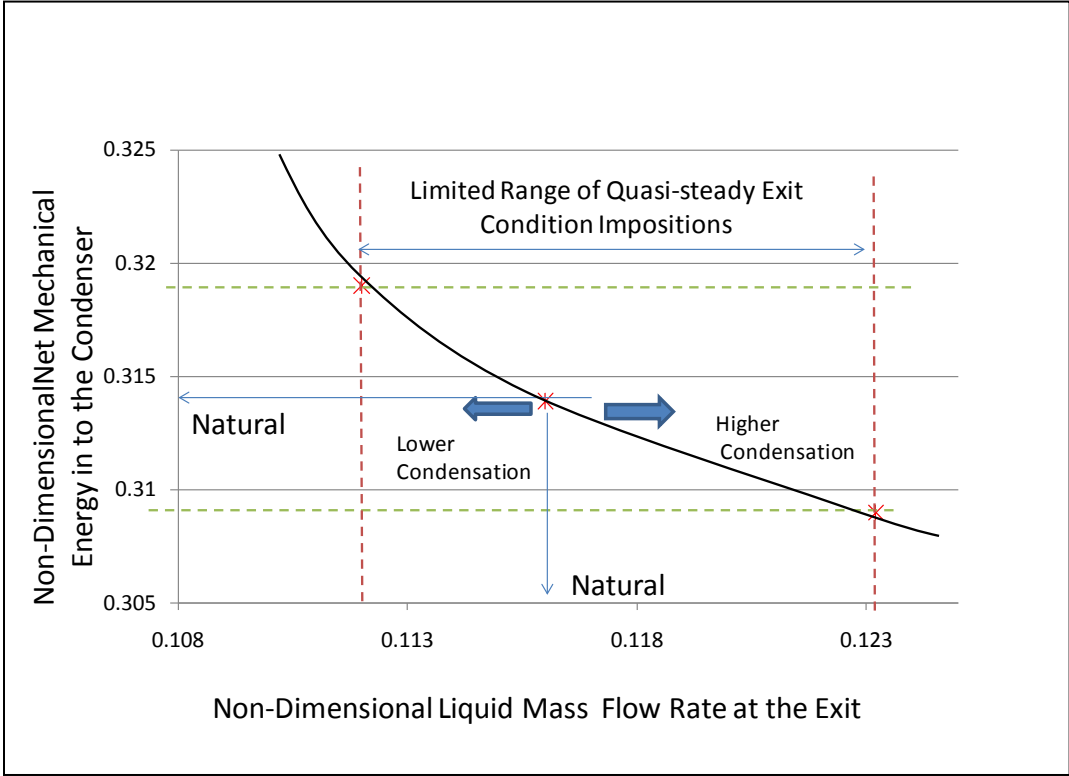
Figure 29: Mechanical energy in the condenser control volume for different quasi-steady exit condition prescriptions for shear driven internal condensing flows

For 0g shear driven flows, this figure shows eventual mean values of net mechanical energy into the condenser for *on-off* type prescriptions with the mean prescription values on either side of the "natural" exit condition. It is shown that even though annular/stratified quasi-steady solutions exist for such *on-off* prescriptions in the vicinity of the "natural" (bounded by the two red lines); the range of available values may be limited for the annular/stratified flow regime.
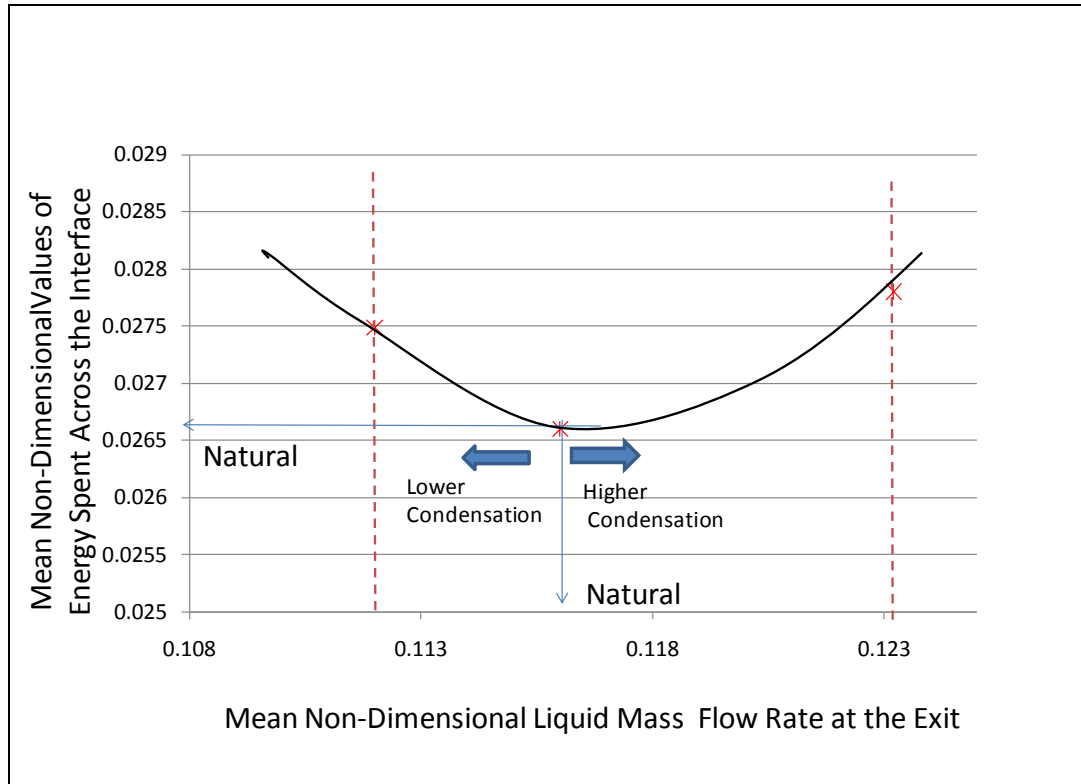
Figure 30: Interfacial energy transfer for different quasi-steady exit condition

controls for shear driven internal condensing flows

For 0g flows, this figure shows mean values of total energy transfer ($\dot{D}_\Sigma$) at the interface for *on-off* type prescriptions with the mean control values on either side of the "natural" exit condition. It can be seen that the value of total interfacial energy transfer increases on both sides of the "natural" exit condition and it is least at the "natural" exit condition. This "spring" like behavior is indicative of "active" and energetic imposition needed for "elliptic-sensitive" boundary condition imposition.

Again, it should be noted that the eventual impossibility of this imposition is different from outright impossibility for strictly parabolic unsteady equations. It should also be noted that relative to the strictly steady "natural" flow, the quasi-steady flows show significant differences (about 7% for the total heat load) in the heat transfer rates

$q''_w(x)$ and Nu_x values where $q''_w(x) \equiv h_x(\Delta T) \approx (k_1 \Delta T)/(h\, \delta(x))$ and $Nu_x \equiv h_x\, h / k_1 \approx$

$1 / \delta(x)$.

However, for these special time-periodic *on-off* impositions with a steady mean near the "natural" value, mean energy in the condenser settles (see Figure 29) to steady values near the steady "natural" value associated with the unique steady solution.

Table 2: Table showing non-dimensional values of different energies associated with condenser control volume for different quasi-steady exit liquid mass flow rate controls for a shear driven internal condensing flow

Type of Exit Liquid Mass Flow Rate Control	Time averaged mean value of exit liquid mass flow rate	Net mechanical energy in to the control volume,	Absolute value of net energy dissipated across the interface $\dot{D}_\Sigma$	Net energy dissipated in the control volume $\Phi_L + \Phi_V$
Continuous control at the "natural" value	0.1161	0.3139	0.0266	0.3405
On-off control with the mean higher than the 'natural' value	0.1232	0.3090	0.0278	0.3368
On-off control with the mean less than the 'natural' value	0.1120	0.3190	0.0274	0.3464

Just as a different quasi-steady flow can be achieved through such quasi-steady (mean plus fluctuation) exit-condition impositions at slightly higher mean value of liquid exit mass flow rate than the natural one (Figure 29), it can also be achieved at slightly lower mean value of liquid exit mass flow rate than the "natural" one. But the responses in Figure 23, Figure 26, Figure 28, and Figure 30 suggest that fluctuating impositions at a mean lower than the natural are more difficult that the fluctuating impositions at a mean higher than the natural. In other words, Figure 30 suggests that the interfacial energy transfer behaves like a non-linear spring towards "non-natural" elliptic impositions. It should also be noted though that the ratio of time periods for the '*on*' and '*off*' portions for the *on-off* impositions (which, in the experiments, are self-selected) that have a mean higher than the natural (Figure 20) is quite different than the one for an "on-off" imposition which has a mean on the lower side of the natural (Figure 21). This suggests that intrinsic character of the flow decide the frequency content of the fluctuating component of quasi-steady exit condition impositions in any self-selection process (also see experimental results in next section).

4.6.2 Stability of the Flow at "Parabolic/Natural" and "Elliptic/Non-Natural" Specifications

For the *constant steady* "non-natural" control, the above-suggested impossibility of sustaining any sort of quasi-steady annular/stratified flow near the unique steady "natural" flow is further substantiated by the instability of these evolving flows.

Figures 31-32 show response of the flow to the initial disturbances on the interface for two different strictly steady exit condition impositions.

93

The result in Figure 31 is for *constant steady* liquid exit mass flow rate imposition at the "natural" value while for the result in Figure 32, the liquid exit mass flow rate imposition is strictly steady and at slightly higher constant value ($\dot{M}_{L-e}|_{constant} \approx 0.123$) than the "natural."

Initial disturbance $\delta'(x,t)$ added to the "natural" solution at t = 0

Disturbance dies at t = 125
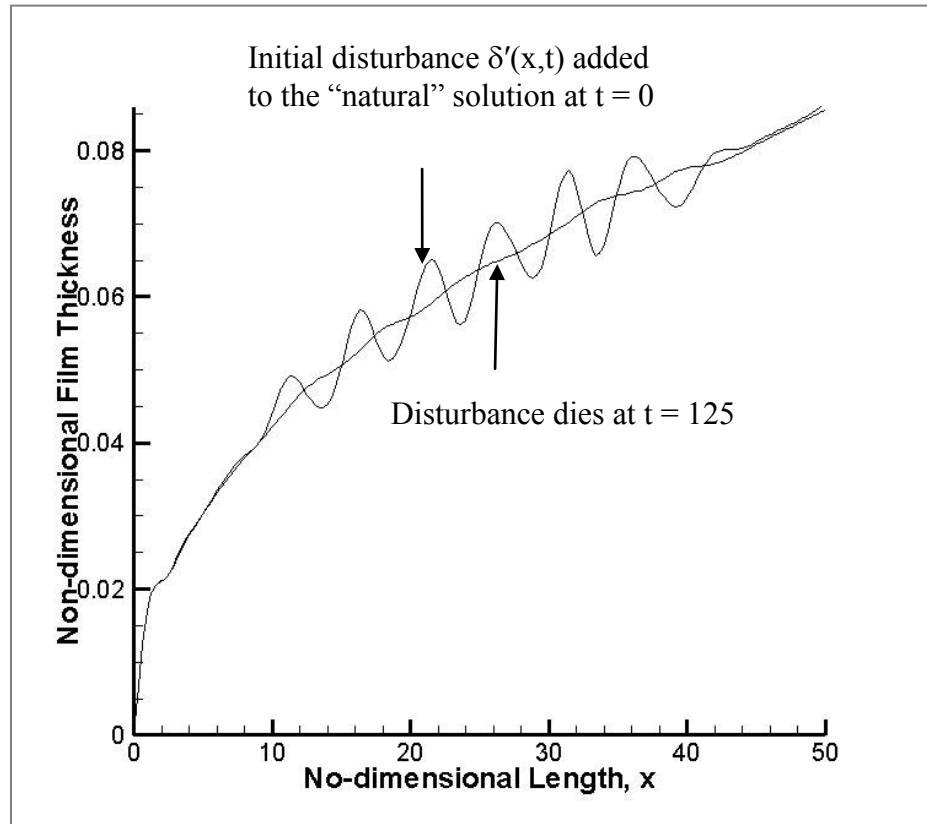
Figure 31: Dynamic stability investigation for a shear driven internal condensing

flow with unspecified exit condition

For condensing flow in zero gravity with inlet vapor speed of 0.6 m/s and vapor-to-wall temperature difference of 5ºC, this figure shows the stable response of the flow to an initial disturbance on the interface if the exit condition for the flow is free or controlled to be exactly at the "natural" value ($\dot{M}_{L-e}(t) = \dot{M}_{L-e}|_{Na} = 0.116$).

It can be seen that the initial disturbance in Figure 31 has died out at non-dimensional time t = 125 while initial disturbance in Figure 32 has significantly grown over the same non-dimensional time. Characteristic curves (given by Eq. (25) here or by Eq. (26) in [2]) for growing disturbance of Figure 32 are given in Figure 33.
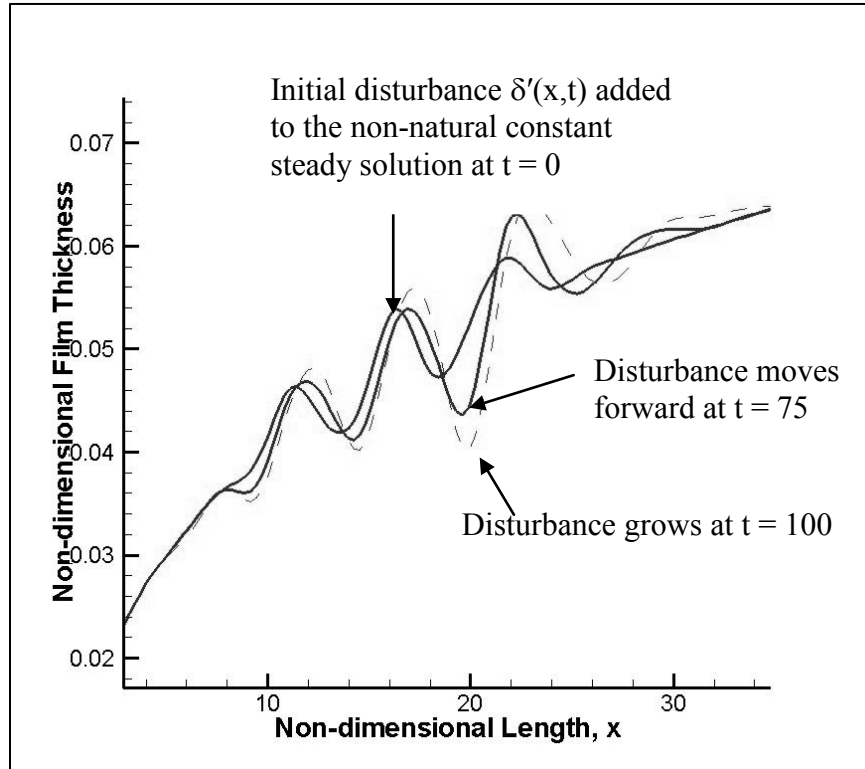
Figure 32: Dynamic stability investigation for a shear driven internal condensing flow with exit condition controlled at an "off-natural" value

For flow conditions of Figure 31 this figure shows the unstable response of flow to an initial disturbance on the interface if the exit of the flow is controlled at a *constant* "off-natural" value ($\dot{M}_{L-e}(t) = \dot{M}_{L-e}|_{constant} \approx 0.123$).

It can be seen that as the disturbance travels downstream, the characteristic curves tend to intersect indicating possible interface break-up and transition to non-annular regime.

The break up time t* as well as t→ ∞ behavior for the constant steady off-natural exit condition imposition (green curve in Figure 20) are expected to depend on whether or not the boundary conditions will allow a fluctuation to sustain such an imposition.
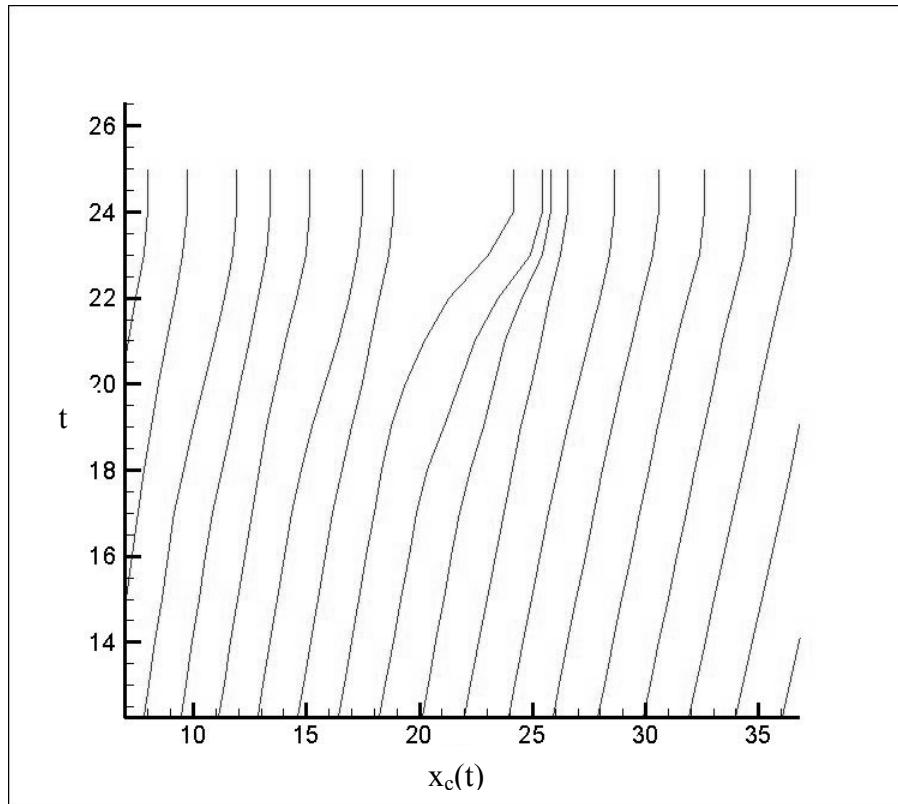
Figure 33: Computationally obtained characteristic curves for shear driven internal condensing flow's response to an initial disturbance

This figure shows the characteristic curves $x_c(t)$ originating at different x values for the initial disturbance case of Figure 32. The intersecting nature of characteristic curves indicates possible film break-up.

These results are consistent with the facts that: (i) annular/stratified partially condensing "natural" flow or a more complex fully condensing "natural" flow is compatible with only one unique self-sought *constant steady* exit condition (for a given inlet conditions, method of cooling, and condenser geometry) – termed "natural" exit condition, and (ii) the flows still allow imposition of suitable steady-in-the-mean quasi-steady exit condition imposition.

This result is important because other fluctuating conditions may inadvertently be imposed – particularly for shear driven flows – depending on the nature of the system to which the condenser belongs. Therefore, in any practical application in 0g or micrometer scale shear driven flow, where the "natural" solution is a weak "attractor," the choice is to either ensure "parabolic" conditions with one unconstrained or unspecified boundary condition or to exploit the above described "elliptic sensitivity."

4.6.3 Mathematically/Physically Sensible Response of the System to Time-Periodic Exit Condition Impositions

It should be noted that only a limited type (self-selected or imposed) of exit condition impositions are compatible with stable realizations of quasi-steady annular flows for horizontal/0g flows and this fact is depicted in the computational result shown in Figure 29. Figure 29 shows the time average *mean* values of net mechanical energy input rate to the condenser for fluctuating time-periodic impositions whose mean values lie on either sides of the "natural" value and the condensing flow responds by achieving a long-term quasi-steady annular/stratified solutions (as per the computations and experiments). It is seen from Figure 29 that for the flow to stay in the annular/stratified

regime, not only the *mean* ($\dot{M}_{L-e}\,|_{\text{on-off-mean}}$) of any *on-off imposition* on exit liquid mass flow rate cannot be very far from the "natural" value but it must also be such that it leads to a mean steady mechanical energy input close to the "natural" value associated with the annular/stratified condensing flow situation. Mean value for any *on-off* type control can be adjusted in practical situations by suitably adjusting a compressor or a pump speed (see section 5-6 of [7]). The result in Figure 29 suggests that for quasi-steady annular/stratified flows in practice, there is a whole range of energy values around the "natural" value that can keep the flow in the annular/stratified regime and yet may have significant impact on heat transfer rates and overall system behavior.

4.7   Preliminary   Computational   Results   on   "Quasi-steady Parabolicity" of Shear Driven Internal Condensing Flows

As discussed in section 4.5, the "*quasi-steady* parabolicity" result says that when fluctuations are added on the prescribed conditions of the strictly steady parabolic problem, fluctuations appear within the flow as well as in the unspecified variables at the boundary (including thermal boundary).

This "quasi-steady parabolciity" has been recently discovered by our experiments and experimental results are discussed in the next section (4.8). Computational investigations of "quasi-steady parabolicity" are limited to the preliminary level for this thesis work. The computational work is aimed to show that:

(i)   The effects of fluctuations depend on the cooling approach. For fixed condensing surface temperature cooling, the mean flow variables in the interior and the boundary are not significantly affected.

(ii)   For the cooling approach that allows variation in *most of* the local condensing surface temperatures, the fluctuations in the parabolic boundary (when the elliptic boundary is not specified) indeed can bring thermal transients in the condensing surface. To investigate this, one needs to understand and define a conjugate problem through which condensing surface temperature may get determined in response of fluctuations at the parabolic boundary.

Conjugate Problem for Condensing Wall for Shear Driven Flow inside a Channel

Different models of varying complexity levels can be used to define conjugate problem that relates condensing surface temperature to the cooling method employed. The simplest model used here assumes that condensing wall has zero thickness, is being cooled by water flowing underneath at ambient temperature T_∞ and heat transfer coefficient h^o which remains constant over given length of the condensing wall.

It is assumed that even though flow fluctuations at the inlet (parabolic boundary for this problem) can change the condensing surface temperature, the ambient temperature T_∞ remains fixed at any time. For the length of the condenser where assumption of linear condensate temperature profiles hold, following set of approximate equations apply:

$$q''(x, t) \approx k_1 \cdot (T_{sat} - T_w(x, t))/\Delta(x, t)$$

$$q''(x, t) = h^o \cdot (T_w(x, t) - T_\infty)$$

$$T_w(x, t) = (k_1 \cdot T_{sat} + \Delta(x, t) \cdot h^o \cdot T_\infty)/(k_1 + \Delta(x, t) \cdot h^o) \tag{26}$$
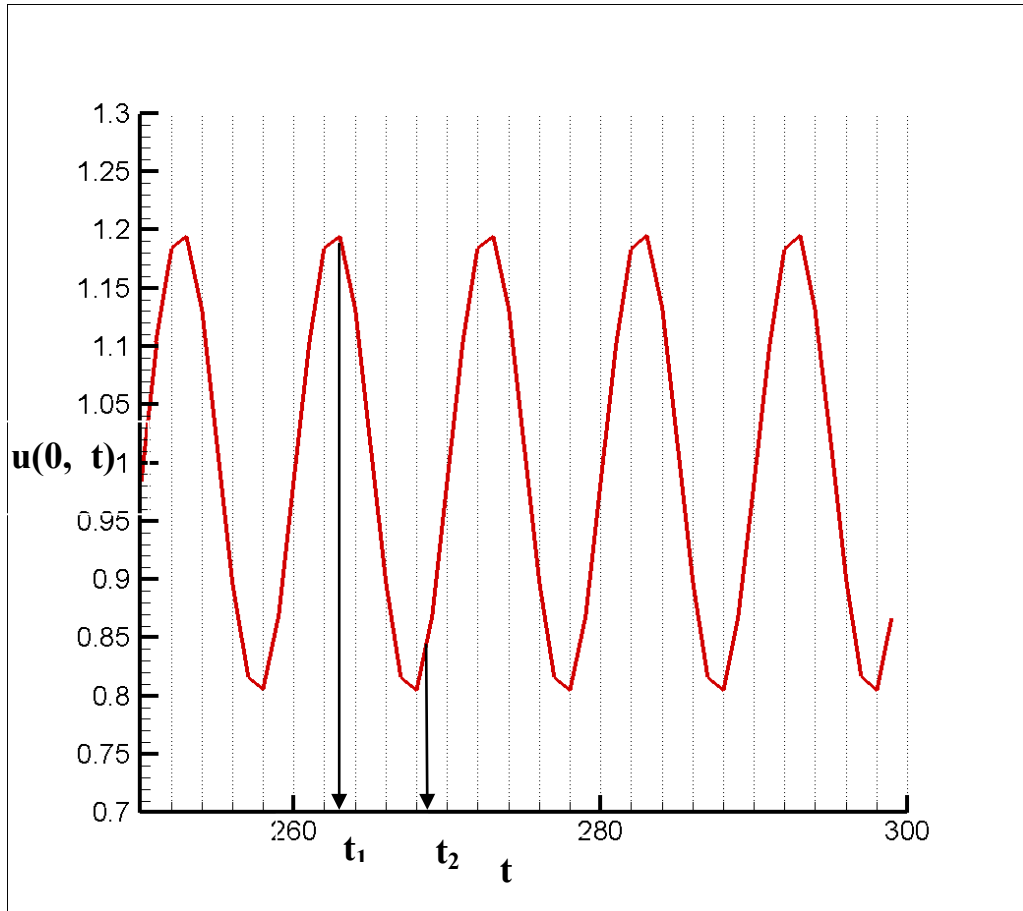
Figure 34: Fluctuating vapor velocity profile at the inlet of horizontal 0g channel

This figure shows non-dimensional values of fluctuating vapor velocity with time at the inlet of a horizontal channel (0g). The figure also marks two times t_1 and t_2 the response of the flow at which times is shown in Figure 35.

This set of model equations assumes that the slab is very thin and thermal inertia of the slab is small. To more accurately model the conjugate problem, thermal inertia of the bottom plate should be taken in to account.

For given inlet vapor velocity $u_2(0, t)$ (equivalently vapor mass flow rate), inlet pressure p_{in} (equivalently interfacial temperature T_{sat}), and assumed fixed values of T_∞ and h^o, an unsteady algorithm given in the Appendix A.2 for unspecified exit condition (formulation [A] of section 2.1) is applied at each time t until converged values of $T_w(x, t)$, $\Delta(x, t)$, and $q''(x, t)$ are obtained.

Figure 34 shows sample fluctuations in non-dimensional inlet vapor speed $u_2(0, t)$. The fluctuations start appearing at the inlet only after certain time t^*. The fluctuating velocity at the inlet is given as: $u_2(0, t) = 1 + A_0(t) \cdot \sin(2\pi t/\Gamma)$, where $A_0(t)$ is amplitude of fluctuations and Γ is time period of the sine wave. For this sample inlet time varying vapor speed, $A_0(t) = 0.2$ and $\Gamma = 10$.

For constant temperature condition of the condensing surface, these fluctuations, as expected, do not change the mean film thickness by much but film (along with the other flow variables) keeps on oscillating in a very narrow band with the *mean* remaining the same as the steady film thickness in absence of any fluctuations. When the same fluctuations are applied in presence of conjugate problem defined by Eq. (26), there is not much effect on film thickness variations but miniscule thermal transients are observed on the condensing surface and these are shown in Figure 35.

Figure 35 shows non-dimensional temperature of condensing surface $\theta(x, 0, t)$ versus non-dimensional distance x before and after the application of conjugate problem

101

model. The black dotted line in Figure 35 shows constant steady wall temperature *before* the conjugate problem algorithm is switched on. The two sets of curves shown by red and blue lines show the response of condensing surface temperature for two different assumed values of h^o (1000 W/m^{2}K and 500 W/m^{2}K respectively) when the conjugate problem is switched on and eventually (beginning from time t*) fluctuations shown in Figure 34 are applied. It can be seen that before the fluctuations begin, the wall temperature steadies up at different values for two different assumed values of h^o. Figure 35 also shows that when fluctuations in the mass flow rate start appearing at the inlet there are thermal transients induced (shown at time t_1 and t_2 in the fluctuation cycle in Figure 34) in the wall temperatures.

In general following observations were made from this computational exercise:

(i)   In presence of fluctuations, condensing surface temperature profiles (see red and blue curves shown at times t_1 and t_2 in fluctuation cycle) do not necessarily oscillate around the steady profiles (thick red and thick blue curves shown in Figure 35). The values of thermal transients in condensing surface temperature induced for amplitude, time period of fluctuations in the inlet mass flow rate considered in Figure 34 are found to be minuscule in amplitude, and thus they insignificantly affect film thickness and heat transfer rates. However, it can be expected that there will be considerable thermal transients (and corresponding heat transfer changes) for large values of amplitude $A_0(t)$ and varying ranges of time periods Γ.

(ii)   It should also be noted that the response of conjugate problem shown in Figure 35 differs for different h^o values. It is indicative of the fact that the "quasi-steady parabolicity" sensitivity depends upon modeling of conjugate problem in computations and actual cooling method in experiments. More complex models with finite thickness of condensing plate, which consider thermal inertia of the plate can be applied and response of the flow can be investigated.
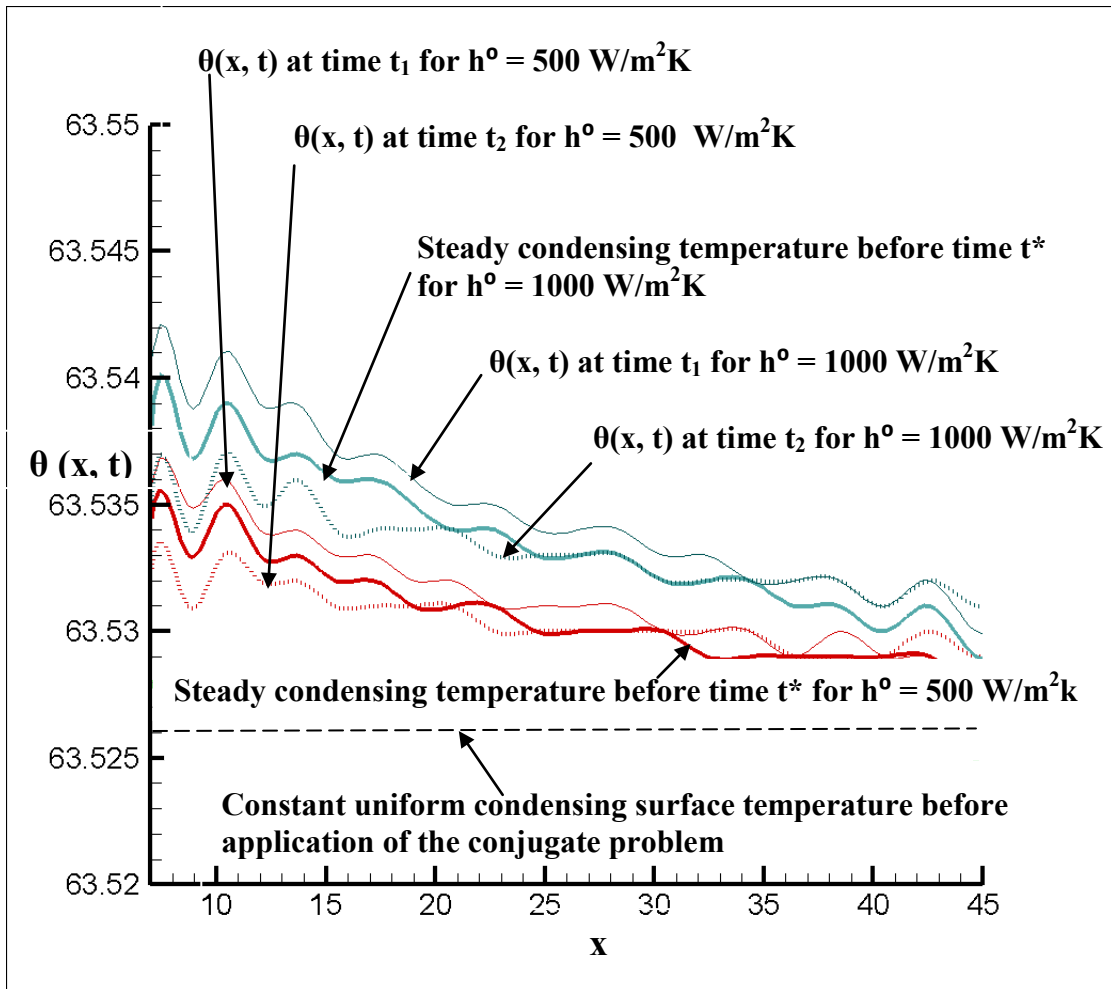
Figure 35: thermal transients induced in condensing surface because of inlet mass flow rate fluctuations in Figure 34 and underlying conjugate problem

103

The computational results shown above only indicate that in presence of fluctuations in the parabolic boundary (inlet for the cases considered in Figures 34-35) can bring in thermal transients in the condensing surface. Detailed investigations about changes in mean flow variables in response to different types of fluctuations at the inlet, modeling of different conjugate problems, and comparisons with experiments are part of computational work of Soumya Mitra.

4.8 Experimental Investigation of a Shear Driven Flow and Its Qualitative Comparisons with the Computational Problem/Results

4.8.1 Physical Arrangement of the Experimental System

To study the experimental verification of the computational results regarding unsteady/quasi-steady condensing flows' "ellipticity," the 2-D flow in Figure 1 is approximated by the 3-D situation of Figure 36. This involves fully condensing flows of FC-72 vapor in a rectangular cross-section (2 mm gap height and 15 mm wide) duct of 1m length. Its horizontal condensing surface area (15 mm x 1 m) is the top of a 12.7 mm thick stainless plate.

The channel's top and side surfaces are made of a thick transparent material (lexan), which is covered with an insulation that can be removed to allow flow visualization. The test-section shown in Figure 36 is used in the flow loop facility depicted in 38.
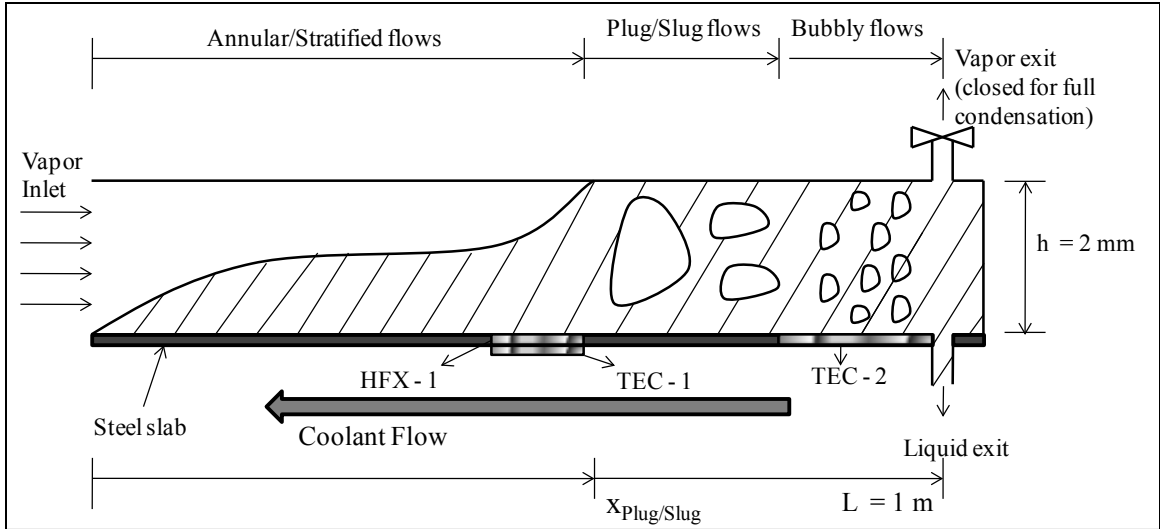
Figure 36: A schematic showing horizontal channel test section and a particular realization of shear driven fully condensing flow in it

The condensing surface's "cooling approach" (which defines its thermal boundary condition) consists of:

(i)   Coolant water flows under the thick condensing plate at a controlled steady flow rate and a nearly uniform temperature T_{res}.

(ii)   A thermo-electric cooler underneath the heat-flux meter (HFX-1 on top of a thermo-electric cooler TEC-1 in Figure 36) cools the condensing-surface approximately over 50 cm$\le$ x $\le$ 60 cm in a fashion that keeps the mean surface temperature fixed at an average and approximate constant value. This is done with the help of feedback control of TEC-1 through a thermocouple which holds the local temperature at x = 58.5 cm fixed.

(iii)   A thermo-electric cooler (TEC-2 in Figure 36) underneath the condensing surface cools an approximate region of 80 cm $\le$ x $\le$ 1 m. The thermo-electric cooler

105

TEC2 is operated at a fixed maximum driving voltage (17.5 Volt). The thermo-electric cooler lowers the condensing surface temperature (for the reported full condensation cases) past the onset of bubbly regime – thereby ensuring that the subsequent flow morphology changes rapidly to an all liquid flow over this zone.

The above described "cooling approach" defines the following thermal boundary condition for the condensing surface:

(a)   At all locations other than the ones associated with HFX-1/ TEC-1 and TEC-2 in Figure 36, let R''_{slab} and R''_{conv} denote the respective thermal resistances – on per unit area basis – that model steady or quasi-steady heat flow through the slab and the water flow (at temp T_{res}). Furthermore, if h_{ext} is given by $1 / h_{ext} \equiv R''_{slab} + R''_{conv}$, then the thermal boundary condition at these "x" locations are of the convection type (Eq. (11)) and is given by (for $R''_{slab} \ll R''_{conv}$):

$$-k_1 \frac{\partial T_1}{\partial y}\big|_{y=0} = h_{ext}[T_1(x, 0, t) - T_{res}]$$

where $0 \leq x \leq 50$ cm or 60 cm $\leq x \leq 80$ cm. For non-negligible R''_{slab}, the model above is best replaced by a conjugate analysis which correctly models the thermal inertia (effects of specific heat and the volume of the slab) issues for the transient heat flow through the slab.

(b)   At the thermo-electric cooler TEC-1 and heat flux meter HFX-1 location, a nearly steady temperature boundary condition of:

$$T_1(x, 0, t) \approx 58.5 \,°C \quad \text{for } 50 \text{ cm } \leq x \leq 60 \text{ cm}$$

can be assumed since the surface temperature variation in this region was measured to be small.

(c) If one respectively denotes the bottom and top temperatures of the thermo-electric cooler (TEC-2 in Figure 36) by T_{bot} and T_{top}, and the area-averaged heat flux by $\overline{q}''$, then the constant voltage operation of TEC-2 defines a known function $\tilde{f}_{TEC}$ such that

$$\Delta T_{TEC} \equiv \quad T_{bot} - T_{top} \quad = \tilde{f}_{TEC}(\overline{q}'')$$
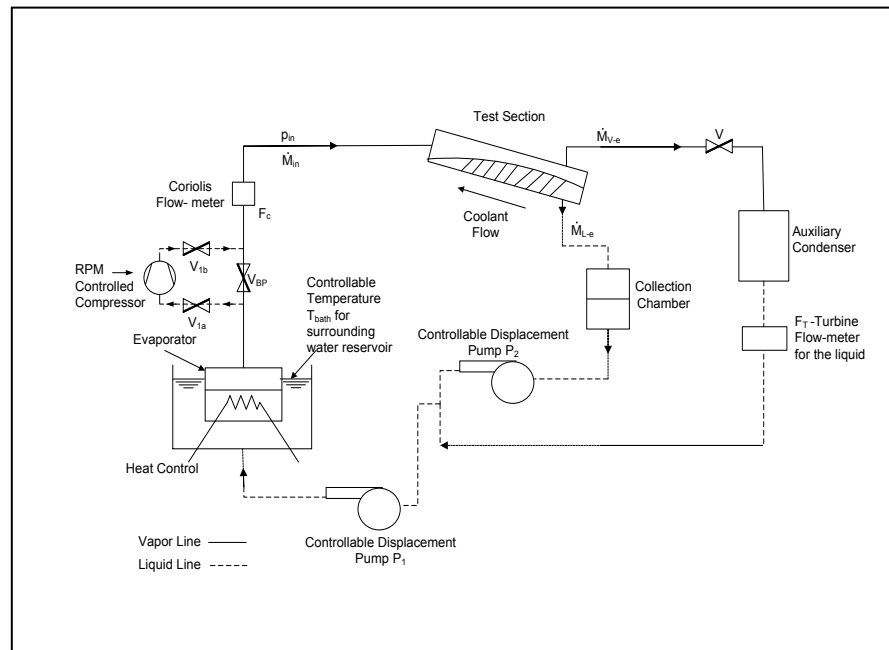
Figure 37: Schematic of flow loop for shear driven partial or fully condensing flow experiments

This non-linear function $\tilde{f}_{TEC}$ is experimentally known and follows the trends implied by the manufacturer's specification. If the per unit area thermal resistance between the top of the TEC-2 and the condensing-surface is denoted by R''_{top}, and the thermal resistance between the bottom of TEC-2 and water flow is denoted by R''_{bot}; then the thermal boundary condition over the TEC-2, under quasi-steady conditions, is well approximated by:

$$[T_1(x, 0, t) - T_{res}] \quad = \quad \overline{q}''\left(R''_{bot} + R''_{top}\right) - \tilde{f}_{TEC}\left(\overline{q}''\right)$$

for 80 cm $\leq$ x $\leq$ 1m, where

$$\overline{q}'' \equiv -k_1 \left.\frac{\partial T_1}{\partial y}\right|_{y=0}$$

It is evaluated at a suitable x-location. For truly unsteady conditions and non-negligible conductive thermal resistance contributions to R''_{top} and R''_{bot}, the model above is best replaced by a conjugate analysis which correctly models the thermal inertia (effects of specific heat and the volume of the slab) issues for the transient conduction heat flow.

Although, both computations and experiments deal with purely shear driven horizontal channel flows, the condensing surface thermal boundary condition for the experiments – as given above – are not the same as the one assumed for the theory (i.e. $T_1(x, 0, t) = T_w(x) = $ constant. The computational simulations for the above experimental thermal boundary condition and the results' comparisons with experiments are part of a forthcoming research.

4.8.2 Experimental Procedure and Observations

Procedure and observations for the first quasi-steady realization (for $t \leq t_0$) in Figures 38-40

      For the reported cases, the valve V in Figure 37 is closed and the pump P_2 in Figure 37 is removed and eventually attained steady operating values of inlet mass flow rate, p_{in}, and   are such that the point of full condensation is within the test-section and the "Collection Chamber" in Figure 37 is filled with liquid. This procedure involves: (i) removing the compressor from the flow loop by keeping the compressor running at a very low speed with the bypass valve (V_{BP} in Figure 37) fully open, (ii) holding fixed the Coriolis mass flow meter F_C (in Figure 37) reading of the mass flow rate by a PID control of the evaporator heater, (iii) fixing the evaporator bath temperature T_{bath}, (iv) steadying condensing surface temperature T_W (x) through a control that achieves a steady coolant flow rate for the water that flows underneath the condensing surface and maintains a nearly uniform temperature, and (v) using the controllable displacement pump P_1, through a PID control, to hold the exit pressure fixed at $p_{exit} = p_{exit}*$. This procedure allows the inlet pressure p_{in} to freely seek its natural steady value $p_{in}|_{Na}$.

      As depicted in Figure 36, it is found that the morphology of the fully condensing flow cases (depending on inlet mass flow rate and ΔT values) were found to vary from: (i) cases where the flows are annular/stratified almost up to the point of full condensation (and only a small amount of "plug/slug" flows are seen near the point of full condensation) to (ii) cases where the flows are significantly non-annular over approximately half of the test-section.
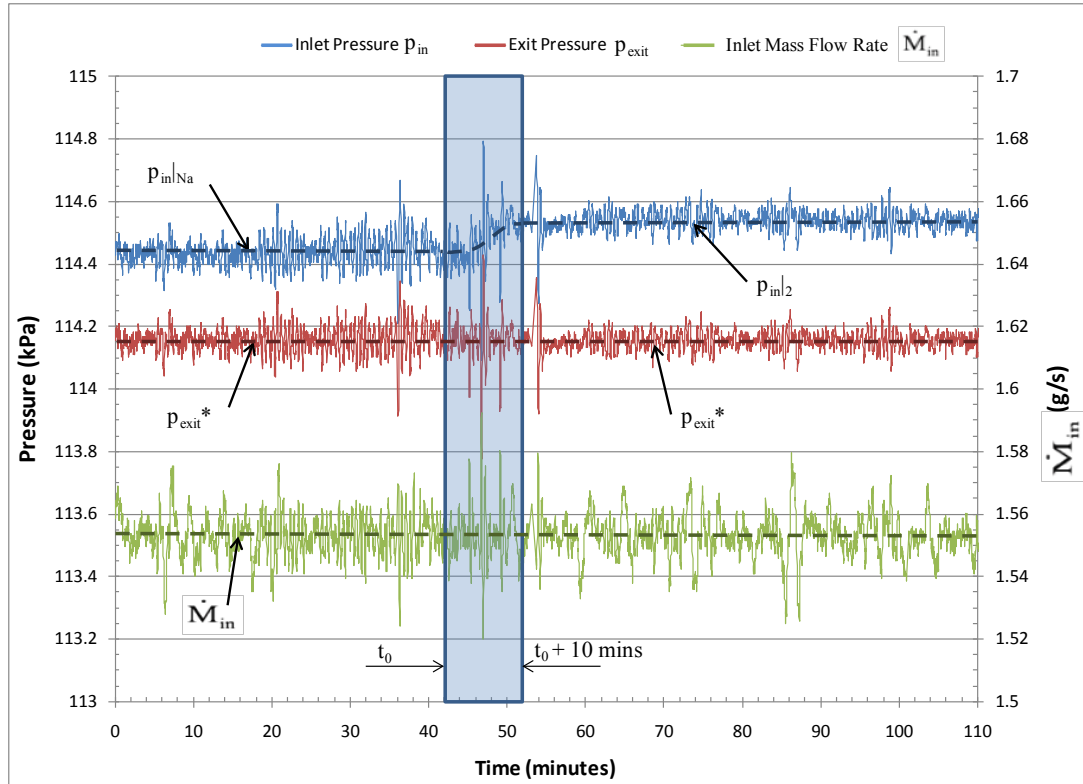
Figure 38: Response of pressure drop and heat flux to the "elliptic" constraining of a fully condensing shear driven flow inside a horizontal channel

This figure shows time histories of inlet mass flow rate, inlet pressure, and exit pressure for a "natural" ($t < t_0$) and an "elliptically" constrained ($t > t_0 + 10$) realization of a fully condensing shear driven flow in the horizontal test-section of Figure 36.

It was experimentally observed that even though fully condensing flows exhibit different flow regimes (annular, non-annular, plug-slug, bubbly, etc.) inside the test section, the observed transition locations (schematically shown in Figure 36) by $x_{Plug/Slug}$, x_{Bubbly}, etc. were experimentally found to be robust and repeatable. Along with this, the mean measured values of flow variables in Figures 38-39 were also found to be

repeatable for $t \leq t_0$. In Figures 38-39, the mean values of inlet mas flow rate, p_{in}, $p_{exit}*$, Δp, etc. are accurate to within 5%, the temperatures are accurate to within $\pm$ 1°C, but the absolute values of the mean heat-flux $q''_{W|HFX-1}$ is not representative (because the heat flux-meter was not calibrated) - though the relative magnitude of changes in $q''_{W|HFX-1}$ (i.e. $\Delta q''_{W|HFX-1}/q''_{W|HFX-1}$) are representative and correct to within 5%. Therefore, the results reliably tell that one can achieve repeatable and stable "natural" fully condensing flows if the flow loop is designed in a way that all the "parabolic" boundary condition impositions are well controlled and repeatable.
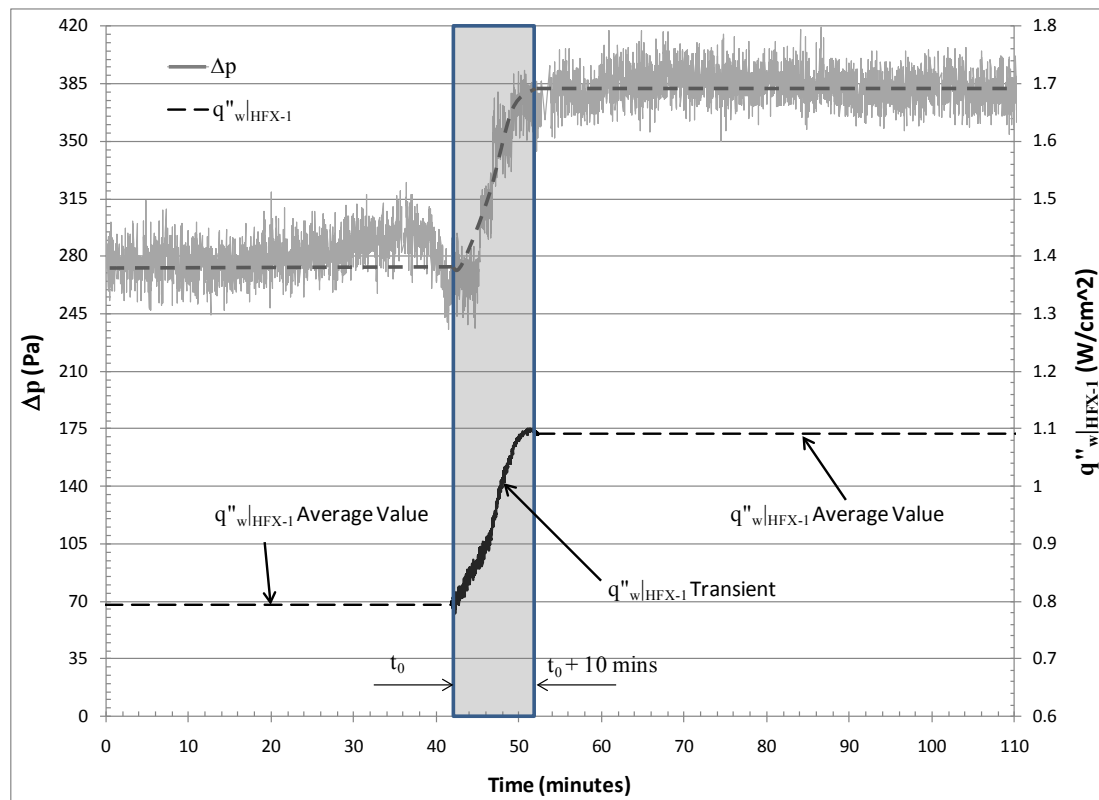
Figure 39: Response of pressure drop and heat flux to the "elliptic" constraining of a fully condensing shear driven flow inside a horizontal channel

111
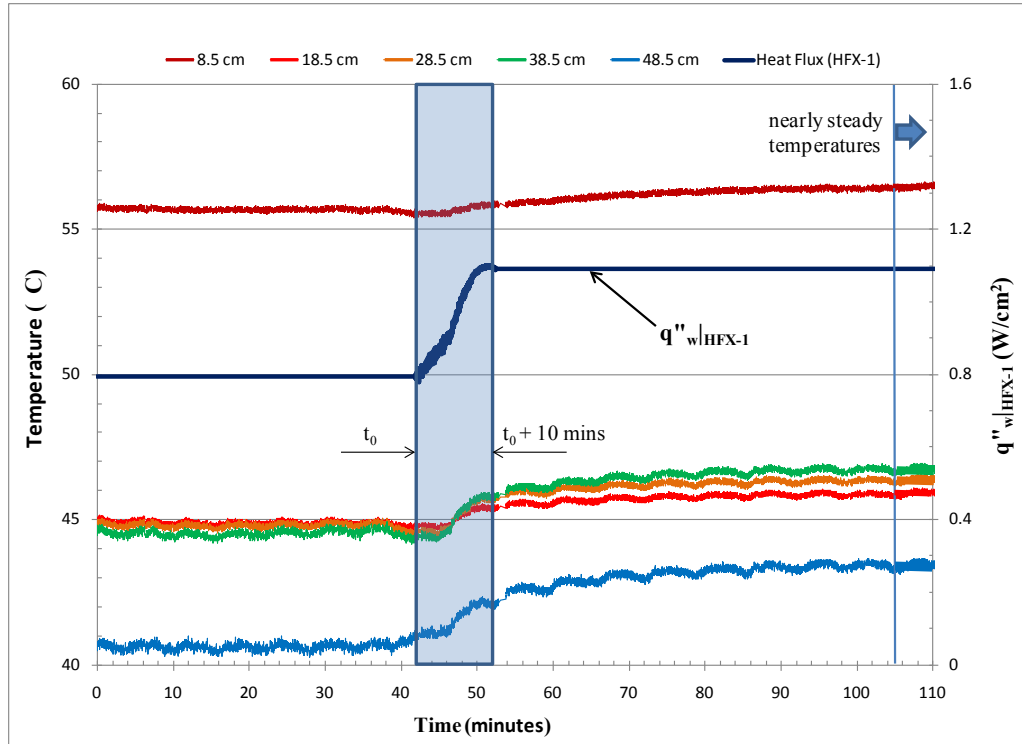
Figure 40: Thermal transients introduced because of constraining of a shear driven fully condensing flow inside a horizontal channel

For constraining shown in Figures 38-39, this figure shows thermal transient response (notice the green curve for temperature takes 65 minutes to become steady after time t_0) and compares it shorter hydrodynamic response of the average heat flux q''_{HFX-1} which becomes steady in only 10 minutes after time t_0.

Additonally the flow loops design needs to allow the flow to seek its own pressure condition at the inlet ($p_{in}|_{Na}$). However, as discussed next, when an unsteady "elliptic" boundary condition is imposed for shear driven flows, not only do the flow regime transition boundary locations (marked $x_{Plug/Slug}$, x_{Bubbly}, etc. in the schematic of Figure 36) change in time but, also, the mean values of the flow variables changes in time.
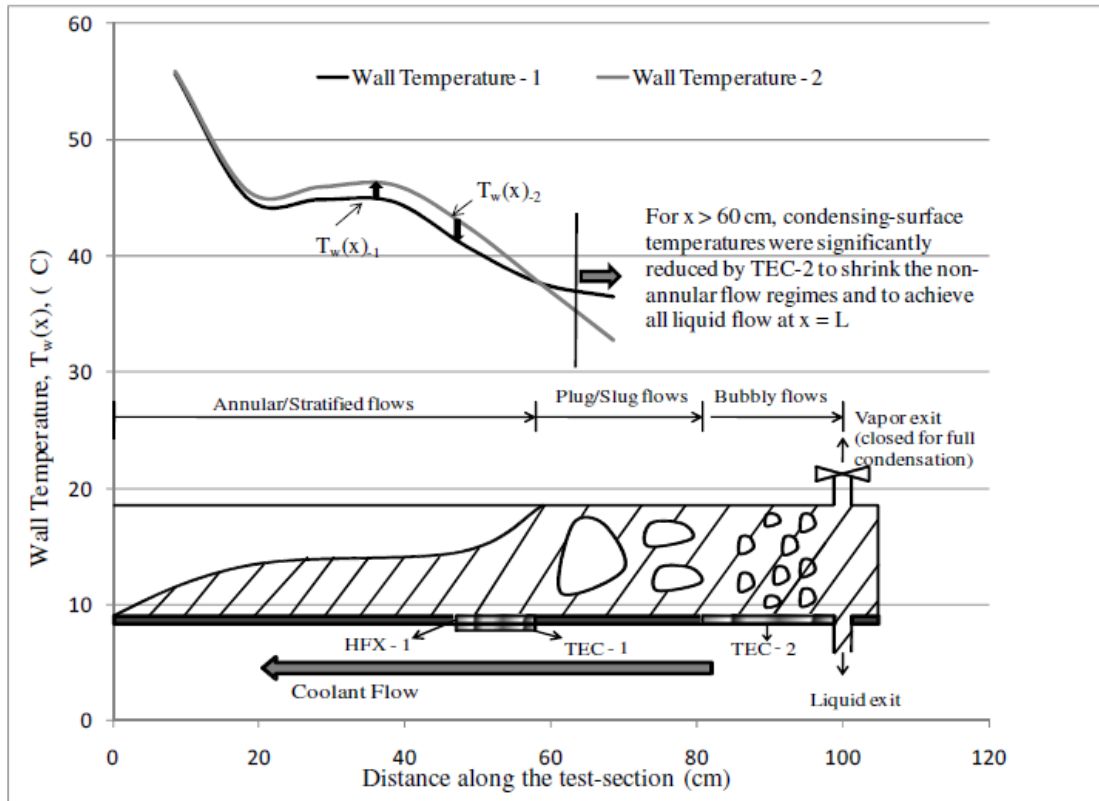
Figure 41: Shift in flow regimes and condensing surface temperature response for "elliptic" constraining of a shear driven fully condensing flow inside a channel

This figure shows the steady $T_w(x)_{-1}$ values for $t < t_0$ and new steady $T_w(x)_{-2}$ for $t > t_0 + 65$ minutes in Figures 38-40

Procedure for imposition of an unsteady/quasi-steady "elliptic" pressure boundary condition at the inlet

To begin with, the quasi-steady flow was "natural" for $t \le t_0$ with the inlet mass flow rate, natural inlet pressure $p_{in|Na-1}$, fixed exit pressure p_{exit}^*, natural pressure difference Δp, and the heat flux $q''_{W|HFX-1}$ values were as shown in Figures 38-39. The steady condensing - surface temperature variation $T_W(x)_{-1}$ was as in Figure 41.

113

The subsequent ($t \geq t_0$) imposition of unsteady "elliptic" boundary condition procedure involves:

Use the flow controls to continue to hold fixed the earlier (for $t \leq t_0$) values of mean exit pressure p_{exit}^*, inlet mass flow rate, bath temperature T_{bath} (to stabilize boiler pressure variations during compressor aided imposition of inlet pressure), the coolant flow rate, and the coolant temperature for $t \geq t_0$ while increasing the inlet pressure $p_{in}(t)$ in time (over $t_0 \leq t \leq t_0 + 10$) with the help of the compressor by increasing the speed of the compressor and partly closing the bypass valve (V_{BP} in Figure 37) to a new value $p_{in}|_2 > p_{in-1}$. Because the steady cooling approach in the experiments allows time variations in the values of condensing surface temperature $T_W(x)$, it is found that this unsteady "elliptic" imposition causes the shear driven flow to respond unsteadily – exhibiting thermal transients (see Figure 40) before a final quasi-steady state is reached at $t > t_0 + 65$. This final steady state is another "quasi-steady parabolic" state associated with the new condensing surface temperature distribution $T_w(x)_{-2}$ in Figure 41.

These results in Figures 38-41 show that the mean inlet pressure has been successfully increased with the help of the compressor induced fluctuations while the exit pressure has remained constant. Concurrent to this imposition, at the end of the 10 minutes long hydrodynamic transient (during which the unsteady imposition occurs), the pressure-difference Δp between the inlet and the exit increases and, as in the computational results, the mean film thickness of the wavy interface decreases in the annular/stratified region and this leads to significantly enhanced heat-transfer rates (see representative $\dot{q}''|_{HFX-1}$ values in Figure 39). It should be noted that the significant

114

enhancement in heat-transfer rate is there because an increase in Δp by 60 Pa is quite significant compared to the original pressure difference (about 275 Pa) for the annular stratified portion of the flow (see Figure 39).

The role of fluctuations in the experimentally observed elliptic sensitivity

This imposition of non-natural quasi-steady inlet pressure $p_{in}|_2$ and associated heat-transfer enhancements (which may yield a total heat transfer rate significantly above the one that is obtained without fluctuations due to energy contained within the inlet vapor fluctuations being absorbed by the interface) are accompanied/enabled by the time-periodic fluctuations in the inlet pressure and in the inlet mass flow rate. For the fluctuations accompanying the mean inlet pressure, the compressor provides a significant additional flow work and an additional inlet enthalpy flux. Since, eventually, the mean inlet pressure is what is experimentally imposed at a non-natural quasi-steady value, the inlet fluctuations that enabled the requisite changes in the mean value of the flow variables were self-selected by the flow. Because the thermal transients accompany the hydrodynamic transients (see Figure 40), the heat-transfer enhancements gradually become permanent as the new steady temperatures $T_w(x)|_2$ are reached. Unlike the computational cases where $T_w(x)$ was constant, the new quasi-steady flow at $t > t_0 + 65$ is another quasi-steady parabolic flow and it does not have the feature of elastic bounce-back between the two quasi-steady states – one associated with $t \leq t_0$ and the other with $t > t_0 + 65$. These two states can only be interchanged gradually with the help of thermal transients.

115

4.9 Computational Results on Micro-scale Effects in Internal Condensing Flows

Under certain flow conditions, effects arising due to micro-scale nature of condensate film may become very important. As far as micro-scale effects are concerned, this thesis work limits itself to the basic investigations of impact of **non-equilibrium thermodynamics** ([36], [42] - [43]) induced interfacial thermal resistance and **disjoining pressure effects** ([36], [42] - [13]) on "natural" steady internal condensing flows. For some commonly occurring operating conditions considered for Figures 42 and 43, the condensate motion is μm-scale (0-5 μm) over the entire length (x_e = 5) of a mm-scale (channel gap is 0.4 mm) condenser. After including the effects ([36], [42] - [43]) of **disjoining pressure** p_d for thin film flows, the corresponding simulation result in Figure 42 show non-dimensional film thickness δ and non-dimensional interfacial pressure difference $\{(\rho_2 * \pi_2/\rho_1) - \pi_1\}$. To obtain these results, the interface pressure condition (see Eq. (A.5) of [6]) was modified as:

$$p_1^i = p_2^i + \dot{m}^2(1/\rho_2 - 1/\rho_1) - (\sigma\Delta_{xx})/[1+\Delta_x^2]^{2/3} + p_d,$$

(27)

where $p_d = -A/\Delta^B$ with A = $1.3*10^{-4}$ - $4*10^{-4}$ Pa-m$^{0.6}$ and B = 0.6 as representative constants in this model (see Eq. (3.46) of [36]). The chosen range of constants in the above equation is merely representative and needs to be made precise with the help of carefully conducted micro-scale experiments that can yield results which can be compared with simulation results of the type indicated in Figure 42.

To account for non-zero interfacial thermal resistance due to a possibly significant role of **non-equilibrium steady thermodynamics** ([36], [42] - [43]) that is expected for thin condensate flows with relatively larger interfacial mass-flux values, one allows interfacial temperature T_1^i in the liquid phase to be different from the interfacial vapor temperature $T_2^i = T_{sat}(p_2^i)$. One way to compute the $T_1^i \neq T_2^i$ values is to obtain the interfacial heat-flux value $q^{ri} \approx [k_1 \cdot \partial T_1 / \partial n|^i - k_2 \cdot \partial T_2 / \partial n|^i]$ from the computational simulations in the absence of interfacial resistance effects (e.g. from simulation results in Figure 43 under $T_1^i = T_2^i$ assumption) and then use these values to solve for T_1^i as a zero of the well known model equation (see Eq. (4.139) of [36]):

$$q^{ri} = \bar{\sigma} h_{fg} \left(\frac{M_{vap}}{2\pi R_u} \right)^{1/2} \left[\left[1 + a\sqrt{\pi} \right] \frac{p_2^i}{\sqrt{T_2^i}} - \frac{p_{sat}(T_1^i)}{\sqrt{T_1^i}} \right]$$

(28)

under representative values of a = $1.3 * 10^{-4}$, accommodation co-efficient $\hat{\sigma} = 0.3 - 1.0$, M_{vap} = M_{R-113} = 187.38 kg/kmol, and $p_{sat}(T)$ being the known saturation pressure function for R-113, and universal gas-constant R_u = $8.314 * 10^3$ J/Kmol-K.

By finding the root of Eq. (28) above at each x for the above described first-guess value of q^{ri}, we obtain the first-guess value of the liquid interfacial temperature profile T_1^i. A subsequent guess of q^{ri} is obtained by solving the liquid domain energy equation in the simulation scheme under the above obtained first-guess new values of $T_1^i \neq T_2^i$. Inserting this subsequent estimate of q^{ri} in Eq. (28) above, one can obtain the second estimate for the liquid interfacial temperature profile T_1^i. Repeating the above process yields a converged set of q^{ri} and T_1^i values that satisfies the interfacial resistance model equation given by Eq. (28) above.
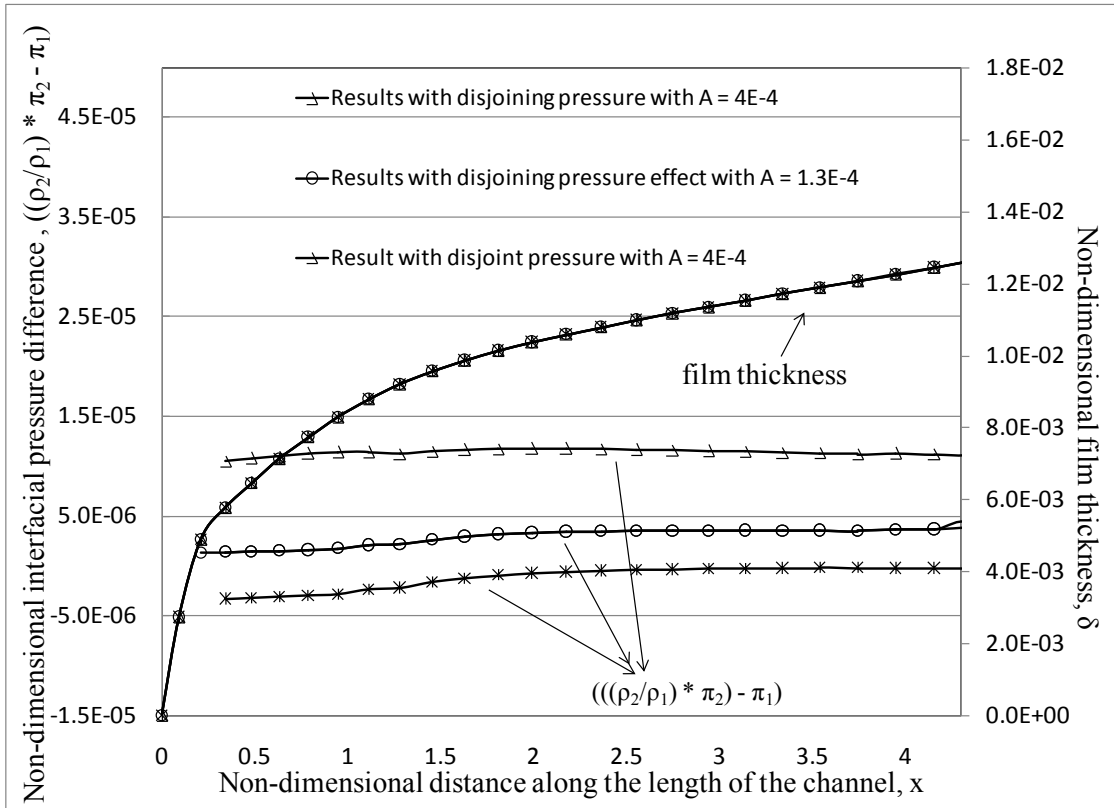
Figure 42: Effects of disjoining pressure at the interface for a micro-meter scale

internal condensing flow

For the flow of R-113 vapor through a vertical channel of 0.4 mm, vapor inlet speed Uin = 6 m/s, and $\Delta T = 3$ °C, this figure shows the effects of disjoining pressures on pressure-difference across the interface on "natural" steady solutions. Figure plots non-dimensional film thickness values and the difference between non-dimensional pressures on the two sides of interface for three different cases: (i) without the disjoining pressure effect, (ii) inclusion of the disjoining pressure effect through Eq. (27) and model constant A = 1.3*10-4, and (iii) inclusion of the disjoining pressure effect through Eq. (27) and model constant A = 4*10-4. It is seen that though the effect of disjoining pressure is small on the film thickness variation for this micro-scale condensing flow (film thickness values around 5 microns), there is a considerable effect on the pressure-difference across the interface.

118
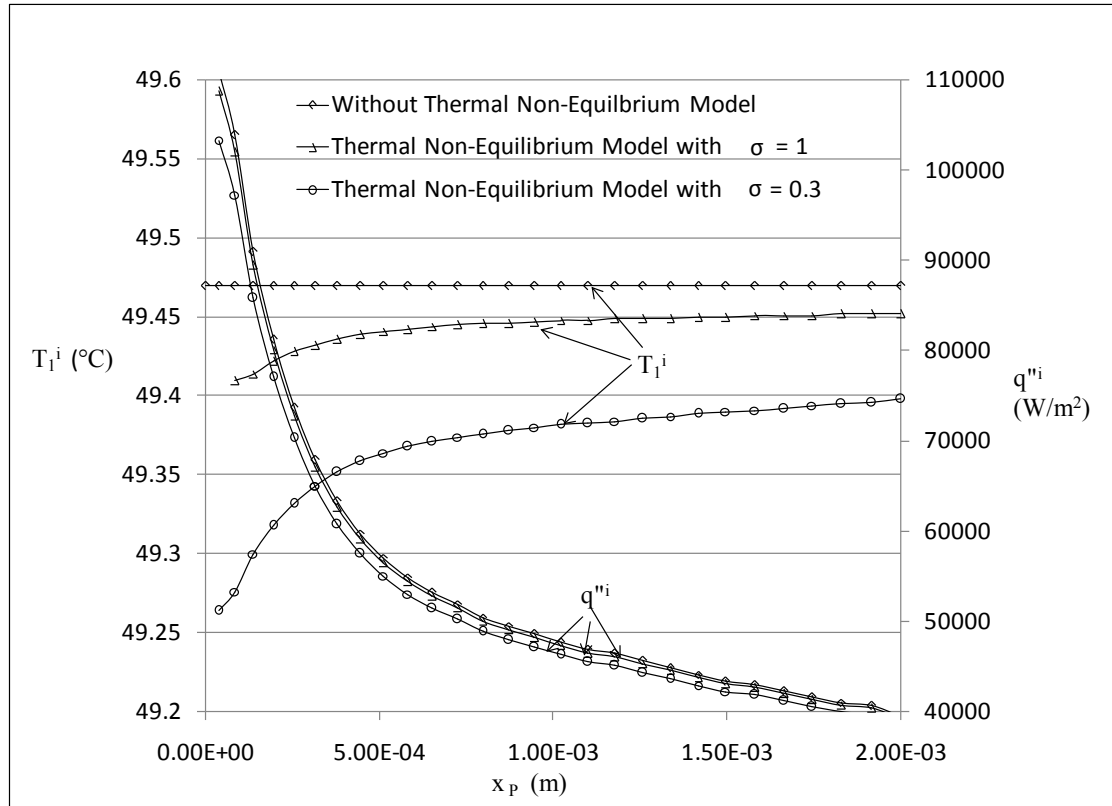
Figure 43: Effects of thermal non-equilibrium at the interface for a micro-meter scale internal condensing flow

For the flow of R-113 vapor through a vertical channel of 0.4 mm, vapor inlet speed Uin = 6 m/s, and $\Delta T = 3$ °C, this figure shows the effects of non-equilibrium thermodynamics at the interface. The temperatures on the liquid side of the interface and the heat flux values are plotted for three different cases: (i) without employing any non-equilibrium thermodynamic model, (ii) inclusion of an interfacial non-equilibrium thermodynamic model in Eq. (28) with $\hat{\sigma} = 1.0$, and (iii) inclusion of an interfacial non-equilibrium thermodynamic model in Eq. (28) with $\hat{\sigma} = 0.3$. The temperature on the vapor side of the interface $T_{sat} (p_2{}^i)$ was approximately constant at 49.47 °C. It is seen that there is a noticeable impact on the heat transfer rate because of the micro scale film thickness (around 5 microns). This is because heat-flux values and the temperature on the liquid side of the interface decrease after inclusion of effects of the non-equilibrium thermodynamic model.

119

Figure 42 results show that the influence of disjoining pressure is negligible on film thickness values (in 0 - 5 μm range) but has significant impact on interfacial pressure-difference values (5 – 15%). In Figure 42 the influence of interfacial thermal resistance is also negligible on film thickness values (in 0 - 5 μm range), but affects the heat transfer rate by 0.6 - 2.5% (if accommodation co-efficient $\hat{\sigma}$ is varied between 0.3 – 1.0).

The above reported computational approach for accounting for these effects is important because, in conjunction with suitable forthcoming experiments, this approach can be used for better and more precise estimation of the constants/equations that model these effects.

In addition to the micro-scale effects discussed above, these micro-scale flows are also prone to "quasi-steady parabolcity" and "elliptic sensitivity" effects discussed for macro-scale internal condensing flows in earlier sections. Investigation of these effects for micro-scale internal condensing flows is outside the scope of this thesis work.

4. 10 Regularity and Accuracy of the Computational Methods

For a computational solutions presented in section4 to be accurate, it needs to meet the following criteria: (i) satisfaction of the convergence criteria in the interior of each fluid (since finite volume SIMPLER technique is used, it means smallness of "b" defined on p.125 of Patankar [44]), (ii) satisfaction of all the interface conditions, (iii) grid independence of solutions for grids that are sufficiently refined, and (iv) unsteady

simulations' time varying predictions of the interface location should be free of computational noise in the absence of physical noise. The steady and unsteady simulations presented here satisfy all the above criteria.

The satisfaction of the governing equations in the interior and all the conditions at the interface is demonstrated in Liang et. al. [3]. Let the number of spatial grid lines $\left(n_i \times n_{j|L} \times n_{j|V}\right)_{I \text{ or } II}$ in grid-I or grid-II respectively indicate the number of grid lines over $0 < x < x_e$, $0 < y < \delta_{steady}(x)$, and $\delta_{steady}(x) < y < 1$ for the interface location at $t = 0$.
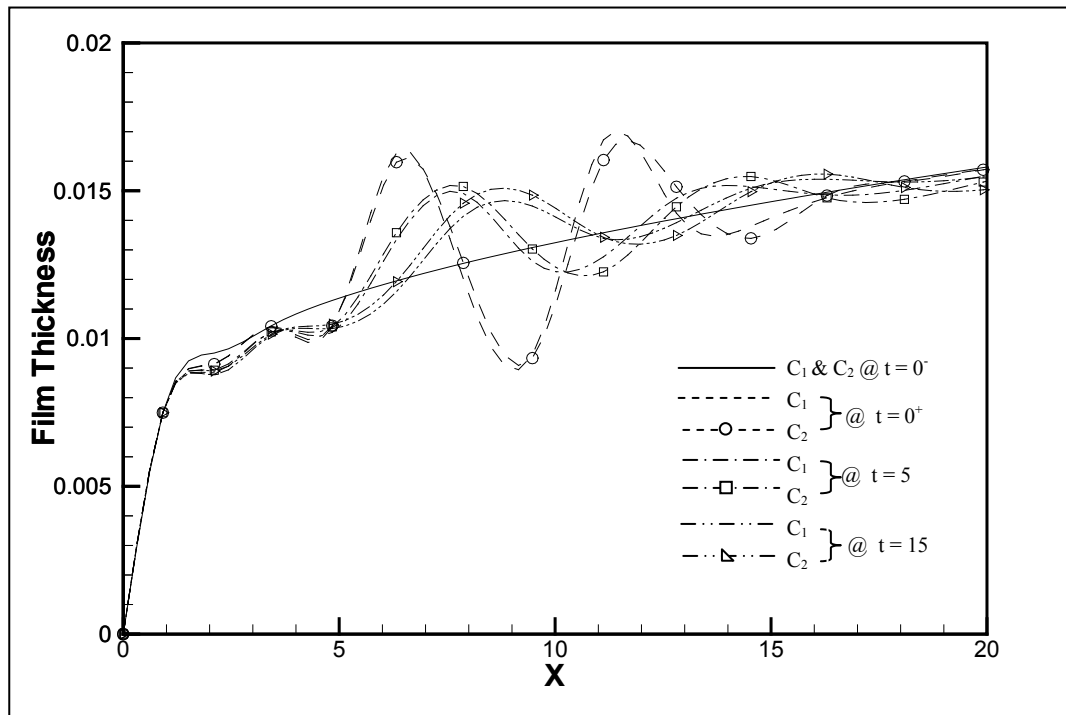
Figure 44: Figure showing grid independence of the solution in response to an imposed initial disturbance.

These numbers undergo minor changes as one marches forward in time in integer multiples of a time step Δt. We consider two different sufficiently refined choices of grid, viz. grid-I and grid-II, for computing the unsteady results in Figure 44. For these grids I and II, we have: $\left(n_i \times n_{j|L} \times n_{j|V}\right)_I \times \Delta t = \left(30 \times 30 \times 20\right) \times 2.5$ and $\left(n_i \times n_{j|L} \times n_{j|V}\right)_{II} \times \Delta t = \left(50 \times 50 \times 30\right) \times 5$. For these two refined grids, the combined sum of truncation and round off errors are minimized to a plateau level and the solutions in Figure 44 are seen to be grid independent to within 1–2%. For a technical estimate of total discretization error say for a representative flow variable, film thickness in Figure 44, the analysis leads to an approximate total error of around 3%. The error in other converged flow variables for this representative flow situation was found to be of the same order of magnitude (within 2-5 %).

Chapter 5 COMPUTATIONAL RESULTS FOR EXTERNAL CONDENSING FLOW OF A VAPOR CONDESNING OVER A FLAT PLATE[2]

After understanding features of shear driven *internal* condensing flows, to gain hitherto unavailable understanding of exact nature of steady and unsteady features of *external* condensing shear driven flows, an academic problem (see Figure 3) of vapor condensing over a flat plate (Koh's problem [10]) was thoroughly investigated ([8]) and compared with the analytical solution. The computational results are based on the formulation discussed in section 2.2.1. The formulation for the analytical solution is given in section 2.2.2.

5.1 Computational Results Obtained for Steady Solutions

5.1.1 Results Obtained for the Full Steady Problem and Comparison with Koh Solution [10]

Even though refrigerant R113's properties were used to run most of the computational simulations performed for this thesis work for external condensation,

---

[2] Some of the results described in this section have been published in: Kulkarni, S. D., A. Narain, S. Mitra, and L. Phan, 2010, "Forced Flow of Vapor Condensing over a Horizontal Plate (Problem of Cess and Koh*) - Steady and Unsteady Solutions of the Full 2D Governing Equations," ASME *Journal of Heat Transfer*, Vol. 132, pp. 101502:1-18. Please see Appendix A.6 for the copyright permission to reproduce these results in this thesis.

similar results are expected, in principle, for any non-metallic pure vapor flowing over a flat plate.

The Koh formulation [10] discussed in section 2.2.2 for computational domain in Figure 3 is best represented by solution of the steady problem under unspecified exit conditions (see eq. (19)) as described in section 2.2.1 After establishing near equivalence of solutions obtained by imposing exit conditions under formulations [A] and [B] of section-2.2.1, the formulation [B] is used here to obtain the computational solutions of the steady problem and to discuss their comparisons with the corresponding Koh solutions [10]. For a representative R113 flow case, specified by sufficiently fast $U_\infty = 2$ m/s, $x_e = 45$, $\Delta T = 5^\circ$ C, and $g_y = 0$, the results obtained from steady solution are shown in Figures 45-49. Figure 45 compares, for a representative case, non-dimensional film thickness values predicted by computational solution of the complete steady version of the formulation described in section 2.2.1 with the numerical solution of the Koh formulation [10] described in section 2.2.2.

It is seen that the computationally obtained values of film thickness are in good agreement with the classical similarity solution as the underlying boundary layer approximations for the Koh formulation [10] are approximately valid. For the case in Figure 45, comparisons of vapor and liquid u-velocity profiles and liquid and vapor temperature profiles as obtained from the two different solution approaches were found to agree with each other (not shown here for brevity).

Thus film thickness, velocity profiles, and the temperature profiles from the simulations are in good agreement with Koh's approximate solution. This establishes

that, for the ranges of vapor speeds investigated here, the solution obtained from Koh's similarity formulation (see section 2.2.2) yields film thickness, velocity, and temperature profiles with reasonable accuracy (e.g., both the formulations yield, as expected, linear velocity and temperature profiles in the liquid domain for the laminar condensate flow).

For the case in Figure 45, Figure 46 shows the non-dimensional pressure variation $\pi_2(x, y)$ for $0 \le x \le 45$ in the vapor domain al ong the x direction at $y = 0.8$ Note that, for the corresponding case in Figure 45, $\delta(x_e) < 0.8$.
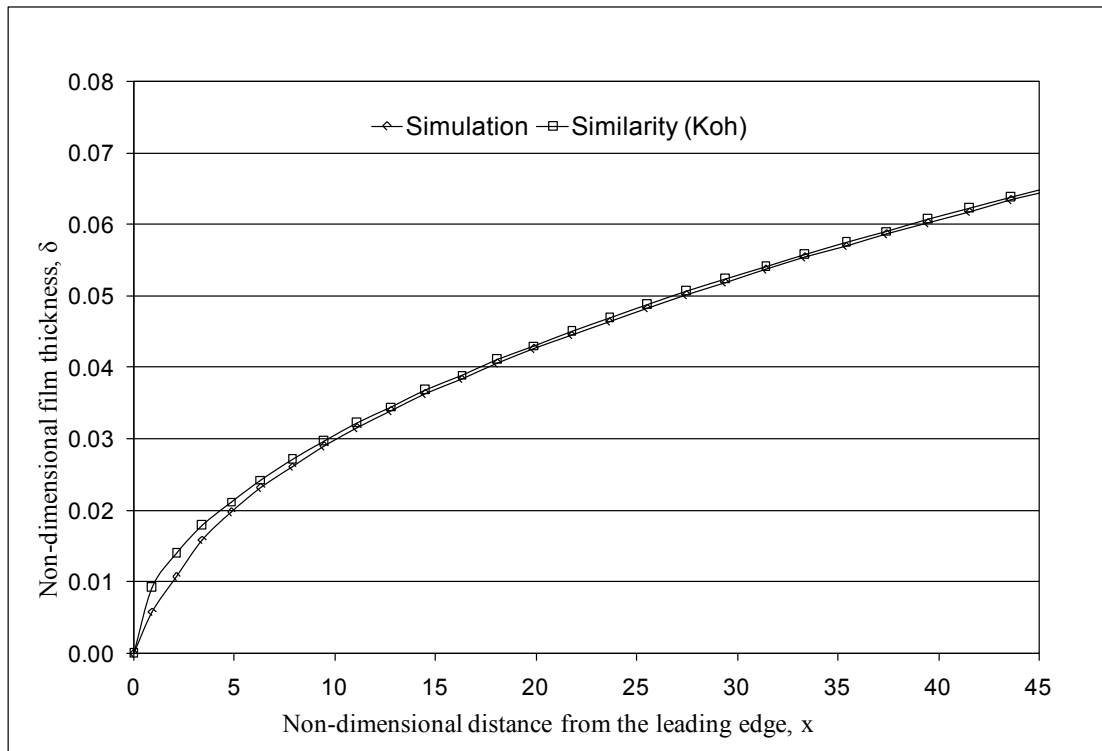
Figure 45: Comparison of film thickness profiles for steady solution of an external

condensing flow of vapor over a horizontal plate

For flow of R113 vapor with $U_\infty = 2$ m/s, $\Delta T = 5\,^oC$, $p_\infty = 1$ atm, $x_e = 45$, $g_y = 0$, and $Y_e = 0.004$ m, this figure compares non-dimensional film thickness (δ) values for the steady solution (obtained from solving the steady governing equations) with those obtained from Koh's similarity solution [10].

125

Figure 46: Pressure variation along the plate obtained from simulations for steady

solution of an external condensing flow of vapor over a horizontal plate

For the steady solution of Figure 45, this figure shows, at a fixed y = 0.8 location, computationally obtained variation of non-dimensional pressure π_2 with non-dimensional distance x.

The Koh formulation [10] in section 2.2.2 neglects the pressure gradient terms in the governing momentum equations but, as seen from Figure 46, there is a zone $0 < x \leq$ x* near the leading edge, up to which there exists a significant adverse pressure gradient that is needed to slow the vapor down by the amount that is consistent with the slow motion of the adjacent condensate and mass transfer across its interface. After this length x* (= x*/Y_e), pressure gradient $d\pi_2/dx$ reduces nearly to zero value and Koh's [10] assumption of uniform pressure is valid.

126
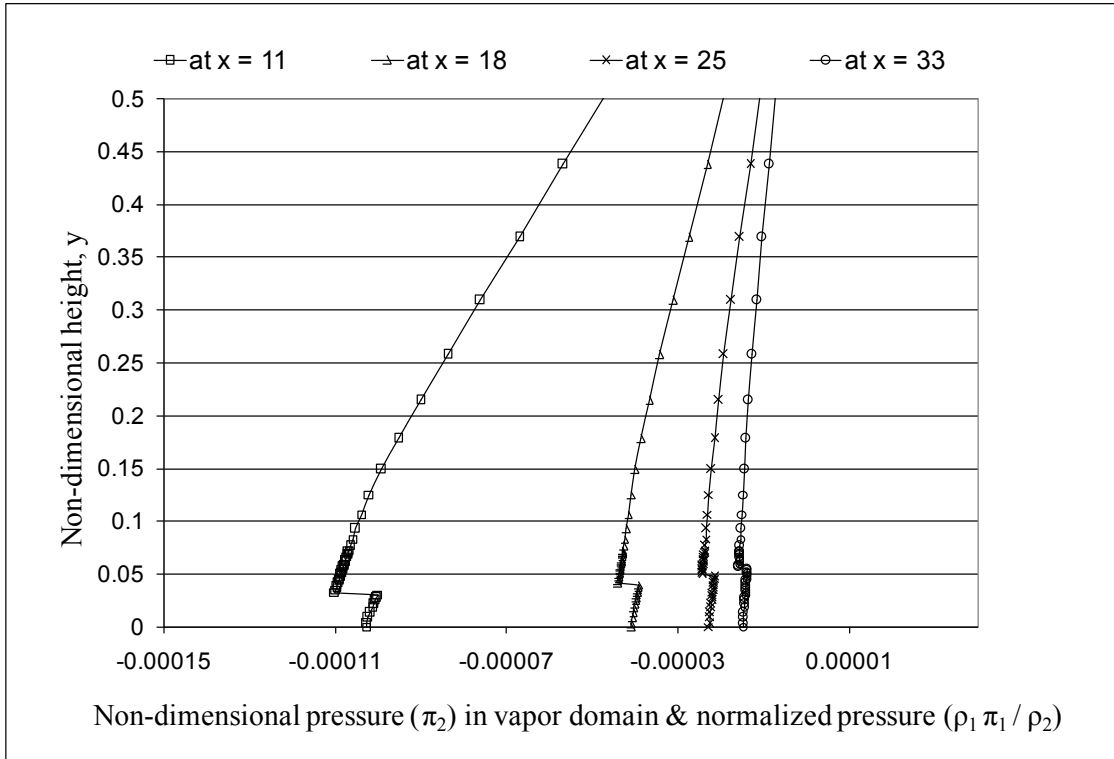
Figure 47: Pressure variation across the plate obtained from simulations for steady

solution of an external condensing flow of vapor over a horizontal plate

For the steady solution of Figure 45, Figure 47 shows computationally obtained y-directional variation of non-dimensional pressure π across different cross sections along the domain.

The pressure gradient in this frontal zone ($0 < x \leq x^*$) is very significant in determining the vapor and condensate dynamics for this horizontal condensing flow problem. As the vapor speed reduces, this pressure gradient is found to increase.

For the same case, the non-dimensional pressure profiles (values of $\pi_2(y)$ for $y \geq \delta(x)$ and values of $\rho_1\pi_1(y)/\rho_2$ for $0 \leq y \leq \delta(x)$) across the plate at different cross sections are shown in Figure 47. The pressure discontinuities across the interface in Figure 47 arise from the last two terms on the right side of Eq. (3) and are found to be inconsequential because of

127

their smallness. The cross-sectional pressure rise seen in Figure 47 over the same frontal part, is needed to provide the necessary centripetal acceleration for bending some of the streamlines (see Figure 48) towards the condensate. As seen from Figure 46, the pressure variations over the locations $x \gtrless x^*$ are insignificant as π_2 (x, y = 0.8) $\approx$ 0. In the computational results obtained from the formulation described in section 2.2.1, this bending of streamlines is assisted by pressure variations along and across the vapor domain as well as the variations in interfacial velocities (see, e.g., u_1^i variations in Figure 49). Unlike this solution of the full formulation, in the similarity solution obtained from the formulation summarized in section 2.2.2, the pressure and interfacial velocity variations are not present and the bending of the streamline is kinematically enforced by an assumed constant value of pressure, constant value of interfacial velocity ($u_1^i \approx u_2^i$) independent of x, and condensate thickness values constrained by Eq. (19). Though, in the frontal portion of the plate, the computational solution of the full problem significantly differs in its pressure predictions from the Koh solution [10] obtained under the assumption of constant pressure, the two solutions differ by less than 1 % in the important heat transfer rate controlling values of film thickness variation. This agreement (within 1-2%) for film thickness variations was found to be valid over a range of flow parameters ($2 \cdot 10^5 \leq Re_x \leq 6 \cdot 10^7$, $0.02 \leq Ja \leq 0.12$, $0.0052 \leq (\rho_2/\rho_1) \leq 0.00526$, $0.020 \leq (\mu_2/\mu_1) \leq 0.0212$, $7 \leq Pr_1 \leq 7.5$) investigated by during this research.

The differences in the pressure fields cause the differences between the simulation and the Koh solution in the converged values of the vertical and horizontal component of

condensate velocities at the interface viz. $v_1^i = v_1(x, \delta(x))$ (not shown) and in $u_1^i = u_1(x, \delta(x))$ shown in Figure 49.

Figure 49 shows a mismatch between the horizontal components of interfacial velocities as obtained by computational solution of the full steady problem and those obtained by the Koh similarity solution [10]. This mismatch occurs over a leading edge zone ($0 \leq x \leq x^*$) that is the same for which there is significant variation in vapor pressure field (see Figure 46).
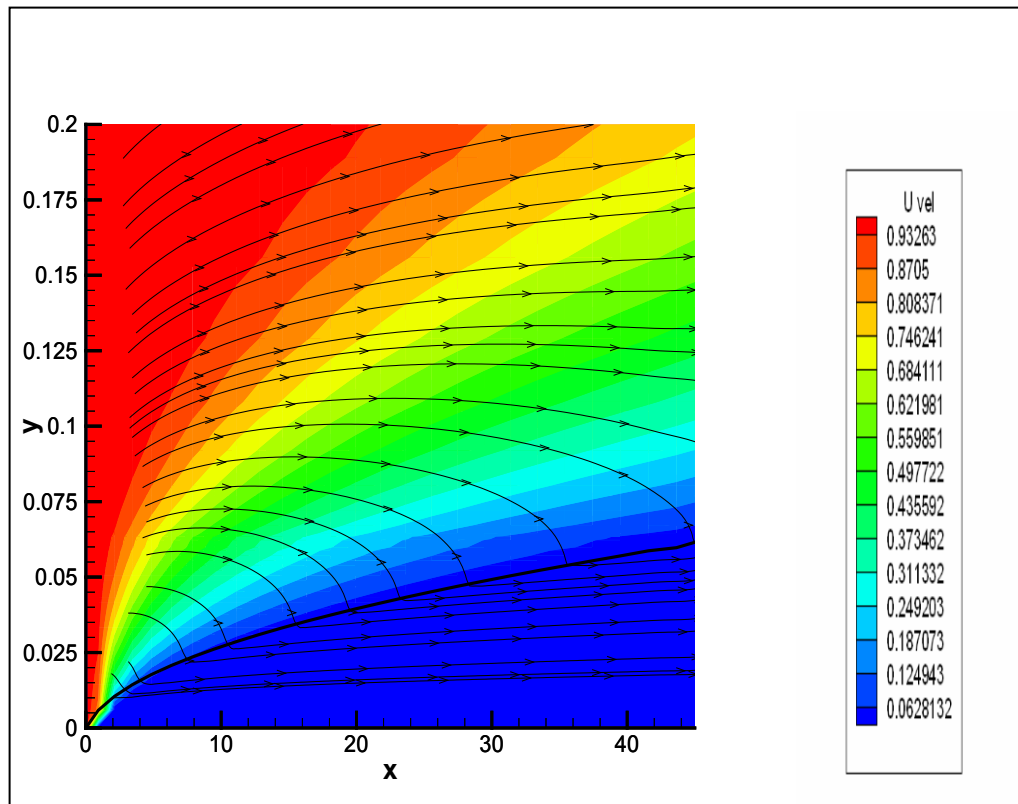
Figure 48: Streamline pattern obtained from simulation for steady solution of external condensing flow of vapor over a horizontal plate

The streamline pattern (Figure 48) obtained from computations has been compared with the streamline pattern obtained from the Koh solution [10] for the same case. Both of the patterns were found to be very similar to each other. It is seen that the streamlines bend at the interface and that this bending reduces at the interface as one moves further downstream in x direction. The background color in Figure 48 denotes the magnitude of x-directional component of velocity.
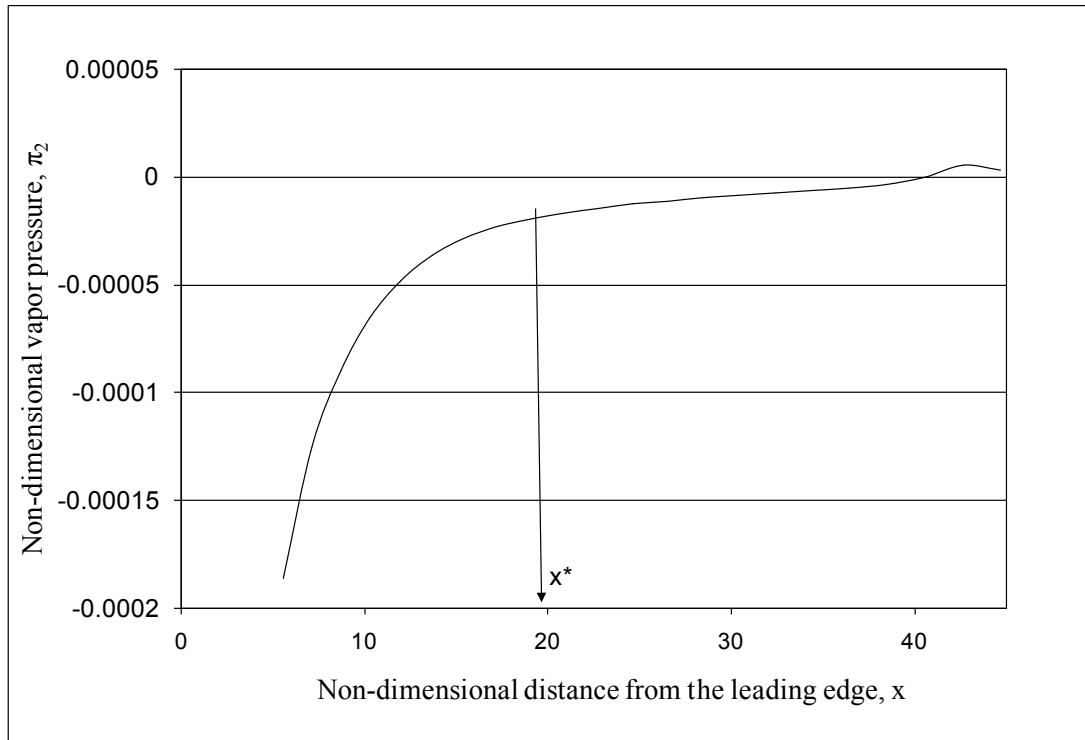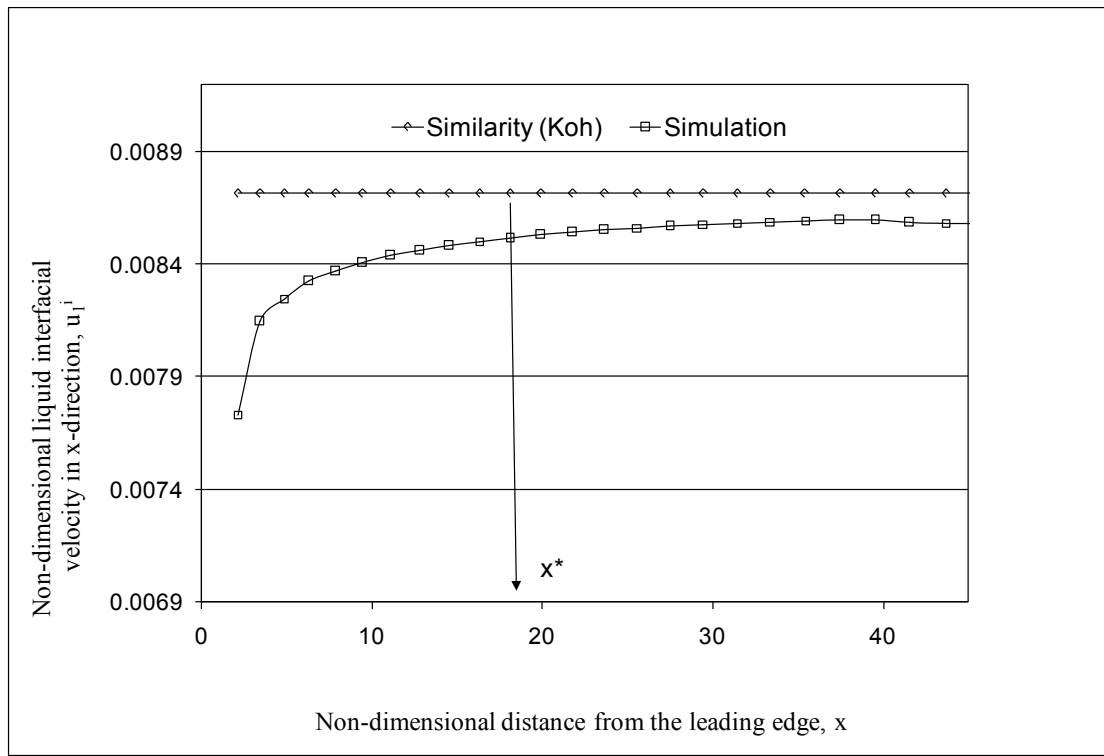

Figure 49: Comparison of liquid velocity profile in x-direction for steady solution of an external condensing flow of vapor over a horizontal plate

For the steady solution of Figure 45, this figure compares non-dimensional values of x-directional liquid velocities at the interface (u_1^i) as obtained from the similarity solution [10] with those obtained from the computational solution.

It is also found that, over the relatively short distances and vapor speeds considered for this research, the transverse component of gravity insignificantly affects the film thickness values and velocity profiles of the steady solution. The transverse component of gravity does, however, affect the condensate pressure profiles in the y direction and it is also known - from the results given [1] for internal condensing flows in horizontal channels – that transverse component of gravity does affect the flow at sufficiently long downstream distances once condensate thickness is "sufficiently" large. This version of the simulation tool developed for this external flow problem is not able to go far enough downstream to detect the phenomena we have observed, in [1], for internal flows in horizontal channels.

The above discussions for $U_\infty = 2$ m/s describe a region $0 \leq x \leq x^*$ (≈ 20) for which the pressure variations in the vapor phase (Figures 46-47) and interfacial speed u_1^i (Figure 49) differ from the Koh solution [10] and yet the film thickness variations in Figure 45 are close to the Koh solution [10] for all $x > 2$ and not just $x > 20$. If U_∞ is reduced, it is found that the value of x^* decreases, film thickness values increase, and the physical values of interfacial shear $S^i \approx \mu_1 (\partial u_1/\partial y)|^i$ also decrease as per Koh [10] predictions.

5.1.2 Numerical Accuracy and Regularities of the Computationally Obtained Solutions

The computational procedure for obtaining steady and unsteady solutions as described in section 3.2, was verified for accuracy and consistency with regard to different choices of the number of grid points as well as different choices of the

131

characteristic length Y_e appearing in Figure 3 and in the definition of non-dimensional parameters listed in Eq. (16).

Even though Figure 50 shows only the grid independence for the steady solution scheme employed here though similar grid independence has also been established for the reported unsteady solution scheme.
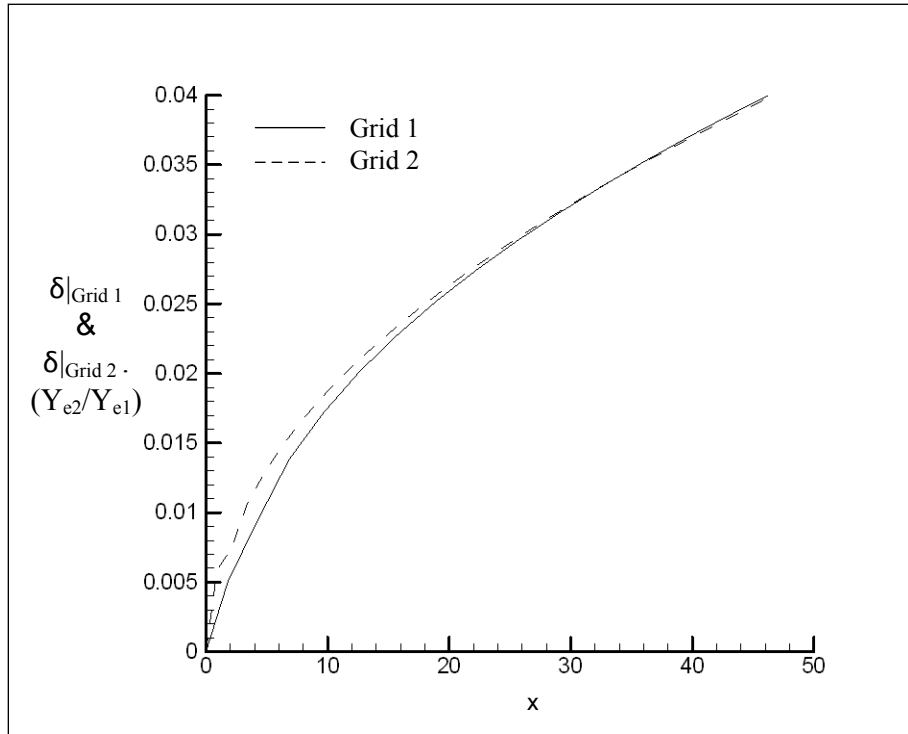
Figure 50: Grid independence of computational solutions for external condensing

flow of vapor on a horizontal plate

For flow of R113 vapor with $U_\infty = 2$ m/s, $\Delta T = 5\,^\circ C$, $p_\infty = 1$ atm, $x_e = 50$, and $g_y = 0$, this figure compares non-dimensional values of film thickness δ obtained from simulations for the same steady conditions under two different choices of grids (ni x nj) and domain heights Y_e. Grid 1 corresponds to the grid size of 30 x 50 with $Y_{e1} = 0.004$ m and Grid 2 corresponds to the grid size of 35 x 70 with $Y_{e2} = 0.008$ m. Non-dimensional values of δ and x for grid 2 are converted and compared in terms of grid 1 (by multiplying them by Y_{e2}/ Y_{e1}).

In Figure 50, film thickness variations for the same flow situation is computationally obtained for two different grids and two different choices of Y_e values. In Figure 50, $Y_e = 0.004$ m is used for "Grid 1" and $Y_e = 0.008$ m is used for "Grid 2." Furthermore, for "Grid 1" and "Grid 2," the number of grid points represented by "ni x nj" values (see Narain et al. [2]) are respectively given as 30 x 50 and 35 x 70.

Although Figure 50 only shows the nearly equal values of the two equivalent non-dimensional film thickness values, similar proximity of the two solutions was confirmed for velocity, temperature, and relative pressure profiles as well. From computational point of view, it should be observed that shear driven horizontal condensing flows, as opposed to gravity driven flows ([2] , [20], etc.), require more iterations to converge.

5.1.3 Other Comments/Results

Since the computational cases deal with high vapor velocities ($U_\infty = 0.2 - 20$ m/s), it is natural to ask whether the Koh [10] assumption of *laminar* nature of the vapor flow holds for the near interface region. Since the near interface vapor flow is qualitatively similar to a boundary layer flow with suction, it can be assumed that the transition to turbulence criteria for such boundary layer flows – as given by Eq. (17.10) of Schlichting [45] – will yield reasonable estimates for determining whether or not the vapor boundary layer flow in the Koh problem [10] is laminar or turbulent. The computationally obtained vapor boundary layer (momentum) thickness Δ_v values in the Koh solution as well as the values obtained from the computational solution was used to verify that Eq. (17.10) of [45], viz. $\rho_2 U_\infty \Delta_v(x)/\mu_2 \ll 70{,}000$, holds for all cases considered

133

here. That is, these vapor flows, because of the suction effects, appear to be strongly laminar at all x locations considered here. However, such vapor-phase boundary-layer stability arguments based on vapor suction rates, may miss "stability" or "noise-sensitivity" of the associated condensate motion and this must be separately assessed in determining attainability and waviness of these flows.

5. 2 Computational Results Obtained from Unsteady Solutions

5.2.1 Unsteady Simulation Results That Indicate the Domain and Attraction Rates of the Steady Solution

The unsteady computational solutions based investigations cover speeds U_∞ in a range of 0.2 m/s $< U_\infty <$ 20 m/s (for the reported R-113 and similar vapors) and, for temperature difference ΔT, a range of $3 - 15°C$ is covered. For this range, it is found that, if the unsteady solution was started at $t = 0$ from a reasonable initial guess for $\delta(x, 0)$, it would always seek a long–term time independent steady solution.

The long-term ($t \to \infty$) steady solution of the unsteady governing equations is found to be computationally equal (within 3 to 5% of computational error) to the steady solution obtained by solving the steady governing equations. This long-term ($t \to \infty$) steady solution obtained this way is termed an "attractor" (like the way it is done for internal condensing flows) because unsteady solutions starting at different initial guesses are attracted to it.

Though these solutions in Figure 51 show the existence of a steady attractor, it is observed that the phenomenon of attraction in Figure 51 shows a different attraction rate

to the steady solution at different downstream locations. The example shown in Figure 51 is for R-113 vapor at $U_\infty = 1.7$ m/s and $\Delta T = 5\degree C$.

In Figure 51, the unsteady solution is started at t = 0 with an initial guess of $\delta(x, 0)$ that is about 16% below the final attracting steady solution. A similar attracting behavior, though not shown here, exists if the initial guess was somewhat above the long-term steady solution.
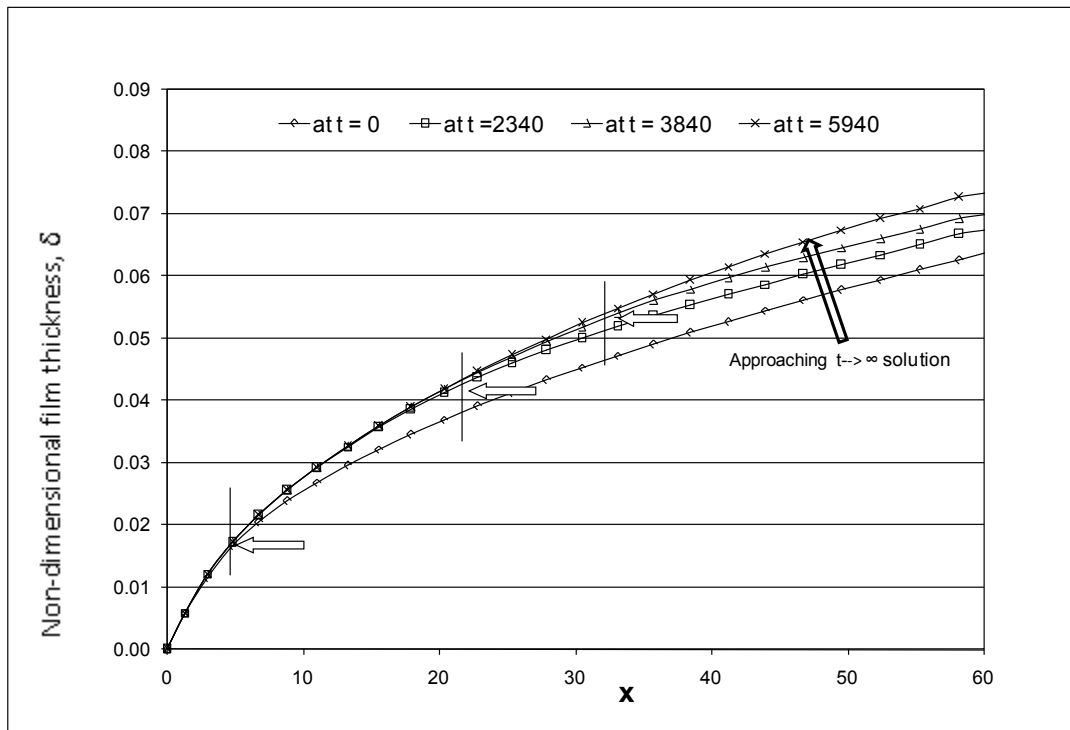
Figure 51: Computationally obtained attracting zones for steady solution of external condensing flow of vapor over a horizontal plate

For flow of R113 vapor with $U_\infty = 1.7$ m/s, $\Delta T = 5\degree C$, and $g_y = 0$, this figure shows non-dimensional film thickness values at different non-dimensional times given by the unsteady solution of the problem. An initial guess given at time t = 0 (about 16 % below the final long term solution) is seen to get attracted to the long term steady solution at different rates. The markings, at different times, demarcate the zones that have "nearly" converged to the steady solution from the zones that have not.
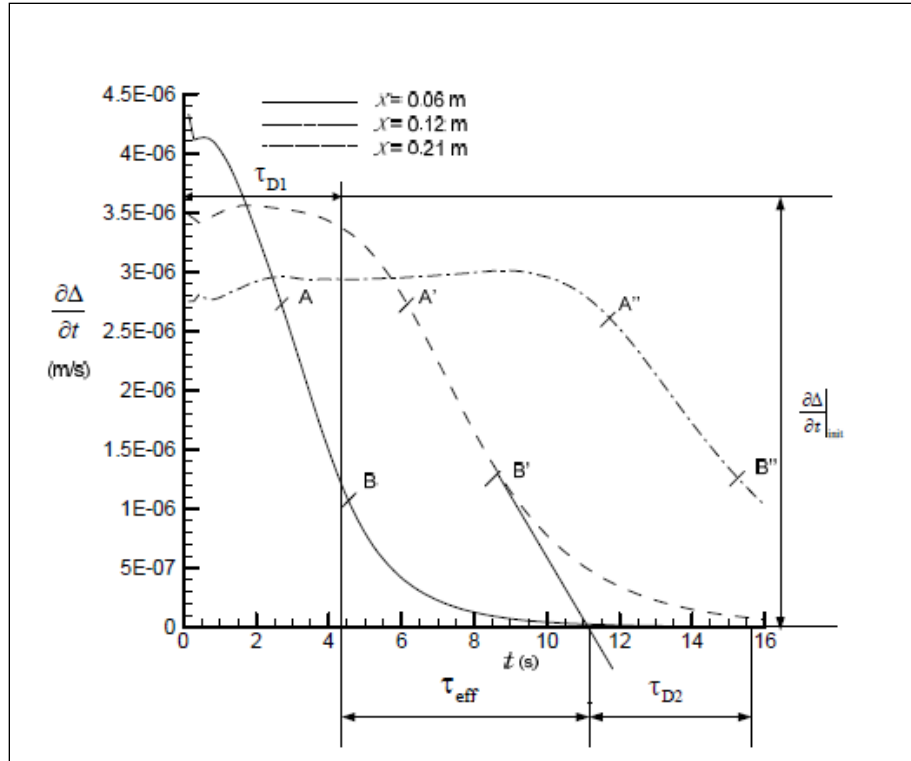
Figure 52: Rates of attraction at different x values for steady solution of external condensing flow of vapor over a horizontal plate

For flow of R113 with U_∞ = 1.7 m/s, ΔT = 5°C and g_y = 0, this figure shows different rates of attraction versus time - as indicated by different representative deceleration rates - for different x values along the length of the plate. The value of the initial attraction rate $\partial\Delta/\partial t$ (x,0) $\equiv$ $\partial\Delta/\partial t|_{init}$ as well as the "strength" of the attractors (as marked by the representative magnitude of deceleration rates associated with the slopes of the lines AB, A'B', etc.) decrease with increasing x. The initial guess of $\delta(x, 0)$ for the unsteady solution was 16% below the long term steady solution.

It is seen from Figure 51 that the attraction to the steady solution takes progressively longer times for locations that are farther and farther downstream of the inlet. The steady solution "attractor" in Figure 51 is said to have a "strength" which diminishes with x. Here, by "strength," one means the rate of steadily falling values of

136

$\partial\Delta/\partial t$ as indicated by representative slopes of "$\partial\Delta/\partial t$ vs. t" curves for different values of x

(these slopes are indicated by representative line segments AB, A'B', etc. in Figure 52).

As shown in Figure 52, for the no-noise unsteady simulation results at x = 0.12 m,

initial guess at any x has a delay time τ_{D1} over which the attraction speed$\partial\Delta/\partial t|_{init}$ does

not change by much.
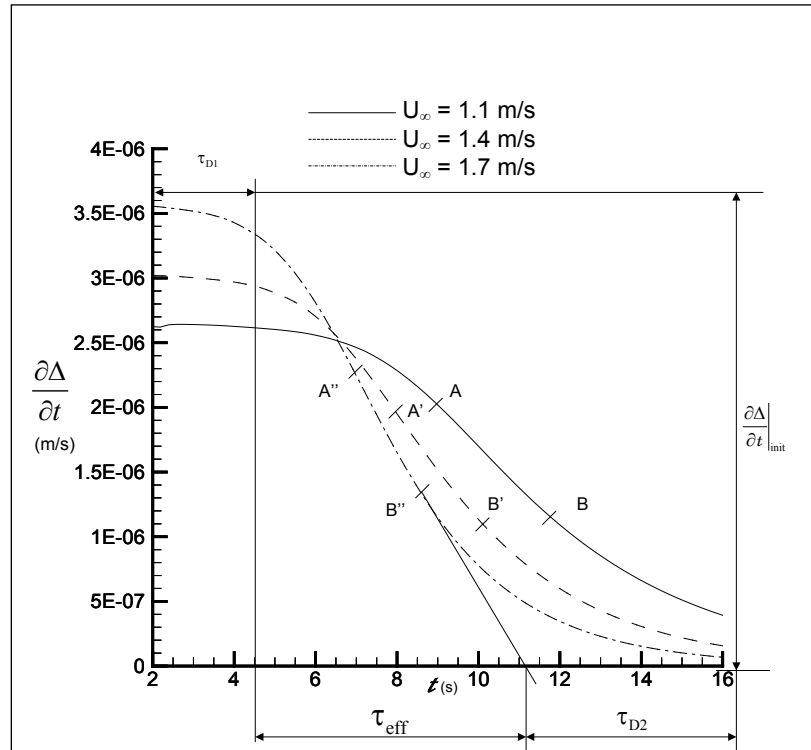
Figure 53: Rates of attraction at different vapor speed values for steady solutions of

external condensing flow of vapor over a horizontal plate

For flow of R113 with $\Delta T = 5°C$, $g_y = 0$, and x = 30, the figure shows different rates of attraction versus time - as indicated by different representative magnitudes of deceleration rates associated with the slopes of the lines AB, A'B', etc. - at different vapor speeds. The initial guess of $\delta(x,0)$ for the unsteady solution was 16% below the long term steady solution. The Figure demonstrates higher rates of attraction for higher speeds.

137
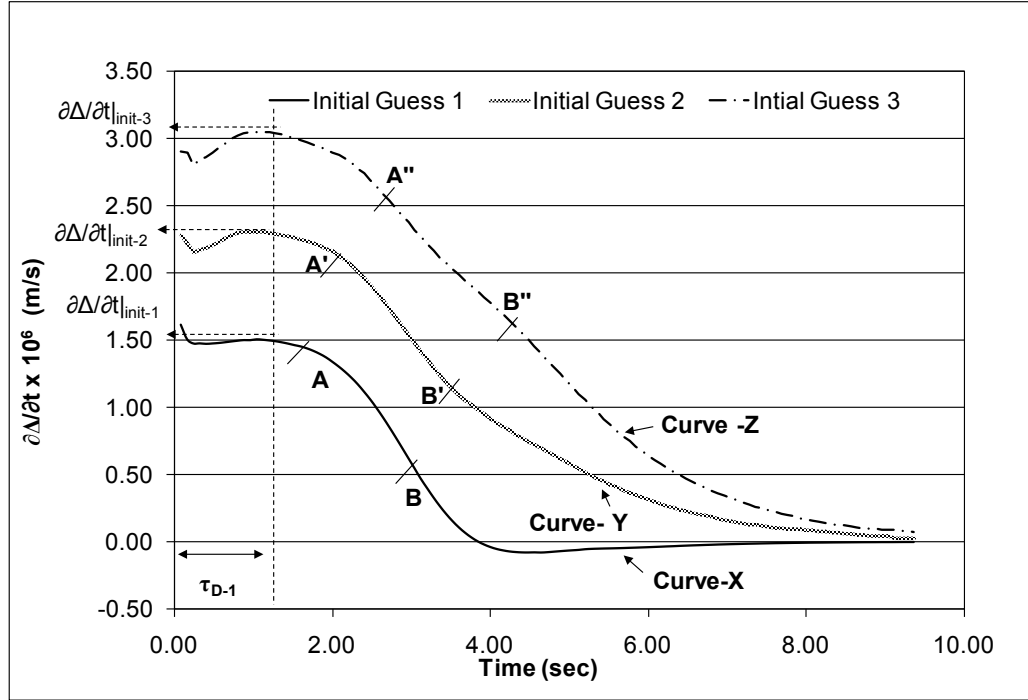
Figure 54: Characterization of attraction rate for external condensing flow of vapor

over a horizontal plate

This figure shows computationally obtained curves depicting the rate of change of film thickness at x = 23 when the unsteady solutions approach the same long-term steady attractor from three different initial guesses for flow of R-113 vapor at $U_\infty = 2$ m/s, $g_y = 0$ and $\Delta T = 5°$ C. The three initial guesses 1, 2, and 3 are respectively 2 %, 5 %, and 7 % away from the unique long-term steady attractor. The subsequent time duration (marked τ_{Rep}) over which a nearly constant deceleration rate ($\partial^2\Delta/\partial t^2$) exists is marked by nearly equal constant decelerating slopes of lines AB, A'B', A"B" on curves X, Y, and Z. This shows that for a given vapor speed, the above characterized attraction rates over τ_{Rep} are associated with the long term steady solutions rather than the values of the initial guesses.

Following this, over time duration τ_{eff}, there is a nearly constant representative

deceleration rate $\left|\partial^2\Delta/\partial t^2\right|_{Rep|(no-noise)}$ (termed "attraction rates" and measured by the slopes

of lines AB, A′B′, etc.). This deceleration rate is needed to impede the attracting solution

so it can reach a nearly steady ($\partial\Delta/\partial t \approx 0$) behavior over a subsequent time duration τ_{D2}.

138

Figure 53 shows "$\partial\Delta/\partial t$ vs. t" curves at x = 30 for three different vapor speeds. For all the speeds compared in Figure 53, initially guessed $\delta(x, 0)$ values were approximately 16 % below their corresponding long-term steady solutions. In Figure 53, it can be seen that the attraction rate $\left|\partial^2\Delta/\partial t^2\right|_{Rep|(no-noise)}$ increases with increasing speed U_∞ and, through Figure 52, it can be seen that the attraction rate decreases with downstream distance.

Figure 54 shows, at x = 23 and U_∞ = 2 m/s, "$\partial\Delta/\partial t$ vs. t" curves for different initial guesses. It is shown in this Figure that the "attraction rates" obtained over the time segment τ_{Rep} are, indeed, more or less independent of initial conditions and thus represent the inherent character of the attracting steady solution. This justifies use of the magnitude of deceleration rates - given by the approximate slopes of the line segments AB, A'B', etc. - as "attraction rates." The above described trends were established for R113 flows for a range of vapor speeds 0.2 m/s$\leq U_\infty \leq$ 20 m/s, a range of temperature differences 3˚C $\leq \Delta T \leq$ 15˚C, and a range of domain lengths $0 \leq X_e \leq$ 0.4 m.

5.2.2 Stability of the "Steady Attractors"/Steady Solutions to Initial Interfacial Disturbances

The long term steady limit of the unsteady solution was found to exist (and be the same as the steady solution of the steady problem) for this horizontal external flow problem if the inlet speed U_∞ was above a certain threshold value (about 0.2 m/s for the example case discussed here). These solutions were tested for their response to the initial disturbances on the interface. Different vapor speeds ranging from 0.2 to 25 m/s were

tested for interfacial disturbances of different non-dimensional wavelengths ranging from

5 to 30. Over the downstream distances investigated here, these external flows of vapor

were found to be quite stable to the forward moving disturbances on the interface -

whether or not transverse gravitational field was present.
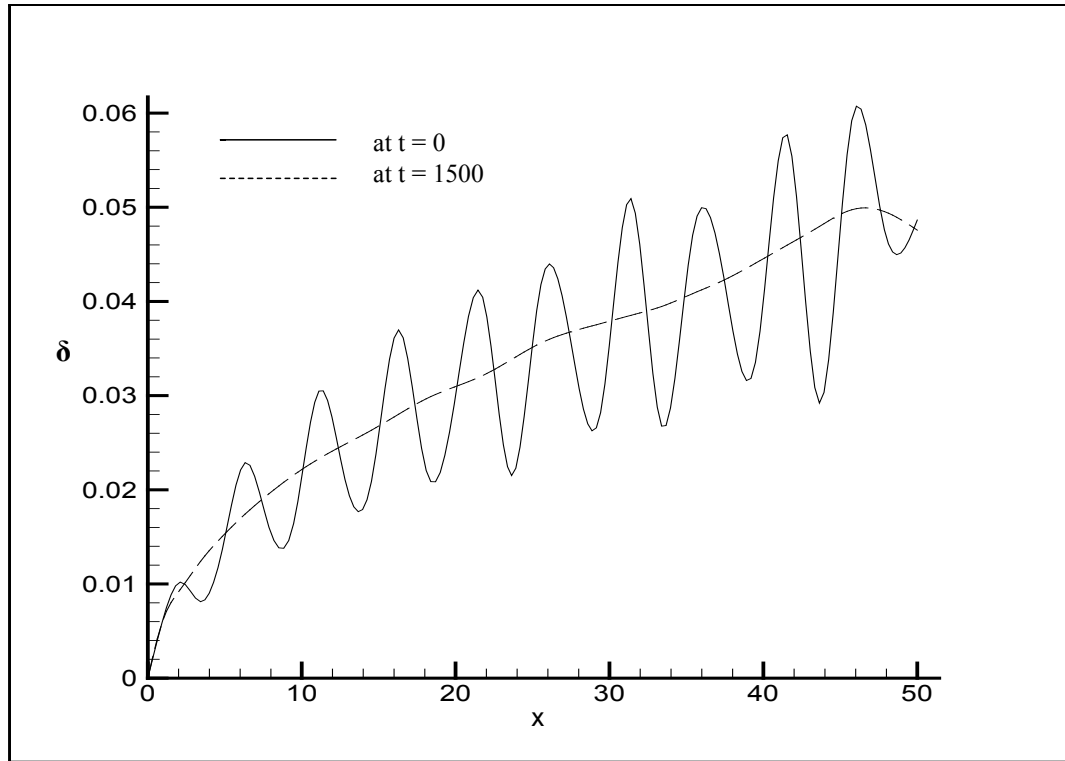
Figure 55: Dynamic stability investigation of external condensing flow of vapor over

a horizontal plate

For flow of R113 vapor with $U_\infty = 3$ m/s, $x_e = 50$, $\Delta T = 5^o$C, $g_y = 0$, this figure shows the stable response of the long term steady solution to the rather large initial disturbance given at time t = 0. The non-dimensional disturbance is given as $\delta(x, 0) = \delta_{steady}(x) [1 + \varepsilon_o \delta'(x, 0)]$, where $\delta'(x, 0) \equiv \sin(2\pi x/\lambda_o)$, $\varepsilon_o = 0.35$ and $\lambda_o = 5$. The disturbance dies out, almost completely, by the time t = 1500.

A representative example of this stable response to interfacial disturbances is shown in Figure 55 where - even in the absence of the transverse component of gravity - the large initial disturbances die out for the inlet vapor speed of $U_\infty = 3$ m/s and $\Delta T = 5^oC$.

Computations show very stable response to these disturbances and all of these disturbances die out as the waves move downstream. The response to imposed disturbances in the initial (t = 0) values of velocities (not shown here) was found to be similar to the ones in Figure 55. However the unsteady solutions, as expected, showed longer persistence (i.e. smaller "decay rates") in the weakly attracting (i.e. smaller "attraction rates") downstream portions of the flow. Recall that the measure of "attraction rates" was chosen over "decay rates" for this analysis because: (a) they are computationally easier to obtain, (b) they are physically meaningful even in the non-linear context (i. e. without the requirement of modeling time behavior by an exponential function of time), and (c) they also relate to physical attainability of steady flows. The response of the solution to disturbances when transverse downward component of gravity is present was also found to be equally stable because of the thinness of the film over the distances our computations could be implemented.

The above described response is different than the response [20] for the gravity driven external flow problem of Nusselt [28], where the gradually speeding condensate allows disturbances on the interface to grow only after a certain critical distance x and only for wavelengths $\lambda \geq \lambda_{cr}$, where λ_{cr} is a certain critical wavelength. For gravity-driven

141

flows, it was this inertial instability associated with speeding condensate that marked the transition from smooth laminar to wavy laminar flows. This typically happened when the condensate Reynolds number $\mathrm{Re}_\delta\ (\equiv 4\int_0^\Delta \rho_1 u_1(x,y).\mathrm{d}y/\mu_1)$ - which represents the size of inertia to viscous forces associated with fluctuations (a quantity which increases with x) - was computationally found to be higher than some critical value in the range of $20 \leq \mathrm{Re}_\delta \leq 40$. In contrast, the above described stable response for the Koh problem involved a much more weakly increasing Re_δ values with $\mathrm{Re}_\delta \leq 10$.

Therefore the reasons for this external flow showing very strong and stable response to initial disturbances are:

- The condensate flow is slow because it is not driven by gravity, and hence, the mechanism for the wave evolution on the interface is very different as compared to the gravity driven flows in which the liquid condensate accelerates.

- The well defined far field pressure prescription of p_∞ (along AB and BD' in Figure 3) and the process of condensation (mass transfer at the interface) make the flow more stable as compared to the known Kelvin Helmholtz instability (see [46] − [47]) for adiabatic (air water type) flows which do not involve gas-phase suction or mass transfer in to the liquid phase. As shown in Figure 55, this well known dynamic instability for adiabatic flows is truly suppressed. This suppression of Kelvin Helmholtz instability for the interface is over and above the earlier described issue of delayed transition to turbulence in the vapor boundary layer due to vapor suction effects.

142

Despite the fact that, in the presence of non-zero interfacial mass flux, these flows show no instabilities over the distances considered, one still expects that at larger downstream distances, the flow will undergo transition to waviness whether or not transverse gravity is present.

5.2.3 Sensitivity of "Attractors"/Steady Solutions to Persistent Condensing-Surface Noise and Stability Analysis

Irrespective of their stability to initial disturbances superposed on the interface, the stable solutions obtained for this external condensing flow over a horizontal plate are found to be sensitive to small and persistent condensing-surface noise of standing wave types - whose single representative Fourier component is modeled as shown in Figure 56. While response of condensing flows to these types of noise has been considered for internal condensing flows in [2]-[6] and also for an external condensing flow ([28]), this thesis reports, for the first time, a quantitative analysis of the resulting wave forms along with a quantitative measurement of the resulting noise-sensitivity. The ever-present miniscule condensing surface noise is assumed to have a standing wave pattern in transverse displacement of the plate (of the type indicated in Figure 56) with a representative Fourier component of the form:

$$\mathcal{D}_{w}(x,t) = \mathcal{D}_{max}\sin\frac{2\pi x}{\lambda_{p}} \cdot \cos 2\pi f_{p}t \tag{29}$$

where, λ_{p} ($\equiv \lambda \cdot Y_{e}$) is a physical wavelength ($\geq$ 0.02 m), f_{p} ($\equiv$ f·U_{∞}/Y_{e}) is a physical frequency (0 - 15 Hz), and $\mathcal{D}_{max}$ is a physical amplitude (0 − 5 μm) with which the condensing-surface is likely to vibrate under typical ever-present noise conditions that are

143

neither seen nor heard. The flow sees this noise through the following boundary condition for the vertical component of liquid velocity at the bottom wall location ($y = 0$):

$$v_1(x, 0, t) = v_{max}\sin(2\pi x/\lambda_p)\cdot\sin(2\pi f_p t). \tag{30}$$

Since, $v_1(x, 0, t) = \partial \mathcal{D}_w(x, t)/\partial t$, it follows that the amplitude v_{max} ($\equiv \varepsilon_w\cdot U_\infty$) in Eq. (30) above is related to $\mathcal{D}_{max}$ in Eq. (29) by

$$v_{max} = -2\pi\mathcal{D}_{max}f_p \ . \tag{31}$$

It has been established – by post processing the details of the resulting wave forms – that the response of the interface is of the form

$$\Delta(x, t) - \Delta(x)_{steady} = \{a(x)\sin[(2\pi x/\lambda_p) + \gamma_0(t)]\cdot\cos[(2\pi f_p t)+\psi_0(x)]\}, \tag{32}$$

where, $a(x)$ is the x-dependent amplitude of the resulting standing wave pattern on the interface.

Thus, waves on the interface, in response to the bottom wall noise, do have the same spatial wavelength λ_p and temporal frequency f_p as that of the displacement noise component $\mathcal{D}_w(x, t)$ experienced by the condensing-surface. However, the phases of the interfacial waves slightly differ from that of the condensing-surface's transverse displacement wave. The spatial phase difference is time dependent and is denoted by "$\gamma_0(t)$" and the temporal phase difference is location dependent and is denoted by "$\psi_0(x)$."

Figure 57 shows the unsteady interface at different times in response to the representative condensing-surface noise. For the cases considered in this research, over a wide range of different affecting parameters, it is found that the amplitude $a(x)$ of these interfacial waves increases with x and can be determined.

144
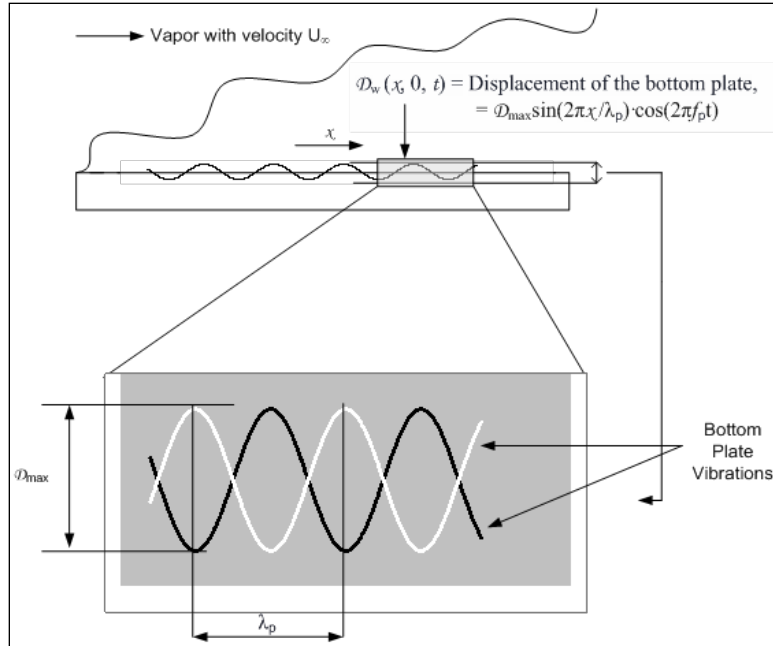
Figure 56: A schematic defining structure of ever-present condensing wall

This figure depicts the definition of the type of miniscule ever-present noise given to the condensing surface to investigate the sensitivity of condensing flows to persistent disturbances. The inset shows the displacement profile of the condensing surface at two out-of-phase instants associated with a mode of the standing wave.

However spatial phase difference function $\gamma_0(t)$ is a sufficiently weak function of time and the temporal phase difference $\psi_0(x)$ is a sufficiently weak function of space that they cannot be determined, with sufficient precision, with the help of the simulation tool employed here. The spatially growing noise-induced waves are expected to be related to Re_δ values – which represents both the cross-sectional liquid mass-flux and the effects of local interfacial mass-flux $\dot{m}$. The noise-sensitive values of the amplitudes a(x) ($\equiv$ $a(x)/Y_e$) of these interfacial waves were computationally obtained for different flow cases for a range of different non-dimensional parameters viz. wavelength λ ($\equiv$ λ_p/Y_e), bottom

145

wall velocity amplitude ε_w ($\equiv v_{max}/U_\infty$), and frequency f (f$\equiv$ $1/T_w$ $\equiv$ $f_p \cdot Y_e/ U_\infty$). The amplitude $a(x)$ values were measured by looking at several peak values of computationally obtained "$\delta(x,t) - \delta(x)_{steady}$" signals in the space-time domain.
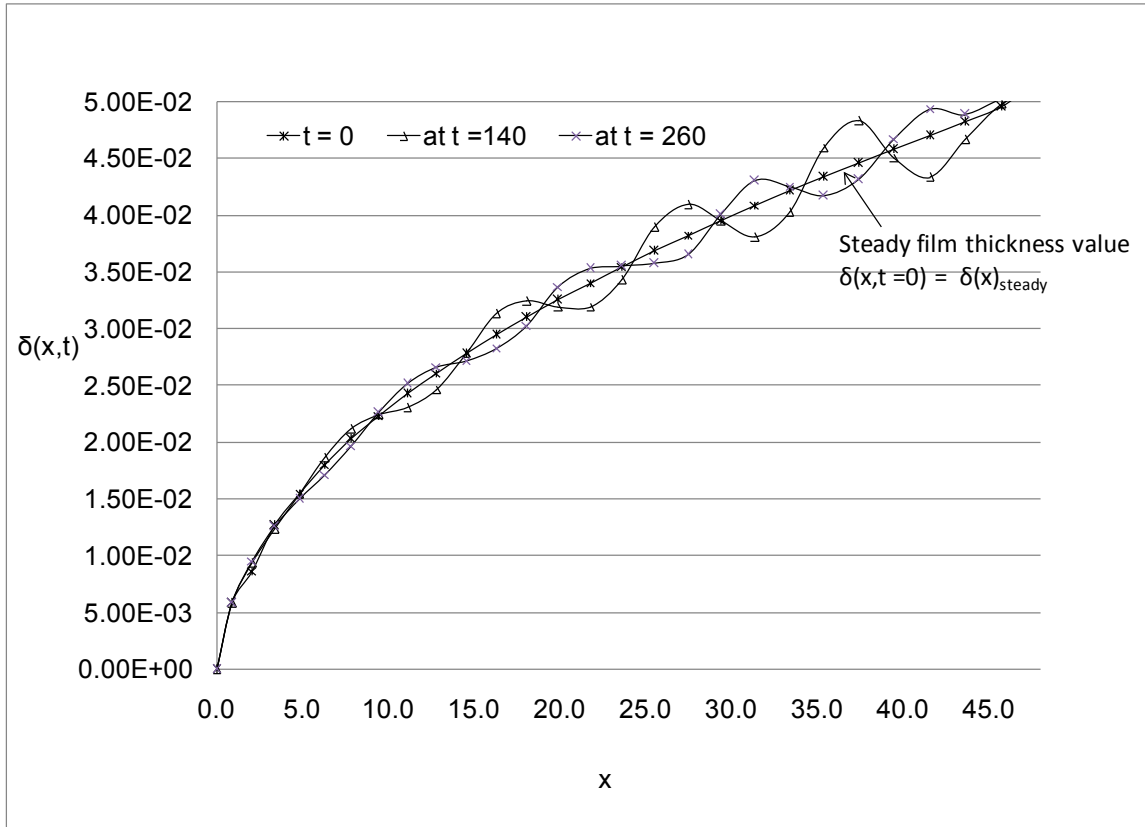
Figure 57: Response of external condensing flow of vapor over a horizontal plate to the ever-present minuscule condensing surface vibrations

For R113 vapor with $U_\infty = 3$ m/s, $x_e = 48$, $\Delta T = 5^oC$, $g_y = 0$, this figure shows unsteady response of the flow to the typical condensing surface noise with λ ($\equiv$ λ_p/Y_e) = 10, T_w ($\equiv$ $U_\infty/(f_p \cdot Ye)$) = 240, ε_w ($\equiv$ v_{max}/U_∞) = 3$\cdot$10^{-6}. The noise given to the condensing surface is represented as $v_1(x, 0, t) = v_{max}\sin(2\pi x/\lambda_p)\cdot\sin(2\pi f_p t)$, where $v_1(x, 0, t)$ is condensing surface velocity. Figure shows non-dimensional film thickness $\delta(x,t)$ plotted vs. x at two different non-dimensional times t = 140 and t = 260. The steady film thickness values $\delta(x)_{steady}$ are shown as an initial solution at time t = 0.
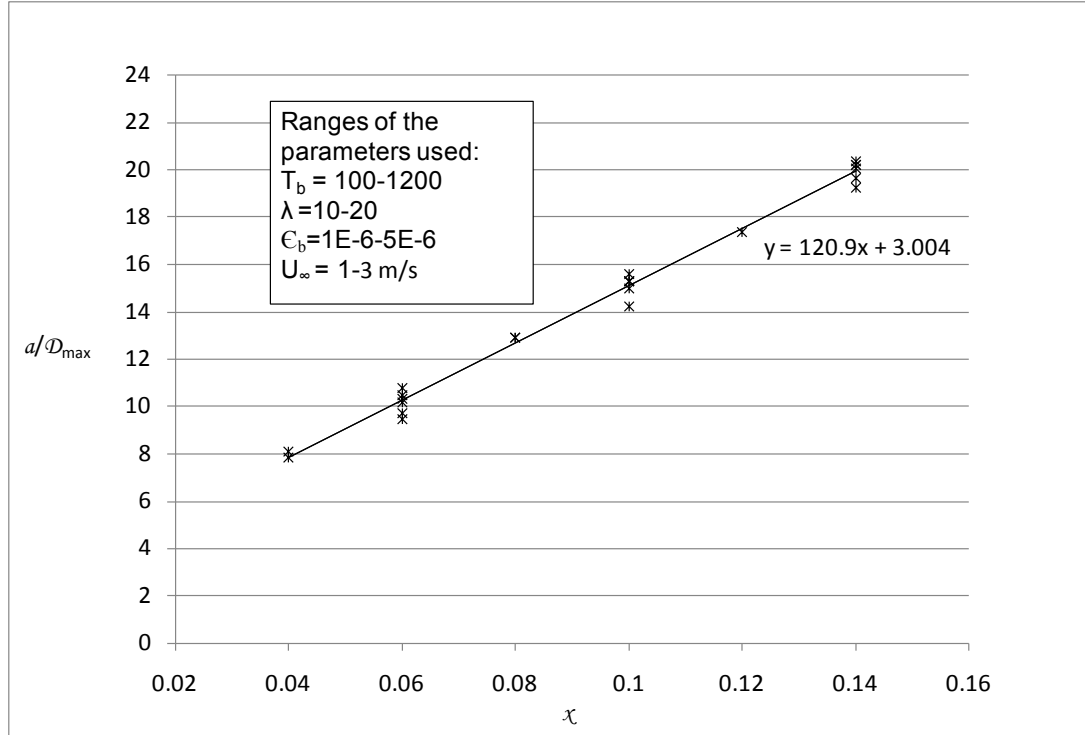
Figure 58: Growth rate of amplitude of interfacial wave in response to the ever-present noise for an external condensing flow of vapor over a horizontal plate

For different ranges of condensing surface noise parameters, namely: time period T, wavelength λ, and condensing surface velocity vibration amplitude ε_w, and different vapor speeds U_∞; this figure plots computationally obtained non-dimensional $a/\mathcal{D}_{max}$ values (amplitude of interfacial waves divided by amplitude of bottom wall displacement waves) against dimensional values of $\chi (= x \cdot Y_e)$. The range of R-113 vapor (with $g_y = 0$) flows considered here is described in the inset.

After obtaining the values of $a(x)$ at different χ locations, for different flow cases involving different $\mathcal{D}_{max}$ values , linear curves – as in Figure 58 - were found to be adequate fits to the data of a(x) over the range of distances considered. This linear relation can be expressed as

$$a(\chi)/\mathcal{D}_{max} = \overline{c_1} \chi + c_2 \qquad (33)$$

147

where $\bar{c}_1$ and c_2 are respectively found to be 120.9 (m^{-1}) and 3.00 for R-113 flow parameters indicated in the inset of Figure 58.

If the intrinsic characteristic speed definition $U_{Char} = h_{fg}^{1/2}$ and characteristic length definition $L_{Char} = \mu_1/(\rho_1 \cdot h_{fg}^{1/2})$ are used, Eq. (33) is rewritten in the following non-dimensional form:

$$a(x)/\mathcal{D}_{max} = c_1(x/L_{Char}) + c_2,\tag{34}$$

where $c_1 \equiv \bar{c}_1 \cdot L_{Char} = 1.1 \cdot 10^{-7}$, $c_2 = 3.00$, and

$$x/L_{Char} \equiv x\rho_1 h_{fg}^{1/2}/\mu_1 = Re_x/u^*,\tag{35}$$

where $Re_x = \rho_1 U_\infty x/\mu_1$ and $u^* = U_\infty/h_{fg}^{1/2}$. Combining equations (34)-(35), the result in Figure 58 is summarized by the following important non-dimensional form of Eq. (34):

$$a(x)/\mathcal{D}_{max} = \Phi \cdot Re_x + c_2\tag{36}$$

where, $\Phi \equiv (c_1/u^*)$, $c_1 = 1.1 \cdot 10^{-7}$, and $c_2 = 3.00$.

By looking at the parameter variations considered for Figure 58, it is easy to conclude that the reported values of constants c_1 and c_2 in Eq. (34) can, at most, depend on passive fluid parameters ρ_2/ρ_1, μ_2/μ_1, and Pr_1. Figure 59 shows three different curves C_1, C_2, and C_3 representing $a(x)/\mathcal{D}_{max}$ vs. Re_x for three different non-dimensional vapor speeds u^* (corresponding to $U_\infty = 1$ m/s, 2 m/s, and 3 m/s).

It can be seen that for the same set of fluid parameters (μ_1, ρ_1, etc.) that correspond to the same value of the constants c_1 and c_2 in Eq. (34), as the vapor speed U_∞ reduces the rate of growth of $a(x)/\mathcal{D}_{max}$ (denoted by the slope value Φ) with respect to Re_x increases (in Figure 59, $\Phi_1 < \Phi_2 < \Phi_3$).
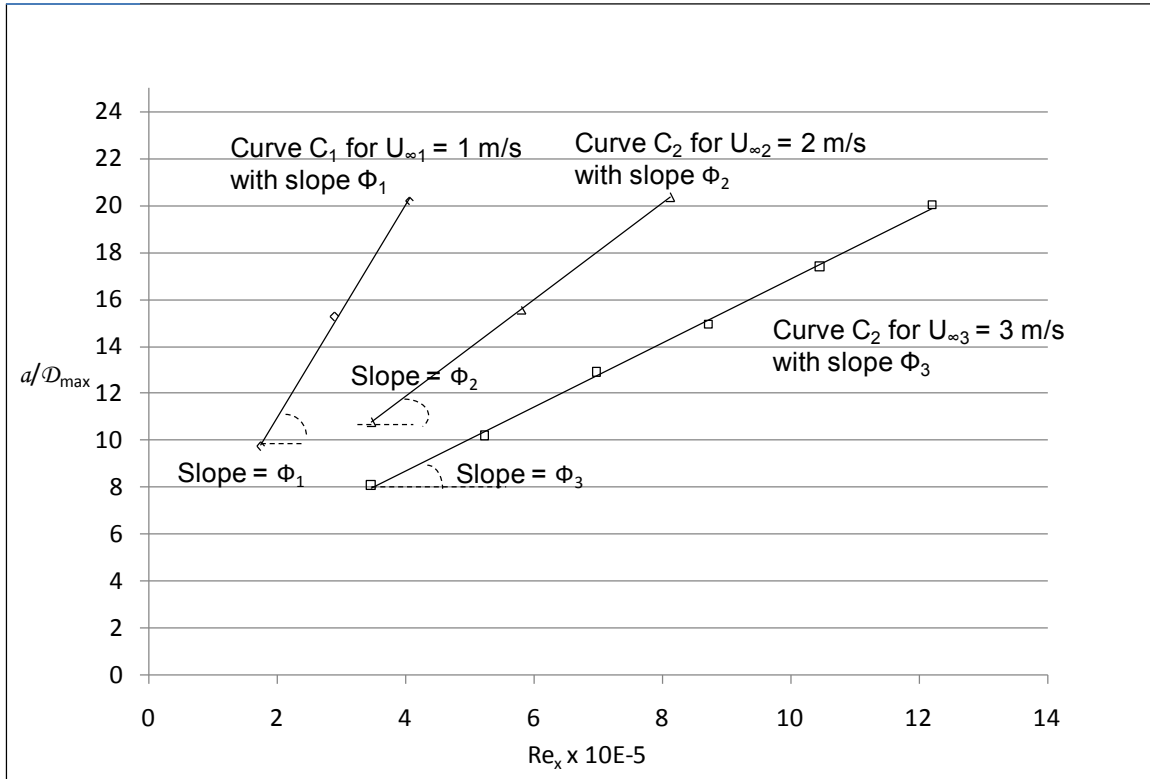
Figure 59: Effects of vapor speed on growth rate of interfacial wave amplitude in response to the ever-present noise for an external condensing flow of vapor over a horizontal plate

For different cases considered in Figure 58, this figure plots computationally obtained $a/\mathcal{D}_{max}$ values (amplitude of interfacial waves divided by amplitude of bottom wall displacement waves) vs. Re_x (= $\rho_1 U_\infty x/\mu_1$) for different vapor speeds U_∞. Three curves C_1, C_2 and C_3 have different slopes Φ_1, Φ_2, Φ_3 such that the slope value Φ increases while speed U_∞ decreases. The ranges of T_b, ε_b, and λ values are same as in the inset of Figure 58.

Retrospectively, Eqs. (33)-(36) summarize the important wave amplitude growth relation obtained from computational experiments. But it leaves the question open as to what combination of local physical variables bring about the presence of the physical variable x in Eq. (33) so as to make the right side of Eq. (33) independent of changes in

149

U_∞ and ΔT (see Figure 58). We conjecture that x in Eq. (33) represents the ratio of

$\dot{M} / \dot{m}$, where $\dot{M} \equiv \int_0^\Delta \rho_1 u_1 \cdot dy \equiv \int_0^x \dot{m} \cdot d\chi$ is the cross sectional liquid mass-flux associated

with the underlying steady flow and $\dot{m}$ is associated interfacial mass-flux. This conjecture

is based on the fact that $\chi = (\frac{1}{2}) \cdot \dot{M} / \dot{m}$ because $\dot{m} \cong k_1 [\Delta T / \Delta(\chi)] \cdot [1 / h_{fg}]$ and $\Delta(x)$

approximately satisfies Eq. (23). Since both $\dot{M}$ and $\dot{m}$ scale linearly with U_∞ and ΔT,

this conjecture seems to be a valid generalization for the variable χ appearing in Eq. (33).

Since Figures 58-59 establish nature of spatially growing interfacial waves in response to ever present noise, one needs to address: (i) the issue of *waviness* with an intent to identify the downstream zones for which wave-amplitudes are sufficiently large relative to the mean thickness (say > 15%) and, therefore, one cannot effectively treat the underlying laminar flow as essentially smooth; (ii) the issue of onset of *turbulence* which requires identification of downstream zones, where the various noise-induced waves will grow so much beyond 15% of the amplitude that they will non-linearly superpose to define a steady-in-the mean flow which is fundamentally different from the underlying smooth and steady laminar attractor.

In the above context, when attractors are attainable over $U_\infty > U_\infty^*$ (see next section for computational value of this lower speed), it is meaningful to characterize *waviness* by comparing the steadily growing amplitude $a(x)$ of interfacial waves to the local steady film thickness $\Delta(x)$ values. The steady local film thickness values are predicted with good accuracy by Koh's analytical solution [10] and are well correlated by

150

the following approximate correlations (given by Fujii and Uehara in [48] and utilized by

Rose in [24]):

$$\Delta(x)/x = [0.45\text{Re}_x^{1/2}(1.2 + G^{-1})^{1/3}]^{-1}, \quad 0.1 \leq G \leq 10 \tag{37}$$

where $\text{Re}_x (\equiv \rho_1 U_\infty x /\mu_1)$ is called the local Reynolds number, and $G \equiv [\text{Ja} /\text{Pr}_1][(\rho_1\mu_1/\rho_2\mu_2)^{1/2}]$.

In order to obtain a criterion for determining $\text{Re}_{x|wavy\text{-}cr}$ values such that $\text{Re}_x > \text{Re}_{x|wavy\text{-}cr}$

implies:

$$a(x)/\Delta(x) \geq 0.15, \tag{38}$$

Eq. (36) and (37) can be combined and written in the form:

$$a(x)/\Delta(x) = \mathcal{D}^*_{max}\cdot\psi(\text{Re}_x, G, u^*) \tag{39}$$

where

$$\mathcal{D}^*_{max} \equiv \mathcal{D}_{max}\cdot\rho_1\cdot h_{fg}^{1/2}/\mu_1, \tag{40}$$

and

$$\psi(\text{Re}_x, G, u^*) \equiv c_1\cdot[0.45\text{Re}_x^{1/2}(1.2 + G^{-1})^{1/3}] +[c_2\cdot\{0.45\text{Re}_x^{1/2}(1.2 + G^{-1})^{1/3}\}/\{\text{Re}_x/u^*\}].$$

$$\tag{41}$$

Since the relative interfacial wave amplitude $a(x)/\Delta(x)$ depends strongly on the

value of displacement wave amplitude $\mathcal{D}_{max}$, it is only meaningful to compare these

values at the same values of $\mathcal{D}_{max}$. For ever-present miniscule bottom wall vibrations

involving $\mathcal{D}_{max}$ values of $1 - 2$ microns, the value of $\mathcal{D}^*_{max}$ ranges, for R-113 cases, from

1000–2000. In this thesis work, therefore, $\mathcal{D}^*_{max} = 2000$ will be considered the

characterizing level of maximum condensing-surface noise present and will be used in

the waviness characterization criterion given by Eq. (38).

Choosing $\mathcal{D}^*_{max} = 2000$, for a representative flow of R-113, corresponding to u* = 0.0079 ($U_\infty = 3$ m/s) and (5°C < ΔT < 100 °C), a plot of $\psi \equiv (1/\mathcal{D}^*_{max}) \cdot a(x)/\Delta(x)$ versus Re_x is shown in Figure 60. Figure 60 shows an increase with Re_x in the values of the relative amplitude $a(x)/\Delta(x)$. The criterion given by Eq. (38) results in

$$5 \cdot 10^5 \leq Re_{x|wavy-cr} \leq 14.25 \cdot 10^5, \tag{42}$$

for the range of G values ($0 \leq G \leq 10$) con   sidered. It is clear from Figure 60 that $Re_{x|wavy-cr}$ for a given value of u* = 0.0079, and D^*_{max} = 2000, depends on the value of G and can be written as $Re_{x|wavy-cr} = Re_{x|wavy-cr}(u^*, D^*_{max}, G) = \tilde{Re}_{x|wavy-cr}$ (G). The graph of this $\tilde{Re}_{x|wavy-cr}$ (G) as function of G, for a constant value of u*, is shown in Figure 59.

For G = 1 ($\Delta T \approx 10°$ C) and D^*_{max} = 2000, and a range of u* values from 0.00132 to 0.0132 ($U_\infty = 0.5$ m/s to 5 m/s), a plot of $\psi \equiv (1/\mathcal{D}^*_{max}) \cdot a(x)/\Delta(x)$ versus Re_x is shown in Figure 62. Figure 62 also shows an increase in the values of the relative amplitude $a(x)/\Delta(x)$ with Re_x. For the range of u* values (0.00132 to 0.0132) considered, the criterion given by Eq. (38) results

$$6.25 \cdot 10^5 \leq Re_{x|wavy-cr} \leq 12.75 \cdot 10^5, \tag{43}$$

It is clear from Figure 62 that $Re_{x|wavy-cr}$ for a given value of G = 1 and D^*_{max} = 2000, depends on the value of u* and can be written as $Re_{x|wavy-cr} = Re_{x|wavy-cr}(u^*, D^*_{max}, G) = \hat{Re}_{x|wavy-cr}$ (u*). The graph of this $\hat{Re}_{x|wavy-cr}$ (u*) as function of u*, for a constant value of G, is shown in Figure 63.
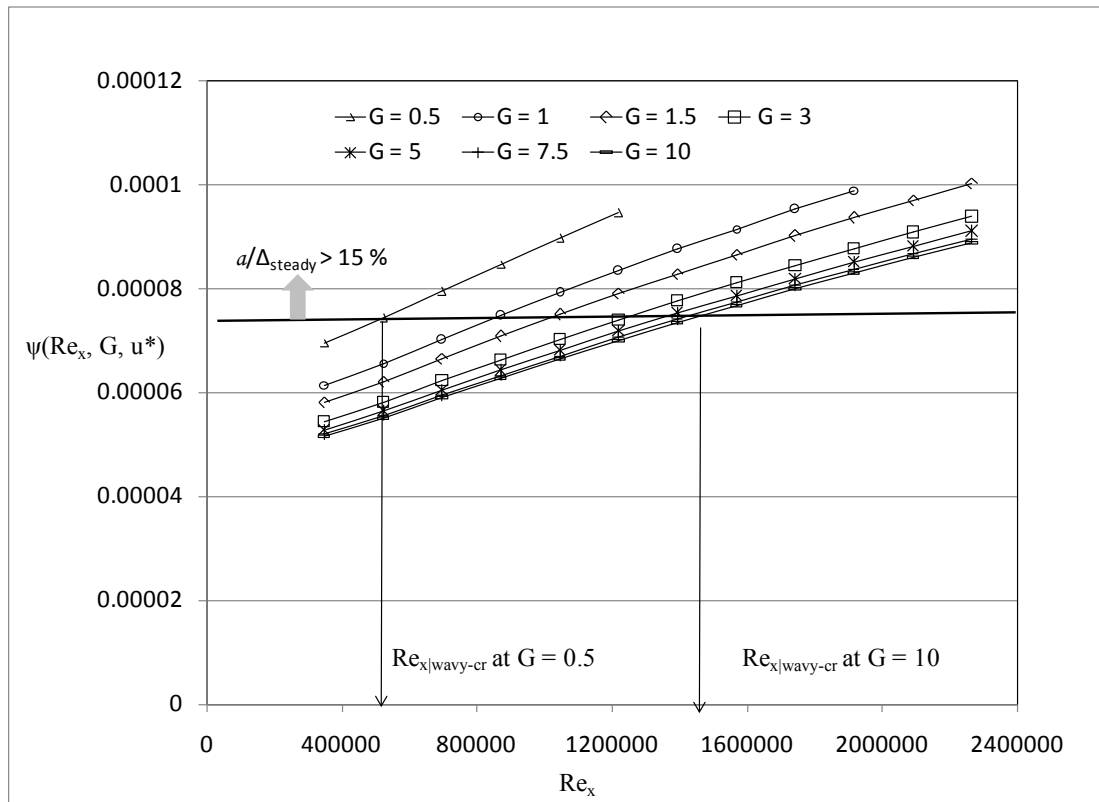
Figure 60: Characterization of critical Reynolds number Re$_{x|wavy-cr}$ which marks transition from smooth to wavy annular regime for different 'G' values for an external condensing flow of vapor over a horizontal plate

For R-113 vapor with constant value of u* ($\equiv$ U∞/UChar) = 0.0079 (i.e. U∞ = 3 m/s) and gy = 0, this figure plots function ψ(Rex, G, u*) versus Re$_x$ ($\equiv$ ρ_1U∞ x /μ_1) for a range of G values varying from 0.5 to 10. G is given as (Ja /Pr1)·(ρ1μ1/ ρ2μ2)1/2 This Figure marks the critical Reynolds number Rex|wavy-cr for Δmax = 2 microns, such that for Rex values higher than this the growth of amplitude of waves on the interface relative to mean film thickness due to condensing-surface vibrations exceeds the value 0.15. This growth is given by a(x)/Δsteady(x) ($\equiv$ D*max· ψ(Rex, G, u*)) where the function ψ(Rex, G, u*) is given by Eq. (41) and G is given as (Ja /Pr1)·(ρ1μ1/ ρ2μ2)1/2. As seen from the figure, the value of Rex|wavy-cr increases with increase in value of G.

153
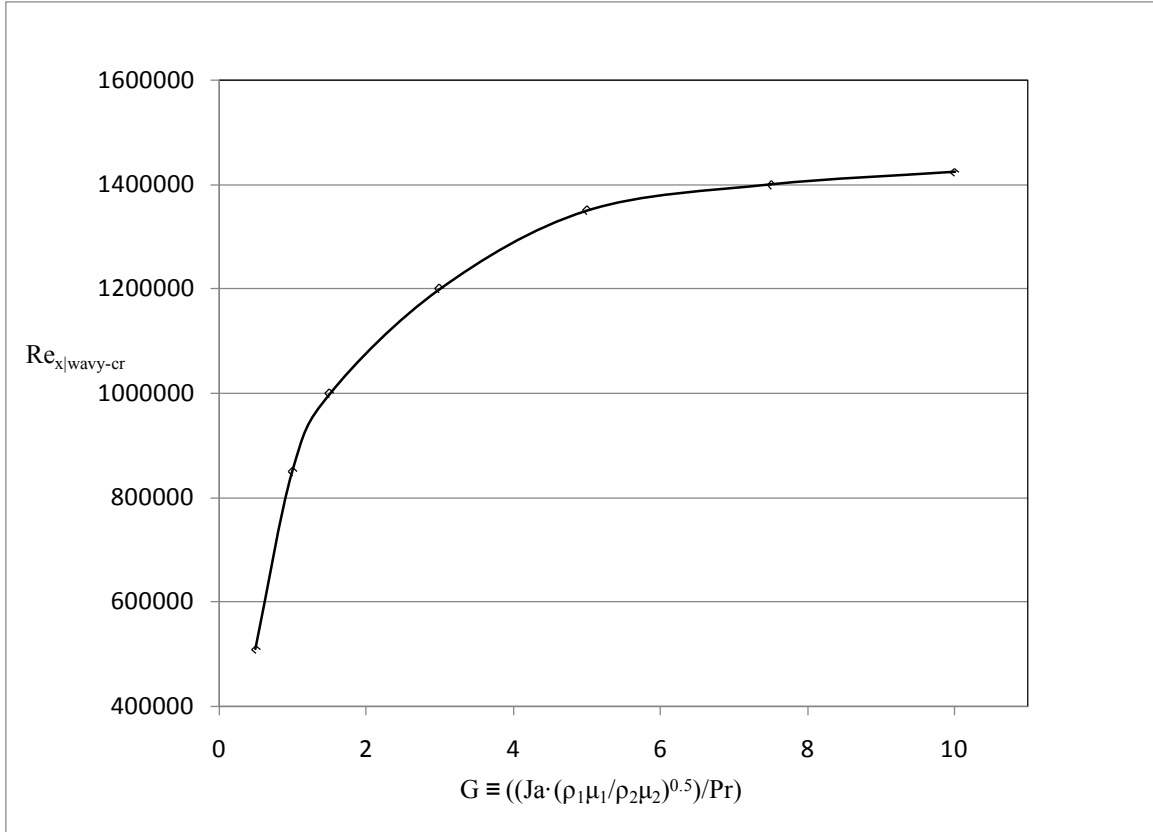
Figure 61: Variation of critical Reynolds number $Re_{x|wavy-cr}$ with 'G' for external condensing flow of vapor over a horizontal plate

For the data in Figure 60, this figure plots variation in $Re_{x|wavy-cr}$ with respect to G at a fixed value of u* ($\equiv U\infty/UChar$) = 0.0079 ($U\infty$ = 3 m/s).

The spatially increasing amplitude of these waves with increasing Re_x (or Re_δ) suggests, at some $x \approx x_{cr}$ (or $Re_x \approx Re_{x|Trans-cr}$) various Fourier modes of noise induced waves will grow so much that they will non-linearly interact to form a mean quasi-steady solution that is qualitatively different from the underlying steady laminar "attractor" and such an $Re_{x|Trans-cr}$ can be said to mark the onset of turbulence or a qualitatively different wavy-laminar flow.

154
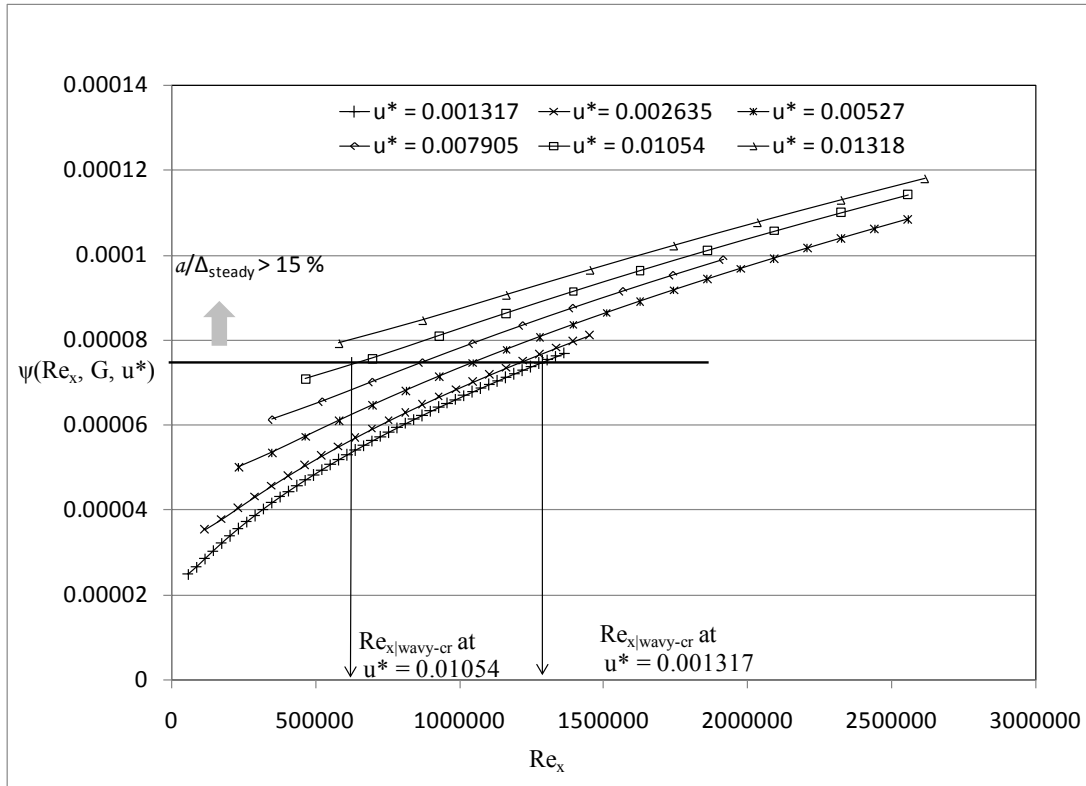
Figure 62: Characterization of critical Reynolds number Re$_{x|wavy-cr}$ which marks transition from smooth to wavy annular regime for different vapor speeds for an external condensing flow of vapor over a horizontal plate

For pure R-113 vapor flow with constant value of G = 1 and g$_y$ = 0, this figure plots function $\psi(Re_x, G, u^*)$ versus Re$_x$ ($\equiv \rho_1 U_\infty x/\mu_1$) for a range of u* ($\equiv U_\infty/U_{Char}$) values varying from 0.001317 to 0.01318. This figure marks the critical Reynolds number Re$_{x|wavy-cr}$ for Δ_{max} = 2 microns, such that for Re$_x$ values higher than this the growth of amplitude of waves on the interface relative to mean film thickness due to condensing-surface vibrations exceeds the value 0.15. This growth is given by $a(x)/\Delta_{steady}(x)$ ($\equiv \mathcal{D}^*_{max} \cdot \psi(Re_x, G, u^*)$) where function $\psi(Re_x, G, u^*)$ is given by Eq. (41) and G is given as $(Ja/Pr_1) \cdot (\rho_1\mu_1/\rho_2\mu_2)^{1/2}$. As seen from the figure, the value of Re$_{x|wavy-cr}$ increases with decrease in the value of u*.
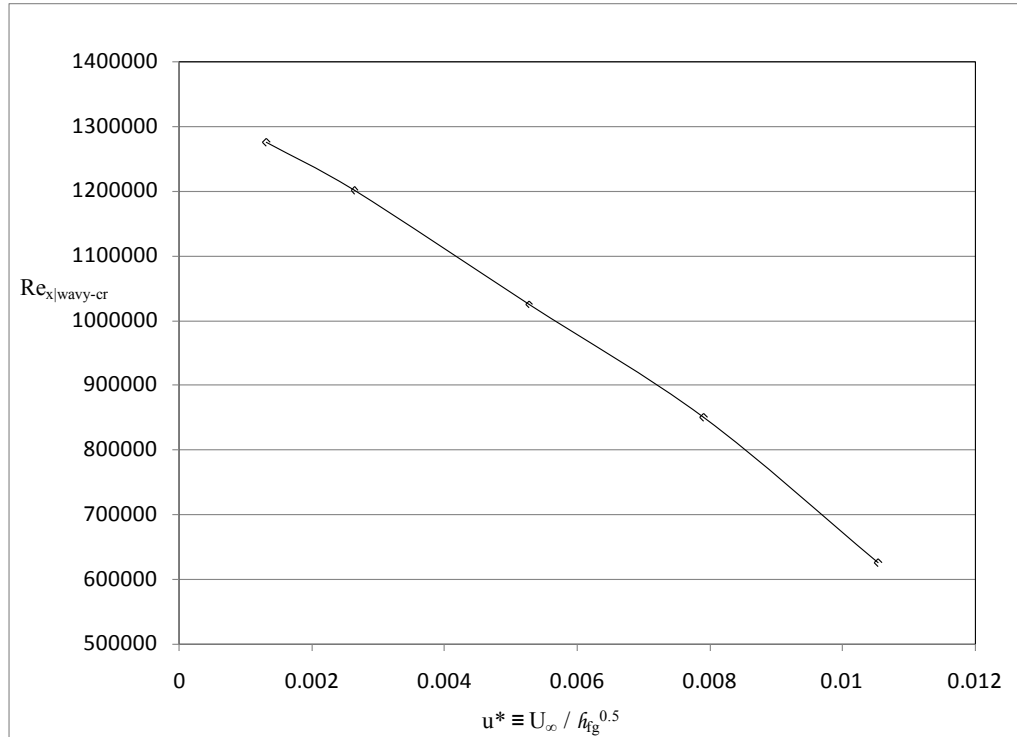
Figure 63: Variation of critical Reynolds number $Re_{x|wavy-cr}$ with vapor speed for an external condensing flow of vapor over a horizontal plate

For the data in Figure 62, this figure plots variation in $Re_{x|wavy-cr}$ with respect to u* ($\equiv$ U_∞/U_{Char}) at a fixed value of G =1.

Towards understanding the relevant physics for the onset of this type of transition, this thesis presents an investigation of the unsteady physics of the solutions obtained for $U_\infty > U_\infty$*. A combination of the analysis reported below and future experiments may help anybody to obtain $Re_{x|Trans-cr} > Re_{x|wavy-cr}$ that marks the above stated transition. If one were to investigate the likelihood of an evolution of a solution from its initial guess (t = 0) to its final long term attractor in the presence of noise source and instabilities (instabilities are absent for this case), one needs a measure of the ratio of the tendency of

156

the waves to grow – hence to move away from the relevant smooth laminar attractor - to the tendency of the initial guess to move towards the relevant smooth laminar attractor (which is, for this problem, the long term steady solution). As established earlier for Figure 54 in the absence of persistent noise,

$$\text{Strength of attraction rate} \propto \left|\partial^2\Delta/\partial t^2\right|_{\text{Rep}|(no-noise)} \tag{44}$$

Since the interfacial noise, in the presence of persistent condensing surface noise, is given by Eq. (32), a measure of acceleration associated with the tendency of interfacial waves to move away from the underlying smooth attractor is obtainable by taking the maximum magnitude of the principle second time derivative of Eq. (32). This gives:

$$\text{Acceleration associated with growing interfacial waves} \propto \left|\partial^2\Delta/\partial t^2\right|_{\text{(for noise)}} \approx a(x)(2\pi f_p)^2$$

$$\tag{45}$$

The ratio of the noise-induced destabilizing acceleration to the acceleration associated with the underlying stabilizing "attraction rate," as suggested respectively by Eqs. (44) and (45), is defined by the parameter P given below:

$$P \equiv \{a(x)(2\pi f_p)^2\} / \left\{\left|\partial^2\Delta/\partial t^2\right|_{\text{Rep}|(no-noise)}\right\} \tag{46}$$

Clearly, based on discussions of dependency of terms in (45) and (46), one expects the parameter P to have significant dependence on the downstream distance x and inlet vapor speed U_∞. Since $a(x)$ and $\left|\partial^2\Delta/\partial t^2\right|_{\text{Rep}|(no-noise)}$ in (46) are obtained directly from computational simulations for any flow of interest. If Y_e in Eq. (16) is replaced by $L_{\text{Char}} \equiv \mu_1/(\rho_1 \cdot h_{fg}^{1/2})$, the non-dimensional parameter P depends on a non-dimensional value of x given by Re_x/u^* and the original non-dimensional parameters (see Eq. (16)): $\text{Re}_1 = u^*$, Ja,

157

Fr^{-1}_y, ρ_2/ρ_1, μ_2/μ_1, Pr_1, and We. In addition, the non-dimensional noise parameters associated with physical values of $\mathcal{D}_{max}$ and f_p in Eq. (46) become $\mathcal{D}^*_{max}$ and $f = f_p^*/u^*$, where $f_p^* \equiv (\mu_1 \cdot f_p)/(\rho_1 \cdot h_{fg})$. An assumed "typical" range, taken here to be: 0.5 μm $\leq \mathcal{D}_{max} \leq$ 2 μm, 5 Hz $\leq f_p \leq$ 15 Hz, is needed for determining a "typical" range of critical values of P (viz. P_{cr} values) that are expected to mark the onset of the expected transition to turbulence or a qualitatively different wavy-laminar flow. In what follows, for the "typical" range of noises, it will be assumed that P – like $a(x)/\Delta(x)$ - depends significantly on u^*, Re_x, and G and insignificantly on other remaining non-dimensional parameters.

As stated earlier, the evolution of initial guess in the vicinity of the underlying steady solution or attractor depends on the parameter P - since this parameter compares the tendency of the solution to move away from the smooth steady solution to the tendency of the solution to move towards the steady solution. If this parameter P approaches a certain critical value (obtained by experiments), the noise components will reach a threshold level that would initiate mutual non-linear interactions that would fundamentally alter the nature of the underlying steady solution/attractor. This critical value of P, denoted as P_{cr} could be assumed, to begin with, to be of the form $P_{cr} = P_{cr}(Re_x, u^*, G, D^*_{max})$ as is the dependence for $a(x)/\Delta(x)$ in Eq. (39). However, only experiments can determine which of the parameters besides Re_x and $\mathcal{D}^*_{max}$ are really important in determination of P_{cr} values which must yield a critical value of Re_x (termed $Re_{x|Trans-cr}$) that satisfies $Re_{x|Trans-cr} > Re_{x|wavy-cr}$. For discussion purposes, instead of experimentally determining $Re_{x|Trans-cr}$ and P_{cr} for a given flow, here it is illustrated how to use a computationally obtained relationship of $P = P (Re_x, u^*, G, D^*_{max})$ and an a priori

estimate of P_{cr} to obtain an estimate of $Re_{x|Trans-cr}$ for a specific flow case. For example consider an R-113 flow case with G = 0.48, u* = 0.0036, D^*_{max} = 2000 (which corresponds to D_{max} = 2 μm), f_p = 15 Hz, and P_{cr} = $P_{cr-guessed}$ ≈ 2.2·10^6. Using the earlier described methodology (see Eq. (38)-(41)) for estimating $Re_{x|wavy-cr}$, it is found that $Re_{x|wavy-cr}$ ≈ 7.8·10^5. The resulting P versus Re_x curve is shown in Figure 64.
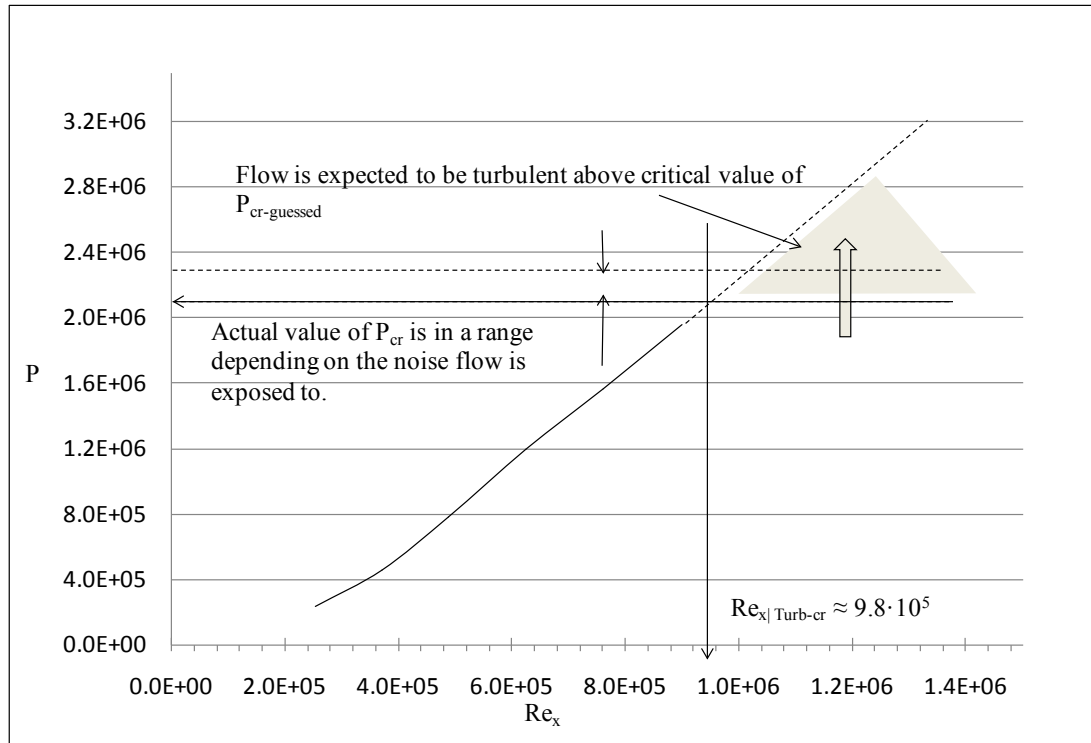
Figure 64: Computational criteria to determine critical Reynolds number $Re_{x|Trans-cr}$

which marks transition from laminar to turbulent regime for an external

condensing flow of vapor over a horizontal plate

For an R-113 flow case with G = 0.48 (i.e. ΔT = 5°C), D^*_{max} = 2000 (i.e. $\mathcal{D}_{max}$ = 2 μm), u* = 0.0036 (i.e. $U_∞$ = 1.4 m/s), f_p = 15 Hz, the value of P is computationally obtained from Eq. (46) and plotted as a function of Re_x. For $P_{cr-guessed}$ ≈ 2.2·10^6, the shaded portion marks the post –transition flow regime.

159

The shaded portion in Figure 64 represents the post transition flow regime of Re_x ≥ $Re_{x|Trans-cr}$ ≈ $9.8 \cdot 10^5$ and P ≥ P_{cr}.

General Remarks About Onset the Proposed Transition Criterion for $Re_{x|Trans-cr}$

It is clear from the results described above that for the transition scenario presented above, the estimate of critical value or values of P_{cr} for the parameter P introduced in this thesis work plays a very important role in describing the flow behavior at very high Re_x > $Re_{x|wavy-cr}$ values - even as the underlying steady flow remains stable to initial disturbances. The interplay of decreasing attraction strength to the attractor and increasing strength of the growing waves tries to dictate a transition away from the underlying attractor. This analysis for marking the onset of transition to turbulence or a qualitatively different wavy-laminar flows by looking at high Re_x behavior in the range of $Re_{x|wavy-cr}$ ≤ Re_x ≤ $Re_{x|Trans-cr}$ could not have been achieved by the traditional method of sole reliance on analyses that are based on classical instability mechanisms associated with initial disturbances. Therefore the methodology presented here is valuable for marking the onset of transition for many flows whose turbulence type transition criterion is not preceded by instability to initial disturbances. Furthermore, even for flows whose march to turbulence is preceded by a series of instabilities (an example of which is progressively repeated occurrences of oscillatory instabilities in the so called Ruelle-Takens [49] scenario), a synthesis of stability analysis based on initial disturbances and an analysis of the type introduced here for persistent noise-induced disturbances may give more meaningful results.

160

5.2.4 Non-attainability of Steady Film Flows at Lower Vapor Speeds

The computational results presented so far in sections 5 were mainly for R113 vapor flows at speeds: 10 m/s > U_∞ > 0.2 m/s. As one approaches the lower vapor speeds ($U_\infty \leq 0.2$ m/s) in Figure 65, unsteady solutions show non-existence of a steady long term (t → ∞) limit that exists for U_∞ > 0.2 m/s. One is tempted to say that the steady solutions for U_∞ > 0.2 m/s loses stability as speed U_∞ is lowered further but the situation is different because one does not find, at least computationally, a steady solution for U_∞ < 0.2 m/s. Since one does not have a steady solution in this range, one cannot say that the steady solution for U_∞ < 0.2 m/s has lost its stability. This non-existence of a steady limit is a gradual phenomena which is depicted in Figure 65. The signs of non-existence of a steady limit is especially apparent in the aft portion of the flow for vapor speed U_∞ = 0.08 m/s. This is different than noise-sensitive steady limits discussed earlier for higher speeds (also see U_∞ = 0.2 m/s in Figure 65 which exhibits existence of a steady limit). This fact is more apparent through Figure 66 which plots long term physical values of rate of change of film thickness ($\partial\Delta/\partial t$) at a fixed 'x' location (x = 30). It can be seen that as vapor speed reduces below some critical value (below 0.2 m/s), the rate of change of film thickness starts increasing indicating above its effectively zero value (which is defined in Figure 66, within computational errors, to be 1.5×10^{-7}).

This sustained unsteadiness at such low vapor speeds implies non-attainment of any limiting steady solution of the film condensation type and one expects an eventual long time behavior that involves a more complex liquid-vapor morphology.
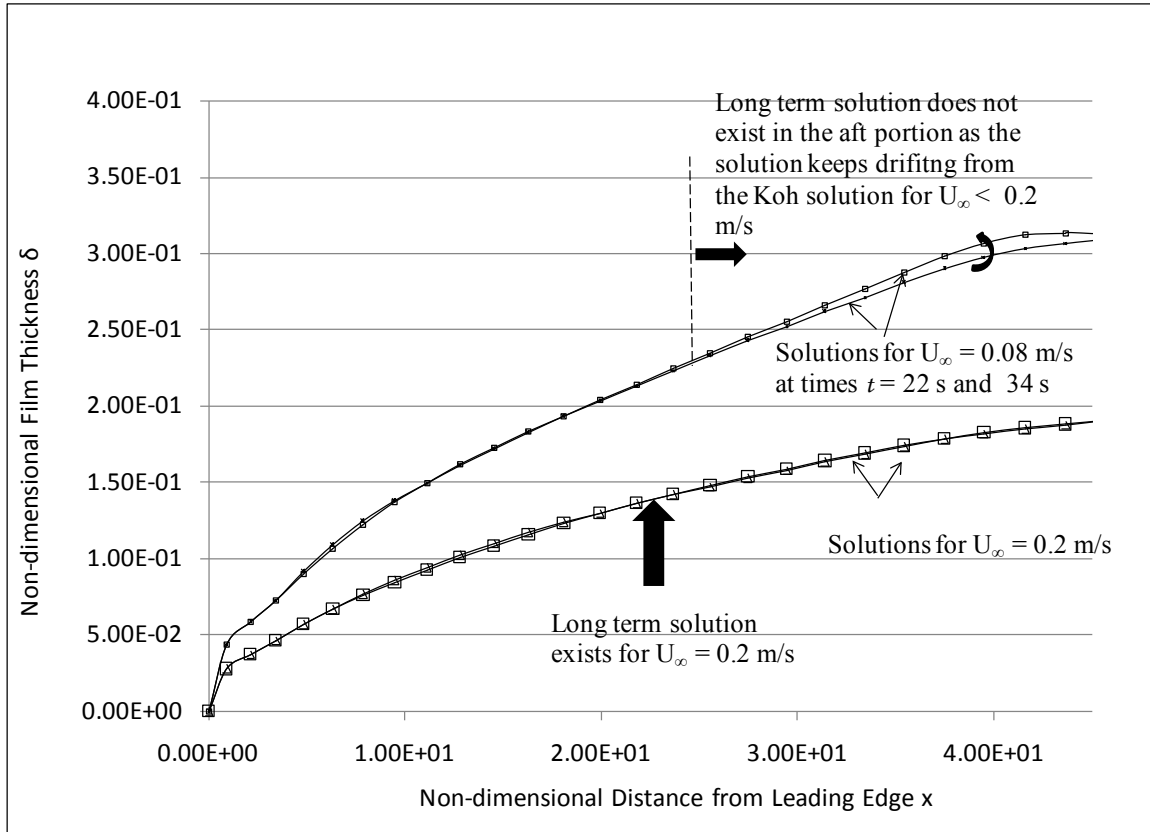
Figure 65: Unsteady behavior of solutions at low vapor speeds for an external condensing flow of vapor over a horizontal plate

The figure plots two different sets (for $U_\infty = 0.2$ m/s and $U_\infty = 0.08$ m/s) of long term film thickness values δ (x, t) with x at large non-dimensional times t = 22 s and 34 s. The flows are of R113 vapor at $\Delta T = 5°C$ and initial conditions (not shown) for each of these cases was the Koh similarity solution [10]. For $U_\infty < 0.2$ m/s, the aft portions of these curves suggest non-existence of $\lim\limits_{t\to\infty}\delta(x,t)$

It is known that, as vapor speed reduces, the available shear stress for driving the thin liquid film reduces and, also, more kinetic energy of the vapor is deflected away from the condensate (the upward bending streamlines in Figure 48 cover more of the leading edge and pressure gradients near the leading edge – as shown in Figure 66 - become sharper).

162
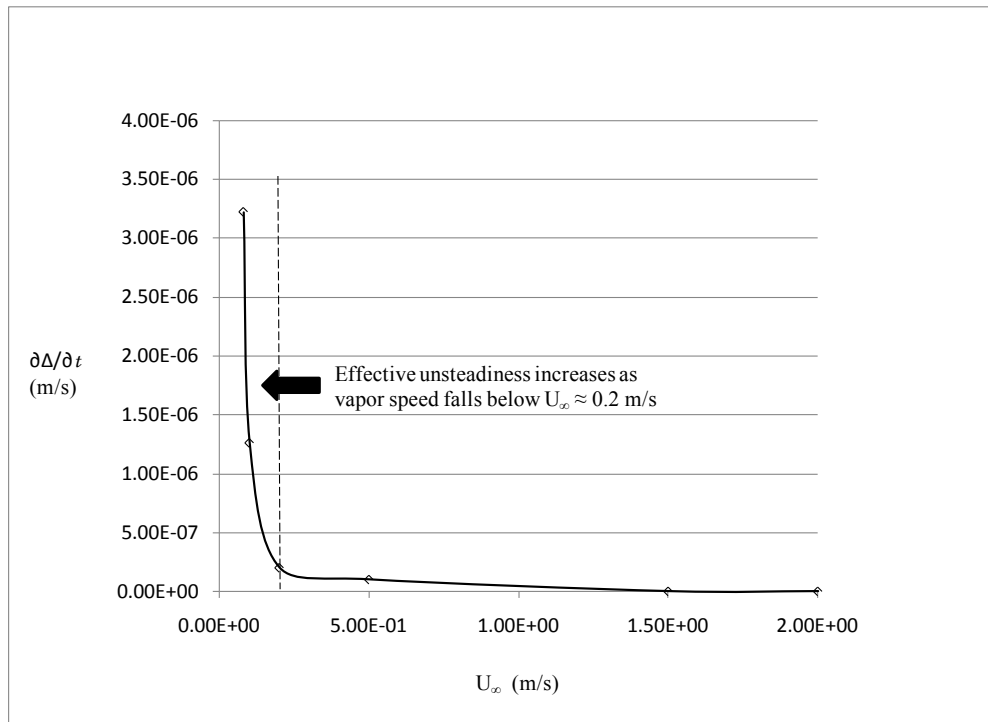
Figure 66: Increasing nature of effective unsteadiness at lower vapor speeds for an external condensing flow of vapor over a horizontal plate

The figure plots long term steadiness measure $\left|\dfrac{\partial \Delta}{\partial t}\right|$ (estimated at x = 40) with free stream speed U_∞. The flows are of R113 vapor at $\Delta T = 5°C$. The values of $\left|\dfrac{\partial \Delta}{\partial t}\right|$ for $U_\infty > 0.2$ m/s is considered effectively zero within computational error. This suggests existence of a long time steady solution. However the rising positive values of $\left|\dfrac{\partial \Delta}{\partial t}\right|$ for $U_\infty < 0.2$ m/s suggest non-existence of a long time steady solution.
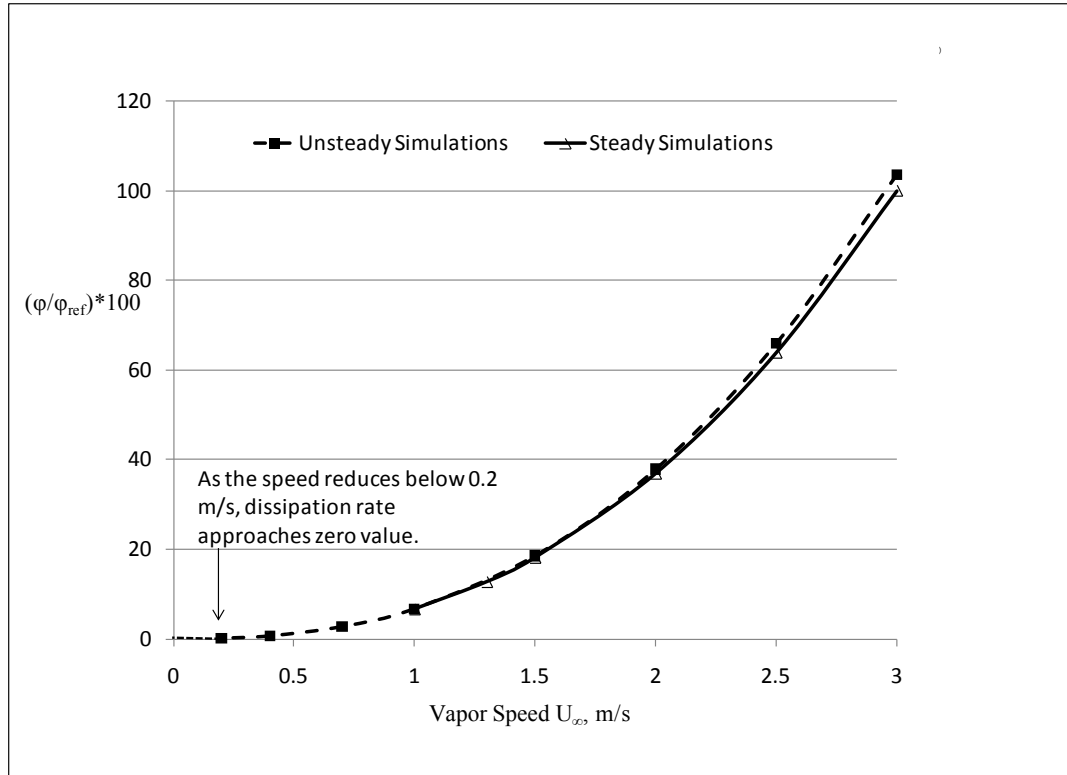
Figure 67: Trend of normalized dissipation rates with vapor speeds for an external condensing flow of vapor over a horizontal plate

For flow of R113 vapor with $\Delta T = 5°C$, $X_e = 0.2$ m, and $g_y = 0$, this figure plots normalized viscous dissipation rates φ/φ_{ref} (see Eq. (A.27) in the Appendix for the definition of φ) obtained from steady and unsteady (long-term) steady solutions in a representative control volume given by $0 < x < 40$ and $0 < y < 0.5$. As the vapor speed U_∞ reduces below 0.2 m/s, dissipation rates can be seen becoming effectively equal to the zero value associated with $U_\infty = 0$.

The gradualness of the loss of the above described steady limit (i. e. existence of steady film wise solution) is further demonstrated by insufficient availability of mechanical energy (i.e. near zero values of viscous dissipation rates in Figure 67). In Figure 67, the viscous dissipation rate φ (see Eq. (A27) in the Appendix at which energy is dissipated in the interior of the vapor and the liquid phases inside any representative control volume for which long term steady solutions exist, it is observed that, as vapor

164

speed decreases (and approaches values below $U_\infty = 0.2$ - 0.3 m/s), the dissipative energy *asymptotically* approaches negligible or near zero value.Figure 67 shows normalized dissipative energies (φ/φ_{ref}) as obtained by steady as well as long-term steady solutions of this problem in a representative control volume defined by $0 < x < 40$ and $0 < y < 0.5$.

Even though the energy dissipated in any control volume depends on its size, it was observed that the normalized values follow exactly the same trend irrespective of the size of the control volume. Here the normalizing dissipation rate φ_{ref} is the value of φ for the chosen control volume at speed $U_\infty = 3$ m/s. In Figure 67, the value of $\varphi_{ref} = 3.48 \times 10^{-2}$ W for $U_\infty = 3$ m/s and a control volume defined by $0 < x < 40$ and $0 < y < 0.5$. For vapor speeds between 1 m/s $< U_\infty <$ 3 m/s, the thick line in Figure 67 shows φ/φ_{ref} values as obtained from the steady solutions while the dotted line in Figure 67 shows φ/φ_{ref} values obtained from long-term steady limits of unsteady solutions for 0.2 m/s $< U_\infty <$ 3 m/s.

There were some algorithmic issues in the steady solver for 0.2 m/s $< U_\infty <$ 1 m/s whose improvements were not considered necessary and therefore were not included for results in Figure 67. It should be noted that the integral *theorem on expended mechanical power* (see Ch. 15, [50]) or the integral form of *mechanical energy equation* (see Eq. (5.4.13) of [51]) says that a steady solution exists if and only if $\varphi/\varphi_{ref} > 0$ and this condition is hard to satisfy in Figure 67 for 0 m/s $< U_\infty <$ 0.2 m/s because the energy for $U_\infty = 0$, where the theorem is violated, is effectively equivalent to the energy at $U_\infty = 0.2$ m/s. This fact that energy available to dissipate at $U_\infty <$ 0.2 m/s (say $U_\infty = 0.08$ m/s) is effectively the zero value associated with $U_\infty = 0$ should lead to a response that is also

somewhat similar to what is expected at $U_\infty = 0$ and fixed ΔT. Clearly, for $U_\infty = 0$ and fixed ΔT, one expects a rising unsteady film type solution which is similar to what is being found in Figure 66. However the flow for $0 < U_\infty < 0.2$ m/s also has an option to come to a new quasi-steady flow under a more complex liquid/vapor morphology.

Because of the mutually supportive nature of the above described independent facts, one can reliably state that film wise steady condensation solution for this problem is not possible for effectively zero inlet speeds that correspond to a certain finite range of values of the type: $0 < U_\infty < U_\infty^*$. This result states that Koh solution [10] for $0 < U_\infty < U_\infty^*$ is not valid.

Chapter 6 CONCLUSIONS OF THESIS WORK

6.1 Summary of Computational Results

6.1.1 Internal Condensing Flows (Gravity Driven and Shear Driven)

1. This thesis work establishes an important result that there exists a unique steady "natural" solution of the strictly steady parabolic problem for the gravity and shear driven internal condensing flows. This result has been confirmed by a 1D tool and by experiemtns as well. It also shows that this "unique" solution can be obtained as an "attracting" solution (as t $\rightarrow$ ∞) of the unsteady parabolic problem.

2. The simulation results presented in this thesis show the remarkable differences between gravity driven and shear driven condensing flows.

3. 2-D computational results show that there could be multiple quasi-steady/unsteady solutions of the unsteady governing equations (which exhibit "elliptic sensitivity") for shear driven cases under different quasi-steady impositions of the elliptic boundary condition. This thesis presents novel categorization of internal condensing flow behavior based on its elliptic sensitivity. It is shown that steady governing equations of shear driven internal condensing flow are "parabolic" while the unsteady equations are "elliptic." However, it is also found that the unsteady behavior remains "parabolic" (even under quasi-steady/unsteady fluctuations on the parabolic boundary conditions) for: (i) gravity dominated flows, and (ii) thermal boundary conditions which hold the wall heat-flux profile fixed.

167

4. Computational and experimental results presented in this thesis show that shear driven internal condensing flows are sensitive to the nature of fluctuations present at the inlet/outlet boundaries and, in addition, the condenser response also depends on the method of cooling used.

5. The computational and experimental synthesis accomplished for gravity driven in-tube condensing flows provides a basic framework for analyzing two-phase component and characterizing its flow regime boundaries.

6. Preliminary results for micro-scale flows presented here can predict importance of parameters (non-equilibrium thermodynamics and disjoining pressure effects) at such small scales.

6.1.2 External Condensing Flow of a Vapor Condensing Over a Flat Plate

1. For the ranges of the flow parameters investigated, the analytical solution of Koh [10] for film thickness is found to be reasonably accurate for horizontal condensing flows over a flat plate under conditions of sufficiently fast vapor speeds and nearly uniform far field pressure p_∞. Over this range, it is found that, there is some departure from the Koh solution [10] in the frontal portion of the plate with regard to the values of interfacial velocities and pressure variations in the liquid and vapor domains. The gradients in pressure become sharper as vapor speed reduces and such dynamics cannot be captured using analytical solution of Koh [10].

2. The computational results show that the presence or absence of transverse component of gravity does not change the steady solution by much if only a certain

length from the leading edge (lengths investigated here) is considered. Over this length only changes in the hydrostatic pressure variations, resulting from presence or absence of gravitational component of pressure, are observed in the liquid film.

3. For the ranges of the flow parameters investigated, unsteady solutions predict, just like internal condensing flows, that there exists a long-term (t → ∞) steady solution (*attractor*) for this external condensing flow problem. A new measure termed "attraction rate" is introduced for the reported "non-linear" stability analysis. This value decreases with increasing distance and increases with increasing vapor speeds. The qualitative and quantitative variation in the strength of the attractor is presented for the cases of $U_\infty >$ U_∞^*. Unsteady results, along with several supporting results, find that at low vapor speeds $(0 < U_\infty < U_\infty^* \approx 0.2$ m/s) a film wise steady solution does not exist.

4. It is established here that the smooth underlying steady solutions for these cases are stable to the momentary initial disturbances (of various wavelengths and amplitudes) on the interface because of prominent vapor suction effects.

5. The computational results show that the stable attracting solutions for this condensing flow over a horizontal plate, found for $U_\infty > U_\infty^*$ are very sensitive to persistent but minuscule condensing-surface noise. It is shown here that for $U_\infty > U_\infty^*$, an $Re_{x|wavy-cr}$ ($\approx$ $5 \cdot 10^5$ - $12 \cdot 10^5$ for representative flows) can be obtained from the given criterion. For Re_x $> Re_{x|wavy-cr}$, the flow shifts to a wavy laminar flow regime in which amplitudes of the waves are more than 15% of the steady mean film thickness values.

6. A new parameter P has been introduced in this research to characterize stability of flows. With the help from suitable experimental research, critical values of parameter P can be obtained. Such analysis can yield identifiable values of $Re_{x|Trans-cr}$ which can be used to mark the onset of turbulence or a qualitatively different wavy-laminar flow.

6.2   Benefits/Applications of Research

1.   2-D computational tools developed during this research can predict flow behavior/flow regime boundaries for annular stratified internal/external condensing flows in a two-phase flow component. These tools are of great importance in designing ground based or 0g two-phase thermal systems, which will have improved attainability, repeatability, and stability.

2. The computational results obtained from this thesis work will keep on aiding designing of the lab experiments and analysis of experimental future results for the ongoing shear driven channel experiments.

3. The codes (on FORTRAN platform) and algorithms used/developed for this thesis work will be guidelines for the ongoing development of a new version of 2D/3D computational tool being developed on MATLAB/COSMSOL platform.

4. The differences between gravity and shear driven internal condensing flows and newly discovered sensitivities of shear driven flows predicted by computations can be exploited for achieving better condenser performance in different applications. These sensitivities, corresponding flow regime maps, and controllability of shear driven flows discussed in this thesis can be used in a novel thermal system to:

   a.   Improve predictability of flow behavior in a thermal system.

b. Design condenser geometry to operate in the required flow regime (gravity insensitive, gravity driven, shear driven, etc.).

c. Provide real time controls at specific locations to improve the heat transfer and maintain flow regimes.

d. Isolate systems from unwanted boundary conditions at the inlet, exit, and walls to utilize "natural" selection of boundary condition and avoid flow oscillations.

e. Allow to pass only certain "desirable" frequency ranges from boundary locations to avoid dynamic instability.

f. Provide thermal control at the condensing boundaries to realize different flow sensitivities and use them towards improving performance of condensers/thermal systems.

5. The dynamic stability analysis of external condensing flow accomplished for this thesis work is first of its kind in characterizing effects of ever-present fluctuations in determining flow regimes and transition to turbulence. Such analysis can be repeated for any condensing flow system to better understand different flow transitions and impacts on heat transfer rates.

6.3 Future Directions

6.3.1 Computational Tool Development

Current computational tools (based on FORTRAN platform) used to solve condensing flows in this research are limited to solving annular stratified flows with laminar vapor

and laminar liquid. These tools can only predict flow situations when the film may break and form droplets and enter in to non-annular regime but can not resolve the physics of non-annular regime. This tool is currently being transferred to COMSOL/MATLAB platform. In a new tool, commercially available code (COMSOL) will be used to solve individual domains (liquid and vapor). Interface conditions (Eqs. (4)-(9)) will be applied through user written MATLAB programs. Through the use of commercial software, one can address the following issues that can not be addressed with the current computational tool:

a.   Effects of compressibility in vapor domain (high Mach number flows):

b.   Effects of vapor turbulence.

c.   Steady and unsteady solutions at longer condenser lengths for fully condensing shear driven flows.

d.   Micro-scale effects (surface tension, etc.) for micro-meter scale flows.

e.   Better meshing techniques, faster and better solvers (steady/unsteady), and inbuilt high-end graphics.

Development of a New Method to Solve the Interface

In the current 2-D approach (see [2]-[7]), at any instance of time t, the liquid domain and the vapor domain are solved separately after a tentative guess of interfacial location δ – which is modeled as a sharp interface (this is unlike popular level-set approaches [13], [52]-[53]). The liquid domain is solved subject to stress and pressure boundary condition (values of shear stress are denoted as τ_1^i and pressure as p_1^i) on the

172

interface and any exit condition if imposed, and the vapor domain is solved subject to the velocity-component boundary condition (denoted as u_2^i and v_2^i) on the interface. The temperature boundary condition at the interface (viz. values denoted as θ_1^i and θ_2^i) is specified by the thermodynamic saturation temperature at the interface. In this approach, the five guesses of $\{u_2^i,\ v_2^i,\ \tau_1^i,\ p_1^i,\ \delta\}$ are iteratively updated with the help of five interfacial conditions, viz. two from tangential and normal stress conditions, two from interface mass balance, and one from continuity of tangential velocities. One of the interface conditions that determine the steady/unsteady interface location (given by $\phi(x,$ t$) = 0$) results in an interface-tracking equation of the level-set type: $\partial\phi/\partial t + \mathbf{v}_{\text{eff}} \cdot \mathbf{grad}\ \phi = 0$, where $\mathbf{v}_{\text{eff}}$ is a vector that can be easily obtained from mass-flux equalities, e.g. $\mathbf{v}_{\text{eff}}$ is available in Eq. (15) of [53]. The current approach ([2]-[8]) uses an explicit form $\phi(\mathbf{x},\ t) = y - \delta\ (x,\ t) = 0$ but the proposed approach will use an implicit form to identify $x_{\text{Plug/Slug}}$. In the new tool, this equation will be solved through a newly developed MATLAB subroutine. This subroutine will employ a *modified level-set type solver*. By doing this, different flow physics involving non-annular flows, film break-up, etc. can be captured effectively.

6.3.2 Condensing Flow Problems that Need to be Investigated in Future

After the development of the new computational tool, following flow problems related to this thesis need to be investigated with the help of a new tool:

(i)   For shear driven internal condensing flows, phenomenon of inducement of thermal gradients in condensing plate needs to be studied in detail and the results should be synthesized with the experiments.

(ii)   Current computational tool can not capture the condensing physics downstream of the shear driven condensing flows in presence of transverse component of gravity where flow are highly likely to enter in to non-annular regime. The new tool should investigate these effect implementing the level set method ([13], [52]-[53]) and these results need be synthesized with the ongoing experiments of condensation in horizontal channel.

(iii)   Investigations of sensitivity of ever-present bottom wall noise for internal shear driven flows (on the parallel line of what has been done for external shear driven condensing flows in thesis) need to be carried out. This will throw light on transition of these flows in to wavy annular and interfacial turbulence regime.

(iv)   Based on the preliminary synthesis of computational and experimental results for gravity driven in-tube condensing flows carried out for this thesis work, detailed synthesis for the same geometry has been done using 1D tool for development of heat flux, pressure drop correlations etc. Such synthesis needs to be done for shear driven internal condensing flows.

6.3.3 System Level Analysis

To apply the results presented in this thesis for a two-phase thermal system including a flow condenser and a flow boiler, a 2D (or 1D) computational tool needs to

174

be developed for *annular flow boiling* as well. With the help of such a tool, boundary condition sensitivities found for flow condensation should be investigated for flow boiling phenomena. After synthesizing the results for flow boiling and flow condensation, system level analysis can be undertaken to design novel thermal system discussed in section 6.2. This is the topic of ongoing research in our group at MTU.

REFERENCES

1. S. Mitra, A. Narain, R. Naik, S.D. Kulkarni, 2010, " Quasi One-dimensional Theory for Shear and Gravity Driven Condensing Flows and their Agreement with Two-dimensional Theory and Selected Experiments," Submitted for publication in *International Journal of Heat and Mass Transfer*.

2. Narain, A., Q. Liang, G. Yu, and X. Wang, 2004, "Direct Computational Simulations for Internal Condensing Flows and Results on Attainability/Stability of Steady Solutions, Their Intrinsic Waviness, and Their Noise-Sensitivity," *Journal of Applied Mechanics,* Vol. 71, pp. 69-88.

3. Liang, Q., X. Wang, and A. Narain, 2004, "Effect of Gravity, Shear and Surface Tension in Internal Condensing Flows - Results from Direct Computational Simulations." ASME *Journal of Heat Transfer*, 126 (5), pp. 676-686.

4. Phan, L., X. Wang, and A. Narain, 2006, "Exit Condition, Gravity, and Surface-Tension Effects on Stability and Noise-sensitivity Issues for Steady Condensing Flows inside Tubes and Channels," *International Journal of Heat and Mass Transfer*, Vol. 49, Issues 13-14, pp. 2058-2076.

5. Narain, A., J. H. Kurita, M. Kivisalu, S. D. Kulkarni, A. Siemionko, T. W. Ng, N. Kim, and L. Phan, 2007, "Internal Condensing Flows Inside a Vertical Pipe – Experimental/Computational Investigations of the Effects of Specified and Unspecified (Free) Conditions at Exit," ASME *Journal of Heat Transfer*, pp. 1352-1372.

6. Narain, A., S. Kulkarni, S. Mitra, J. H. Kurita, M. Kivisalu, 2009, "Computational

and Ground Based Experimental Investigations of the Effects of Specified and Unspecified (Free) Pressure Conditions at Condenser Exit for Condensing Flows in Terrestrial and Micro-Gravity Environments," *Annals of New York Academy of Sciences , Interdisciplinary Transport Phenomena in Space Sciences*, Vol. 1161, pp. 321-360.

7. S. D. Kulkarni, A. Narain, S. Mitra, J. H. Kurita, M. Kivisalu, M. M. Hasan, 2010, "Flow Control and Heat Transfer Enhancement in Presence of Elliptic-Sensitivity for Shear Driven Annular/Stratified Internal Condensing Flows," Submitted for publication in the Journal of Transport Processes, Also see: http://www.me.mtu.edu/~narain/

8. Kulkarni, S. D., A. Narain, S. Mitra, and L. Phan, 2010, "Forced Flow of Vapor Condensing over a Horizontal Plate (Problem of Cess and Koh*) - Steady and Unsteady Solutions of the Full 2D Governing Equations," ASME *Journal of Heat Transfer*, Vol. 132, pp. 101502:1-18.

9. Cess, R. D., 1960, "Laminar Film Condensation on a Flat Plate in the Absence of a Body Force," *Zeitschrift für Angewandte Mathematik und Physik*, 11, pp. 426-433.

10. Koh, J. C. Y., 1962, "Film Condensation in a Forced-Convection Boundary-Layer Flow," *International Journal of Heat and Mass Transfer,* Vol. 5, pp. 941-954.

11. J. H. Kurita, M. Kivisalu, S. Mitra, A. Narain, 2010, "Experimental Results on Partial and Fully Condensing Flows in Vertical Tubes, Their Agreement with Theory, and Recommended Correlations," Being Submitted for publication in *International Journal of Heat and Mass Transfer*.

12. Son, G. and V. K. Dhir, 1998, "Numerical Simulation of Film Boiling Near Critical pressures with a Level Set Method," Journal of Heat Transfer 120, pp. 183-192.

13. Sussman, M., P. Smereka, and S. Osher, 1994 "A Level Set Approach for Computing Solutions to Incompressible Two-Phase Flow," J. of Comput. Phys., Vol. 114, pp. 146-159.

14. Hirt, C. W. and B. D. Nichols, 1981, "Volume of Fluid (VOF) Method for the Dynamics of Free Boundaries," Journal of Comput. Phys. 39, pp. 201-255.

15. Esmaeeli, A. and G. Tryggvason, 2004, "Computations of Film Boiling - Part I: Numerical Method," Int. J. of Heat and Mass Transfer Vol. 47, 25, pp. 5451-5461.

16. Juric, D. and G. Tryggvason, 1998, "Computations of Boiling Flows," International Journal of Multiphase Flow 24, pp. 387-410.

17. Tezduyar, T. E. 2001, "Finite Element Methods for Flow Problems with Moving Boundaries and Interfaces," Archives of Computational Methods in Engineering,8, 83-130.

18. Cruchaga, M. A., D. J. Celentano and T. E. Tezduyar, 2005, "Moving-Interface Computations with the Edge-Tracked Interface Locator Technique (ETILT)," International Journal for Numerical Methods in Fluids 47, 451-469.

19. Abbott, M. B. and D. R. Basco, 1989, "Computational Fluid Dynamics – An Introduction For Engineers," Longman, Chap. 3, pp. 86-88 and Chap. 5, pp. 151-155.

20. Phan, L. and A. Narain, 2007, "Non-linear Stability of the Classical Nusselt Problem of Film Condensation and Wave-Effects," ASME *Journal of Applied Mechanics*, Vol. 74, No.2, pp. 279-290.

21. H.Y. Wu, P. Cheng, 2005, "Condensation Flow Patterns in Microchannels," Int. J. Heat and Mass Transfer 48 pp. 286-297.

22. X.J. Quan, P. Cheng, H.Y. Wu, 2008, "Transition from Annular to Plug/Slug Flow in Condensation in a Microchannel," Int. J. Heat and Mass Transfer 51 pp. 707-716.

23. J.W. Coleman, S. Garimella, 2003, "Two-phase Flow Regimes in Round, Square, and Rectangular Tubes during Condensation of Refrigerant R134a, Int. J. Refrig. 26 pp. 117-128.

24. Rose, J. W., 1998, "Condensation Heat Transfer Fundamentals," Feb 1998, Trans. I Chem E, Vol. 76, Part A.

25. Balasubramaniam R., V. Nayagam, M. M. Hasan, and L. Khan, 2006, "Analysis of Heat and Mass Transfer During Condensation over a Porous Substrate," Annals of the Newyork Academy of Sciences, 1077: 459-470.

26. Sparrow, E. M. and G. L. Gregg, 1959, "A Boundary Layer Treatment of Laminar Film Condensation," *ASME J. Heat Transfer*, 81, pp. 13-18.

27. Koh, J. C. Y., E. M. Sparrow, and J. P. Hartnett, 1961, "The Two-phase Boundary Layer in Laminar Film Condensation," *Int. J. Heat and Mass Transfer*, 2, pp. 69-82.

28. Nusselt, W., 1916, "Die Oberflächenkondesation des Wasserdampfes," *Z. Ver. Dt. Ing.* 60 (27), pp. 541-546.

29. Incropera, F. P. and D. P. DeWitt, 1996, *Fundamentals of Heat and Mass Transfer*, Fourth Edition, Wiley.

30. S. Mitra, A. Narain, S. Kulkarni, R. Naik, and J. H. Kurita, 2009, "Annular /Stratified Internal Condensing Flows in Millimeter to Micrometer Scale Ducts," MNHMT

2009-18507, Proceedings of ASME 2nd Micro/Nanoscale Heat & Mass Transfer International Conference, December 18-22, 2009, Shanghai, China.

31. Rabas, T. J., and B. Arman, 2000, "Effects of the Exit Condition on the Perofromance of In-Tube Condensers," *Heat Tranfer Engineering*, 21(1), pp. 4-14.

32. Chen, Y. P., and P. Cheng, 2005, "Condensation of Steam in Silicon Microchannels," *Int. Comm. of Heat Mass Transfer*, v.32, pp.175-183.

33. Garimella, S., 2004, "Condensation Flow Mechanisms in Microchannels: basis for Pressure Drop and Heat Transfer Models," *Heat Transfer Eng.*, 25, pp. 104-166.

34. Phan Lucas, 2007, "Flow Simulations, Code Developments, and Comparison with Experiments for Internal and External Condensing Flows," PhD Thesis, MEEM, Michigan Tech University.

35. Delhaye, J. M., 1974, "Jump Conditions and Entropy Sources in Two-phase Systems; Local Instant Formulation," *Int. J. of Multiphase Flow*, 1, pp. 395-409.

36. Carey, V. P., 1992, *Liquid-Vapor Phase-Change Phenomena*, Series in Chemical and Mechanical Engineering, Hemisphere Publishing Corporation.

37. Greenberg, M. D., 1978, *Foundations of Applied Mathematics*, Prentice Hall, New Jersey.

38. G.L. Wedekind, B.L. Bhatt, 1977, "An Experimental and Theoretical Investigation in to Thermally Governed Transient Flow Surges in Two-Phase Condensing Flow," ASME Journal of Heat Transfer 99 (4) (1977) pp.561-567.

39. Bhatt, B. L. and G. L. Wedekind, 1980 "A Self-Sustained Oscillatory Flow Phenomenon in Two-Phase Condensing Flow Systems," ASME *Journal of Heat Transfer*, Vol. 102, No. 4, pp. 695-700.

40. Bhatt, B. L., G. L. Wedekind, and K. Jung., 1989, "Effects of Two-Phase Pressure Drop on the Self-Sustained Oscillatory Instability in Condensing Flows," *Journal of Heat Transfer*, Vol. 111, pp. 538-545.

41. Bhatt, B. L., G. L. Wedekind, and K. Jung, 1989, " Effects of Two-phase pressure Drop on the Self-Sustained Oscillatory Instabilty in Condensing Flow," ASME *Journal of Heat Transfer* 111, 538-545.

42. Faghri, A., 1995, *Heat Pipe Science and Technology*, Taylor and Francis, Washington D. C.

43. Faghri, A. and Y. Zhang, 2006, *Transport Phenomena in Multiphase Systems*, Elsevier Academic Press.

44. Patankar, S. V., 1980, "*Numerical Heat Transfer and Fluid Flow*," Hemisphere, Washinton DC.

45. Schlichting, H., 1968, *Boundary Layer Theory*, Sixth Edition, McGraw Hill.

46. Turner, J. S., 1973, *Buoyancy Effects in Fluids*, Cambridge Univrsity Press, London.

47. Kundu, P. K., 1990, *Fluid Mechanics*, Academic Press, Sandiego, CA, USA.

48. Fujii, T., H. Uehara, and C. Kurata, 1972, "Lainar Filmwise Condensation of Flowing Vapor on a Horizontal Cylinder," *International Journal of Heat and Mass Transfer*, 15: 235-246.

49. Ruelle, D. and Takens, F. 1971, "On the Nature of Turbulence," *Communications in*

Mathematical Physics, Vol. 20, pp. 162-192.

50. Gurtin, M. E., 1981, *An Introduction to Continuum Mechanics*, Academic Press, New York.

51. Whitaker, S., 1977, *Fundamental Principles of Heat Transfer*, Pergamon Press, New York.

52. Enright, D., R. Fedkiw, J. Ferziger, and I. Mitchell, 2002, "A Hybrid Particle Level Set Method for Improved Interface Capturing," *Journal of Computational Physics*, volume 183, number 1, pp. 83-116.

53. Mukherjee, A. and V. K. Dhir, 2005, "Study of Lateral Merger of Vapor Bubbles During Nucleate Pool Boiling," Journal of Heat Transfer, Vol. 126, pp. 1023-1039.

54. Weatherburn, C. E., 1930, *Differential Geometry of Three Dimensions* (Vols. 1 and 2), Cambridge University Press.

55. Plesset, M. S. and Prosperetti, A., 1976, "Flow of Vapour in a Liquid Enclosure," *Journal of Fluid Mechanics*, 78 (3), pp. 433-444.

APPENDIX A.1

The interface conditions that apply at $\Phi\,(x,\,y,\,t) = y - \Delta(x,\,t) = 0$, involve values of flow variables at the interface that are denoted by a superscript 'i'. The unit normal at any point on the interface, directed from the liquid towards the vapor, is denoted by $\hat{\mathbf{n}}$ and is equal to $\nabla\phi\,/\,|\nabla\phi|$. The unit tangent at any point on the interface, directed towards increasing x, is denoted by $\hat{\mathbf{t}}$. Each phase is modeled as a viscous and incompressible Newtonian fluid with stress tensor $\mathbf{T} = -\mathrm{p}_I\mathbf{1} + \mathbf{S}_I$ where

$\mathbf{S}_I = \mu_I\{(\mathrm{grad}\cdot\mathbf{v}_I) + (\mathrm{grad}\cdot\mathbf{v}_I)^T\}/2$ and $\mathbf{1}$ is the identity tensor.

• The surface velocity $\mathbf{v}_s$ of a point on the interface ($\phi = 0$) at time t is associated with this point's movement to a new mapped position on the interface at time t + Δt. All such mappings must be such that the normal component of this $\mathbf{v}_s$ is given by:

$$\mathbf{v}_s\cdot\hat{\mathbf{n}} = -(\partial\phi\,/\,\partial t)\,/\,|\nabla\phi| \ . \tag{A.1}$$

• The tangential component of the vapor and liquid velocities at the interface must be continuous, i.e.

$$\mathbf{v}_1^i\bullet\hat{\mathbf{t}} = \mathbf{v}_2^i\bullet\hat{\mathbf{t}}. \tag{A.2}$$

• Allowing for variations in surface tension σ over the interface such that the vector $\nabla_s\sigma$ is in the tangent plane and ignoring the normal component of viscous stresses in

183

comparison to interfacial pressures, the normal component of momentum balance at a point on the interface is given by:

$$p_1^i = p_2^i + \dot{m}^2(1/\rho_2 - 1/\rho_1) + \sigma \nabla_s \bullet \hat{\mathbf{n}} - \nabla_s \sigma \bullet \hat{\mathbf{n}} + (\mathbf{S}_1^i - \mathbf{S}_2^i)\hat{\mathbf{n}} \bullet \hat{\mathbf{n}}$$
$$\cong p_2^i + \dot{m}^2(1/\rho_2 - 1/\rho_1) - (\sigma \Delta_{xx})/[1+\Delta_x^2]^{2/3}. \qquad (A.3)$$

The symbols for the vector $\nabla_s \sigma$ and the curvature $\nabla_s \bullet \hat{\mathbf{n}}$ in the first equality of the above equation respectively denote surface-gradient operator and surface-divergence operator and their meanings are well defined in suitable differential geometry textbooks (see, e.g., Weatherburn [54]).

• The tangential component of momentum balance at any point on the interface, which allows for surface variations in the surface tension σ, reduces to:

$$\mathbf{S}_1^i \hat{\mathbf{n}} \bullet \hat{\mathbf{t}} = \mathbf{S}_2^i \hat{\mathbf{n}} \bullet \hat{\mathbf{t}} + \nabla_s \sigma \bullet \hat{\mathbf{t}}. \qquad (A.4)$$

• The mass-fluxes $\dot{m}_{VK}$ and $\dot{m}_{LK}$ as determined by the kinematic restrictions imposed by interfacial values of vapor and liquid velocities are:

$$\dot{m}_{VK} \equiv -\rho_2(\mathbf{v}_2^i - \mathbf{v}_s) \bullet \hat{\mathbf{n}} \quad \text{and} \quad \dot{m}_{LK} \equiv -\rho_1(\mathbf{v}_1^i - \mathbf{v}_s) \bullet \hat{\mathbf{n}} \qquad (A.5)$$

• The energy balance at a point on the interface, with energy fluxes being relative to the interface, imposes a restriction on the interfacial mass flux $\dot{m}_{Energy}$, and this restriction is given by:

184

$$\dot{m}_{Energy} = \frac{1}{h_{fg}}[\{k_1 \nabla T_1|^i \cdot \hat{n} - k_2 \nabla T_2|^i \cdot \hat{n}\} + \frac{d\sigma}{dt}\Big|_s + \frac{1}{2}\dot{m}\{|\mathbf{v}_1^i - \mathbf{v}_s|^2 - |\mathbf{v}_2^i - \mathbf{v}_s|^2\}$$
$$+ \{\mathbf{S}_1^i \hat{n} \cdot (\mathbf{v}_1^i - \mathbf{v}_s) - \mathbf{S}_2^i \hat{n} \cdot (\mathbf{v}_2^i - \mathbf{v}_s)\}]$$
$$\cong \frac{1}{h_{fg}}[k_1 \frac{\partial T_1}{\partial n}\Big|^i - k_2 \frac{\partial T_2}{\partial n}\Big|^i].$$

(A.6)

In deriving the first equality in Eq. (A.6) above, the equality of surface energy per unit area to surface tension force per unit length is assumed as per usual assumption regarding equilibrium interfacial thermodynamics. The symbol $\dfrac{d\sigma}{dt}\Big|_s$ denotes rate of change of surface energy per unit area per unit time and equals $\dfrac{\partial\sigma}{\partial t} + \mathbf{v}_s \cdot \nabla_{,s}\sigma$. This term along with interfacial kinetic energy exchanges and exchanges associated with the workings of the normal components of the viscous stresses are considered negligible to the net interfacial heat transfer.

• Mass Balance at any point on the interface requires a single-valued interfacial mass-flux. That is:

$$\dot{m}_{LK} = \dot{m}_{VK} = \dot{m}_{Energy} \equiv \dot{m}.$$

(A.7)

• To account for the non-equilibrium thermodynamic effects of non-zero interfacial mass flux $\dot{m}$, the interfacial pressures p_1^i and p_2^i along with their difference $\Delta p^i \equiv p_1^i - p_2^i$ that appear in Eq. (A.3) are additionally considered to be controlled by non-equilibrium thermodynamics and are thought as $p_1^i \equiv p_{1\,n\text{-}eq}^i(T_1^i)$ and $p_2^i \equiv p_{2\,n\text{-}eq}^i(T_2^i)$, where T_1^i is the liquid side interfacial temperature and T_2^i is the vapor side interfacial temperature. In

185

the limit of zero mass flux $\dot{m}$, these thermodynamic pressures reach their equilibrium thermodynamic values and are denoted as $p_1^i \equiv p_{sat}(T_1^i)$ and $p_2^i \equiv p_{sat}(T_2^i)$, where p_{sat} is the inverse function of the saturation temperature $T_s(p)$. Here, the non-equilibrium and equilibrium values of the interfacial pressure differences are denoted as $(\Delta p^i)_{\text{n-eq}}$ and $(\Delta p^i)_{\text{sat}}$. To allow for a temperature discontinuity (i.e. interfacial thermal resistance) across the interface, one must set $(\Delta p^i)_{\text{n-eq}}$ equal to $\Delta p^i \equiv p_1^i - p_2^i$ as obtained from Eq. (A.3), and, in addition, one must provide an *explicit* or *implicit model* for a function f of the type ($\Delta p^i)_{\text{n-eq}} = f\{(\Delta p^i)_{\text{sat}}, \dot{m}\}$, where f allows the two pressure differences to become the same for zero mass flux $\dot{m}$. It is common to *model* f by considerations that involve kinetic theory of gas for the vapor phase (see, e.g., section 4.5 of Carey [36], Plesset and Prosperetti [55], etc.). At all points away from x ~ 0, the assumption that use of either $(\Delta p^i)_{\text{n-eq}}$ or $(\Delta p^i)_{\text{sat}}$ as Δp^i in Eq. (A.3) do not significantly affect the *near zero* value of $\Delta T^i \equiv T_s(p_2^i + \Delta p^i) - T_s(p_2^i)$ is well known and well justified in the present context where interfacial thermal resistances are overshadowed by significantly larger thermal resistance of the thin condensate (see section 4.5 of Carey [36]). Furthermore, the computations in this thesis also show: (i) that the solution further downstream is not affected by the nature of the singular solution at x ~ 0 (where non-equilibrium thermodynamics is important), and, (ii) that the computed downstream values of $\Delta T^i \equiv T_s(p_2^i + \Delta p^i) - T_s(p_2^i)$, where Δp^i values are obtained from Eq. (A.3, satisfy $\Delta T^i \cong 0$ in the sense that $\Delta T^i \ll \Delta T$, where ΔT is the number defined for Eq. (1).

Therefore, under negligible interfacial resistance approximation, the interfacial temperature values satisfy: $\mathcal{T}_1^i \cong \mathcal{T'}_2^i = \mathcal{T}_s(p_2^i)$.

$$(A.8)$$

• The term [t] on the right side of Eq. (5) is given by:

$$[t] = \{\frac{\mu_2}{\mu_1}\frac{\partial v_2}{\partial x}\Big|^i - \frac{\partial v_1}{\partial x}\Big|^i\} + \frac{2\delta_x}{[1-\delta_x^2]}\{\frac{\partial u_1}{\partial x}\Big|^i - \frac{\partial v_1}{\partial y}\Big|^i\} - \frac{2\delta_x}{[1-\delta_x^2]}\frac{\mu_2}{\mu_1}\{\frac{\partial u_2}{\partial x}\Big|^i - \frac{\partial v_2}{\partial y}\Big|^i\}$$

$$(A.9)$$

APPENDIX A.2

<u>Summary of the algorithm used by 2-D computational approach to solve internal</u>

<u>condensing flow problem :</u>

1. At discrete number of spatial locations, following variables are guessed: δ, u_{1s}^i, v_{1s}^i, θ_{1s}^i, u_2^i, v_2^i, θ_2^i. These seven guess functions are adjusted with the help of seven interface conditions and imposed exit condition if any. The following steps implement this philosophy by separate single-phase (liquid and vapor domain) calculations (see Figures 4-5) for a "sharp interface" model.

2. After fixing $\{u_{1s}^i, v_{2s}^i, \theta_{1s}^i\}$ on shifted interface (see Figure 4), liquid domain is solved under shifted interface by a *finite-volume* (SIMPLER) or a *finite-element* method. The $\{u_{1s}^i, v_{1s}^i, \theta_{1s}^i\}$ are adjusted to satisfy tangential stress (Eq. (5)), normal stress (Eq. (4)), and saturation temperature (Eq. (9)) conditions at the interface respectively. If it is an unspecified exit condition case, exit condition given by formulation [A] (see Eq. (11)) is used. If it is a specified exit condition case (formulation [B]) is used. For the specified case in Eq. (14), after using an initial guess of $u_1^i = u_1^i\big|_{guess}$ and a desired imposition function on the right side of Eq. (14) (this function agrees with the exit mass flow rate values for the unspecified case for $t < t^*$), the tentative value of the specified imposition at $t = t^* + \Delta t$ is imposed by changing the guess for $u_1^i = u_1^i\big|_{guess}$ for $t = t^* + \Delta t$ as: $u_1^i\big|_{guess} = \beta \cdot u_1^i\big|_{current}$ with β found so as to equate the left and right side of Eq. (14). Based on these modified values of u_1^i, u_{1s}^i values are adjusted to satisfy tangential stress condition. Finally, in this computational approach, it is the converged value of β at $t = t^* + \Delta t$ as obtained at the end of iterative completion of all

188

the steps (steps 1 -5) for this time (t = t* + Δt) that determines the right side of Eq. (14) and, hence, the actual value of the imposed exit liquid mass flow rate. The value of imposed exit liquid mass flow rate is usually in the neighborhood of the original choice for the value of the function on the right side of Eq. (14). Clearly, other superior algorithms for imposing the exit condition on the right side of Eq. (14) are possible.

3. After fixing $\{u_2^i, v_2^i, \theta_2^i\}$ on interface δ (see Figure 5), vapor domain *above* the interface is solved by the same *finite-volume* method (SIMPLER). The guesses for u_2^i, v_2^i, and θ_2^i are updated with the help of: continuity of tangential velocity (Eq. (3)), interfacial mass flux equality $\dot{m}_{VK} = \dot{m}_{Energy}$, and saturation temperature (Eq. (9)) conditions at the interface respectively.

4. The interface location is updated (by tracking the interface) on an adaptive Eulerian Grid which remains fixed over a time interval [t, t + Δt] of interest. This is done by solving the following equation obtained through the remaining interface condition, namely: $\dot{m}_{LK} = \dot{m}_{Energy}$

$$\frac{\partial\delta}{\partial t} + \overline{u}(x,t)\frac{\partial\delta}{\partial x} = \overline{v}(x,t)$$
$$\delta(0,t) = 0$$
$$\delta(x,0) = \delta_{steady}(x) \quad \text{or} \quad \delta_{any}(x) \tag{A.10}$$

189

The numerical solution of Eq. (A.10) yields a converged value of δ (x, t+Δt) on the fixed Eulerian grid. These values are then used to obtain the δ (x, t+Δt) values on the fixed (for all t) CFD grid being used for the liquid and vapor CFD calculations.

5. Next the newly obtained liquid and vapor domains for time t + Δt under the new interface locations define a change of the domains in Figure 1 (i.e., $\mathcal{L}_t \rightarrow \mathcal{L}_{t+\Delta t}$ and $\mathcal{V}_t \rightarrow \mathcal{V}_{t+\Delta t}$). A simple mapping technique is used to map the computed values of the flow variables (velocity, pressure, etc.) to the newly updated extents for the vapor and liquid domains.

The above steps 1-5 are repeated in such a way that all the interface conditions, differential equations, etc. are satisfied (and, for the specified exit condition case, the specified exit flow rate is consistent with the converged values of β at all times t). It should be noted that while solving strictly steady governing equations, the same algorithm is followed but all the time dependencies are made equal to zero and, also, no exit condition is (or can be) prescribed as steady equations are essentially parabolic in nature.

APPENDIX A.3

Net mechanical energy $\dot{W}_{\text{Mech-in}}$ input rate into the condenser control volume

Net rate of mechanical energy going in to the control volume $\dot{W}_{\text{Mech-in}}$ is obtained from the integral form of *mechanical energy equation* (see [51]) for individual liquid and vapor domains and then adding them together. For any control-volume "CVf–total" that represents the condenser and encloses separate liquid and vapor domains of the type in Figures 4-5, if one denotes the liquid-vapor interface by Σ, the bounding surface of the control volume by "CSf-total," and unit normal on the bounding surface by $\mathbf{n}$, the expression for $\dot{W}_{\text{Mech-in}}$ is given as:

$$\dot{\mathbf{W}}_{\text{Mech-in}} = \int_{\text{Csf-total}} -p_{rel}(\mathbf{n} \cdot \mathbf{V})da + \int_{\text{Csf-total}} -(1/2)\rho|\mathbf{V}|^2(\mathbf{n} \cdot \mathbf{V})da + \int_{\text{Cvf-total}} \{\rho \boldsymbol{g} \cdot \mathbf{V}\}d\boldsymbol{v}$$

(A.11)

where $p_{rel} \equiv p - p_0$ are the relative values of the absolute pressures p_I (I = 1 or 2) with respect to the reference inlet pressure p_0. The above expression for the net mechanical energy into the control volume is also obtained from the differential form of *mechanical energy equation* (see Eq. (5.4-13) in Whitaker [51]) integral over individual liquid ($\mathcal{L}$) and vapor ($\mathcal{V}$) volumes and then adding them together. This analysis relates $\dot{W}_{\text{Mech-in}}$ to total viscous dissipations within each of the two domains ($\Phi_L > 0$ for the liquid and $\Phi_V > 0$ for the vapor) and the net mechanical energy consumed $\dot{D}_\Sigma$ across the interface as:

The analysis yields the following form of (A.11):

$$\dot{W}_{\text{Mech-in}} = \Phi_L + \Phi_V + \dot{D}_\Sigma$$

(A.12)

191

where we have,

$$\dot{\mathbf{D}}_\Sigma \equiv \int_\Sigma \left[\frac{\dot{m}}{\rho_2} - \frac{\dot{m}}{\rho_1} \right] p_{ref} da + 0.5 \int_\Sigma \dot{m} \left[\left| \mathbf{V}_2^i \right|^2 - \left| \mathbf{V}_1^i \right|^2 \right] da$$

$$\Phi_L \equiv \quad_1 \{[\nabla \mathbf{v}_1] + [\nabla \mathbf{v}_1^T]\} : [\nabla \mathbf{v}_1] d\upsilon$$

$$\Phi_V \equiv \quad_2 \{[\nabla \mathbf{v}_2] + [\nabla \mathbf{v}_2^T]\} : [\nabla \mathbf{v}_2] d\upsilon$$

(A.13)

Φ_L and Φ_V are well known viscous dissipation rates (see [51]) over the control volume Cvf-total. The interface energy transfer rate $\dot{\mathbf{D}}_\Sigma$ is made up of pressure energy transferred across the interface and kinetic energy transferred across the interface and these are given by (A.14) and (A.15) below.

$$\text{Pressure energy transferred across the interface} = \int_\Sigma \left[\frac{\dot{m}}{\rho_2} - \frac{\dot{m}}{\rho_1} \right] p_{ref} da$$

(A.14)

$$\text{Kinetic energy transferred across the interface} = 0.5 \int_\Sigma \dot{m} \left[\left| \mathbf{V}_2^i \right|^2 - \left| \mathbf{V}_1^i \right|^2 \right] da$$

(A.15)

APPENDIX A.4

The differential forms of mass, momentum (x and y components) and energy equations in terms of non-dimensional variables for flows in the interior of either of the phases (I = 1 or 2) for the external flow problem of Koh [10] are given as

$$\frac{\partial u_I}{\partial x} + \frac{\partial v_I}{\partial y} = 0 \tag{A.16}$$

$$\frac{\partial u_I}{\partial t} + u_I \frac{\partial u_I}{\partial x} + v_I \frac{\partial u_I}{\partial y} = -\left(\frac{\partial \pi_I}{\partial x}\right) + \frac{1}{Re_I}\left(\frac{\partial^2 u_I}{\partial x^2} + \frac{\partial^2 u_I}{\partial y^2}\right) \tag{A.17}$$

$$\frac{\partial v_I}{\partial t} + u_I \frac{\partial v_I}{\partial x} + v_I \frac{\partial v_I}{\partial y} = -\left(\frac{\partial \pi_I}{\partial y}\right) + Fr_y^{-1} + \frac{1}{Re_I}\left(\frac{\partial^2 v_I}{\partial x^2} + \frac{\partial^2 v_I}{\partial y^2}\right) \tag{A.18}$$

$$\frac{\partial \theta_I}{\partial t} + u_I \frac{\partial \theta_I}{\partial x} + v_I \frac{\partial \theta_I}{\partial y} \approx \frac{1}{Re_I Pr_I}\left(\frac{\partial^2 \theta_I}{\partial x^2} + \frac{\partial^2 \theta_I}{\partial y^2}\right), \tag{A.19}$$

where $Re_I \equiv \rho_I U_\infty Y_e/\mu_I$, $Pr_I \equiv \mu_I Cp_I/k_I$, and $Fr_y^{-1} \equiv g_y Y_e/U_\infty^2$.

Under assumptions of: uniform pressure throughout the flow, steadiness ($\partial/\partial t = 0$), horizontalness ($g_x = 0$), and boundary layer approximations ($\partial/\partial x \ll \partial/\partial y$ & $v_I \ll u_I$) associated with thin condensate flow; the Koh formulation ([10]) effectively replaces A(16)-A(19) by:

$$u_I \frac{\partial u_I}{\partial x} + v_I \frac{\partial u_I}{\partial y} \cong \frac{1}{Re_I}\frac{\partial^2 u_I}{\partial y^2},$$

$$-\frac{\partial \pi_I}{\partial y} + Fr_y^{-1} \cong 0, \text{ and}$$

$$u_I \frac{\partial \theta_I}{\partial x} + v_I \frac{\partial \theta_I}{\partial y} \approx \frac{1}{Re_I Pr_I}\left(\frac{\partial^2 \theta_I}{\partial y^2}\right) \tag{A.20}$$

In addition to the above, the Koh formulation [10] also assumes negligible interfacial slope approximation $(\delta'(x)^2 \ll 1)$ and, as a result, interface conditions given by Eqs. (3)-(9) in the section 2.1 are simplified and respectively replaced by eqs. (A.21) - (A.25) given below:

$$u_2^i = u_1^i \tag{A.21}$$

$$\pi_1^i = \frac{\rho_2}{\rho_1}\pi_2^i , \tag{A.22}$$

$$\frac{\partial u_1}{\partial y}\Big|^i = \frac{\mu_2}{\mu_1}\frac{\partial u_2}{\partial y}\Big|^i . \tag{A.23}$$

$$\dot{m}_{LK} \equiv \left[u_1^i(d\delta/dx) - v_1^i\right],$$
$$\dot{m}_{VK} \equiv (\rho_2/\rho_1)\left[u_2^i(d\delta/dx) - v_2^i\right], \text{ and} \tag{A.24}$$

$$\dot{m}_{Energy} \equiv Ja/(Re_1\,Pr_1)\{\partial\theta_1/\partial y\Big|^i - (k_2/k_1)\partial\theta_2/\partial y\Big|^i\}. \tag{A.25}$$

The remaining interface conditions given by Eqs. (7)-(8) in section 2 continue to hold as they need no further approximations. Furthermore, for the Koh formulation [10], no top or exit condition regarding pressure is necessary. Instead, the inlet and the far-field conditions respectively become:

$$u_2(0,y) = U_\infty, \text{ and } \lim_{y\to\infty}u_2(x,y)=U_\infty .$$

$$\tag{A.26}$$

Total *integral* viscous dissipation rate φ (= φ_1 + φ_2) inside any control volume is obtained from *power law theorem* ([50]) or the integral form of *mechanical energy equation* (see [51]) for individual liquid and vapor domains and then adding them

together. For any control-volume "CVf –total" of the type OABD in Figure 3, if one

denotes the liquid-vapor interface by Σ, the bounding surface by "CSf-total," unit normal

on the bounding surface by n, it results in the following expression:

$$\varphi = \int_{Csf\text{-}total} -p_{rel}(\mathbf{n}\cdot\mathbf{V})da + \int_{\Sigma}\left[\frac{\dot{m}}{\rho_1} - \frac{\dot{m}}{\rho_2}\right]p_{rel}da - 0.5 \int_{Csf\text{-}total} \rho|\mathbf{V}|^2(\mathbf{n}\cdot\mathbf{V})da - 0.5 \int_{\Sigma} \dot{m}\left[\left|\mathbf{V}_2^i\right|^2 - \left|\mathbf{V}_1^i\right|^2\right]da$$

(A.27)

where $p_{rel} \equiv p - p_\infty$ is the relative value of absolute pressure $p = p_I$ (I = 1 0r 2) with respect

to the far field pressure p_∞ .

APPENDIX A.5 COPYRIGHT PERMISISION 1

The following copy right permission obtained from New York Academy of Sciences is for the data and plots reproduced in Chapter 4 of this thesis work.

Dear Sir/Madam,

I am a doctoral candidate at Michigan Technological University. A paper co-authored by me has been published in the Annals of New York Academy of Scicenses. The paper is titled:

Narain, A., S. Kulkarni, S. Mitra, J. H. Kurita, M. Kivisalu, 2009, "Computational and Ground Based Experimental Investigations of the Effects of Specified and Unspecified (Free) Pressure Conditions at Condenser Exit for Condensing Flows in Terrestrial and Micro-Gravity Environments," Annals of New York Academy of Sciences , Interdisciplinary Transport Phenomena in Space Sciences, Vol. 1161, pp. 321-360.

I am writing my PhD thesis and I wish to include some of the results published through the above mentioned paper in my PhD thesis.I am writing to obtain copyright permission letter from NYAS to include those results in my thesis.

Please guide me in this matter.

Thanking you,
Yours sincerely,

Shantanu Kulkarni
Doctoral Candidate,
Michigan Tech.

___

Dear Shantanu,

Thank you for your request.
Permission is hereby granted for you to use the material requested for your thesis/dissertation subject to the usual acknowledgements and on the understanding that you will reapply for permission if you wish to distribute or publish your thesis/dissertation commercially.

Best Wishes

Verity Butler
Permissions Assistant
John Wiley & Sons Ltd.

APPENDIX A.6 COPYRIGHT PERMISION 2

The following copyright permission obtained from the ASME's Journal of Heat Transfer is for the data and plots reproduced in Chapter 4 and Chapter 5 of this thesis work.

Dear Sir/Madam,
I am a doctoral candidate at Michigan Technological University. A paper co-authored by me has been published in the Annals of New York Academy of Sciences. The paper is titled: Narain, A., S. Kulkarni, S. Mitra, J. H. Kurita, M. Kivisalu, 2009, "Computational and Ground Based Experimental Investigations of the Effects of Specified and Unspecified (Free) Pressure Conditions at Condenser Exit for Condensing Flows in Terrestrial and Micro-Gravity Environments," Annals of New York Academy of Sciences , Interdisciplinary Transport Phenomena in Space Sciences, Vol. 1161, pp. 321-360.

I am writing my PhD thesis and I wish to include some of the results published through the above mentioned paper in my PhD thesis.

I am writing to obtain copyright permission letter from NYAS to include those results in my thesis.

Please guide me in this matter.

Thanking you,

Yours sincerely,

Shantanu Kulkarni
Doctoral Candidate,
Michigan Tech.

Dear Mr. Kulkarni:

It is our pleasure to grant you permission to use ASME paper "Forced Flow of Vapor Condensing Over a Horizontal Plate, Problem of Cess and Koh.: Steady and Unsteady Solutions of the Full 2D Problem," by Shantanu Kulkarni, Journal of Heat Transfer, Volume 132, cited in your letter for inclusion in a PhD thesis to include computational results to be published by Michigan Technological University.
 As is customary, we ask that you ensure full acknowledgment of this material, the author(s), source and ASME as original publisher on all printed copies being distributed.

Many thanks for your interest in ASME publications.
Sincerely,
Beth Darchi
Permissions & Copyrights
ASME, 3 Park Avenue
New York, NY 10016
Dear Beth,

Thanks for your permission.

Regarding the same, I would also like to request the permission to include results in my thesis from another JHT paper titled:

Narain, A., J. H. Kurita, M. Kivisalu, S. D. Kulkarni, A. Siemionko, T. W. Ng, N. Kim, and L. Phan: "Internal Condensing Flows Inside a Vertical Pipe - Experimental/Computational Investigations of the Effects of Specified and Unspecified (Free) Conditions at Exit," ASME Journal of Heat Transfer, Vol. 129, pp. 1352-1372, 2007.

Please grant me the permission to include the results from this journal paper as well.

Best,

Shantanu Kulkarni

Dear Mr. Kulkarni:
This permission has been revised to reflect all requests. It is our pleasure to grant you permission to use ASME paper s"Forced Flow of Vapor Condensing Over a Horizontal Plate, Problem of Cess and Koh.: Steady and Unsteady Solutions of the Full 2D Problem," by Shantanu Kulkarni, Journal of Heat Transfer, Volume 132, and "Internal Condensing Flows Inside a Vertical Pipe - Experimental/Computational Investigations of the Effects of Specified and Unspecified (Free) Conditions at Exit," by Narain, A., J. H. Kurita, M. Kivisalu, S. D. Kulkarni, A. Siemionko, T. W. Ng, N. Kim, and L. Phan: Journal of Heat Transfer, Vol. 129, pp. 1352-1372, 2007, cited in your letter for inclusion in a PhD thesis to include computational results to be published by Michigan Technological University.
As is customary, we ask that you ensure full acknowledgment of this material, the author(s), source and ASME as original publisher on all printed copies being distributed.

Many thanks for your interest in ASME publications.
Sincerely,
Beth Darchi
Permissions & Copyrights